Quantum Dynamics of optically interacting quantum emitter arrays in confined optical fields

Dissertation

zur Erlangung des akademischen Grades

Doctor of Philosophy

eingereicht an der

Fakultät für Mathematik, Informatik und Physik

der Leopold-Franzens-Universität Innsbruck

von

Martin Fasser M.Sc.

Betreuer: Univ.-Prof. Dr. Helmut Ritsch
Institut für Theoretische Physik

Innsbruck, Juli 2026

Abstract

Understanding how quantum emitters interact with each other is central in explaining many optical phenomena. When the particles interact with each other, new stationary states inaccessible in the non-interacting case will be occupied exhibiting novel physics and offering new application possibilities. A key example are entangled states, which allow for Quantum Key Distribution in order to realize secure communication, can be exploited in Quantum Metrology for precise measurement and are essential in understanding phenomena such as light-harvesting complexes in biological systems or how lasers are able to create coherent light. However, while these new states offer many new possibilities, it becomes increasingly challenging to keep track of them.

Particularly interesting is the interaction of quantum particles mediated by the electromagnetic field, as these interactions are common in nature. Depending on the surroundings, the modes of the electromagnetic field change, allowing us to engineer the interaction: The quantum particles behave differently depending on their environment, e.g. free space allows different interaction lengths than a cavity or a waveguide. The quantum emitters are able to exchange energy via the modes with a so-called coherent energy exchange rate Ω_{ij}. Moreover, their decay is influenced by the surrounding emitters described by the collective decay rates Γ_{ij}, leading to faster decay (superradiance) or slower decay (subradiance). Depending on the emitters and the environment one can therefore engineer the radiating behavior of the emitters, allowing for applications such as a quantum battery or a quantum memory.

In this thesis, we explore how atoms interacting via a cavity mode can constitute a superradiant laser, where the phase coherence is stored in the atoms and not in the cavity field. Hence, cavity mirror fluctuations have only negligible effects on the linewidth. However, the challenge with this setup is that continuous lasing and high laser power are difficult to achieve. We show that with a sample of atoms with finite temperature one can improve the output power by including an optical lattice guiding potential. In contrast, including a velocity filter to filter out the fast atoms seems to have undesired effects and does not improve power.

Next, we explore atoms interacting via the modes of a waveguide. Here, spacing of the atoms allows us to engineer the radiation properties of the whole sample, enabling e.g. fast storage and retrieval of energy: Depending on the pumping scheme, the mere existence of unpumped atoms can inhibit excited atoms from decaying. We find an excitation threshold above which the decay blockade breaks and the energy is transferred to the ground state ensemble. This fast energy transfer fully excites an unpumped ensemble, which can then be used as a gain medium for superradiant lasing. Moreover, the threshold-like behavior can be used to switch from subradiance to superradiance efficiently, which is an important ingredient for building a quantum battery.

In order to simulate big ensembles of quantum emitters, one necessarily has to introduce approximations. One noteworthy approximation is the so-called cumulant expansion. However, there exists no general proof of convergence, so one has to verify and check the results whenever possible. We benchmark the cumulant expansion for different expansion orders and ensemble sizes using the example of Dicke Superradiance. In particular, we investigate the difference between the cumulant expansion on the basis of the individual operators and on the basis of collective operators.

After having investigated the sub- and superradiance properties of atoms in a waveguide, we now turn to the spectral properties of the ensemble for different distances and different pumping schemes. We find enhanced superradiant emission with narrow output spectrum close the resonance frequency of the bare emitters. By analytically calculating the spectrum of a pumped and an unpumped atom, we show how the interaction between them narrows the linewidth.

Finally, we investigate the aggregation dynamics of non-polar molecules in picocavities. Employing a toy model to describe the aggregation due to Van-der-Waals forces, we analyze the influence of viscosity and temperature on the aggregation. Including a cavity alters the interaction potentials, allowing for unique aggregation pathways. Our results underline the role of electromagnetic confinement in the aggregation processes.

Zusammenfassung

Das Verständnis der Wechselwirkungen zwischen Quantenemittern ist von zentraler Bedeutung, um viele optische Phänomene zu erklären. Wenn die Teilchen miteinander interagieren, werden neue stationäre Zustände besetzt, die im Fall ohne Wechselwirkung nicht zugänglich sind; diese weisen neuartige physikalische Eigenschaften auf und bieten neue Anwendungsmöglichkeiten. Ein wichtiges Beispiel sind verschränkte Zustände, die den Quantenschlüsselaustausch zur sicheren Kommunikation ermöglichen, in der Quantenmetrologie für präzise Messungen genutzt werden können und für das Verständnis von Phänomenen wie Lichtsammelkomplexen in biologischen Systemen oder der Erzeugung kohärenten Lichts durch Laser unerlässlich sind. Doch während diese neuen Zustände viele neue Möglichkeiten bieten, wird es zunehmend schwieriger, den Überblick über sie zu behalten.

Besonders interessant ist die durch das elektromagnetische Feld vermittelte Wechselwirkung von Quantenteilchen, da diese Wechselwirkungen in der Natur weit verbreitet sind. Je nach Umgebung ändern sich die Moden des elektromagnetischen Feldes, was es uns ermöglicht, die Wechselwirkung zu steuern: Die Quantenteilchen verhalten sich je nach ihrer Umgebung unterschiedlich, z. B. erlaubt der freie Raum andere Wechselwirkungslängen als ein Resonator oder ein Wellenleiter. Die Quantenemitter sind in der Lage, über die Moden Energie mit einer sogenannten kohärenten Energieaustauschrate Ω_{ij} auszutauschen. Zudem wird ihr Zerfall durch die umgebenden Emitter beeinflusst, was durch die kollektiven Zerfallsraten Γ_{ij} beschrieben wird und zu einem schnelleren Zerfall (Superradianz) oder einem langsameren Zerfall (Subradianz) führt. Abhängig von den Emittern und der Umgebung kann man daher das Strahlungsverhalten der Emitter steuern, was Anwendungen wie eine Quantenbatterie oder einen Quantenspeicher ermöglicht.

In dieser Arbeit untersuchen wir, wie Atome, die über einen Hohlraum interagieren, einen superradianten Laser darstellen können, bei dem die Phasenkohärenz in den Atomen und nicht im Hohlraumfeld gespeichert ist. Deshalb haben Schwingungen der Hohlraumspiegel nur vernachlässigbare Auswirkungen auf die Linienbreite. Die

Herausforderung bei diesem Aufbau besteht jedoch darin, dass ein kontinuierlicher Laserstrahl und eine hohe Laserleistung nur schwer zu erreichen sind. Wir zeigen, dass man bei einer Atomwolke mit endlicher Temperatur die Laserleistung verbessern kann, indem man ein optisches Gitter-Leitpotential einbezieht. Im Gegensatz dazu scheint die Berücksichtigung eines Geschwindigkeitsfilters zum Herausfiltern der schnellen Atome unerwünschte Effekte zu haben und verbessert die Leistung nicht.

Als Nächstes untersuchen wir Atome, die über die Moden eines Wellenleiters interagieren. Über den Abstand der Atome zueinander können wir die Strahlungseigenschaften der gesamten Probe beeinflussen, was z. B. eine schnelle Speicherung und Rückgewinnung von Energie ermöglicht: Je nachdem, wie das Ensemble optisch gepumpt wird, kann allein die Anwesenheit ungepumpter Atome den Zerfall angeregter Atome verhindern. Wir finden eine Anregungsschwelle vor, oberhalb derer die Zerfallsblockade aufgehoben wird und die Energie an das Ensemble im Grundzustand übertragen wird. Dieser schnelle Energietransfer regt ein ungepumptes Ensemble vollständig an, das dann als Verstärkungsmedium für superradiante Laserstrahlung genutzt werden kann. Darüber hinaus kann das schwellenwertartige Verhalten genutzt werden, um effizient von Subradianz zu Superradianz zu wechseln, was ein wichtiger Bestandteil für den Bau einer Quantenbatterie ist.

Um große Ensembles von Quantenemittern zu simulieren, muss man zwangsläufig Näherungen einführen. Eine bedeutende Näherung ist die sogenannte Kumulantenentwicklung. Da es jedoch keinen allgemeinen Konvergenzbeweis gibt, muss man die Ergebnisse nach Möglichkeit überprüfen und verifizieren. Wir führen einen Vergleich der Kumulantenentwicklung für verschiedene Entwicklungsordnungen und Ensemblegrößen am Beispiel der Dicke-Superradianz durch. Insbesondere untersuchen wir den Unterschied zwischen der Kumulantenentwicklung auf der Basis der einzelnen Operatoren und auf der Basis kollektiver Operatoren.

Nachdem wir die Sub- und Superradianz-Eigenschaften von Atomen in einem Wellenleiter untersucht haben, wenden wir uns nun den spektralen Eigenschaften des Ensembles bei unterschiedlichen Abständen und verschiedenen Pump-Mechanismen zu. Wir stellen eine verstärkte superradiante Emission mit einem schmalen Ausgangsspektrum nahe der Resonanzfrequenz der einzelnen Emitter fest. Durch die analytische Berechnung des Spektrums eines angeregten und eines unangeregten Atoms zeigen wir, wie die Wechselwirkung zwischen ihnen die Linienbreite verkleinert.

Abschließend untersuchen wir die Aggregationsdynamik unpolarer Moleküle in Pico-

Hohlräumen. Unter Verwendung eines Toy-Modells zur Beschreibung der durch Van der Waals-Kräfte bedingten Aggregation analysieren wir den Einfluss von Viskosität und Temperatur auf die Aggregation. Die Einbeziehung eines Hohlraums verändert die Wechselwirkungs-Potenziale und ermöglicht so einzigartige Aggregationsverläufe. Unsere Ergebnisse unterstreichen die Rolle der elektromagnetischen Einschränkung bei den Aggregationsprozessen.

Danksagung

Zuallererst bedanke ich mich bei Helmut Ritsch für die ausgezeichnete Betreuung während meiner Zeit in der Arbeitsgruppe. Seine zahlreichen Ideen haben mir immer weitergeholfen und meinen physikalischen Horizont erweitert. Durch seine freundliche Art schafft er ein entspanntes Arbeitsklima, wodurch ich meine Zeit in der Gruppe als sehr angenehm empfand. Großer Dank gilt auch meinem Co-Betreuer Christoph Hotter, der mein engster Ansprechpartner war und mir immer mit Rat und Tat zur Seite stand.

Weiters möchte ich mich auch bei den ehemaligen und aktuellen Mitglieder der Gruppe Ritsch bedanken: Elvia Colella, Daniela Holzmann, Matthias Sonnleitner, Wolfgang Niedenzu, Maria Moreno-Cardoner, David Plankensteiner, Julian Moser, Verena Scheil, Christoph Hotter, Raphael Holzinger, Natalia Masalaeva, Anna Bychek, Karol Gietka, Arkadiusz Kosior, Farokh Mivehvar, Arpita Pal, Laurin Ostermann, Johannes Kerber, Simon Brunner und Barna Mendei.

Außerdem durfte ich eine tolle Zeit in Erlangen in der Gruppe von Claudiu Genes verbringen, ich bedanke mich bei Claudiu und seiner Gruppe für die herzliche Aufnahme, ich habe mich vom ersten Tag an sehr wohl gefühlt. Ein besonderer Dank gilt Sofia Ribeiro, die mit ihrer Expertise ein gemeinsames Projekt ermöglicht hat, bei dem ich sehr viel gelernt habe.

Claudiu war gemeinsam mit Gregor Weihs und Helmut Ritsch Mitglied meines Thesis Comittee; ihre Rückmeldungen haben mir gezeigt, dass ich mich auf einem guten Weg befinde. Weiters möchte ich mich bei dem Doktoratskolleg Atoms, Light, and Molecules (DK-ALM) bedanken, das mir Summer Schools, Konferenzen, Auslandsaufenthalte und vor allem den engen Kontakt zu anderen PhD-Studenten ermöglicht hat. Besonders hervorheben möchte ich Heide Streicher, die für jede Frage ein offenes Ohr hat.

Privat möchte ich mich bei meinen Studienkollegen, allen voran Lorenz Panzl, bedanken, ohne die die Zeit des Studiums nicht mal halb so schön gewesen wäre.

Der größte Dank gilt meiner Familie, im Besonderen meinen Eltern Roman und Bettina und meiner Schwester Eva, welche mich immer unterstützt und ermutigt haben.

Contents

1 Introduction **1**

1.1 Historical Background 1

1.2 Basic physics of sub- and superradiance using the Dicke Triangle . . . 3

1.3 Outline of this thesis 9

2 The quantum description of atoms, fields and their interaction **11**

2.1 The atomic Hamiltonian 11

2.2 The dipole interaction 13

2.3 Quantum harmonic oscillator 14

2.4 The quantum description of the electromagnetic field of free space . . 16

2.5 The interaction Hamiltonian 23

3 Atomic dynamics in a quantized radiation field **27**

3.1 Transition rates from Fermi's Golden Rule 27

3.2 The Wigner-Weisskopf ansatz for spontaneous emission of an excited atom 33

4 Collective coupling of atoms in a one dimensional optical waveguide **43**

4.1 Connection between master equation for density operator and system operator 50

4.2 Sokhotski-Plemelj theorem 51

5 The cumulant expansion **55**

6 Publication: Threshold studies for a hot beam superradiant laser **59**

6.1 Introduction 60

6.2 Methods: Theoretical Model 61

6.3 Photon number dependence on temperature 63

6.4 Adding a velocity filter 65

6.5 Dynamics including an optical lattice potential 66

6.6 Conclusions . . . 69
6.7 Appendix . . . 69

7 Publication: Subradiance and superradiant long-range excitation transport in a waveguide 75
7.1 Introduction . . . 76
7.2 Model . . . 77
7.3 Subradiant States . . . 79
7.4 Superradiance and Superabsorption . . . 81
7.5 Uniform Distribution: Coherent Dipole-Dipole Interaction Effects . . . 84
7.6 Conclusions . . . 86
7.7 Supplemental document . . . 87

8 Publication: Benchmarking the Cumulant Expansion Method Using Dicke Superradiance 91
8.1 Introduction . . . 92
8.2 Theoretical description . . . 94
8.3 Cumulant Expansion Method . . . 95
8.4 Benchmarking cumulant expansion convergence . . . 96
8.5 Conclusions . . . 102

9 Publication: Continuous Narrow-Linewidth Superradiance in Waveguide-QED 105
9.1 Introduction . . . 106
9.2 Theoretical description . . . 109
9.3 Steady-state results . . . 115
9.4 Conclusions . . . 123
9.5 Supplemental Material . . . 124

10 Ongoing work: Molecular Aggregation Dynamics inside picocavities 139
10.1 Introduction . . . 140
10.2 Theoretical Framework and Intermolecular Interaction Potentials . . . 141
10.3 Modeling Nonpolar Molecule-Cavity Interactions . . . 147
10.4 Numerical Results . . . 154
10.5 Experimental Feasibility and Potential Applications . . . 171
10.6 Conclusions . . . 175
10.7 Appendix . . . 177

11 Conclusions and Outlook **185**

Bibliography **189**

1 Introduction

1.1 Historical Background

At the end of the 19th century physicists believed, that the physics knowledge about the world is approaching completion. Isaac Newton's work on classical mechanics could explain the movement of celestial bodies, Maxwell's equations explained the phenomenons of electricity and electromagnetism. Statistical mechanics allowed important problems in thermodynamics to be investigated. People assumed, that, knowing the state of a system with sufficient accuracy, they could (in principle) predict the fate of the system in the future. This view is known as determinism.

However, there were a few open problems, one of them being blackbody radiation or cavity radiation. A blackbody is a an idealized source of thermal radiation, which completely absorbs electromagnetic radiation of all wavelengths. While such an ideal blackbody does not exist, some real devices come very close to the properties of an ideal blackbody. Their radiation was studied in great detail and in particular the spectrum, i.e. the distribution of intensity depending on wavelength. While the Rayleigh-Jeans law, developed from classical considerations of a cavity, agreed with experimental observations for low frequencies, the law predicted higher and higher radiation power for higher frequencies, e.g. at the frequency of ultraviolet light. This conundrum is known as the "ultraviolet catastrophe" and was in direct contradiction to the observed spectra. Planck practically resolved the problem by finding an interpolation between the Rayleigh-Jeans law and Wien's distribution law, which could predict the spectra at high and low frequencies. For this explanation, Planck needed to use the assumption (known as Planck postulate), that the energy of the radiation at each frequency in this blackbody is quantized. In 1905 Einstein used this quantization to explain the photoelectric effect, which would later earn him the Nobel prize. The quantization was later used to explain the spectrum of hydrogen by Niels Bohr.

While the Planck postulate certainly was instrumental in the explanation of many

phenomena, the foundation for a revolutionary new theory was laid in 1925, when Schroedinger discovered the equation that governs the time evolution of quantum system: the Schroedinger equation. From then on, quantum mechanics conquered physics and led to many advancements: By combining quantum physics with special relativity, Dirac discovered his improved equation predicting antimatter. Eventually further advancements led to quantum field theories, such as the Standard Model of Particle Physics, which explain the physics of the smallest known particles as quarks, leptons and bosons and is the closest thing we have to a world-formula, a formula which could explain the whole physical world.

In this work, however, we focus on quantum optics as an effective theory on the interaction between atoms described quantum mechanically and photons as the elements of quantized electromagnetic fields. Atoms interact with the electromagnetic field by absorbing or emitting photons. Energy and momentum conservation must be fulfilled, such that the energy of the atom is raised when absorbing a photon and lowered when emitting a photon. The absorption can happen preferentially when a photon with appropriate energy hits the atom. As postulated by Einstein the emission can be spontaneous, with no other photon initiating the process or it can be stimulated, meaning that one photon triggers the emission of a second photon. The rates of these processes of absorption, spontaneous emission and stimulated emission are given by the Einstein coefficients [1]. Together, they allow to set up rate equations which can lead to a simple model of a laser. The stimulated emission already gives us a hint at what is to come: We can influence the radiation properties of a single atom by changing its surroundings. A single atom may decay through spontaneous emission, but the resulting photon has the capabilities to trigger a whole avalanche of photons through stimulated emission. These collective effects allow a multitude of new effects and open the door to many new applications, such as the laser as the most important example.

In 1954, Robert Dicke published the paper "Coherence in Spontaneous Radiation Processes" [2] in which he considered a radiating gas as a single quantum-mechanical system and showed, how the collective coupling of the atoms changed its radiation properties. This sparked more and more interest into these collective radiation phenomena and culminated in 1982 in the review "Superradiance: An Essay on the theory of collective spontaneous emission" [3] by Gross and Haroche. In this review, the Dicke model was revisited and the equations for a system of N two-level atoms are derived, ending up in a master equation for superradiance.

Developing the theoretical framework of many-atom master equations to describe open quantum systems allowed to describe and explain lasers fully quantum. Nowadays lasers are so precise, that they can be used to test the most advanced theories with unprecedented accuracy. To further investigate their properties, Cavity Quantum Electrodynamics (QED) was born: Within this framework one is able to consider models with high numbers of atoms and a strong collective coupling to the electromagnetic field. In recent years, waveguides have gained importance as a platform for studying such collective dynamics. Here, the interaction between atoms is mediated via the modes of the fiber, allowing for strong coupling between atoms and electromagnetic field over a large distance.

However, not only superradiance emerges from such a collective coupling. Depending on the coupling, the opposite effect, called subradiance, where the emission of radiation is suppressed, can occur. This even occurs in nature, where so-called light-harvesting-complexes are responsible for absorbing and retaining the radiation in order to make use of it later [4, 5]. The interplay between superradiance and subradiance is exploited in quantum memories [6–10] and quantum batteries [11–15], allowing us to store states and energy quickly for later use. A better understanding of the phenomena of superradiance and subradiance will also allow us to build better quantum memories, which in turn can be used for quantum networks [16]. These networks have a whole variety of applications like quantum communication or distributed quantum computing. Understanding collective radiation and the interplay between superradiance and subradiance is therefore critical in order to advance in the quest for promising applications like quantum communication.

1.2 Basic physics of sub- and superradiance using the Dicke Triangle

In order to understand superradiance and subradiance on a conceptual (mathematical) level, the so-called Dicke triangle is useful, as it allows us to clearly depict the coupling of N two-level systems. Superradiant and subradiant states can be identified using minimal effort then. We will see how symmetries decide, whether our system is in a superradiant state to get rid of its excitation quickly or in a subradiant state, where the excitation can be stored for a long time.

Let us start with a dilute sample of excited atoms in free space. As long as the

atoms are placed sufficiently far apart to each other, each atom will decay individually through spontaneous emission. The atoms are simply too far apart to noticeably influence each other. The length scale here is given by the wavelength of the emitted radiation. In the case, that the distance between atoms is several wavelengths, the atoms will decay individually. Increasing the number of atoms or reducing the sample size, one observes a faster and stronger emission compared to the sum of emissions from the individual atoms [3]. This phenomenon is called superradiance. To get an intuitive understanding for the underlying mechanism, let us go to the extreme case, where the atoms are all located within a region much smaller than the wavelength λ of the emitted radiation.

In principle, here we have to take into account different mechanisms and forces, like collisions between atoms or van der Waals-forces. Some of these mechanisms and their influence on the system have been discussed in [3].

In order to gain an intuitive insight, however, we neglect these effects. In the extreme case of the ensemble occupying a region much smaller than the wavelength λ, the positions of the atoms cannot be resolved anymore by the emitted radiation of the atoms because of the Heisenberg uncertainty. Therefore we can no longer refer to the atoms individually, now they are collectively coupled to the electromagnetic field. The atoms are now indistinguishable and the state of the ensemble of atoms stays the same under any permutation of atoms. In fact, the whole time evolution of the atomic system then will stay in this symmetric subspace of the complete Hilbert space. This effective model of superradiance is called the Dicke Model [2]. The indistinguishability of the atoms allows us to write down the states in a more convenient form: We label the excited state of the atoms $|e\rangle$ and the ground state $|g\rangle$. This two-level system is equivalent to a spin-$\frac{1}{2}$ system, so we can use the Pauli spin matrices for transitions between the states. The coupling of N two-level systems is now equivalent to the addition of angular momentum. In the simple case of $N = 3$, we write for the initial state, where all atoms are excited, $|\Psi(0)\rangle = |eee\rangle$. Due to the analogy to the angular momentum addition, in order to denote these states we use the terminology of their total angular momentum J and its projection onto some axis M according to $|J, M\rangle$. As the symmetric subspace corresponds to the the biggest possible angular momentum subspace and the angular momentum for one atoms is $\frac{1}{2}$, we have $J = \frac{N}{2}$ for all symmetric states. Then, the projection M is restricted to values between $-J$ and J, while $J + M$ gives us the number of excitations in the system. We write now $|\frac{3}{2}, \frac{3}{2}\rangle = |\Psi(0)\rangle = |eee\rangle$. In order to find the other states in the symmetric subspace,

let us find out what happens if one photon is emitted from the initial state $|\frac{3}{2},\frac{3}{2}\rangle$. Due to the symmetric nature of the atomic ensemble, the decay operators must also be symmetric. Here, we define the collective decay operator

$$\hat{S}^- = \sum_i^N \hat{\sigma}_i^- \tag{1.1}$$

as the sum over the individual decay operators $\hat{\sigma}_i^-$, where the sum runs over the index i numbering each atom to the total number of atoms N. Applying the collective decay operator $\hat{S}^-$ to our inital state, we arrive at the state of the system after the emission of one photon. Repeated application of the collective decay operator allows us to go down this so-called Dicke ladder. Because we start at a symmetric state and the collective decay operator is also symmetric, all these states on the Dicke ladder are symmetric. Eventually we will end up in the ground state of the system, where all individual atoms are in the ground state. Together, these states make up the Dicke subspace or symmetric subspace of the full Hilbert space. Including normalization and for a general J (but still $J = \frac{N}{2}$) one finds [3]

$$|J,M\rangle = \sqrt{\frac{(J+M)!}{N!(J-M)!}} \cdot (\hat{S}^-)^{J-M}|eee...e\rangle \tag{1.2}$$

As the rate of emission scales with the norm of $\hat{S}^-|J,M\rangle$, let us compute this norm for general J and M:

$$\begin{aligned}
\langle J,M|\hat{S}^+\hat{S}^-|J,M\rangle &= ||\hat{S}^-|J,M\rangle||^2 \\
&= \frac{(J+M)!}{N!(J-M)!}||\hat{S}^-(\hat{S}^-)^{J-M}|ee..ee\rangle||^2 = \\
&= \frac{(J+M)!}{N!(J-M)!}||(\hat{S}^-)^{J-M+1}|ee..ee\rangle||^2 = \\
&= \frac{(J+M)!}{N!(J-M)!} \cdot \frac{N!(J-M+1)!}{(J+M-1)!}||\ |J,M\rangle||^2 = \\
&= \frac{(J+M)!}{(J-M)!} \cdot \frac{(J-M+1)!}{(J+M-1)!} = (J+M)\cdot(J-M+1)
\end{aligned}$$

For the first emission of a photon, $J = \frac{N}{2}$ and $M = \frac{N}{2}$ we arrive at $(J+M)\cdot(J-M+1) = N$, meaning that the emission is N times faster than the emission of a single atom. This is the same rate as just the N individual rates of each atom summed up. The ensemble decays therefore just as fast as an ensemble of individually decaying atoms at the very

beginning of cascading down the Dicke ladder. However, the rate of decay increases: In the middle of the Dicke ladder, at $M \approx 0$, the rate becomes $(J+M)\cdot(J-M+1) \propto N^2$. The radiation rate now scales quadratically, not linearly as expected in the individual case. This enhancement of the radiation rate is known as Superradiance, in this simple case in the Dicke Model one calls it the Dicke Superradiance. The underlying cause of this enhanced radiation rate is the symmetric coupling of the atoms to the environment.

This naturally raises questions about the behavior of the system when this symmetry is broken. When breaking this symmetry, we leave the symmetric subspace and therefore the Dicke ladder and explore the rest of this so-called Dicke Triangle (see figure 1.1): The right edge of the Dicke triangle is the Dicke ladder (blue shaded area), where all the symmetric states are located and $J = \frac{N}{2}$. Due to the rules of angular momentum addition, where $J \leq \frac{N}{2}$ and $-J \leq M \leq J$ for each corresponding J, the area of allowed states corresponds to a triangle, the Dicke triangle. In figure 1.1 we depict J on the x-axis and M on the y-axis. One can acquire the states by repeatedly applying the collective decay operator to each state. However, as in the case for the Dicke ladder, this only leads straight down the Dicke triangle. To explore the non-symmetric states one can start by diagonalizing the subspace with $N-1$ excitations, while having the symmetric state with $N-1$ as the first basis state of this manifold. This will lead to an expression for the state(s) $|J-1, M-1\rangle$ (note, that this state has multiplicity $N-1$). From this state, the collective decay operator $\hat{S}^-$ leads to the state $|J-1, M-2\rangle$ and one can extend the Dicke Triangle in vertical direction by the collective decay operator and in horizontal direction by diagonalizing the subspace of the so-called n-excitation manifold, where $0 \leq n \leq N$. Individual decay from $|J, M\rangle$ does not only lead straight down to $|J, M-1\rangle$, but also to the neighboring states $|J-1, M-1\rangle$ and $|J+1, M-1\rangle$. Concluding from our observation, that the fast superradiant decay brings states vertically down, we might ask what is happening to the states on the lower border of the Dicke triangle. The collective decay would lead outside of the triangle and is therefore not allowed. Hence, these states cannot decay via the collective decay and are therefore much more long-lived. These states are then called subradiant states (red shaded area in figure 1.1) and are useful for storing the excitation. In order to access these states, one needs to relax this condition of symmetry. Let us take the simplest case with $N = 2$, then the symmetric states are

$$|1, -1\rangle = |ee\rangle \tag{1.3a}$$

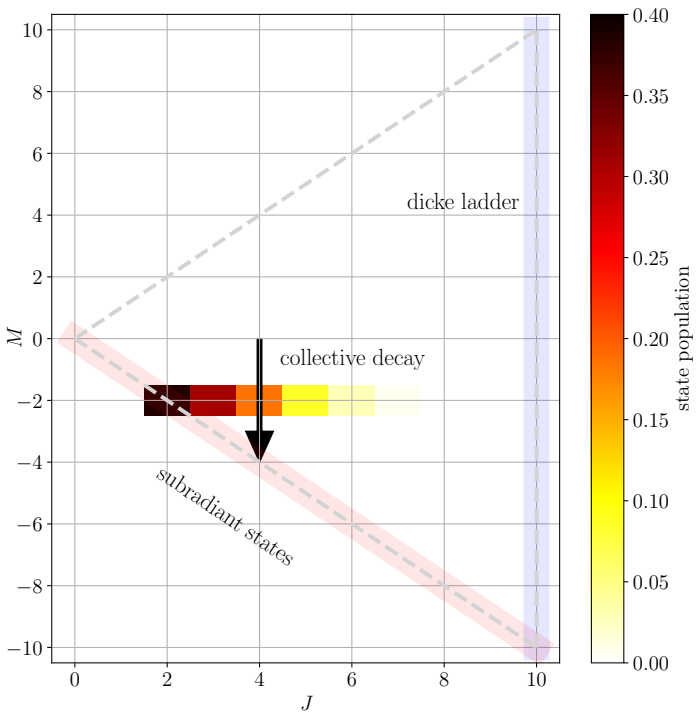

Figure 1.1: *The Dicke triangle for $N = 20$ atoms.* Here we can visualize the coupling of $N = 20$ atoms. The colour denotes the population of a particular state, when expressed in these collective spin states. The normal rules for angular momentum addition lead to the restrictions of $J \leq \frac{N}{2}$ and $-J \leq M \leq J$. The symmetric states in the Dicke ladder are located at the very right column of the Dicke triangle (blue shaded area). As a collective decay event in the diagram leads straight down, the states at the lower line of the triangle (red shaded area) are protected against the superradiant decay and are therefore called subradiant.

$$|1,-1\rangle = \frac{1}{\sqrt{2}} \cdot \Big(|eg\rangle + |ge\rangle\Big) \tag{1.3b}$$

$$|1,-1\rangle = |gg\rangle \tag{1.3c}$$

Together they make up the Dicke ladder. The only remaining state is the antisymmetric state

$$|0,0\rangle = \frac{1}{\sqrt{2}} \cdot \Big(|eg\rangle - |ge\rangle\Big) \tag{1.4}$$

An easy algebraic check confirms, that $\hat{S}^-|0,0\rangle = 0$. This state is located on the left corner of the associated Dicke triangle. In order to prepare this state, let us

assume we pump both atoms with a laser. The according Hamiltonian is given by $\hat{H}_{\text{pump}} = |\Omega| \cdot e^{-i\phi}(\hat{\sigma}^+ + \hat{\sigma}^-)$, where $|\Omega|$ is the amplitude and ϕ is the phase of the laser pulse. One can analytically calculate the time evolution of the atom (see e.g. [17] p. 57-60) starting from the ground state and is left with

$$|\psi(t)\rangle = -ie^{-i\phi} \sin\theta \, |e\rangle + \cos\theta \, |g\rangle, \tag{1.5}$$

where $\theta = \frac{|\Omega|t}{2}$. Without loss of generality, we assume that the first atom is driven with zero phase $\phi_1 = 0$ and the second with an arbitrary phase $\phi_2 = \phi$. Then the collective state is given by

$$\begin{aligned} |\Psi(t)\rangle = &- e^{-i\phi} \sin^2\theta \, |ee\rangle + \cos^2\theta \, |gg\rangle + \\ &- i \sin\theta\cos\theta \, |eg\rangle - ie^{-i\phi} \sin\theta\cos\theta \, |eg\rangle \end{aligned}$$

After a $\pi/2$ pulse ($\theta = \pi/4$) we have, projected onto the single excitation manifold, the following state

$$\langle \bullet, 0|\Psi\rangle \propto |eg\rangle + e^{-i\phi} \, |eg\rangle \tag{1.6}$$

Comparing this to equations 1.3b and 1.4, we see that the phase (difference) ϕ decides, in which state we end up. For the same phases ($\phi = 0$) and therefore symmetric coupling we end up on the Dicke ladder in the symmetric state, which is subject to superradiant decay. For opposite phases ($\phi = \pi$) and so-called antisymmetric coupling we end up in the antisymmetric state, which is not subject to the superradiant decay and therefore subradiant.

In conclusion, the symmetric/antisymmetric coupling determines if we end up in a superradiant or a subradiant state. Through careful preparation of our ensemble of atoms, we thus can engineer the radiation properties of the ensemble. If we extend the pulse to a full π-pulse, we end up in the fully inverted state $|ee\rangle$, regardless of the chosen phase. For a higher number of atoms, the calculations get more tedious, but the qualitative behavior stays the same. A numerical implementation allows us to depict the state of the ensemble with $N = 16$ in figure 1.2. As one can see, during the pumping (at least in the first half) most of the population is close to or even in the subradiant states. If we stop the pumping at that time, the system will decay via superradiant decay straight down into the subradiant states, where it gets trapped and holds on to its excitation. These mechanisms are further investigated in chapter 7.

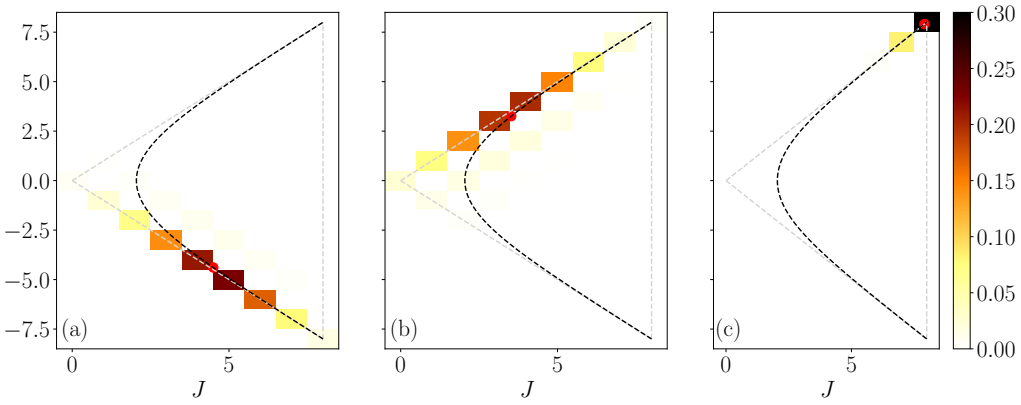

Figure 1.2: *The Dicke triangle for $N = 16$ atoms.* We see the population in the Dicke triangle for asymmetric pumping during the first half of the pump (a), the second half of the pump (b) and almost at the end (c). The red dot shows the current expectation values for J and M. During the pump, the red dot moves along the dashed line. During the first half of the pumping, the state is very close to the lower bound of the triangle where the subradiant states are. Further pumping necessarily leads to the state distancing itself to the subradiant states and after the pulse is complete, we are in the fully excited state $|\frac{N}{2}, \frac{N}{2}\rangle$.

1.3 Outline of this thesis

After we understood the importance of superradiance and subradiance for various applications and have gained a conceptual insight into the mechanisms using the Dicke triangle, let us be more thorough and investigate the emission of photons by atoms in different surroundings more carefully.

To this end, we start by introducing a proper quantum description of atoms, of the electromagnetic field and their interaction. Based on these findings, one can use the Fermi Golden Rule to find an expression for the radiation rate of an atom. Using the Wigner-Weisskopf ansatz, we will explore how to the atom decays exponentially and ends up in the ground state. These results can be derived solely from the Schroedinger equation with some appropriate approximations, most notably the Markov approximation. Then we are ready to investigate the radiation properties of atoms surrounded by other atoms. The interactions between these atoms are mediated by, in our case, one dimensional optical waveguides. For this system, we will derive a master equation governing the dynamics. Once again, the Markov approximation will prove helpful. To conclude the introductory part, we make remarks about how to

implement these equations numerically by using the so-called cumulant expansion.

In chapter 6 we explore atoms interacting with a cavity mode constituting a superradiant laser and investigate in particular the influence of a finite temperature on the laser power and how a velocity filter for the atoms or an atomic guiding potential affect the photon numbers.

In chapter 7 we turn to atoms in a waveguide and investigate their radiation properties. On the basis of different pumping schemes and the distance between atoms one can engineer subradiant and superradiant states, allowing a fast energy transfer between atomic ensembles.

In chapter 8 we study the cumulant expansion in a systematic way using Dicke Superradiance. In particular, we explore the differences between the cumulant expansion on the basis of the individual operators and on the basis of collective operators and when to use which expansion depending on atom numbers.

In chapter 9 we turn back to atoms in a waveguide and focus now on the spectral properties. Pumping only a part of the atoms, we find superradiant emission and a narrow spectrum. The coupling of the atoms induced by the waveguide enables a narrow linewidth, which can be seen by analytical calculations of a simple model.

In chapter 10 we look into the aggregation of molecules in a picocavity. To this end, we build a toy model for the molecules and simulate their aggregation first without the cavity. Then we show how including the cavity alters the aggregation, allowing for new aggregation pathways.

2 The quantum description of atoms, fields and their interaction

2.1 The atomic Hamiltonian

We start by finding a description for the atom [17] to make our calculations as simple as possible. While in reality atoms have many different energy levels, for many calculations we do not need to take them into account. In fact, restricting our model of the atom to a two level system will already be sufficient to capture many relevant physical properties. Even in the event of a laser driving onto the atom, only transitions between levels that are close in energy to the laser frequency have a big impact on the dynamics. Off-resonant states are not excited, but lead to a slight shift of the energy values of the states, which is known as the AC Stark shift and can be derived by using second order perturbation theory. A more detailed description of this can be found in [17] (p. 52). As the only effect of these off-resonant transitions is to introduce a small energy shift for both our chosen levels, we can incorporate these shifts directly into the transition frequency between the two levels.

We call the lower state $|g\rangle$ the ground state with energy E_g and the upper state $|e\rangle$ the excited state with energy E_e. The energy difference $E_\mathrm{e} - E_\mathrm{g} = \hbar\omega_\mathrm{a}$ fixes the transition frequency ω_a, that a laser resonant to that transition would have to be at to strongly excite the atom. As a spin-$\frac{1}{2}$-particle also has two energy levels, we utilize the spin formalism to find the Hamiltonian for the two level system. We define

$$|e\rangle = \begin{pmatrix} 1 \\ 0 \end{pmatrix}, \quad |g\rangle = \begin{pmatrix} 0 \\ 1 \end{pmatrix} \tag{2.1}$$

and then the Pauli Matrices

$$\sigma^\mathrm{z} = \begin{pmatrix} 1 & 0 \\ 0 & -1, \end{pmatrix}, \quad \sigma^\mathrm{x} = \begin{pmatrix} 0 & 1 \\ 1 & 0 \end{pmatrix}, \quad \sigma^\mathrm{y} = \begin{pmatrix} 0 & -i \\ i & 0 \end{pmatrix}, \quad \sigma^0 = \mathbb{1} = \begin{pmatrix} 1 & 0 \\ 0 & 1 \end{pmatrix} \tag{2.2}$$

give a basis of hermitian 2 by 2 matrices, which will allow us to describe all Hamiltonians that can act on this two level system. The energy of the atom is given by

$$\hat{H} = \frac{\hbar\omega_\mathrm{a}}{2}\hat{\sigma}^z \tag{2.3}$$

analogous to the case of a spin-$\frac{1}{2}$-particle in a magnetic field, where ω is the transition frequency. For our case it is also convenient to introduce a new notation

$$\hat{\sigma}^{ij} = |i\rangle\langle j|. \tag{2.4}$$

Note, that now products of operators are trivial: $\hat{\sigma}^{ij} \cdot \hat{\sigma}^{kl} = |i\rangle\langle j| \cdot |k\rangle\langle l| = |i\rangle\langle l|\delta_{jk} = \hat{\sigma}^{il}\delta_{jk}$. With this new notation we straightforwardly define the ladder operators

$$\hat{\sigma}^+ = \hat{\sigma}^{\mathrm{eg}} = |e\rangle\langle g| = \begin{pmatrix} 0 & 1 \\ 0 & 0 \end{pmatrix}, \quad \hat{\sigma}^- = \hat{\sigma}^{\mathrm{ge}} = |g\rangle\langle e| = \begin{pmatrix} 0 & 0 \\ 1 & 0 \end{pmatrix}, \tag{2.5}$$

and the projectors onto the excited and ground state respectively

$$\hat{\sigma}^{\mathrm{ee}} = |e\rangle\langle e| = \begin{pmatrix} 1 & 0 \\ 0 & 0 \end{pmatrix}, \quad \hat{\sigma}^{\mathrm{gg}} = |g\rangle\langle g| = \begin{pmatrix} 0 & 0 \\ 0 & 1 \end{pmatrix}, \tag{2.6}$$

From our definitions we now determine the relations between these two sets of basis matrices and find

$$\begin{aligned} \hat{\sigma}^z &= \hat{\sigma}^{ee} - \hat{\sigma}^{gg} = \hat{\sigma}^{ee} - (\mathbb{1} - \hat{\sigma}^{ee}) = 2 \cdot \hat{\sigma}^{ee} - \mathbb{1} \\ \mathbb{1} &= \hat{\sigma}^{ee} + \hat{\sigma}^{gg} \\ \hat{\sigma}^x &= \hat{\sigma}^{eg} + \hat{\sigma}^{ge} \\ \hat{\sigma}^y &= -i\hat{\sigma}^{ge} + i\hat{\sigma}^{ge} \end{aligned}$$

which allows us to express the Hamiltonian by

$$\hat{H}_{\mathrm{atom}} = \hbar\omega_\mathrm{a}\hat{\sigma}^{ee} = \hbar\omega_\mathrm{a}|e\rangle\langle e| \tag{2.7}$$

where we shifted the energy such that the ground state has zero energy.

2.2 The dipole interaction

As typical optical frequencies have wavelengths of at least a few hundred nm, but the length scale of an atom given by e.g. the Bohr radius of 0.0529 nm is orders of magnitudes smaller, we can assume that the electric field is constant over the extent of the atom. This allows to treat the interaction simply in the dipole approximation [18]. The interaction energy E_{int} of a classical (neutral) particle at position $\mathbf{r}$ in the dipole approximation is then given as [19]

$$E_{\text{int}} = -\mathbf{d} \cdot \mathbf{E}(\mathbf{r}) \tag{2.8}$$

For canonical quantization, we need to find the corresponding quantum operators. Let us first start with the classical dipole, which is given by $\mathbf{d} = q\mathbf{r}$, where q is the charge and $\mathbf{r}$ is the (relative) position of the electron versus the nucleus from the atom. In our simple case of a two-level atom we only look at one transition, therefore one electron and we have as a charge $q = -e$ with the elementary charge e. The position $\mathbf{r}$ is straightforwardly quantized and then the dipole operator looks like

$$\hat{\mathbf{d}} = -e\hat{\mathbf{r}} \tag{2.9}$$

To work with this dipole operator, we need to find its matrix expression in terms of the previously defined operators $\hat{\sigma}^{ij}$. The dipole operator in matrix representation is

$$\hat{\mathbf{d}} = \begin{pmatrix} \langle i|q\mathbf{r}|i\rangle & \langle i|q\mathbf{r}|j\rangle \\ \langle j|q\mathbf{r}|i\rangle & \langle j|q\mathbf{r}|j\rangle \end{pmatrix} = \begin{pmatrix} \mathbf{d}_{ii} & \mathbf{d}_{ij} \\ \mathbf{d}_{ji} & \mathbf{d}_{jj} \end{pmatrix} \tag{2.10}$$

where the matrix elements can be calculated by

$$\mathbf{d}_{ij} = q \int d\mathbf{r}^3 \langle \psi_i | \hat{\mathbf{r}} | \psi_j \rangle. \tag{2.11}$$

If $i = j$, then the integrand is odd (as the position operator is odd) and the integral vanishes. If $i \neq j$, we carry out the integral and arrive at some value, which is determined by the structure of the atomic orbitals in question. To leave this as general as possible, we assume for the integral some value $\mathbf{d}_{ij}$. Note, that by definition $\mathbf{d}_{ij} = \mathbf{d}_{ji}^*$.

For certain symmetries the integral is 0, a transition between these states is not allowed (in dipole approximation) which leads to the well-known selection rules. These

transitions are called dipole-forbidden, and can only decay via quadrupole interaction or even higher order radiation. As the quadrupole moment of typical transitions is usually much smaller than typical dipole moments, forbidden transitions are long-lived, making them candidates for superradiant lasing and precise atomic clocks [20–22].

Using the matrix element 2.11 and our operators $\hat{\sigma}^{ij}$ as a basis, we can write

$$\hat{\mathbf{d}} = \mathbf{d}_{eg} \cdot \hat{\sigma}^{eg} + \mathbf{d}_{ge} \cdot \hat{\sigma}^{ge} \tag{2.12}$$

where the vector $\mathbf{d}$ is a classical dipole amplitude.

2.3 Quantum harmonic oscillator

In this section we introduce the quantum harmonic oscillator. Later, we will see that the electromagnetic field can be described as a sum over different modes, each mode corresponding to a quantum harmonic oscillator. The underlying reason for this is the wave equation for the electromagnetic field, which can be derived from the Maxwell equations. After a spatial Fourier transform, one ends up with the equation of a harmonic oscillator for each frequency, from where the quantization scheme is the same as for a mechanical harmonic oscillator, which is presented in the following.

As usual, we start from the classical harmonic oscillator with Hamiltonian

$$H = \frac{p^2}{2m} + \frac{1}{2} m\omega^2 q^2, \tag{2.13}$$

where p and q are the canonical momentum and position variables, m is the mass and ω denotes the frequency of the oscillator. Canonical quantization allows us to replace the canonical variables by their respective operator counterparts $\hat{p}$ and $\hat{q}$ with commutation relations

$$[\hat{p}, \hat{p}] = 0 \qquad [\hat{q}, \hat{q}] = 0$$
$$[\hat{q}, \hat{p}] = i\hbar$$

It has turned out to be useful to define new operators a and $a^\dagger$ (for motivation see [23])

$$\hat{a} = \frac{1}{\sqrt{2\hbar m\omega}} \cdot \left(\omega\hat{q} + i\hat{p}\right) \tag{2.14}$$

$$\hat{a}^\dagger = \frac{1}{\sqrt{2\hbar m\omega}} \cdot \Big(\omega\hat{q} - i\hat{p}\Big). \tag{2.15}$$

Using these definitions and the canonical commutation relations for $\hat{p}$ and $\hat{q}$ one finds

$$[\hat{a}, \hat{a}^\dagger] = 1 \qquad\qquad [\hat{a}^\dagger, \hat{a}] = -1. \tag{2.16}$$

Rewriting the Hamiltonian in terms of the new operators $\hat{a}$ and $\hat{a}^\dagger$ yields

$$\hat{H} = \frac{\hat{p}^2}{2m} + \frac{1}{2}m\omega^2\hat{x}^2 = \hbar\omega\Big(\hat{a}^\dagger\hat{a} + \frac{1}{2}\Big) \tag{2.17}$$

The last term $\frac{1}{2}\hbar\omega$ is just an energy shift and can be dropped from the Hamiltonian, as it is just introducing a global phase. Making the observation, that $[\hat{H}, \hat{a}] = -\hbar\omega\hat{a}$ and $[\hat{H}, \hat{a}^\dagger] = \hbar\omega\hat{a}^\dagger$, we find the reason for defining these new operators: From the spectral theorem (e.g. [24] (p. 562)), we know that the eigenvectors of a hermitian operator form an eigenbasis, so let's label these eigenstates $|n\rangle$ with the index n and corresponding eigenvalue E_n. From

$$\hat{H}\hat{a}^\dagger|n\rangle = \Big([\hat{H}, \hat{a}^\dagger] + \hat{a}^\dagger\hat{H}\Big)|n\rangle = \Big(\hbar\omega\hat{a}^\dagger + \hat{a}^\dagger E_n\Big)|n\rangle = \Big(E_n + \hbar\omega\Big)\hat{a}^\dagger|n\rangle \tag{2.18}$$

we conclude, that $\hat{a}^\dagger|n\rangle$ is also an eigenstate of the Hamiltonian but with the higher energy $E_n + \hbar\omega$. The operator $\hat{a}^\dagger$ has raised the energy of the state, therefore we call it the raising operator or creation operator. Similar calculations with $\hat{a}$ lead to $\hat{H}\hat{a}|n\rangle = \Big(E_n - \hbar\omega\Big)\hat{a}|n\rangle$, so we call $\hat{a}$ the lowering operator or the annihilation operator. Together they make up the ladder operators and create/annihilate one quantum of energy. In mechanical systems these quanta are named phonons, whereas in optical systems these quanta are called photons. As there has to be a lowest state, let us label it with $|0\rangle$, so the index already tells us how many quanta of energy this state has. By applying the raising operator $\hat{a}^\dagger$ n-times we find the higher energy eigenstates. These number states are called Fock states, the resulting basis is the Fock basis. For the derivations in the next chapters these states will be very useful and provide a basis, in which we can work efficiently. Summarizing, we find

$$\begin{aligned}
\hat{H}|n\rangle &= n\hbar\omega \\
\hat{a}^\dagger|n\rangle &= \sqrt{n+1}|n+1\rangle \\
\hat{a}^\dagger|n\rangle &= \sqrt{n}|n-1\rangle
\end{aligned}$$

with $n \in \mathbb{N}_0 = 0, 1, 2, 3, ...$, where we dropped the constant term in the Hamiltonian.

The coefficients for the raising and lowering operators can be found by requiring the normalization using

$$\langle n|\hat{a}\hat{a}^\dagger|n\rangle = \langle n|[\hat{a},\hat{a}^\dagger] + \hat{a}^\dagger\hat{a}|n\rangle = \langle n|1+n|n\rangle = n+1. \tag{2.19}$$

This recursive relation allows us to get all eigenstates from the ground state by

$$|n\rangle = \frac{(\hat{a}^\dagger)^n}{\sqrt{n!}}|0\rangle \tag{2.20}$$

2.4 The quantum description of the electromagnetic field of free space

In this chapter we want to find operator expressions for the electromagnetic field and the respective Hamiltonian. The derivation can be found in many textbooks, e.g. [25] or [26]. This will allow us to set up a Schroedinger equation for a single atom interacting with the electromagnetic field. The time evolution of an excited atom can then be derived analytically with the Wigner-Weisskopf ansatz and yields a decay of the atom into the ground state via the emission of a photon.

As we want to find the electromagnetic modes of vacuum, we start by stating the Maxwell equations in free space [19, 27] in a given rest frame:

$$\nabla \cdot \mathbf{B}(\mathbf{r},t) = 0 \tag{2.21a}$$

$$\nabla \times \mathbf{E}(\mathbf{r},t) = -\frac{\partial \mathbf{B}(\mathbf{r},t)}{\partial t} \tag{2.21b}$$

$$\nabla \cdot \mathbf{E}(\mathbf{r},t) = 0 \tag{2.21c}$$

$$\nabla \times \mathbf{H}(\mathbf{r},t) = \frac{\partial \mathbf{D}(\mathbf{r},t)}{\partial t} \tag{2.21d}$$

with the electric field $\mathbf{E}(\mathbf{r},t)$, the magnetic field $\mathbf{B}(\mathbf{r},t)$, the displacement field $\mathbf{D}(\mathbf{r},t)$ and the magnetizing field $\mathbf{H}(\mathbf{r},t)$. As we are in vacuum, we assume that there are no free charges $\rho(\mathbf{r},t) = 0$ and no currents $\mathbf{j}(\mathbf{r},t) = 0$, the relation for the displacement field $\mathbf{D}(\mathbf{r},t)$ and the magnetizing field $\mathbf{H}(\mathbf{r},t)$ are straightforward and read

$$\mathbf{B}(\mathbf{r},t) = \mu_0 \mathbf{H}(\mathbf{r},t) \tag{2.22a}$$

$$\mathbf{D}(\mathbf{r},t) = \epsilon_0 \mathbf{E}(\mathbf{r},t) \tag{2.22b}$$

with the vacuum permittivity ϵ_0 and the vacuum permeability μ_0. Note, that $\frac{1}{\epsilon_0\mu_0} = c^2$. If we were in an isotropic medium, the vacuum permittivity and vacuum permeability simply get replaced by their respective values in the particular medium, yielding $\frac{1}{\epsilon_0\mu_0} = c_{\text{med}}^2$, with c_{med} denoting the speed of light in the chosen medium. In anisotropic media, the permittivity and permeability may not be described as a scalar, but rather a tensor and one encounters e.g. non-parallel electric field $\mathbf{E}(\mathbf{r}, t)$ and displacement field $\mathbf{D}(\mathbf{r}, t)$ if the permittivity is a tensor. Here, we restrict ourselves to the vacuum and due to the isotropy the permittivity and permeability are just described by scalars according to equations 2.22a and 2.22b.

To find general solutions for the Maxwell equations, we first make the following observation: Taking the curl of equation 2.21b and using the well known and easy to prove relation $\nabla \times (\nabla \times \mathbf{A}) = \nabla(\nabla \cdot \mathbf{A}) - \Delta\mathbf{A}$ for a general vector field $\mathbf{A}$ yields

$$\text{LHS} : \nabla \times (\nabla \times \mathbf{E}(\mathbf{r}, t)) = \nabla(\nabla \cdot \mathbf{E}(\mathbf{r}, t)) - \Delta\mathbf{E}(\mathbf{r}, t)) = -\Delta\mathbf{E}(\mathbf{r}, t)) \tag{2.23a}$$

$$\begin{aligned}\text{RHS} : \; -\nabla \times \frac{\partial \mathbf{B}(\mathbf{r}, t)}{\partial t} &= -\frac{\partial}{\partial t}\Big(\nabla \times \mathbf{B}(\mathrm{r}, t)\Big) \\ &= -\frac{\partial}{\partial t}\Big(\mu_0\epsilon_0 \frac{\partial}{\partial t}\mathbf{E}(\mathbf{r}, t)\Big) = -\frac{1}{c^2}\frac{\partial^2}{\partial t^2}\mathbf{E}(\mathrm{r}, t)\end{aligned} \tag{2.23b}$$

where in the second line we used the interchangeability of derivatives for reasonably well-behaved functions and then inserted equation 2.21d. Equating both sides gives us the wave equation for the electric field $\mathbf{E}(\mathrm{r}, t)$

$$\Delta\mathbf{E}(\mathbf{r}, t)) - \frac{1}{c^2}\frac{\partial^2}{\partial t^2}\mathbf{E}(\mathrm{r}, t) = 0 \tag{2.24}$$

with $\Delta \equiv \nabla^2$. Taking the curl of equation 2.21d and using 2.21a and 2.21b one can derive the same equation for the magnetic field $\mathbf{B}(\mathrm{r}, t)$. The solutions of these wave equations are planar waves $e^{i(\mathbf{k}\cdot\mathbf{r} - \omega_{\mathbf{k}}t)}$ with some wavevector $|\mathbf{k}| = \frac{\omega_k}{c}$. This suggests decomposing the electric field into its Fourier components and looking at the Maxwell equations in momentum space. We define the Fourier components of the electric field $\mathbf{E}(\mathbf{k}, t)$ by

$$\mathbf{E}(\mathbf{r}, t) \equiv \int \frac{d\mathbf{k}}{(2\pi)^3}\mathbf{E}(\mathbf{k}, t) \cdot e^{i\mathbf{k}\cdot\mathbf{r}} \tag{2.25}$$

The Fourier decomposition of the magnetic field $\mathbf{B}(\mathbf{r}, t)$ shall be defined accordingly. Note, that there exist slightly different definitions of the Fourier transform, in particular the $(2\pi)^3$ and the sign in the exponent are sometimes chosen differently. As long as one stays consistent within ones chosen definition, in particular the inverse Fourier

transform, these minor modifications cancel out.

Now we want to look at the Maxwell equation in momentum space. To this end, we note some so-called "replacement rules"

$$\nabla \cdot \to i\mathbf{k} \cdot \qquad\qquad \nabla \times \to i\mathbf{k} \times . \tag{2.26}$$

which allow us to immediately rewrite the Maxwell equations in Fourier space. These rules are easy to derive, e.g. for $\nabla\cdot$

$$\nabla\cdot\mathbf{E}(\mathbf{r},t) = \int \frac{d\mathbf{k}}{(2\pi)^3}\mathbf{E}(\mathbf{k},t)\cdot\left(\nabla e^{i\mathbf{k}\cdot\mathbf{r}}\right) = \int \frac{d\mathbf{k}}{(2\pi)^3}\mathbf{E}(\mathbf{k},t)\cdot i\mathbf{k}\cdot e^{i\mathbf{k}\cdot\mathbf{r}} = \int \frac{d\mathbf{k}}{(2\pi)^3} i\mathbf{k}\cdot\mathbf{E}(\mathbf{k},t)\cdot e^{i\mathbf{k}\cdot\mathbf{r}} \tag{2.27}$$

Inserting this into 2.21c and using the orthogonality between modes with different wavevector $\mathbf{k}$ leads to

$$i\mathbf{k}\cdot\mathbf{E}(\mathbf{k},t) = 0 \tag{2.28}$$

The other Maxwell equations can be transformed into momentum space likewise and we get

$$i\mathbf{k}\cdot\mathbf{B}(\mathbf{k},t) = 0 \tag{2.29a}$$

$$i\mathbf{k}\times\mathbf{E}(\mathbf{k},t) = -\frac{\partial\mathbf{B}(\mathbf{k},t)}{\partial t} \tag{2.29b}$$

$$i\mathbf{k}\cdot\mathbf{E}(\mathbf{k},t) = 0 \tag{2.29c}$$

$$i\mathbf{k}\times\mathbf{B}(\mathbf{k},t) = \frac{1}{c^2}\frac{\partial\mathbf{E}(\mathbf{k},t)}{\partial t} \tag{2.29d}$$

From equation 2.29a and 2.29c we conclude, that the direction of the magnetic and the electric field must be perpendicular to the wavevector $\mathbf{k}$, such that in three-dimensional space we can choose two different polarizations. The components of the electric and magnetic fields are zero along the direction of the wavevector $\mathbf{k}$.

Introducing a scalar potential $\phi(\mathbf{r},t)$ and a vector potential $\mathbf{A}(\mathrm{r},t)$ will allow us to trivially solve the equations 2.21a and 2.21b

$$\mathbf{B}(\mathbf{r},t) = \nabla\times\mathbf{A}(\mathbf{r},t) \qquad\qquad \mathbf{E}(\mathbf{r},t) = -\nabla\phi(\mathbf{r},t) - \frac{\partial\mathbf{A}(\mathbf{r},t)}{\partial t}. \tag{2.30}$$

Note, that both potentials can be arbitrary functions and still solve the first two Maxwell equations, which is easy to verify using $\nabla\cdot(\nabla\times\mathbf{A}) = 0$ and $\nabla\times(\nabla\phi) = 0$. Moreover, even for the same resulting electric field and magnetic field, the potentials

are not unique and we are allowed to use gauge transformations according to

$$\mathbf{A}' = \mathbf{A} + \nabla\chi \qquad\qquad \phi' = \phi - \frac{\partial\chi}{\partial t} \tag{2.31}$$

for an arbitrary χ. Inserting equations 2.30 into the Maxwell equations yields

$$-\Delta\phi(\mathbf{r},t) - \frac{\partial}{\partial t}\Big(\nabla\cdot\mathbf{A}(\mathbf{r},t)\Big) = 0 \tag{2.32a}$$

$$-\Delta\mathbf{A}(\mathbf{r},t) + \frac{1}{c^2}\frac{\partial^2\mathbf{A}(\mathbf{r},t)}{\partial t^2} + \nabla\Big(\frac{1}{c^2}\frac{\partial\phi(\mathbf{r},t)}{\partial t} + \nabla\cdot\mathbf{A}(\mathbf{r},t)\Big) = 0 \tag{2.32b}$$

where the identity $\nabla\times\Big(\nabla\times\mathbf{A}\Big) = \nabla\Big(\nabla\cdot\mathbf{A}\Big) - \Delta\mathbf{A}$ once more proves useful. For our problem it is suitable to choose the so-called Coulomb gauge defined by $\nabla\cdot\mathbf{A}(\mathbf{r},t) = 0$ (in this particular case with no charges $\rho(\mathbf{r},t)) = 0$ we simultaneously satisfy the Lorenz gauge), which leads to $\phi(\mathbf{r},t) = 0$ according to equation 2.32a and equation 2.32b simplifies further to the same wave equation that we already had for the electric field $\mathbf{E}(\mathbf{r},t)$ and the magnetic field $\mathbf{B}(\mathbf{r},t)$:

$$-\Delta\mathbf{A}(\mathbf{r},t) + \frac{1}{c^2}\frac{\partial^2\mathbf{A}(\mathbf{r},t)}{\partial t^2} = 0. \tag{2.33}$$

Like the electric field and the magnetic field, also the vector potential $\mathbf{A}(\mathbf{r},t)$ now is perpendicular to the wavevector $\mathbf{k}$ as we required by $\nabla\cdot\mathbf{A}(\mathbf{r},t) = 0$ translating into $i\mathbf{k}\cdot\mathbf{A}(\mathbf{k},t) = 0$ in momentum space.

The general solution to equation 2.33 are plane waves like $\boldsymbol{\epsilon}_\mathbf{k}\cdot e^{i(\mathbf{k}\cdot\mathbf{r}-\omega t)}$ with $\boldsymbol{\epsilon}$ as a polarization direction. From the equation $\mathbf{k}\cdot\boldsymbol{\epsilon}_\mathbf{k} = 0$ follows that to each wavevector $\mathbf{k}$ there exist two independent (in general complex) solutions corresponding to the two independent polarizations λ. In consequence, we choose two solutions such that

$$\epsilon_{\mathbf{k}\lambda_1}\cdot\boldsymbol{\epsilon}^*_{\mathbf{k}\lambda_2} = \delta_{\lambda_1\lambda_2} \quad \text{for } \lambda = 1,\ 2 \tag{2.34}$$

Adding up all these Fourier components we arrive at the general solution for the vector potential

$$\mathbf{A}(\mathrm{r},t) = \sum_\lambda \int \frac{d\mathbf{k}}{(2\pi)^3}\sqrt{\frac{\hbar}{2\epsilon_0\omega_\mathbf{k}}}\cdot\Big[\boldsymbol{\epsilon}_{\mathbf{k},\lambda}\alpha_\lambda(\mathbf{k})\cdot e^{i(\mathbf{kr}-\omega_\mathbf{k}t)} + \boldsymbol{\epsilon}^*_{\mathbf{k},\lambda}\alpha^*_\lambda(\mathbf{k})\cdot e^{-i(\mathbf{kr}-\omega_\mathbf{k}t)}\Big] \tag{2.35}$$

where $\alpha_\lambda(\mathbf{k})$ are unknown coefficients of the Fourier components. The particular choice of normalization constant $\sqrt{\frac{\hbar}{2\epsilon_0\omega_\mathbf{k}}}$ will later become apparent. Using the definitions

for the vector potential $\mathbf{A}$ in equations 2.30 and keeping in mind our chosen gauge, we can find corresponding expressions for the electric field $\mathbf{E}(\mathbf{r},t)$ and the magnetic field $\mathbf{B}(\mathbf{r},t)$ respectively:

$$\mathbf{E}(\mathbf{r},t) = -\frac{\partial \mathbf{A}(\mathbf{r},t)}{\partial t} = \tag{2.36}$$
$$= i\sum_{\lambda}\int \frac{d\mathbf{k}}{(2\pi)^3}\sqrt{\frac{\hbar}{2\epsilon_0\omega_{\mathbf{k}}}}\omega_{\mathbf{k}}\Big[\boldsymbol{\epsilon}_{\mathbf{k},\lambda}\alpha_{\lambda}(\mathbf{k})\cdot e^{i(\mathbf{kr}-\omega_{\mathbf{k}}t)} - \boldsymbol{\epsilon}^{*}_{\mathbf{k},\lambda}\alpha^{*}_{\lambda}(\mathbf{k})\cdot e^{-i(\mathbf{kr}-\omega_{\mathbf{k}}t)}\Big]$$
$$\mathbf{B}(\mathbf{r},t) = \nabla\times\mathbf{A}(\mathbf{r},t) = \tag{2.37}$$
$$= i\sum_{\lambda}\int \frac{d\mathbf{k}}{(2\pi)^3}\sqrt{\frac{\hbar}{2\epsilon_0\omega_{\mathbf{k}}}}\Big[\mathbf{k}\times\boldsymbol{\epsilon}_{\mathbf{k},\lambda}\alpha_{\lambda}(\mathbf{k})\cdot e^{i(\mathbf{kr}-\omega_{\mathbf{k}}t)} - \mathbf{k}\times\boldsymbol{\epsilon}^{*}_{\mathbf{k},\lambda}\alpha^{*}_{\lambda}(\mathbf{k})\cdot e^{-i(\mathbf{kr}-\omega_{\mathbf{k}}t)}\Big].$$

Armed with the general expressions for the electric field $\mathbf{E}(\mathrm{r},t)$ and the magnetic field $\mathbf{B}(\mathrm{r},t)$, we are now ready to find the Hamiltonian for the electromagnetic field. As usual, we start with the classical expression for the energy of the electromagnetic field, which reads (in vacuum) [19, 27]

$$E_{\text{field}} = \frac{\epsilon_0}{2}\int d\mathbf{r}\Big(\mathbf{E}^2(\mathrm{r},t) + c^2\mathbf{B}^2(\mathrm{r},t)\Big). \tag{2.38}$$

We insert the general expressions for the electric field $\mathbf{E}(\mathrm{r},t)$ and the magnetic field $\mathbf{B}(\mathrm{r},t)$ and carry out the necessary calculations. For the simplification the definition of the Dirac delta function δ and a cross-product identity

$$\int d\mathbf{r}\; e^{i(\mathbf{k}_1-\mathbf{k}_2)\cdot\mathbf{r}} = (2\pi)^3\cdot\delta(\mathbf{k}_1-\mathbf{k}_2) \tag{2.39a}$$
$$\Big(\mathbf{k}_1\times\mathbf{a}\Big)\cdot\Big(\mathbf{k}_2\times\mathbf{b}\Big) = \Big(\mathbf{k}_1\cdot\mathbf{k}_2\Big)\cdot\Big(\mathbf{a}\cdot\mathbf{b}\Big) - \Big(\mathbf{k}_1\cdot\mathbf{b}\Big)\cdot\Big(\mathbf{k}_2\cdot\mathbf{a}\Big) \tag{2.39b}$$

will prove helpful.

$$\begin{aligned}
E_{\text{field}} = i^2\frac{\epsilon_0}{2}\sum_{\lambda_1\lambda_2}\int d\mathbf{r}\int\frac{d\mathbf{k}_1}{(2\pi)^3}\frac{d\mathbf{k}_2}{(2\pi)^3}\frac{\hbar}{2\epsilon_0\sqrt{\omega_{\mathbf{k}_1}\omega_{\mathbf{k}_2}}}\cdot \\
\cdot\Big[-\omega_{\mathbf{k}_1}\omega_{\mathbf{k}_2}\Big(\boldsymbol{\epsilon}_{\mathbf{k_1}\boldsymbol{\lambda_1}}\cdot\boldsymbol{\epsilon}^{*}_{\mathbf{k_2}\boldsymbol{\lambda_2}}\alpha_{\lambda_1}(\mathbf{k}_1)\alpha^{*}_{\lambda_2}(\mathbf{k}_2)e^{i(\mathbf{k}_1-\mathbf{k}_2)\mathbf{r}-i(\omega_{\mathbf{k}_1}-\omega_{\mathbf{k}_2})t} + c.c.\Big) \\
- c^2\Big((\mathbf{k}\times\boldsymbol{\epsilon}_{\mathbf{k_1}\boldsymbol{\lambda_1}})\cdot(\mathbf{k}_2\times\boldsymbol{\epsilon}^{*}_{\mathbf{k_2}\boldsymbol{\lambda_2}})\alpha_{\lambda_1}(\mathbf{k}_1)\alpha^{*}_{\lambda_2}(\mathbf{k}_2)e^{i(\mathbf{k}_1-\mathbf{k}_2)\mathbf{r}-i(\omega_{\mathbf{k}_1}-\omega_{\mathbf{k}_2})t} + c.c.\Big) \\
+\omega_{\mathbf{k}_1}\omega_{\mathbf{k}_2}\Big(\boldsymbol{\epsilon}_{\mathbf{k_1}\boldsymbol{\lambda_1}}\cdot\boldsymbol{\epsilon}_{\mathbf{k_2}\boldsymbol{\lambda_2}}\alpha_{\lambda_1}(\mathbf{k}_1)\alpha_{\lambda_2}(\mathbf{k}_2)e^{i(\mathbf{k}_1+\mathbf{k}_2)\mathbf{r}-i(\omega_{\mathbf{k}_1}+\omega_{\mathbf{k}_2})t} + c.c.\Big) \\
+ c^2\Big((\mathbf{k}_1\times\boldsymbol{\epsilon}_{\mathbf{k_1}\boldsymbol{\lambda_1}})\cdot(\mathbf{k}_2\times\boldsymbol{\epsilon}_{\mathbf{k_2}\boldsymbol{\lambda_2}})\alpha_{\lambda_1}(\mathbf{k}_1)\alpha_{\lambda_2}(\mathbf{k}_2)e^{i(\mathbf{k}_1+\mathbf{k}_2)\mathbf{r}-i(\omega_{\mathbf{k}_1}+\omega_{\mathbf{k}_2})t} + c.c.\Big)\Big]
\end{aligned}$$

Now the integral over $d\mathbf{r}$ can be carried out. This will lead, according to 2.39a, to the delta function $\delta(\mathbf{k}_1 - \mathbf{k}_2)$ for terms with $e^{i(\mathbf{k}_1 - \mathbf{k}_2)\cdot\mathbf{r}}$ and to the delta function $\delta(\mathbf{k}_1 + \mathbf{k}_2)$ for terms with $e^{i(\mathbf{k}_1 + \mathbf{k}_2)\cdot\mathbf{r}}$. In the same step, we can carry out the integral over $d\mathbf{k}_2$, as the delta functions makes it trivial to compute, as we just replace $\mathbf{k}_2$ by $\mathbf{k}_1$ or $-\mathbf{k}_1$ respectively. Last, we drop the index 1 from $\mathbf{k}_1$, as this is the only wavevector remaining in the expression. Putting this all together yields

$$\begin{aligned} E_{\text{field}} = \frac{1}{2}\sum_{\lambda_1\lambda_2}\int \frac{d\mathbf{k}}{(2\pi)^3}\frac{\hbar}{2\omega_{\mathbf{k}}}\cdot \\ \cdot\Big[\omega_{\mathbf{k}}^2\Big(\boldsymbol{\epsilon}_{\mathbf{k}\boldsymbol{\lambda}_1}\cdot\boldsymbol{\epsilon}^*_{\mathbf{k}\boldsymbol{\lambda}_2}\alpha_{\lambda_1}(\mathbf{k})\alpha^*_{\lambda_2}(\mathbf{k}) + c.c.\Big) \\ + c^2\Big((\mathbf{k}\times\boldsymbol{\epsilon}_{\mathbf{k}\boldsymbol{\lambda}_1})\cdot(\mathbf{k}\times\boldsymbol{\epsilon}^*_{\mathbf{k}\boldsymbol{\lambda}_2})\alpha_{\lambda_1}(\mathbf{k})\alpha^*_{\lambda_2}(\mathbf{k}) + c.c.\Big) \\ - \omega_{\mathbf{k}}^2\Big(\boldsymbol{\epsilon}_{\mathbf{k}\boldsymbol{\lambda}_1}\cdot\boldsymbol{\epsilon}_{-\mathbf{k}\boldsymbol{\lambda}_2}\alpha_{\lambda_1}(\mathbf{k})\alpha_{\lambda_2}(-\mathbf{k})e^{-2i\omega_{\mathbf{k}}t} + c.c.\Big) \\ - c^2\Big((\mathbf{k}\times\boldsymbol{\epsilon}_{\mathbf{k}\boldsymbol{\lambda}_1})\cdot(-\mathbf{k}\times\boldsymbol{\epsilon}_{-\mathbf{k}\boldsymbol{\lambda}_2})\alpha_{\lambda_1}(\mathbf{k})\alpha_{\lambda_2}(-\mathbf{k})e^{-2i\omega_{\mathbf{k}}t} + c.c.\Big)\Big] \end{aligned}$$

where we also used $\omega_{\mathbf{k}} = \omega_{-\mathbf{k}}$, as $\omega_{\mathbf{k}} = c|\mathbf{k}| = ck$. Now we want to have a look at the cross products and using identity 2.39b we can simplify

$$\begin{aligned} (\mathbf{k}\times\boldsymbol{\epsilon}_{\mathbf{k}\boldsymbol{\lambda}_1})\cdot(\mathbf{k}\times\boldsymbol{\epsilon}^*_{\mathbf{k}\boldsymbol{\lambda}_2}) &= (\mathbf{k}\cdot\mathbf{k})\cdot(\boldsymbol{\epsilon}_{\mathbf{k}\boldsymbol{\lambda}_1}\cdot\boldsymbol{\epsilon}^*_{\mathbf{k}\boldsymbol{\lambda}_2}) - (\mathbf{k}\cdot\boldsymbol{\epsilon}^*_{\mathbf{k}\boldsymbol{\lambda}_2})\cdot(\mathbf{k}\cdot\boldsymbol{\epsilon}_{\mathbf{k}\boldsymbol{\lambda}_1}) = k^2\cdot\delta_{\lambda_1\lambda_2} \\ (\mathbf{k}\times\boldsymbol{\epsilon}_{\mathbf{k}\boldsymbol{\lambda}_1})\cdot(\mathbf{k}\times\boldsymbol{\epsilon}_{-\mathbf{k}\boldsymbol{\lambda}_2}) &= (\mathbf{k}\cdot\mathbf{k})\cdot(\boldsymbol{\epsilon}_{\mathbf{k}\boldsymbol{\lambda}_1}\cdot\boldsymbol{\epsilon}_{-\mathbf{k}\boldsymbol{\lambda}_2}) - (\mathbf{k}\cdot\boldsymbol{\epsilon}_{-\mathbf{k}\boldsymbol{\lambda}_2})\cdot(\mathbf{k}\cdot\boldsymbol{\epsilon}_{\mathbf{k}\boldsymbol{\lambda}_1}) = k^2\cdot(\boldsymbol{\epsilon}_{\mathbf{k}\boldsymbol{\lambda}_1}\cdot\boldsymbol{\epsilon}_{-\mathbf{k}\boldsymbol{\lambda}_2}) \end{aligned}$$

Using these simplifications, the energy for the electromagnetic field looks like

$$\begin{aligned} E_{\text{field}} = \frac{1}{2}\sum_{\lambda_1\lambda_2}\int \frac{d\mathbf{k}}{(2\pi)^3}\frac{\hbar}{2\omega_{\mathbf{k}}}\cdot \\ \cdot\Big[(\omega_{\mathbf{k}}^2 + c^2k^2)\Big(\delta_{\lambda_1\lambda_2}\alpha_{\lambda_1}(\mathbf{k})\alpha^*_{\lambda_2}(\mathbf{k}) + c.c.\Big) \\ - (\omega_{\mathbf{k}}^2 - c^2k^2)\Big(\boldsymbol{\epsilon}_{\mathbf{k}\boldsymbol{\lambda}_1}\cdot\boldsymbol{\epsilon}_{-\mathbf{k}\boldsymbol{\lambda}_2}\alpha_{\lambda_1}(\mathbf{k})\alpha_{\lambda_2}(-\mathbf{k})e^{-2i\omega_{\mathbf{k}}t} + c.c.\Big)\Big] \end{aligned}$$

Using the dispersion relation $\omega_{\mathbf{k}} = ck$ again, we see that the last term drops out and we carry out the sum over λ_2 exploiting the delta function and drop the index 1 from λ_1, as now there is only one polarization variable in the expression. Writing out the complex part then leads to

$$E_{\text{field}} = \frac{1}{2}\sum_{\lambda}\int \frac{d\mathbf{k}}{(2\pi)^3}\hbar\omega_{\mathbf{k}}\cdot\Big(\alpha_\lambda(\mathbf{k})\cdot\alpha^*_\lambda(\mathbf{k}) + \alpha^*_\lambda(\mathbf{k})\cdot\alpha_\lambda(\mathbf{k})\Big) = \sum_{\lambda}\int \frac{d\mathbf{k}}{(2\pi)^3}\hbar\omega_{\mathbf{k}}\cdot\alpha^*_\lambda(\mathbf{k})\cdot\alpha_\lambda(\mathbf{k}) \tag{2.40}$$

In order to quantize [25] (p. 21), we proceed as follows: We note, that the differential

evolution of $\alpha_\lambda(\mathbf{k}, t)$, reads

$$\alpha(\mathbf{k}, t) \propto i\frac{\partial \mathbf{A}(\mathbf{k}, t)}{\partial t} + \omega_\mathbf{k}\mathbf{A}(\mathrm{k}, t) \tag{2.41}$$

and now notice the similarities to the solution for a harmonic oscillator

$$\alpha_{\mathrm{HO}} = \frac{1}{\sqrt{2\omega}}(ip + \omega q) \tag{2.42}$$

as the canonical variables p and q are also connected via a time derivative. This motivates us to define, in analogy to the mechanical harmonic oscillator,

$$\alpha_\lambda(\mathbf{k}) = \frac{1}{\sqrt{2\omega_\mathbf{k}}}(\omega_\mathbf{k} q_{\mathbf{k}\lambda} + ip_{\mathbf{k}\lambda}). \tag{2.43}$$

Inserting this into the equation for the energy of the electromagnetic field 2.40 then yields

$$E_{\mathrm{field}} = \sum_\lambda \int \frac{d\mathbf{k}}{(2\pi)^3}\hbar\omega_\mathbf{k} \cdot \left(\frac{1}{2}p^2_{\mathbf{k}\lambda} + \frac{\omega^2_\mathbf{k}}{2}q_{\mathbf{k}\lambda}\right) \tag{2.44}$$

the equation for the harmonic oscillator. Now we are ready to quantize the electromagnetic field by replacing the canonical variable by their quantum mechanical momentum and position operators satisfying the commutation relations

$$[\hat{q}_{\mathbf{k}\lambda}, \hat{q}_{\mathbf{k}'\lambda'}] = 0 \qquad [\hat{p}_{\mathbf{k}\lambda}, \hat{p}_{\mathbf{k}'\lambda'}] = 0 \tag{2.45a}$$

$$[\hat{q}_{\mathbf{k}\lambda}, \hat{p}_{\mathbf{k}'\lambda'}] = i\hbar\delta(\mathbf{k} - \mathbf{k}')\delta_{\lambda\lambda'} \tag{2.45b}$$

As usual, we also introduce the photon creation operator $\hat{a}^\dagger_{\mathbf{k}\lambda}$ and photon annihilation operator $\hat{a}_{\mathbf{k}\lambda}$

$$\hat{a}_{\mathbf{k}\lambda} = \frac{1}{\sqrt{2\omega_\mathbf{k}}}(\omega_\mathbf{k}\hat{q}_{\mathbf{k}\lambda} + i\hat{p}_{\mathbf{k}\lambda}) \qquad \hat{a}^\dagger_{\mathbf{k}\lambda} = \frac{1}{\sqrt{2\omega_\mathbf{k}}}(\omega_\mathbf{k}\hat{q}_{\mathbf{k}\lambda} - i\hat{p}_{\mathbf{k}\lambda}) \tag{2.46}$$

which satisfy the commutation relations

$$[\hat{a}_{\mathbf{k}\lambda}, \hat{a}_{\mathbf{k}'\lambda'}] = 0 \qquad [\hat{a}^\dagger_{\mathbf{k}\lambda}, \hat{a}^\dagger_{\mathbf{k}'\lambda'}] = 0 \tag{2.47a}$$

$$[\hat{a}_{\mathbf{k}\lambda}, \hat{a}^\dagger_{\mathbf{k}'\lambda'}] = \delta(\mathbf{k} - \mathbf{k}')\delta_{\lambda\lambda'} \tag{2.47b}$$

which one can easily verify through the definitions. Rewriting the Hamiltonian for the

electromagnetic field then leads to

$$\hat{H}_{\mathrm{EM}} = \sum_{\lambda} \int \frac{d\mathbf{k}}{(2\pi)^3} \frac{\hbar\omega_{\mathbf{k}}}{2} \left(\hat{a}_{\mathbf{k}\lambda} \hat{a}^{\dagger}_{\mathbf{k}\lambda} + \hat{a}^{\dagger}_{\mathbf{k}\lambda} \hat{a}_{\mathbf{k}\lambda} \right) \tag{2.48}$$

Using the commutation relations we rewrite the Hamiltonian to its final operator expression

$$\hat{H}_{\mathrm{EM}} = \sum_{\lambda} \int \frac{d\mathbf{k}}{(2\pi)^3} \hbar\omega_{\mathbf{k}} \left(\hat{a}^{\dagger}_{\mathbf{k}\lambda} \hat{a}_{\mathbf{k}\lambda} + \frac{1}{2} \right). \tag{2.49}$$

The $\frac{1}{2}$ is a constant energy offset which can be neglected by shifting the energy in most cases, as we will do for the following derivations. However, this constant energy term has effects on a real physical system, the most well known case being the setup of two metallic plates close together. This changes the modes for the electromagnetic field inside compared to the modes outside and results in the so-called Casimir force [28]. For the system under our consideration though, we drop this constant energy offset, as this would just introduce a global phase.

After we have found the operator expression for the Hamiltonian of the electromagnetic field by replacing the complex amplitudes $\alpha_\lambda(\mathbf{k})$ and $\alpha^*_\lambda(\mathbf{k})$ with the corresponding operator expressions $\hat{a}_{\mathbf{k}\lambda}$ and $\hat{a}^{\dagger}_{\mathbf{k}\lambda}$ respectively, we can do the same in the terms for the electric field $\mathbf{E}(\mathbf{r})$ and the magnetic field $\mathbf{E}(\mathbf{r})$ where we drop the explicit time dependence

$$\hat{\mathbf{E}}(\mathbf{r}, t) = i \sum_{\lambda} \int \frac{d\mathbf{k}}{(2\pi)^3} \sqrt{\frac{\hbar\omega_{\mathbf{k}}}{2\epsilon_0}} \left[\boldsymbol{\epsilon}_{\mathbf{k}\lambda} \cdot \hat{a}_{\mathbf{k}\lambda} \cdot e^{i\mathbf{kr}} - \boldsymbol{\epsilon}^*_{\mathbf{k}\lambda} \cdot \hat{a}^{\dagger}_{\mathbf{k}\lambda} \cdot e^{-i\mathbf{kr}} \right] \tag{2.50}$$

$$\hat{\mathbf{B}}(\mathbf{r}, t) = i \sum_{\lambda} \int \frac{d\mathbf{k}}{(2\pi)^3} \sqrt{\frac{\hbar}{2\epsilon_0\omega_{\mathbf{k}}}} \left[\mathbf{k} \times \boldsymbol{\epsilon}_{\mathbf{k},\lambda} \cdot \hat{a}_{\mathbf{k}\lambda} \cdot e^{i\mathbf{kr}} - \mathbf{k} \times \boldsymbol{\epsilon}^*_{\mathbf{k},\lambda} \cdot \hat{a}^{\dagger}_{\mathbf{k}\lambda} \cdot e^{-i\mathbf{kr}} \right]. \tag{2.51}$$

Now that we have an operator expression for the electric field and the Hamilton operator, we can proceed to investigate the interactions between an atom and the electromagnetic modes of free space.

2.5 The interaction Hamiltonian

In the previous chapters we derived the operator expression for the atomic dipole and the electric field, which now means we are ready to find the quantum analog to the classical interaction energy 2.8 between atom and the radiation field. The Hamiltonian

is

$$\hat{H}_{\text{int}} = -\hat{\mathbf{d}} \cdot \hat{\mathbf{E}} \tag{2.52}$$

and using equations 2.12 for the dipole operator and 2.50 for the electric field operator results in

$$\hat{H}_{\text{int}} = (\mathbf{d} \cdot \hat{\sigma}^{ge} + \mathbf{d}^* \cdot \hat{\sigma}^{eg}) \cdot i \sum_{\lambda} \int \frac{d\mathbf{k}}{(2\pi)^3} \sqrt{\frac{\hbar\omega_{\mathbf{k}}}{2\epsilon_0}} \left[\boldsymbol{\epsilon}_{\mathbf{k}\lambda} \cdot \hat{a}_{\mathbf{k}\lambda} \cdot e^{i\mathbf{kr}} - \boldsymbol{\epsilon}^*_{\mathbf{k}\lambda} \cdot \hat{a}^\dagger_{\mathbf{k}\lambda} \cdot e^{-i\mathbf{kr}} \right] \tag{2.53}$$

Multiplying out the brackets, we are left with four terms proportional to

energy conserving terms	non energy conserving terms
$\hat{\sigma}^{eg} \cdot \hat{a}_{\mathbf{k}\lambda}$	$\hat{\sigma}^{eg} \cdot \hat{a}^\dagger_{\mathbf{k}\lambda}$
$\hat{\sigma}^{ge} \cdot \hat{a}^\dagger_{\mathbf{k}\lambda}$	$\hat{\sigma}^{ge} \cdot \hat{a}_{\mathbf{k}\lambda}$

Two of these terms are energy conserving (assuming, that $\omega \approx \omega_{\mathbf{k}\lambda}$, which is the interesting case, as we will see later). The first energy conserving term corresponds to an excitation of the atom ($\hat{\sigma}^{eg}$) and a deexcitation of the radiation field ($\hat{a}_{\mathbf{k}\lambda}$) and therefore the absorption of an photon by an atom, while the second energy conserving term corresponds to the inverse process, the emission of a photon. The non energy conserving terms correspond to a simultaneous excitation of atom and radiation field (first term) and to a simultaneous deexcitation of atom and radiation field (second term).

When switching into the Interaction picture with the bare Hamiltonians of atom and radiation field as $\hat{H}_0$, these terms acquire the following time dependence

energy conserving terms	non energy conserving terms
$\hat{\sigma}^{eg} \cdot \hat{a}_{\mathbf{k}\lambda} \cdot e^{i(\omega_\text{a} - \omega_{\mathbf{k}\lambda})t}$	$\hat{\sigma}^{eg} \cdot \hat{a}^\dagger_{\mathbf{k}\lambda} \cdot e^{i(\omega_\text{a} + \omega_{\mathbf{k}\lambda})t}$
$\hat{\sigma}^{ge} \cdot \hat{a}^\dagger_{\mathbf{k}\lambda} \cdot e^{-i(\omega_\text{a} - \omega_{\mathbf{k}\lambda})t}$	$\hat{\sigma}^{ge} \cdot \hat{a}_{\mathbf{k}\lambda} \cdot e^{-i(\omega_\text{a} + \omega_{\mathbf{k}\lambda})t}$

The interaction picture representation of these operators can be easily derived which is done as an example for $\hat{\sigma}^{eg}$:

$$i\hbar \frac{d}{dt} \hat{\sigma}^{eg}_I = [\hat{\sigma}^{eg}_I, H_{\text{atom}}] = \hbar\omega_\text{a} [\hat{\sigma}^{eg}_I, \hat{\sigma}^{ee}_I] = -\hbar\omega_\text{a} \hat{\sigma}^{eg}_I \tag{2.54}$$

where the index i denotes, that the operator is in the interaction picture. This equation of motion is solved by

$$\hat{\sigma}^{eg}_I = \hat{\sigma}^{eg} \cdot e^{i\omega_\text{a} t} \tag{2.55}$$

Assuming, that $\omega_{\mathrm{a}} \approx \omega_{\mathbf{k},\lambda}$, one concludes that the energy conserving terms oscillate only very slowly as $|\omega_{\mathrm{a}} - \omega_{\mathbf{k},\lambda}| \approx 0$, whereas the non energy conserving terms oscillate very rapidly as $|\omega_{\mathrm{a}} + \omega_{\mathbf{k},\lambda}| \approx 2\omega$. The effect of the rapidly oscillating terms averages to zero, so we can neglect them. This approximation is known as the Rotating Wave Approximation (RWA) [17]. To arrive at the final term for the interaction Hamiltonian, we therefore only need to take into account the energy conserving terms yielding

$$\begin{aligned}\hat{H}_{\mathrm{int}} &= -\mathbf{d}_{eg} \cdot \hat{\sigma}^{eg} \cdot \hat{\mathbf{E}}^{+}(\mathbf{r}) - \mathbf{d}_{ge} \cdot \hat{\sigma}^{ge} \cdot \hat{\mathbf{E}}^{-}(\mathbf{r}) \\ &= -i \sum_{\lambda} \int \frac{d\mathbf{k}}{(2\pi)^3} \sqrt{\frac{\hbar\omega_{\mathbf{k}}}{2\epsilon_0}} \Big[\boldsymbol{\epsilon}_{\mathbf{k}\lambda} \cdot \mathbf{d}_{eg} \cdot \hat{\sigma}^{eg}\, \hat{a}_{\mathbf{k}\lambda} \cdot e^{i\mathbf{kr}} - \boldsymbol{\epsilon}^{*}_{\mathbf{k}\lambda} \cdot \mathbf{d}_{ge} \cdot \hat{\sigma}^{ge} \hat{a}^{\dagger}_{\mathbf{k}\lambda} \cdot e^{-i\mathbf{kr}} \Big]\end{aligned} \tag{2.56}$$

where we split the electric field into a positive frequency part $\hat{\mathbf{E}}^{+}(\mathbf{r}) \sim \hat{\sigma}^{eg}\hat{a}_{\mathbf{k}\lambda}$ corresponding to an absorption of a photon by the atom and a negative frequency part $\hat{\mathbf{E}}^{-}(\mathbf{r}) \sim \hat{\sigma}^{ge}\hat{a}^{\dagger}_{\mathbf{k}\lambda}$ corresponding to an emission of a photon by the atom.

In the previous chapters we have now determined the Hamiltonian for the atom, the radiation field and the interaction between them. Collecting the results we arrive at

$$\hat{H}_{\mathrm{atom}} = \hbar\omega_{\mathrm{a}}\hat{\sigma}^{ee} \tag{2.57}$$

$$\hat{H}_{\mathrm{EM}} = \sum_{\lambda} \int \frac{d\mathbf{k}}{(2\pi)^3} \hbar\omega_{\mathbf{k}} \hat{a}^{\dagger}_{\mathbf{k}\lambda} \hat{a}_{\mathbf{k}\lambda} \tag{2.58}$$

$$\hat{H}_{\mathrm{int}} = -i \sum_{\lambda} \int \frac{d\mathbf{k}}{(2\pi)^3} \sqrt{\frac{\hbar\omega_{\mathbf{k}}}{2\epsilon_0}} \Big[\boldsymbol{\epsilon}_{\mathbf{k}\lambda} \cdot \mathbf{d}_{eg} \cdot \hat{\sigma}^{eg}\, \hat{a}_{\mathbf{k}\lambda} \cdot e^{i\mathbf{kr}} - \boldsymbol{\epsilon}^{*}_{\mathbf{k}\lambda} \cdot \mathbf{d}_{ge} \cdot \hat{\sigma}^{ge} \hat{a}^{\dagger}_{\mathbf{k}\lambda} \cdot e^{-i\mathbf{kr}} \Big]. \tag{2.59}$$

The Hamiltonian for the total system is then given by

$$\hat{H}_{\mathrm{total}} = \hat{H}_{\mathrm{atom}} + \hat{H}_{\mathrm{EM}} + \hat{H}_{\mathrm{int}} = \hat{H}_0 + \hat{H}_{\mathrm{int}}. \tag{2.60}$$

In the next chapters we will use this Hamiltonian to investigate the atom interacting with the vacuum of the electromagnetic field.

3 Atomic dynamics in a quantized radiation field

3.1 Transition rates from Fermi's Golden Rule

After we have found the quantum operators describing the atom and the surrounding electromagnetic field modes of free space, we are ready to investigate spontaneous atomic decay. To this end, we will make use of the so-called Fermi Golden Rule [29] (p. 498-500), which allows us to calculate the transition rate of an atom in the excited state to the ground state, when interacting with a continuum of modes such as the modes of free space.

In order to derive Fermi's Golden Rule, we need the formalism of time-dependent perturbation theory, which can be found in many textbooks, e.g [26]. Let's assume our total Hamiltonian looks like

$$\hat{H} = \hat{H}_0 + \hat{V}(t) \tag{3.1}$$

with $\hat{H}_0$ being a Hamiltonian, which we can diagonalize and know the eigenstates labeled $|\Psi_n\rangle$ with energy E_n. In our particular case, $\hat{H}_0$ will be the bare atomic Hamiltonian plus the Hamiltonian of the free electromagnetic modes, whereas $\hat{V}$ will be the (small) interaction between them. If $\hat{V}(t) = 0$, then the solution of the time dependent Schroedinger equation is trivial, as each eigenstate just acquires the phase oscillation with a frequency related to its energy $|\Psi_n(t)\rangle = e^{-iE_n(t-t_0)}|\Psi_n\rangle$, where $|\Psi_n(t = t_0)\rangle = |\Psi_n\rangle$. Further assume, that $\hat{V}(t) \neq 0$ only for a time t with $t_i \leq t \leq t_f$. For times $t > t_f$ the evolution is once again given by $\hat{H}_0$. Then let us find coefficients c_{mn}, such that the solution for the state for times $t > t_f$ is given by

$$|\Psi_n(t)\rangle = \sum_m c_{mn}|\Psi_m(t)\rangle. \tag{3.2}$$

For $\hat{V} = 0$ for all times, the coefficients would be trivial $c_{mn} = \delta_{mn}$. This means, that nonzero $c_{m\neq n}$ herald transitions from state n into state m. With these transition amplitudes we are able to express the probability $P_{m\neq n}$ that the system has undergone a transition from state n into state m during the time the system was perturbed by $\hat{V}$. Time-dependent perturbation theory tells us, that the first order for these transition amplitudes is given by

$$c^{(1)}_{m\neq n} = -\frac{i}{\hbar}\int_{t_i}^{t_f} d\tau\ V_{mn}(\tau)\cdot e^{\frac{i}{\hbar}(E_m - E_n)\tau} \tag{3.3}$$

where $V_{mn} = \langle\Psi_m|\hat{V}|\Psi_n\rangle$ and we require $|c_{m\neq n}| \ll 1$ for the validity of first order perturbation theory. For the derivation of Fermi's Golden Rule, let us assume a constant perturbation $V(t) = V$ for $t_i \leq t \leq t_f$ and $V(t) = 0$ elsewhere. Then the transition coefficients read

$$\begin{aligned} c^{(1)}_{m\neq n} =& -\frac{i}{\hbar}\int_{t_i}^{t_f} d\tau\ e^{\frac{i}{\hbar}(E_m - E_n)\tau}\cdot\langle\Psi_m|\hat{V}|\Psi_n\rangle = \\ & -\frac{i}{\hbar}\int_{t_i}^{t_f} d\tau\ e^{i\omega_{mn}\tau}\cdot V_{mn} = \\ & -\frac{V_{mn}}{\hbar}\frac{e^{i\omega_{mn}t_f} - e^{i\omega_{mn}t_i}}{\omega_{mn}} \\ =& -\frac{i}{\hbar}V_{mn}e^{i\frac{\omega_{mn}}{2}(t_f+t_i)}\cdot\frac{\sin(\omega_{mn}\Delta t/2)}{\omega_{mn}/2} \end{aligned}$$

where we used $\omega_{mn} = E_m - E_n$, which allows us to write the transition probability as follows

$$P_{m\neq n} = |c^{(1)}_{m\neq n}|^2 = \frac{|V_{mn}|^2}{\hbar^2}\frac{\sin(\omega_{mn}\Delta t/2)}{\omega_{mn}/2} \tag{3.4}$$

This order of perturbation only holds for $|c^{(1)}_{mn}| \ll 1$, which translates into $V_{mn} \ll \omega_{mn}$. Let us investigate the function $F_{\Delta t}(\omega) = \frac{\sin\omega_{mn}\Delta t/2}{\omega_{mn}/2}$ further. In figure 3.1 we plot the graph of the function $F_{\Delta t}(\omega)$. The function appears to be centered at $\omega = 0$ with a maximum value of $(\Delta t)^2$ and a width of $\sim \frac{1}{\Delta t}$. This means, that only states with

$$|E_m - E_n| \leq \frac{\hbar}{\Delta t} \tag{3.5}$$

have a nonzero transition probability within the time interval Δt, here the uncertainty relation for energy appears: If we observe for a long time Δt, then the energy uncertainty is small and vice versa. As Δt approaches zero from above, the function $F_{\Delta t}(\omega)$ looks more and more like the Dirac delta function, albeit scaled with Δt, as

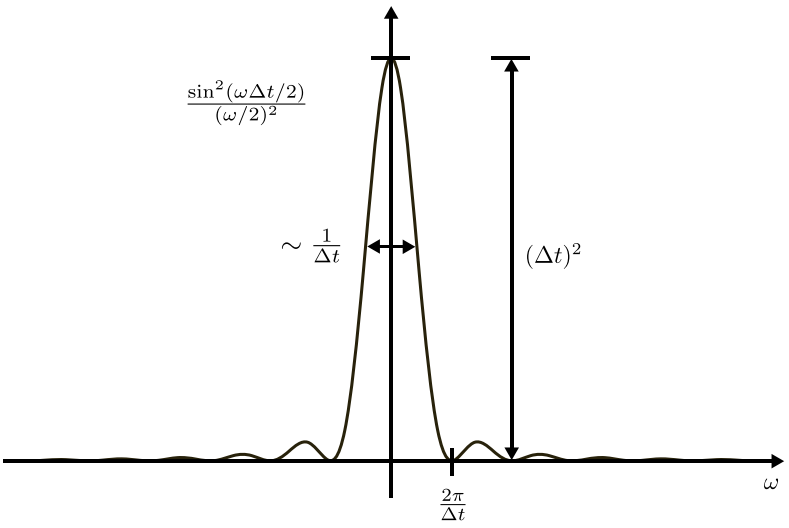

Figure 3.1: *Plot of the function* $\frac{\sin^2(\omega\Delta t/2)}{(\omega/2)^2}$. The function is only nonzero around the origin at $\omega = 0$. The maximum of the function is given by $(\Delta t)^2$, while the width is given by $\sim \frac{1}{\Delta t}$. As Δt approaches zero from above, the function approaches a delta function.

the area under the graph scales with $\sim \frac{1}{\Delta t} \cdot (\Delta t)^2 = \Delta t$. Evaluating the integral of $F_{\Delta t}(\omega)$ we find

$$\int_{-\infty}^{\infty} F_{\Delta t}(\omega) d\omega = [x = \frac{\omega \Delta t}{2}] = 2\Delta t \int_{-\infty}^{\infty} \frac{\sin^2 x}{x^2} dx = 2\pi\Delta t. \tag{3.6}$$

where we used the variable substitution $[x = \frac{\omega\Delta t}{2}]$. The last integral can be transformed by making use of the even property and via integration by parts $[u = sin^2(x), dv = \frac{1}{x^2}dx]$ to the Dirichlet integral $\int_0^{\infty} \frac{\sin x}{x} dx = \pi$, which in turn can be evaluated by different means, such as complex contour integration [30] or differentiation under the integral sign (Feynman's trick). To summarize, the function $F_{\Delta t}(\omega)$ looks like

$$F_{\Delta t}(\omega) \approx 2\pi\Delta t \cdot \delta(\omega) \tag{3.7}$$

Now let us find the transition probability from one initial state into a (dense) continuum of states. The decay probability $P_n = \sum_m P_{mn}$ is then just the sum over all transitions probabilities into the possible final states m. Summing up all contributions, we arrive

at

$$P_n = \sum_m \frac{1}{\hbar^2} |V_{mn}|^2 \frac{\sin^2(\omega_{mn}\Delta t/2)}{(\omega_{mn}/2)^2} \sim \sum_m \frac{1}{\hbar^2} |V_{mn}|^2 \, 2\pi\Delta t \cdot \delta(\omega_{mn})$$
$$= \Delta t \cdot \frac{2\pi}{\hbar} \sum_m |V_{mn}|^2 \, \delta(E_m - E_n) \tag{3.8}$$

where in the last equality we absorbed $\frac{1}{\hbar}$ into the Dirac delta function. As one can see, the transition probability depends linearly on the time interval Δt, so we can reformulate and define the transition rate Γ_n as the transition probability P_n per time interval and finally arrive at Fermi's Golden Rule:

$$\Gamma_n = \frac{P_n}{\Delta t} = \frac{2\pi}{\hbar} \sum_m \delta(E_m - E_n) \, |\langle \Psi_m | \hat{V} | \Psi_n \rangle|^2 \tag{3.9}$$

In order to get the total transition rate Γ_n out of the state n, we need to sum up over all possible final states m with the same energy as the initial state n (energy conservation) and weigh the contributions with the overlap integral $|\langle \Psi_m | \hat{V} | \Psi_n \rangle|^2$. For a dense continuum, we can replace the sum with an integral over the density of states.

Applying Fermi's Golden Rule for the particular case of spontaneous emission in free space, we have the initial state, where the atom is in the excited state and the electromagnetic field is in the vacuum state. In the final state the atom is in the ground state and some mode with polarization λ and wavevector $\mathbf{k}$ carries one photon.

$$|i\rangle = |e\rangle \otimes |0\rangle \qquad\qquad |f\rangle = |g\rangle \otimes \hat{a}^\dagger_{\lambda\mathbf{k}}|0\rangle \equiv |g\rangle \otimes |1_{\mathbf{k}\lambda}\rangle$$

where $|0\rangle$ denotes the vacuum state. The associated energies are $E_i = \hbar\omega_\mathrm{a}$ and $E_f = \hbar\omega_{\mathbf{k}\lambda}$ such that

$$\delta(E_f - E_i) = \frac{\delta(\omega_\mathrm{a} - \omega_{\mathbf{k}\lambda})}{\hbar} \tag{3.10}$$

Both states are eigenstates of the bare atomic Hamiltonian and the Hamiltonian for the electromagnetic modes. The interaction Hamiltonian $\hat{H}_\mathrm{int}$ then corresponds perturbation $\hat{V}$.

Let us first evaluate the overlap integral $\langle f | \hat{H}_\mathrm{int} | i \rangle$. To make our lives simple, assume that the atom sits at $\mathbf{r} = 0$. In our case we only need the negative frequency part of the interaction Hamiltonian, corresponding to the emission of an atom. This can be seen easily as the positive frequency part is proportional to $\hat{\sigma}^{eg}$ and $\langle g | \hat{\sigma}^{eg} | e \rangle = 0$.

Inserting the negative frequency part yields

$$\langle f|\hat{H}_{\text{int}}|i\rangle = \langle g| \otimes \langle 1_{\mathbf{k}\lambda}|\Big(-i\sum_{\lambda'}\int \frac{d\mathbf{k}'}{(2\pi)^3}\sqrt{\frac{\hbar\omega_{\mathbf{k}'}}{2\epsilon_0}}\boldsymbol{\epsilon}^*_{\mathbf{k}'\lambda'}\cdot\mathbf{d}_{ge}\cdot\hat{\sigma}^{ge}\,\hat{a}^\dagger_{\mathbf{k}'\lambda'}\Big)|e\rangle\otimes|0\rangle =$$

$$= \langle g|\hat{\sigma}^{ge}|e\rangle\cdot\Big(i\sum_{\lambda'}\int\frac{d\mathbf{k}'}{(2\pi)^3}\sqrt{\frac{\hbar\omega_{\mathbf{k}'}}{2\epsilon_0}}\boldsymbol{\epsilon}^*_{\mathbf{k}'\lambda'}\cdot\mathbf{d}_{ge}\cdot\hat{\sigma}^{ge}\Big)\cdot\langle 0|\hat{a}_{\mathbf{k}\lambda}\hat{a}^\dagger_{\mathbf{k}'\lambda'}|0\rangle \quad (3.11)$$

where $\langle 1_{\mathbf{k}\lambda}| = \langle 0|\hat{a}_{\mathbf{k}'\lambda'}|$. The first overlap integral gives 1, the second overlap integral can be easily executed using the commutation relations and gives

$$\langle 0|\hat{a}_{\mathbf{k}\lambda}\hat{a}^\dagger_{\mathbf{k}'\lambda'}|0\rangle = \langle 0|\hat{a}^\dagger_{\mathbf{k}'\lambda'}\hat{a}_{\mathbf{k}\lambda} + [\hat{a}_{\mathbf{k}\lambda},\hat{a}^\dagger_{\mathbf{k}'\lambda'}]|0\rangle = \delta(\mathbf{k}-\mathbf{k}')\cdot\delta_{\lambda\lambda'} \quad (3.12)$$

allowing us to trivially carry out the integral and the sum.

$$\langle f|\hat{H}_{\text{int}}|i\rangle = i\sqrt{\frac{\hbar\omega_{\mathbf{k}}}{2\epsilon_0}}\boldsymbol{\epsilon}^*_{\mathbf{k}\lambda}\cdot\mathbf{d}_{ge} \quad (3.13)$$

We can take the absolute value, square it and insert it into Fermi's Golden Rule, yielding

$$\Gamma_{g\leftarrow e} = \frac{2\pi}{\hbar}\sum_f \frac{\delta(\omega-\omega_{\mathbf{k}\lambda})}{\hbar}\,\frac{\hbar\omega_{\mathbf{k}}}{2\epsilon_0}|\boldsymbol{\epsilon}^*_{\mathbf{k}\lambda}\cdot\mathbf{d}_{ge}|^2 \quad (3.14)$$

As we now want to sum over a dense continuum of states, we switch from a sum $\sum_f$ to an integral $\sum_\lambda\int\frac{d\mathbf{k}^3}{(2\pi)^3}$. Using the dispersion relation $|\mathbf{k}| = \frac{\omega_{\mathbf{k}}}{c}$ leading to $d\mathbf{k}^3 = \omega^2 d\omega d\Omega/c^3$ we find

$$\Gamma_{g\leftarrow e} = \frac{2\pi}{\hbar}\sum_\lambda\int\frac{d\mathbf{k}}{(2\pi)^3}\,\frac{\delta(\omega-\omega_{\mathbf{k}\lambda})}{\hbar}\,\frac{\hbar\omega_{\mathbf{k}}}{2\epsilon_0}|\boldsymbol{\epsilon}^*_{\mathbf{k}\lambda}\cdot\mathbf{d}_{ge}|^2$$

$$= \frac{2\pi}{\hbar}\sum_\lambda\int_0^\infty\frac{\omega^2 d\omega}{(2\pi c)^3}\int d\Omega\frac{\delta(\omega-\omega_{\mathbf{k}\lambda})}{\hbar}\,\frac{\hbar\omega_{\mathbf{k}}}{2\epsilon_0}|\boldsymbol{\epsilon}^*_{\mathbf{k}\lambda}\cdot\mathbf{d}_{ge}|^2,$$

where Ω is the solid angle. Carrying out the integral over ω yields

$$\Gamma_{g\leftarrow e} = \frac{2\pi}{\hbar}\frac{\omega^3}{2\epsilon_0(2\pi c)^3}\sum_\lambda\int|\boldsymbol{\epsilon}_\lambda\cdot\mathbf{d}_{ge}|^2\,d\Omega \quad (3.15)$$

where we dropped all indices $\mathbf{k}$ due to the delta function and the complex conjugate for the polarization vector $\boldsymbol{\epsilon}_\lambda$. Here we see some origin of directional emission: The

differential emission rate is proportional to

$$d\Gamma_{g\leftarrow e} \propto |\boldsymbol{\epsilon}_\lambda \cdot \mathbf{d}_{ge}|^2 \, d\Omega. \tag{3.16}$$

Assuming, e.g. a light polarization in z-direction, one gets the typical dipole radiation pattern $\propto \cos^2\theta$.

The only thing left to do is to carry out the integral over $d\Omega$ and sum over the polarizations λ. To this end, consider that the emission direction $\mathbf{n} = \frac{\mathbf{k}}{|\mathbf{k}|}$ together with both polarizations $\boldsymbol{\epsilon}_1$ and $\boldsymbol{\epsilon}_2$ forms an orthonormal basis, such that we can decompose $\mathbf{d}_{ge}$ into this basis by

$$\mathbf{d}_{ge} = (\mathbf{n} \cdot \mathbf{d}_{ge})\, \mathbf{n} + (\boldsymbol{\epsilon_1} \cdot \mathbf{d}_{ge})\, \boldsymbol{\epsilon_1} + (\boldsymbol{\epsilon_2} \cdot \mathbf{d}_{ge})\, \boldsymbol{\epsilon_2} \tag{3.17}$$

Evaluating $|\mathbf{d}_{ge}|^2$ then gives

$$|\mathbf{d}_{ge}|^2 = |\mathbf{n} \cdot \mathbf{d}_{ge}|^2 + |\boldsymbol{\epsilon_1} \cdot \mathbf{d}_{ge}|^2 + |\boldsymbol{\epsilon_2} \cdot \mathbf{d}_{ge}|^2 = |\mathbf{n} \cdot \mathbf{d}_{ge}|^2 + \sum_\lambda |\boldsymbol{\epsilon_\lambda} \cdot \mathbf{d}_{ge}|^2 \tag{3.18}$$

where on the right hand side the sum, that we are interested in, already appears. Let us denote the angle between $\mathbf{d}_{ge}$ and $\mathbf{n}$ as θ such that $\mathbf{n} \cdot \mathbf{d}_{ge} = \cos\theta$ we find

$$|\mathbf{d}_{ge}|^2 \cdot (1 - \cos^2\theta) = |\mathbf{d}_{ge}|^2 \cdot \sin^2\theta = \sum_\lambda |\boldsymbol{\epsilon_\lambda} \cdot \mathbf{d}_{ge}|^2. \tag{3.19}$$

Now that we evaluated the sum, we insert it back into equation 3.15 yielding

$$\Gamma_{g\leftarrow e} = \frac{2\pi}{\hbar} \frac{\omega^3}{2\epsilon_0 (2\pi c)^3} \, |\mathbf{d}_{ge}|^2 \int \sin^2\theta \, \sin\theta \, d\theta \, d\phi \tag{3.20}$$

with the solid angle element $d\Omega = \sin\theta \, d\theta \, d\phi$. The angle integral yields $2\pi \cdot \frac{4}{3}$ allowing us to finally get the spontaneous emission rate as

$$\Gamma_{g\leftarrow e} = \frac{2\pi}{\hbar} \frac{\omega^3}{2\epsilon_0 (2\pi c)^3} \, |\mathbf{d}_{ge}|^2 \, 2\pi \cdot \frac{4}{3} = \frac{\omega^3}{3\hbar\epsilon_0 \pi c^3} |\mathbf{d}_{ge}|^2. \tag{3.21}$$

We computed the spontaneous emission rate of an atom coupled to the electromagnetic field of free space in three dimensions by making use of Fermi's Golden rule. In the next section we continue by deriving the time evolution for the excited state population. For this we again need the total Hamiltonian of the atom, the radiation field and the interaction between them, and then we are able to solve the Schroedinger equation

using a clever ansatz, the so-called Wigner-Weisskopf ansatz.

3.2 The Wigner-Weisskopf ansatz for spontaneous emission of an excited atom

In this section we investigate the spontaneous emission from an excited atom into free space, in particular the time evolution for the excited state. For this simple setup we do not need the full master equation, instead we merely need to solve the Schroedinger equation for the atom and the field modes for a suitably chosen ansatz, the Wigner-Weisskopf ansatz. Well justified approximations allow us to derive analytic expressions for the excited state population and the decay of the atom will become apparent. It will become clear, that the underlying reason for the decay is the interaction of the atoms with the electromagnetic modes and that the structure of the particular modes has an influence on the radiation rate. The original work has been done in [31], while our derivation follows Gardiner and Zoller [18] (p. 148-151). In our case, we choose the electromagnetic modes of free space, whose operator expressions we already found in section 2.4.

The ingredients for this setup are the atom, the electromagnetic modes of free space and the interaction between them. As usual, we model the atom as a two-level system and set the energy of the ground state to zero. The quantized electromagnetic modes can be described as harmonic oscillators. As we want to include the infinite modes of free space, we need to sum over polarizations λ and wavevectors $\mathbf{k}$. In the case of free space, as in free space all wavevectors are allowed, this results in an integral over all possible wave vectors. The modes themselves are orthogonal to each other, which allows us to use them as a basis for the radiation field. To start, we write down the corresponding equations for the Hamiltonian for the atom H_{0A}, the Hamiltonian of the modes of free space H_{0F} and the commutation relations for the operators ensuring orthogonality

$$
\begin{aligned}
H_{0A} &= \hbar\omega_{eg}\,|e\rangle\langle e| \\
H_{0F} &= \sum_{\lambda}\int d^3k\;\hbar\omega_{\lambda k}\,a^{\dagger}_{\lambda\mathbf{k}}\,a_{\lambda\mathbf{k}} \\
\left[a_{\lambda\mathbf{k}},\,a^{\dagger}_{\lambda'\mathbf{k}'}\right] &= \delta_{\lambda\lambda'}\,\delta(\mathbf{k}-\mathbf{k}')
\end{aligned}
$$

where $\omega_{eg} = \omega_\mathrm{a}$ is the atomic transition frequency. The classical interaction Hamiltonian is $H = -\mathbf{d}\cdot\mathbf{E}$, as the dipole tries to align with the electromagnetic field minimizing the potential energy. In quantum optics we just need to find the corresponding operator expression of the dipole and the field. Using previous results for the dipole operator and the operator of the electric field, we write down the interaction Hamiltonian

$$\hat{H}_\mathrm{int} = -\hat{\mathbf{d}} \cdot \hat{\mathbf{E}}(\mathbf{x}=0) \tag{3.22a}$$

$$\hat{H}_\mathrm{int} \overset{\mathrm{RWA}}{\longrightarrow} -\mathbf{d}_{eg} \cdot \hat{\mathbf{E}}^{(+)}(\mathbf{x}=0)\,|e\rangle\langle g| \;-\; \mathbf{d}_{ge} \cdot \hat{\mathbf{E}}^{(-)}(\mathbf{x}=0)\,|g\rangle\langle e|. \tag{3.22b}$$

For simplicity, we set the atom at $\mathbf{x} = 0$ and we also applied the rotating wave approximation keeping only the energy-conserving terms. The operator for the electric field in free space looks like, as derived previously in section 2.4,

$$\hat{\mathbf{E}}(\mathbf{x}) = \hat{\mathbf{E}}^{(+)}(\mathbf{x}) + \hat{\mathbf{E}}^{(-)}(\mathbf{x})$$

$$\hat{\mathbf{E}}^{(+)}(\mathbf{x}) = -i \sum_\lambda \int d\mathbf{k} \sqrt{\frac{\hbar\omega_{\lambda\mathbf{k}}}{2\varepsilon_0(2\pi)^3}}\, \hat{a}_{\lambda\mathbf{k}}\, \boldsymbol{\epsilon}_{\lambda\mathbf{k}}\, e^{i\mathbf{k}\cdot\mathbf{x}}$$

The Hamiltonian describing the whole system is then

$$\hat{H} = \hat{H}_{0A} + \hat{H}_{0F} + \hat{H}_\mathrm{int}. \tag{3.23}$$

Now that we know the Hamiltonian and in consequence how the Schroedinger equation looks like, we need to choose a suitable ansatz. We want to start with an atom in the excited state and the radiation field in the vacuum. Looking at the interaction Hamiltonian, two processes happen. The first part in equation 3.22b includes the operators $\hat{\sigma}^{eg} \cdot \hat{a}_{\lambda\mathbf{k}}$ and describes how the atom gets excited and a particular mode with polarization λ and wavevector $\mathbf{k}$ gets deexcited, so this process describes the absorption of a photon by the atom. The second part includes the operators $\hat{\sigma}^{ge} \cdot \hat{a}^\dagger_{\lambda\mathbf{k}}$ and describes the inverse process of emitting a photon. If this second part of the interaction Hamiltonian acts onto our initial state, we will be left with the atom in the ground state and a particular mode or a continuum of modes being excited. Note how the Hamiltonian does not allow processes of deexcitation of the atom while increasing the excitations in the radiation field. This is ensured by the rotating wave approximation earlier. In conclusion, the excitation is either stored in the atom or in the radiation field, motivating the following ansatz as a superposition of these two

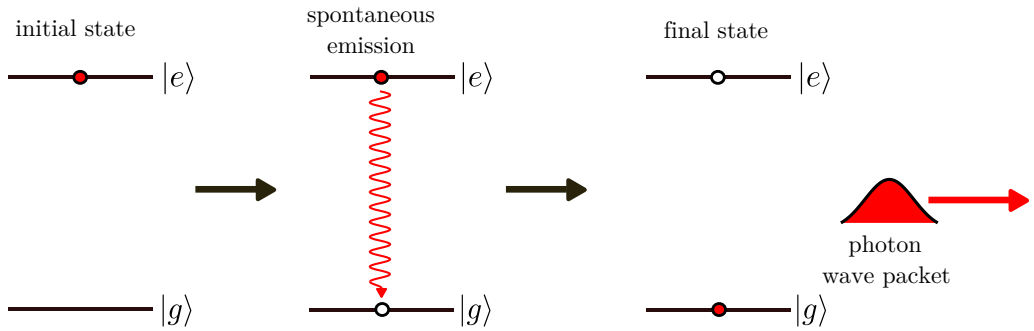

Figure 3.2: *Schematic depiction of an atom spontaneously emitting a photon.* We start with the atom in the excited state. Through the process of spontaneous emission the atom decays into the ground state and emits a photon in form of a wavepacket. The Wigner-Weisskopf approximation allows us to describe this process and derive the time evolution of the decay of the atom into the ground state analytically.

states

$$|\Psi(t)\rangle = c_e(t)|e\rangle \otimes |0\rangle + |g\rangle \otimes \sum_\lambda \int d\mathbf{k}\, c_{\lambda\mathbf{k}}(t) a^\dagger_{\lambda\mathbf{k}}(t)|0\rangle. \tag{3.24}$$

The coefficient $c_e(t)$ is the amplitude of the atom at time t being in the excited state (and therefore the radiation field in the vacuum state) and the continuous coefficients $c_{\lambda\mathbf{k}}(t)$ are the amplitudes of the particular mode with λ and $\mathbf{k}$ being in the state with one excitation. The normalization for the coefficients reads

$$|c_e(t)|^2 + \sum_\lambda \int d\mathbf{k} |c_{\lambda\mathbf{k}}(t)|^2 = 1. \tag{3.25}$$

As we want to start with an excited atom and the vacuum, the initial conditions read

$$c_e(t=0) = 1 \qquad\qquad c_{\lambda\mathbf{k}}(t=0) = 0 \quad \forall\lambda, \forall\mathbf{k} \tag{3.26}$$

Substituting this ansatz into the Schroedinger equation leads to

$$i\hbar|\dot{\Psi}(t)\rangle = i\hbar\dot{c}_e(t)|e\rangle \otimes |0\rangle + i\hbar|g\rangle \otimes \sum_\lambda \int d\mathbf{k}\, c_{\lambda\mathbf{k}}(t) a^\dagger_{\lambda\mathbf{k}}(t)|0\rangle$$

$$\begin{aligned} H|\Psi(t)\rangle = {} & c_e(t)\hbar\omega_{\mathrm{eg}}|e\rangle \otimes |0\rangle + \\ & |g\rangle \otimes \sum_\lambda \int d\mathbf{k} \sum_{\lambda'} \int d^3\mathbf{k}'\, \hbar\omega_{\lambda'\mathbf{k}'}\, a^\dagger_{\lambda'\vec{k}'}\, a_{\lambda'\vec{k}'}\, c_{\lambda\mathbf{k}}(t) a^\dagger_{\lambda\mathbf{k}}(t)|0\rangle + \\ & + H_{\mathrm{int}}|\Psi(t)\rangle = \end{aligned}$$

$$
\begin{aligned}
&= c_e(t)\hbar\omega_{\mathrm{eg}}|e\rangle\otimes|0\rangle + \\
&\quad |g\rangle\otimes\sum_{\lambda}\int d\mathbf{k}\sum_{\lambda'}\int d^3\mathbf{k}'\;\hbar\omega_{\lambda'\mathbf{k}'}\,a^{\dagger}_{\lambda'\mathbf{k}'}\left(a^{\dagger}_{\lambda\mathbf{k}}\,a_{\lambda'\mathbf{k}'}+\left[a_{\lambda'\vec{k}'},\,b^{\dagger}_{\lambda\mathbf{k}}\right]\right)c_{\lambda\mathbf{k}}(t)|0\rangle + \\
&\quad + H_{\mathrm{int}}|\Psi(t)\rangle
\end{aligned}
$$

The last line simplifies, as $a_{\lambda'\mathbf{k}'}|0\rangle = 0$ and the commutator is replaced by $\delta_{\lambda\lambda'}\,\delta(\mathbf{k}-\mathbf{k}')$, which allows to compute the integral over $\mathbf{k}'$ and the sum over λ' trivially. One ends up with

$$
\begin{aligned}
&i\hbar\dot{c}_e(t)|e\rangle\otimes|0\rangle + i\hbar|g\rangle\otimes\sum_{\lambda}\int d\mathbf{k}\,c_{\lambda\mathbf{k}}(t)b^{\dagger}_{\lambda\mathbf{k}}(t)|0\rangle = \\
&= c_e(t)\hbar\omega_{\mathrm{eg}}|e\rangle\otimes|0\rangle + |g\rangle\otimes\sum_{\lambda}\int d\mathbf{k}\,\hbar\omega_{\lambda k}\,a^{\dagger}_{\lambda\mathbf{k}}\,c_{\lambda\mathbf{k}}(t)|0\rangle + \\
&+ H_{\mathrm{int}}|\Psi(t)\rangle
\end{aligned}
$$

with

$$
\begin{aligned}
H_{\mathrm{int}}|\Psi(t)\rangle = &- ic_{\mathrm{e}}(t)|g\rangle\otimes\sum_{\lambda}\int d\mathbf{k}\sqrt{\frac{\hbar\omega_{\lambda\mathbf{k}}}{2\epsilon_0 V}}\;\mathbf{d}_{\mathrm{eg}}\cdot\boldsymbol{\epsilon}^{*}_{\lambda}a^{\dagger}_{\lambda\mathbf{k}}|0\rangle \\
&+ i|e\rangle\otimes\sum_{\lambda}\int d\mathbf{k}\sqrt{\frac{\hbar\omega_{\lambda\mathbf{k}}}{2\epsilon_0 V}}\;\mathbf{d}_{\mathrm{ge}}\cdot\boldsymbol{\epsilon}_{\lambda}c_{\lambda\mathbf{k}}(t)|0\rangle
\end{aligned}
$$

Orthogonality of $|e\rangle$ and $|g\rangle$ and between one-photon states of different polarization λ or different wave vector $\mathbf{k}$ allows us to project the above equation onto the states $|e\rangle\otimes|0\rangle$ and $|g\rangle\otimes a^{\dagger}_{\lambda\mathbf{k}}|0\rangle$, yielding a set of ordinary differential equations for the coefficients $c_e(t)$ and $c_{\lambda\mathbf{k}}(t)$ from the ansatz

$$
i\frac{d}{dt}c_e(t) = \omega_{eg}c_e(t) - i\sum_{\lambda}\int dk\,\kappa_{\lambda\mathbf{k}}c_{\lambda\mathbf{k}}(t) \tag{3.27a}
$$

$$
i\frac{d}{dt}c_{\lambda\mathbf{k}}(t) = \omega_{\lambda\mathbf{k}}c_{\lambda\mathbf{k}}(t) + i\kappa^{*}_{\lambda\mathbf{k}}c_e(t) \tag{3.27b}
$$

Here we used the shorthand notation

$$
\kappa_{\lambda\mathbf{k}} \equiv -\sqrt{\frac{\hbar\omega_{\lambda\mathbf{k}}}{2\epsilon_0 V}}\boldsymbol{\epsilon}_{\lambda}\cdot\mathbf{d}_{eg}. \tag{3.28}
$$

Note, that the equation 3.27b stands for a continuum of equations with continuous parameters λ and $\mathbf{k}$. As there are no crossterms between different polarizations or

wavevectors, we can regard it as a single (parametric) equation. Formal integration (using the Green function $\Theta(t) \cdot \exp(i\omega t)$ for the differential operator $\partial_t - i\omega$) leads to

$$c_{\lambda\mathbf{k}}(t) = \exp(-i\omega_{\lambda\mathbf{k}}t) \cdot c_{\lambda k}(0) + \int_0^t dt' \kappa^*_{\lambda\mathbf{k}} e^{-i\omega_{\lambda\mathbf{k}}(t-t')} c_e(t'). \tag{3.29}$$

Using the initial condition $c_{\lambda\mathbf{k}}(0) = 0$ for all λ and all $\mathbf{k}$, we simplify and resubstitute into the equation for $c_{\mathrm{e}}(t)$ from 3.27a

$$i\frac{d}{dt}c_e(t) = \omega_{eg}c_e(t) - i\int_0^t dt' c_e(t') \left[\sum_\lambda \int d\mathbf{k} |\kappa_{\lambda\mathbf{k}}|^2 e^{-i(\omega_{\lambda\mathbf{k}}-\omega_g)(t-t')}\right]. \tag{3.30}$$

Switching into a rotating frame $c_{\mathrm{e}}(t) = \tilde{c_{\mathrm{e}}}(t)\exp(i\omega_{\mathrm{e}}t)$ and simplifying leads to

$$\frac{d}{dt}\tilde{c}_e(t) = -\int_0^t dt' \tilde{c}_e(t') \left[\sum_\lambda \int d\mathbf{k} |\kappa_{\lambda\mathbf{k}}|^2 e^{-i(\omega_{\lambda\mathbf{k}}-\omega_{eg})(t-t')}\right] \tag{3.31}$$

and we introduce the convenient shorthand notation

$$\gamma(t-t') \equiv \sum_\lambda \int d\mathbf{k} |\kappa_{\lambda\mathbf{k}}|^2 e^{-i(\omega_{\lambda\mathbf{k}}-\omega_{eg})(t-t')}. \tag{3.32}$$

By using the Markov approximation, we are going to show that $\gamma(t-t')$ is essentially a delta function (for more details look in section 3.2.1), which will allow us to perform the integral in the above equation to solve for the excited state population over time.

$$\begin{aligned}
\gamma(t-t') &= \int_0^\infty d\omega_{\lambda\mathbf{k}} \left[\frac{\omega^2_{\lambda\mathbf{k}}}{(2\pi)^3 c^3} \sum_\lambda \int d\Omega_{\mathbf{k}} |\kappa_{\lambda\mathbf{k}}|^2\right] e^{-i(\omega_{\lambda\mathbf{k}}-\omega_{eg})(t-t')} \\
&\equiv \int_0^\infty d\omega_{\lambda\mathbf{k}} g(\omega_{\lambda\mathbf{k}}) e^{-i(\omega_{\lambda\mathbf{k}}-\omega_{eg})(t-t')} \\
&\approx g(\omega_{eg}) \int_{-\infty}^{+\infty} d\omega_{\lambda\mathbf{k}} e^{-i(\omega_{\lambda\mathbf{k}}-\omega_{eg})(t-t')} \approx \Gamma_{e\to g} \cdot \delta(t-t')
\end{aligned}$$

In the first line we change the integration variable from $d\mathbf{k} = \frac{1}{c^3}d^3\omega = \frac{1}{c^3}\omega^2 d\Omega$, where Ω is the solid angle element $d\Omega = \sin\theta \; d\theta \; d\phi$ and write $g(\omega_{\lambda\mathbf{k}})$ for the term in the square brackets. Because of the rapidly changing exponential $\exp(-i(\omega_{\lambda\mathbf{k}}-\omega_{eg})(t-t'))$, as $\omega_{\lambda\mathbf{k}}$ varies between the limits of the integral, the whole integral gives a nonzero contribution only when $(t-t')$ is very small. This allows us replace t' by t and drag

$\tilde{c}_e(t')$ in eq. 3.31 in front of the integral

$$\frac{d}{dt}\tilde{c}_e(t) = -\tilde{c}_e(t)\int_0^t dt' \left[\sum_\lambda \int d\mathbf{k}|\kappa_{\lambda\mathbf{k}}|^2 e^{-i(\omega_{\lambda\mathbf{k}}-\omega_{eg})(t-t')}\right] = -\tilde{c}_e(t)\int_0^t dt'\ \gamma(t-t') \tag{3.33}$$

This approximation is well known in quantum optics as the Markov approximation. The underlying reason for the validity of this approximation is the separation of time scales, as the optical frequencies (ω_{eg}) are on very fast timescales, whereas the decay of the excited state population coefficient $\tilde{c}_e(t)$ happens on a much slower time scale. Getting back to our evaluation of $\gamma(t-t')$, we are allowed to pull $g(\omega_{\lambda\mathbf{k}})$ out of the integral, as, once again, the contribution to the integral is only big if $\omega_{\lambda\mathbf{k}} \approx \omega_{eg}$. As the mode function $g(\omega_{\lambda\mathbf{k}})$ varies much slower compared to the oscillating exponential $\exp -i(\omega_{\lambda k} - \omega_{eg})(t-t')$, $g(\omega_{\lambda\mathbf{k}})$ is essentially a constant over the small interval, where the exponential $\exp -i(\omega_{\lambda\mathbf{k}} - \omega_{eg})(t-t')$ gives a nonzero contribution. A more thorough treatment can be found in the next section and in [18]. Moreover, we can extend the limits of the integral to infinity and then we recognize one definition of the delta distribution as an integral

$$\delta(t) = \int_{-\infty}^{\infty} dx \exp(ixt) \tag{3.34}$$

with $x \equiv \omega_{\lambda\mathbf{k}} - \omega_{eg}$ and $t \equiv t - t'$. This allows us to simplify equation 3.31 even further to

$$\frac{d}{dt}\tilde{c}_e(t) = -\Gamma_{e\to g}\cdot\tilde{c}_e(t)\int_0^t dt'\ \delta(t-t'). \tag{3.35}$$

For the integral over the delta function, we have to be a little careful, as the integration interval happens to end exactly at the peak of our delta function. However, using the well known symmetry property $\delta(x) = \delta(-x)$ and substitution properties of the integral

$$\begin{aligned}
1 = \int_{-\infty}^{\infty} dx\ \delta(x) &= \int_{-\infty}^{0} dx\ \delta(x) + \int_0^{\infty} dx\ \delta(x) = [\bar{x} = x, d\bar{x} = -dx] = \\
&= \int_{-\infty}^{0} dx\ \delta(x) - \int_0^{-\infty} d\bar{x}\ \delta(-\bar{x}) = \\
&= \int_{-\infty}^{0} dx\ \delta(x) + \int_{-\infty}^{0} d\bar{x}\ \delta(\bar{x}) = \\
&= 2\cdot\int_{-\infty}^{0} dx\ \delta(x) = 1,
\end{aligned}$$

where we used the minus for switching the integration limits, one can easily verify that the integral of a delta function is $\frac{1}{2}$, if the peak of the delta function sits at either end of the integration interval. Altogether, for the coefficient of the excited state population $\tilde{c}_e(t)$, we end up with the equation

$$\frac{d}{dt}\,\tilde{c}_e(t) = -\frac{1}{2}\Gamma_{e\to g}\,\tilde{c}_e(t) \tag{3.36}$$

Solving this differential equation gives

$$\tilde{c}_e(t) = \tilde{c}_e(0)\cdot\exp\Big(-\frac{\Gamma_{e\to g}t}{2}\Big) = \exp\Big(-\frac{\Gamma_{e\to g}t}{2}\Big) \tag{3.37}$$

as $\tilde{c}_e(0) = 1$ is the initial condition. For the population $|\tilde{c}_e(t)|^2$ we get

$$|\tilde{c}_e(t)|^2 = \exp(-\Gamma_{e\to g}t) \tag{3.38}$$

and here we see the decay of the atom, as the population in the excited state is decaying exponentially with the rate $\Gamma_{e\to g}$. Substituting our results back into the Schroedinger equation for the coefficient $c_e(t)$ yields

$$i\hbar\,\frac{d}{dt}c_e(t) = \left(E_e - i\hbar\,\frac{1}{2}\Gamma_{e\to g}\right)c_e(t) \tag{3.39}$$

suggesting that the decay can be understood as an imaginary energy shift. This concept will appear later too, when we will investigate the influence of other atoms onto the radiation rates.

In summary, we were able to derive the decay of an atom in the excited state by choosing the Wigner-Weisskopf ansatz. Inserting this ansatz into the Schroedinger equation leads to a set of differential equations, which could be solved to get a result for the excited state population. The existence of the electromagnetic modes and the coupling of the atom to these modes via the Hamiltonian $\hat{H}_{\text{int}} = -\mathbf{d}\cdot\hat{\mathbf{E}}(\mathbf{x})$ leads to decay. Central to solving these equations was the so-called Markov approximation, which we are allowed to perform because of the separation of timescales, in particular the optical timescale and the timescale on which the decay happens. With limited tools we were able to show the decay of the atom.

However, the Wigner-Weisskopf ansatz has its limitations: If we drive our atom e.g. with a laser, the atom gets reexcited, emitting another photon and this cycle continues. We would have to extend our ansatz with every emitted photon and use a superposition

of contributions which correspond to the emission of zero photons emitted, one photon emitted, two photons emitted and so on and so forth:

$$
\begin{aligned}
|\Psi(t)\rangle = |\psi(t)\rangle \otimes |0\rangle + \\
&+ \sum_{\lambda} \int d\mathbf{k}\, |\psi_{\lambda\mathbf{k}}(t)\rangle \otimes a^{\dagger}_{\lambda\mathbf{k}}|0\rangle \\
&+ \sum_{\lambda_1,\lambda_2} \int d\mathbf{k}_1\, d\mathbf{k}_2\, |\psi_{\lambda_1\mathbf{k}_1,\,\lambda_2\mathbf{k}_2}(t)\rangle \otimes \frac{1}{\sqrt{2!}}\, a^{\dagger}_{\lambda_1\mathbf{k}_1}\, a^{\dagger}_{\lambda_2\mathbf{k}_2}|0\rangle \\
&+ \dots \\
&\underset{t=0}{\longrightarrow} |\psi(0)\rangle \otimes |0\rangle
\end{aligned}
$$

Keeping track of all these contributions will be challenging, especially considering that atoms can undergo many excitation and emission cycles in a short time. Hence, for setups where atoms can get reexcited, we will use the approach of a master equation, which allows us to forget about the environment and focus on the system of interest, in this case the driven and radiating atom. Tracing out over the environment variables (in this case the electromagnetic modes of free space), we will find the so-called master equation describing only the state of the system of interest, which in this case is the atom.

3.2.1 Treatment of $\gamma(t-t')$

To further solidify our argument in the previous section, where we just replaced $\gamma(t-t')$ with the delta function $\delta(t-t')$ (Markov approximation), let us be a bit more careful in our approach. We start by noting that, when $t-t'$ is far away from zero, we have no problem evaluating the integral as the extremely fast oscillations will average to zero. However, the difficulties arise when $t-t'$ approaches zero. So let us take this limit carefully:

$$
\int_0^{\infty} \gamma(\tau) d\tau = \lim_{\epsilon\to 0+} \int_0^{\infty} d\tau \int_0^{\infty} d\omega_{\lambda\mathbf{k}} g(\omega_{\lambda\mathbf{k}}) \exp(-i(\omega_{\lambda\mathbf{k}} - \omega_{eg})\tau - \epsilon\tau), \tag{3.40}
$$

where we changed variables $\tau = t-t'$ and extended the upper limit of the integral to infinity, which we are allowed to because the exponential will oscillate even faster with increasing τ and therefore average to zero. In the case, where $\epsilon > 0$, before

we perform the limit, we are allowed to carry out the integral over τ, which we can do by switching the order of the integrals. The inner derivative of the exponential $-i(\omega_{\lambda\mathbf{k}} - \omega_{eg}) - \epsilon)$ now appears in the denominator yielding

$$\begin{aligned}\int_0^\infty \gamma(\tau)d\tau &= \lim_{\epsilon\to 0+}\int_0^\infty d\omega_{\lambda\mathbf{k}}\frac{-g(\omega_{\lambda\mathbf{k}})}{i(\omega_{\lambda\mathbf{k}}-\omega_{eg})+\epsilon}\exp(-i(\omega_{\lambda\mathbf{k}}-\omega_{eg})\tau-\epsilon\tau)|_{\tau=0}^{\tau=\infty} = \\ &= \lim_{\epsilon\to 0+}\int_0^\infty d\omega_{\lambda\mathbf{k}}\frac{-g(\omega_{\lambda\mathbf{k}})}{i(\omega_{\lambda\mathbf{k}}-\omega_{eg})+\epsilon}\Big(0-\exp(0)\Big) = \\ &= \lim_{\epsilon\to 0+}\int_0^\infty d\omega_{\lambda\mathbf{k}}\frac{g(\omega_{\lambda\mathbf{k}})}{i(\omega_{\lambda\mathbf{k}}-\omega_{eg})+\epsilon}.\end{aligned}$$

Splitting this in a real part and an imaginary part by expanding the fractions with their complex conjugate yields

$$\begin{aligned}\int_0^\infty \gamma(\tau)d\tau &= \lim_{\epsilon\to 0+}\int_0^\infty d\omega_{\lambda\mathbf{k}}g(\omega_{\lambda\mathbf{k}})\Big[\frac{\epsilon}{(\omega_{\lambda\mathbf{k}}-\omega_{eg})^2+\epsilon^2)}-i\frac{(\omega_{\lambda\mathbf{k}}-\omega_{eg})}{(\omega_{\lambda\mathbf{k}}-\omega_{eg})^2+\epsilon^2)}\Big] = \\ &= \frac{1}{2}\Gamma_{e\to g}+i\delta\omega\end{aligned}$$

with

$$\Gamma_{e\to g} \equiv 2\pi g(\omega_{eg}) \tag{3.41a}$$

$$\delta\omega \equiv -iP\int\frac{d\omega_k g(\omega_{\lambda\mathbf{k}})}{\omega_{eg}-\omega_{\lambda\mathbf{k}}}. \tag{3.41b}$$

The integrals can be evaluated using techniques of complex analysis, in particular the two integrals

$$\lim_{\epsilon\to 0}\int\frac{\epsilon}{z^2+\epsilon^2}f(z)dz = \pi f(0)$$

$$\lim_{\epsilon\to 0}\int\frac{z}{z^2+\epsilon^2}f(z)dz = P\int\frac{f(z)dz}{z}$$

where $P\int$ means the principal value integral. Inserting equation 3.41a back into 3.33 the Schroedinger equation for the coefficient of the excited state population $\tilde{c}_e(t)$ leaves us with

$$\frac{d}{dt}\tilde{c}_e(t) = -\tilde{c}_e(t)\int_0^t dt'\,\gamma(t-t') = -\tilde{c}_e(t)\cdot\Big(\frac{1}{2}\Gamma_{e\to g}+i\delta\omega\Big) \tag{3.42}$$

Multiplying by $i\hbar$ and undoing the rotating frame we arrive at

$$i\hbar \frac{d}{dt} c_e(t) = \left(E_e - i\hbar \left(\frac{1}{2} \Gamma_{e \to g} + i\delta\omega \right) \right) c_e(t) = \left(E_e + \hbar\, \delta\omega - i\hbar \frac{1}{2} \Gamma_{e \to g} \right) c_e(t), \quad (3.43)$$

suggesting that $\delta\omega$ shifts the bare atomic transition in frequency. This shift actually exists, but leads to a divergence in our simplified treatment. The proper treatment of this case is provided by relativistic quantum electrodynamics, where this divergence can be handled using renormalization theory resulting in the so-called Lamb shift [18], a rather small shift compared to the optical frequencies. The lamb shift itself is important in order to calculate actual and precise transition frequencies, e.g. it appears when deriving the spectrum of the hydrogen atom. For most theoretical calculations however, we can disregard the lamb shift, as we can absorb this minor shift just into the transition frequency itself.

4 Collective coupling of atoms in a one dimensional optical waveguide

In the previous chapters we have investigated the spontaneous decay of an atom in free space. Now let us consider several more atoms and see how this changes the radiation properties. The derivation for atoms in free space can be found in [32], here we restrict us to the one dimensional case, where the atoms interact with each other only via the modes of an optical waveguide. The coming derivations follow L. Ostermann et. al. [33] and carry out the necessary calculations in more detail.

The optical fiber shall be infinitely long along the z-axis with a radius of a. We denote the positions of the atoms by z_i, where the index i goes from 1 to N, the total number of atoms. The cylindrical symmetry of the setup allows us to solve the Maxwell equations inside the fiber and outside. For the outside, we assume a vacuum $n_2 = 1$, whereas the inside consists of a medium with the refractive index $n_1 > 1$. With a plane wave ansatz with a radial component in cylindrical coordinates

$$E_z = A \cdot f(r) e^{i\nu\phi} \cdot e^{i(\omega t - \beta z)} \tag{4.1}$$

we can solve the wave equation for E_z, which in turn has been derived from the Maxwell equations. Here, A is a normalization constant, $f(r)$ the radial component, ν the wave index and β is the wavevector in the medium. The resulting equation for the radial component $f(r)$ is the differential equation of the Bessel functions. From the boundary condition, that the tangential field components at $r = a$ have to be continuous, one can find a system of equations, which has only a solution, if β satisfies an eigenvalue equation. More details on this derivation of the fields inside and outside of the optical fiber are given in [33].

After we know the solution for the electric field, we go into more detail on how to calculate the collective coupling rates for this particular system. In analogy to the case in three dimensions, where the field Hamiltonian is a sum over all modes, the

field Hamiltonian for the fiber field looks like

$$\hat{H}^{1D}_{\text{field}} = \sum_{\eta} \hbar\omega \hat{a}^{\dagger}_{\eta}\hat{a}_{\eta} = \sum_{\lambda f} \int_0^{\infty} d\omega \hbar\omega \hat{a}^{\dagger}_{\eta}\hat{a}_{\eta} \tag{4.2}$$

where we once again have the commutation relations

$$[\hat{a}_{\eta}, \hat{a}'_{\eta}] = 0 \qquad [\hat{a}^{\dagger}_{\eta}, \hat{a}^{\dagger}_{\eta'}] = 0$$
$$[\hat{a}_{\eta}, \hat{a}^{\dagger}_{\eta'}] = \delta$$

The parameter η stands here for all possible modes. In the three-dimensional case, we similarly have summed (or integrated) over all possible modes, namely every wavevector in three dimensions with different direction and different magnitude, and to each of these wavevectors there were two different polarizations to consider. In this lower dimensional case not all of these modes are possible. Especially for the propagation direction we are severely restricted, as the waves can only travel in forward or backwards direction within the waveguide. We still have the sum over the frequency ω and two polarizations λ to consider. Moreover, the waveguide may have higher modes indexed by ν, but the each mode can be treated independently, so we are restricting ourselves to just one mode and therefore drop the mode index ν. The index η then consists of $\eta = (\omega, \lambda, f)$ with $f = \pm 1$ denotes the propagation direction. The Hamiltonian for the atoms reads

$$\hat{H}_{\text{atom}} = \sum_{i}^{N} \hbar\omega_a \hat{\sigma}^{+}_{i}\hat{\sigma}^{-}_{i} = \sum_{i}^{N} \hbar\omega_a \hat{\sigma}^{ee}_{i} \tag{4.3}$$

where the index i denotes the particular atom and runs from 1 to the total number of atoms N. The commutation relations read

$$[\hat{\sigma}^{z}, \hat{\sigma}^{\pm}] = \pm 2\hat{\sigma}^{\pm}$$
$$[\hat{\sigma}^{ee}, \hat{\sigma}^{\pm}] = \pm\hat{\sigma}^{\pm}$$
$$[\hat{\sigma}^{+}, \hat{\sigma}^{-}] = \hat{\sigma}^{z}.$$

where commutators between operators with different index acting on different atoms are trivially zero. The interaction Hamiltonian reads (in dipole and rotating wave

approximation)

$$\hat{H}_{\text{int}}^{\text{1D}} = -i\hbar\frac{1}{\sqrt{2\pi}}\sum_{i}^{N}\int_{0}^{\infty} d\omega \sum_{\eta} g_\eta \mu \cdot (\epsilon_\eta \hat{a}_\eta \hat{\sigma}_j^{+} \cdot e^{if\beta k z_i} - h.c.) \tag{4.4}$$

with

$$g_\eta = \frac{\hbar\omega_\eta}{2\epsilon_0 v_g}\boldsymbol{\mu}\cdot\mathbf{E}(r_j, z_j). \tag{4.5}$$

with the group velocity $v_g = \frac{d\omega}{d\beta}$. As before, we start by finding the evolution in the interaction picture of the field operator $\hat{a}$. The Hamiltonian of the field gives us

$$\begin{aligned}[\hat{H}_{\text{field}}, \hat{a}_\eta] &= \sum_{\lambda' f'}\int_0^\infty d\omega\ \hbar\omega[\hat{a}_{\eta'}\hat{a}_{\eta'}^\dagger, \hat{a}_\eta^\dagger] = \\ &= \sum_{\lambda f}\int_0^\infty d\omega\ \hbar\omega\hat{a}_{\eta'}\delta(\omega'-\omega)\delta_{\lambda\lambda'}\delta_{ff'} = -\hbar\omega\hat{a}_\eta\end{aligned}$$

and

$$\begin{aligned}[\hat{H}_{\text{int}}^{\text{1D}}, \hat{a}_\eta] &= i\frac{1}{\sqrt{2\pi}}\sum_{j}^{N}\sum_{\lambda f}\int_0^\infty d\omega g_\eta^*\hat{\sigma}_j^- \cdot e^{-if\beta k z_i}[\hat{a}_{\eta'}^\dagger, \hat{a}_\eta]) \\ &= -i\frac{1}{\sqrt{2\pi}}\sum_{j}^{N} g_\eta^* e^{-i\beta(\omega)z_j}\sigma_j^-\end{aligned}$$

As the time evolution of the Heisenberg operator $\hat{a}_\eta$ is given by the commutator with the whole Hamiltonian (and the atomic Hamiltonian and $\hat{a}_\eta$ commute), the full time evolution looks like

$$\frac{d}{dt}\hat{a}_\eta = \frac{i}{\hbar}[\hat{H}, \hat{a}_\eta] = -i\omega\hat{a}_\eta + \frac{1}{\sqrt{2\pi}}\sum_{j}^{N} g_\eta^* e^{-i\beta(\omega)z_j}\sigma_j^- \tag{4.6}$$

Similar to what we did already in the section about the Wigner-Weisskopf approach, we can write the formal solution of the differential equation with the Green function $e^{i\omega(t-t')}$

$$\hat{a}_\eta(t) = \hat{a}_\eta(0)e^{-i\omega t} + \frac{1}{\sqrt{2\pi}}\int_0^t dt' e^{-i\omega(t-t')}\sum_{j}^{N} g_\eta^* e^{-i\beta(\omega)z_j}\sigma_j^-(t') \tag{4.7}$$

The first term is the homogeneous solution, while the second term with the integral is due to the source term $\frac{1}{\sqrt{2\pi}}\sum_j^N g_\eta^* e^{-i\beta(\omega)z_j}\sigma_j^-(t')$. As we are only interested in the

field generated by the atoms, but do not want to add an external field, we neglect the first term, which is the so-called in-field. In this derivation we notice the similarity to the equations that we already solved in the Wigner-Weisskopf section, we therefore use similar means (e.g. the Markov approximation) to proceed. The general time evolution of an atomic operator $\hat{O}$ is given by

$$\frac{d}{dt}\hat{O} = i[H, \hat{O}] = i[H_{\text{atom}}, \hat{O}] + i[H_{\text{int}}^{1D}, \hat{O}].$$

As the atomic Hamiltonian $\hat{H}_{\text{atom}}$ just introduces an oscillation phase (which can be seen from the commutation relations), let us focus on the other part

$$\frac{d}{dt}\hat{O} = i[H_{\text{atom}}, \hat{O}] + \frac{1}{\sqrt{2\pi}}\int_0^\infty d\omega \sum_{\lambda f}\sum_j \Big(g_\eta \hat{a}_\eta e^{if\beta(\omega)z_j}[\hat{\sigma}_j^+, \hat{O}] - g_\eta^* \hat{a}_\eta^\dagger e^{-if\beta(\omega)z_j}[\hat{\sigma}_j^-, \hat{O}]\Big) \tag{4.8}$$

We proceed by putting the formal solution of $\hat{a}_\eta(t)$ back into this equation, therefore we get for the time evolution of an operator

$$\begin{aligned}\frac{d}{dt}\hat{O} = \frac{1}{2\pi}\int_0^\infty d\omega \sum_{\lambda f}\sum_{jk} \\ \Big(\int_0^t dt'\ e^{-i\omega(t-t')}|g_\eta|^2 \hat{a}_\eta e^{if\beta(\omega)(z_j - z_k)}\hat{\sigma}_k^-(t')\ [\hat{\sigma}_j^+, \hat{O}] \\ - \int_0^t dt'\ e^{i\omega(t-t')}|g_\eta|^2 \hat{a}_\eta e^{-if\beta(\omega)(z_j - z_k)}[\hat{\sigma}_j^-, \hat{O}]\ \hat{\sigma}_k^+(t')\Big)\end{aligned} \tag{4.9}$$

At this point one might wonder about the order of operators as they do not commute. The full operators $\hat{a}_\eta$ and $\hat{a}_\eta^\dagger$, meaning including the in-field and the term originating from $\sum_j^N g_\eta^* e^{-i\beta(\omega)z_j}\sigma_j^-(t')$, commute with the commutators $[\hat{\sigma}_j^\pm, \hat{O}]$. However, once we neglect the in-field we have choose normal ordering and stick to that ordering. The in-fields will give rise to noise terms in the Langevin equations. However, as we are only interested in the master equation, which we can read off from the Quantum Langevin equation, we do not need to worry about this.

For the evaluation of this integral we, once again, have to do the Markov approximation. In the section about the Wigner-Weisskopf approach we switched into a rotating frame and briefly argued, why we can pull out the operator depending on t' in front of the integral. Let us do the same thing more carefully this time. From the interaction picture we know, that the dominating time evolution of the operator $\hat{\sigma}^\pm$ comes from

the atomic Hamiltonian, as the operators would oscillate with the atomic frequency ω_a. We define new operators $\bar{\hat{\sigma}}_j^{\pm}$ where the oscillating exponential is separated out:

$$\hat{\sigma}_j^+(t) \propto \hat{\sigma}_j^+(0) \cdot e^{i\omega_\mathrm{a} t} \qquad\qquad \bar{\hat{\sigma}}_j^+ = \hat{\sigma}_j^+(t) \cdot e^{-i\omega_\mathrm{a} t} \propto \hat{\sigma}_j^+(0)$$

In the first equation we note that the most dominant part of the time evolution is the oscillating exponential. In the newly defined operators we undo the oscillating exponential, resulting in the fact, that the operator $\bar{\hat{\sigma}}_j^+$ is related to $\hat{\sigma}_j^-(0)$ and, in particular, has a slow time evolution compared to the optical time scale given by the inverse frequency $\frac{1}{\omega_\mathrm{a}}$. Similar definitions for $\hat{\sigma}_j^-$ lead to

$$\hat{\sigma}_j^-(t) \propto \hat{\sigma}_j^-(0) \cdot e^{-i\omega_\mathrm{a} t} \qquad\qquad \bar{\hat{\sigma}}_j^- = \hat{\sigma}_j^-(t) \cdot e^{i\omega_\mathrm{a} t} \propto \hat{\sigma}_j^-(0).$$

Notice, that we transformed into a rotating frame, similar to the procedure using the interaction picture. These new definitions allow us to handle the integrals over t' in equation 4.9 with $\hat{\sigma}_j^{\pm}(t')$ by doing the following kinds of simplifications:

$$\int_0^t dt' \hat{\sigma}_j^-(t') = \int_0^t dt' \bar{\hat{\sigma}}_j^-(t') \cdot e^{-i\omega_\mathrm{a} t'} \approx \bar{\hat{\sigma}}_j^- \cdot \int_0^t dt' e^{-i\omega_\mathrm{a} t'} = \hat{\sigma}_j^- \cdot \int_0^t dt' e^{-i\omega_\mathrm{a}(t'-t)} \tag{4.10}$$

The first equal sign is just inserting the definition, but in the next step we drag the newly defined operator $\bar{\hat{\sigma}}_j^-(t)$ in front of the integral. Here it becomes obvious why we need to require, that $\bar{\hat{\sigma}}_j^-(t')$ changes slowly on the optical time scale: Just as in the Wigner-Weisskopf section, the oscillations are so fast that they average out over each oscillation period, as long as $\bar{\hat{\sigma}}_j^-(t')$ does not change much over the same period. This approximation is the Markov approximation which already encountered multiple times. Therefore the only big contribution comes from the time t. Putting the operator $\hat{\sigma}$ back into the integral yields

$$\int_0^t dt' \hat{\sigma}_j^-(t') = \int_0^t dt' \hat{\sigma}_j^- e^{-i\omega_\mathrm{a}(t'-t)} \tag{4.11}$$

where we identify a replacement rule, namely we can replace the operator depending on the time t' with the operator depending on t and an oscillating exponential. For the adjoint operator $\hat{\sigma}_j^+$ we find a similar rule:

$$\hat{\sigma}_j^-(t') \to \hat{\sigma}_j^- e^{-i\omega_\mathrm{a}(t'-t)} \qquad\qquad \hat{\sigma}_j^+(t') \to \hat{\sigma}_j^+ e^{i\omega_\mathrm{a}(t'-t)} \tag{4.12}$$

These replacement rules help us to proceed with equation 4.9. The operators $\hat{\sigma}_k^-(t')$

and $\hat{\sigma}_k^+(t')$ are now only dependent on the time t and we get the additional exponential, which we write together with the exponential $e^{\pm i\omega(t-t')}$. Looking at the resulting equations

$$\begin{aligned}\frac{d}{dt}\hat{O} = \frac{1}{2\pi}\int_0^\infty d\omega \sum_{\lambda f}\sum_{jk} \\ \Big(\int_0^t dt'\; e^{-i(\omega-\omega_\mathrm{a})(t-t')}|g_\eta|^2\hat{a}_\eta e^{if\beta(\omega)(z_j-z_k)}\hat{\sigma}_k^-\;[\hat{\sigma}_j^+,\hat{O}] \\ -\int_0^t dt'\; e^{i(\omega-\omega_\mathrm{a})(t-t')}|g_\eta|^2\hat{a}_\eta e^{-if\beta(\omega)(z_j-z_k)}[\hat{\sigma}_j^-,\hat{O}]\;\hat{\sigma}_k^+\end{aligned} \tag{4.13}$$

the only part depending on the time t', which we integrate over, is the exponential $e^{\pm i(\omega-\omega_\mathrm{a})(t-t')}$, the rest are constants or operators depending on time t. After we have done this Markov approximation, the integral can be evaluated similarly to our treatment of $\gamma(t-t')$ in the section about the Wigner-Weisskopf approximation. The so-called Sokhotski-Plemelj theorem, that is frequently used in Quantum Optics

$$\int_0^\infty d\omega e^{\pm i(\omega-\omega_\mathrm{a})(t-t')} = \pm iP\frac{1}{\omega-\omega_\mathrm{a}} + \pi\delta(\omega-\omega_\mathrm{a}), \tag{4.14}$$

allows us to perform the integral. Here, P denotes Cauchy's principal value. As this theorem is so useful in Quantum Optics and now already appeared twice in our derivations (albeit in slightly different form), we will motivate the theorem in section 4.2. In this step we also carry out the sum over the propagation direction $f = \pm$, which is how we end up with $\cos(\beta z_{jk})$, as $e^{i\beta z_{jk}} + e^{-i\beta z_{jk}} = 2\cos\beta z_{jk}$, where we use the shorthand notation $z_{jk} = z_j - z_k$. Moreover, we set $\boldsymbol{\mu} = \mu\mathbf{x}$, where $\mathbf{x}$ is the unit vector in x-direction. Altogether, this yields

$$\begin{aligned}\frac{d}{dt}\hat{O} = \int_0^\infty d\omega\;\frac{1}{\pi}\sum_{jk} \\ \Big((-iP\frac{1}{\omega-\omega_a} + \pi\delta(\omega-\omega_a))|g_\omega|^2\cos(\beta z_{jk})\hat{\sigma}_k^-[\hat{\sigma}_j^+,\hat{O}] \\ -(iP\frac{1}{\omega-\omega_a} + \pi\delta(\omega-\omega_a))|g_\omega|^2\cos(\beta z_{jk})[\hat{\sigma}_j^-,\hat{O}]\hat{\sigma}_k^+\end{aligned}$$

Now we define the collective couplings $\Omega_{jk}^{1\mathrm{D}}$ and $\Gamma_{jk}^{1\mathrm{D}}$

$$\frac{\Gamma_{jk}^{1\mathrm{D}}}{2} = \frac{1}{\pi}\int_0^\infty d\omega\pi\delta(\omega-\omega_0)|g_\omega|^2\cos(\beta z_{jk}) \tag{4.15}$$

and

$$\frac{\Omega_{jk}^{1\mathrm{D}}}{2} = \frac{1}{\pi}\int_0^\infty d\omega\Big(-iP\frac{1}{\omega-\omega_0}|g_\omega|^2\cos(\beta z_{jk})\Big)z_{jk}) \tag{4.16}$$

Using these definitions and the relations between adjoint Lindblad operator in the next section 4.1, we can finally write down the master equation

$$\dot{\rho} = i[\rho, \sum_{j\neq k}\Omega_{jk}^{1\mathrm{D}}\hat{\sigma}_j^+\hat{\sigma}_k^-] + \sum_{jk}\frac{\Gamma_{jk}^{1\mathrm{D}}}{2}\Big(2\hat{\sigma}_j^-\rho\hat{\sigma}_k^+ - \hat{\sigma}_j^+\hat{\sigma}_k^-\rho - \rho\hat{\sigma}_j^+\hat{\sigma}_k^-\Big). \tag{4.17}$$

The remaining thing to do is to evaluate the integrals for the collective coupling rates $\Gamma_{jk}^{1\mathrm{D}}$ and $\Omega_{jk}^{1\mathrm{D}}$. The integral for the collective decay rates $\Gamma_{jk}^{1\mathrm{D}}$ is straightforward by making use of the δ function and yields

$$\frac{\Gamma_{jk}^{1\mathrm{D}}}{2} = \frac{1}{\pi}\int_0^\infty d\omega\pi\delta(\omega-\omega_0)|g_\omega|^2\cos(\beta z_{jk}) = \frac{\omega_\mathrm{a}\mu^2E_x^2}{2\epsilon_0 v_\mathrm{g}}\cos(\beta z_{jk}) = \frac{\Gamma^{1\mathrm{D}}}{2}\cos(\beta z_{jk}) \tag{4.18}$$

The integral for the collective dipole shifts $\Omega_{jk}^{1\mathrm{D}}$ can be evaluated using the methods of complex contour integration, which we will sketch in the following. We start by noting that pole of the integral is at $\omega = \omega_\mathrm{a}$. We slightly shift the pole to $\omega_\mathrm{a} + i\epsilon$ into the upper half plane. The residue theorem allows us to calculate the closed contour integral by simply evaluating the residue of the pole contained by the closed contour. The contour itself runs on the real axis and closes in the upper half plane with an infinitely big semicircle. One can show, that for certain functions the contour integral over the big semicircle gives zero, as the integrands approach zero fast enough with increasing radius of the semicircle. This allows us to express the integral over the real axis as a residue. Taking only the real part this yields

$$\Omega_{jk}^{1\mathrm{D}} = -\lim_{\epsilon\to 0}\frac{1}{\pi}\Re\oint d\omega\frac{|g_\omega|^2}{\omega-(\omega_\mathrm{a}+i\epsilon)}\frac{1}{2}(e^{i\beta z_{jk}} + e^{-i\beta z_{jk}}) \tag{4.19}$$

The residue theorem allows us to write this integral as a sum over the residues of the poles; as we only have one pole, a single residue will suffice.

$$\begin{aligned}\Omega_{jk}^{1\mathrm{D}} &= -\frac{1}{\pi}\Re\{\ 2\pi i\cdot|g_\omega|^2e^{i\beta z_{jk}}\} = \\ &= -\Re\{\ i\cdot|g_\omega|^2(\cos\beta z_{jk} + i\sin\beta z_{jk})\} = \\ &= |g_\omega|^2\sin\beta z_{jk}) = \frac{\omega_\mathrm{a}\mu^2E_x^2}{2\epsilon_0 v_\mathrm{g}}\sin\beta z_{jk}\end{aligned} \tag{4.20}$$

4.1 Connection between master equation for density operator and system operator

The master equation for the density operator is given by

$$\frac{d}{dt}\hat{\rho} = \mathcal{L}[\rho] \tag{4.21}$$

with the Lindblad superoperator $\mathcal{L}$ and formal solution

$$\hat{\rho}(t) = e^{\mathcal{L}t}\hat{\rho}(0) \tag{4.22}$$

where the exponential is defined by the Taylor series.

Let us first find the equation that governs the evolution of a system operator $\hat{O}$. We state the definitions of $\mathcal{L}$ and $\mathcal{L}^\dagger$

$$\mathcal{L}[\hat{\rho}] = -i[\hat{H}_0, \hat{\rho}] + \Gamma \cdot \left(2\hat{\sigma}\hat{\rho}\hat{\sigma}^\dagger - \hat{\sigma}\hat{\sigma}^\dagger\hat{\rho} - \hat{\rho}\hat{\sigma}\hat{\sigma}^\dagger\right)$$
$$\mathcal{L}^\dagger[\hat{O}] = +i[\hat{H}_0, \hat{O}] + \Gamma \cdot \left(2\hat{\sigma}^\dagger\hat{O}\hat{\sigma} - \hat{\sigma}^\dagger\hat{\sigma}\hat{O} - \hat{O}\hat{\sigma}^\dagger\hat{\sigma}\right)$$

Second, we observe that

$$\mathrm{Tr}\left\{\hat{O}\mathcal{L}[\hat{\rho}]\right\} = \mathrm{Tr}\left\{\mathcal{L}^\dagger[\hat{O}]\hat{\rho}\right\} \tag{4.23}$$

which is easy to prove using the previous definition and the cyclic property of the trace. We require, that the expectation values of operators are the same, regardless of the choice between Schroedinger picture or Heisenberg picture

$$\langle\hat{O}\rangle(t) = \mathrm{Tr}\left\{\hat{O}(0)\hat{\rho}(t)\right\} = \mathrm{Tr}\left\{\hat{O}(0)e^{\mathcal{L}t}\hat{\rho}(0)\right\} =$$
$$= \sum_k \frac{t^k}{k!} \cdot \mathrm{Tr}\left\{\hat{O}(0)\mathcal{L}^k[\hat{\rho}(0)]\right\}$$

where we use the shorthand notation of $\mathcal{L}^2[\hat{\rho}(0)] = \mathcal{L}[\mathcal{L}[\hat{\rho}(t)]]$, ... Repeatedly applying property 4.23, we arrive at

$$\langle\hat{O}\rangle(t) = \sum_k \frac{t^k}{k!} \cdot \mathrm{Tr}\left\{\left(\mathcal{L}^\dagger\right)^k[\hat{O}(0)]\hat{\rho}(0)\right\} =$$

$$= \mathrm{Tr}\left\{e^{\mathcal{L}^\dagger t}\hat{O}(0)\hat{\rho}(0)\right\} \equiv \mathrm{Tr}\left\{\hat{O}(t)\hat{\rho}(0)\right\}$$

In the last line, one can read off the time evolution of the system operator $\hat{O}$. This time evolution and the corresponding differential equation are

$$\frac{d}{dt}\hat{O} = \mathcal{L}^\dagger[O] \qquad\qquad \hat{O}(t) = e^{\mathcal{L}^\dagger t}\hat{O}(0)$$

In conclusion, to switch from the Schroedinger picture with time-dependent state $\hat{\rho}(t)$ into the Heisenberg picture with time dependent system operators $\hat{O}(t)$ we just have to use the adjoint Lindblad superoperator in the differential equation. A more formal proof is given in [34], while the results presented here can also be found in [35] (p. 124f).

4.2 Sokhotski-Plemelj theorem

In this section we further investigate the relation

$$\int_0^t dt' e^{\pm i(\omega-\omega_\mathrm{a})(t-t')} = \pm iP\frac{1}{\omega-\omega_\mathrm{a}} + \pi\delta(\omega-\omega_\mathrm{a}), \tag{4.24}$$

known as Sokhotski-Plemelj theorem. This theorem is frequently used in Quantum Optics and in our derivation of the collective coupling rates for the one dimensional setup it proved to be useful. Moreover, we had to evaluate a similar integral in the section 3.2 about the Wigner-Weisskopf approach. Analogous to the proceedings in section 3.2, we start by introducing a small offset $\epsilon > 0$ in the exponent. Taking the limit of $\epsilon \to 0$ then is equivalent to the left hand side of equation 4.24. Now the integration over the variable t' can be carried out before taking the limit. This leads us to

$$\lim_{\epsilon\to 0}\int_0^t dt' e^{\pm i(\omega-\omega_\mathrm{a})(t-t')-\epsilon(t-t')} = \lim_{\epsilon\to 0}\frac{e^{\pm i(\omega-\omega_\mathrm{a})(t-t')-\epsilon(t-t')}}{\mp i(\omega-\omega_\mathrm{a})+\epsilon}|_{t'=0}^{t'=t} \tag{4.25}$$

Inserting the lower and upper bound and performing the limit in the numerator yields

$$\lim_{\epsilon\to 0}\int_0^t dt' e^{\pm i(\omega-\omega_\mathrm{a})(t-t')-\epsilon(t-t')} = \lim_{\epsilon\to 0}\frac{0-e^{\pm i(\omega-\omega_\mathrm{a})t}}{\mp i(\omega-\omega_\mathrm{a})+\epsilon} = \pm i\lim_{\epsilon\to 0}\frac{e^{\pm i(\omega-\omega_\mathrm{a})t}}{(\omega-\omega_\mathrm{a})\pm i\epsilon} \tag{4.26}$$

where we already put in the limits $t' = t$ and $t' = 0$. Keep in mind, that eventually the last term in equation 4.26 will serve as an integrand in the integral over the variable ω. Evaluating the integral over ω with this integrand is not straightforward, as the

denominator goes to zero when ω approaches ω_a. In order to prove equation 4.24, we examine this limit of a small imaginary offset in the denominator approaching zero. The integral over ω that we have to evaluate after carrying out the integral over t', looks like

$$\lim_{\epsilon\to 0}\int_a^b d\omega\ \frac{f(\omega)}{(\omega-\omega_\mathrm{a})\pm i\epsilon}, \tag{4.27}$$

with $a<\omega-\omega_\mathrm{a}<b$. First, we make the denominator real by expanding with its complex conjugate. This splits up the integral into two parts

$$\int_a^b d\omega\ \frac{f(\omega)}{(\omega-\omega_\mathrm{a})\pm i\epsilon}=\int_a^b d\omega\ \frac{f(\omega)\cdot(\omega-\omega_\mathrm{a})}{(\omega-\omega_\mathrm{a})^2+\epsilon^2}\pm i\epsilon\int_a^b d\omega\ \frac{f(\omega)}{(\omega-\omega_\mathrm{a})^2+\epsilon^2}. \tag{4.28}$$

Let us proceed by investigating the first term on the right hand side. Using the linearity of the integral, we split it up into three parts:

$$\begin{aligned}\int_a^b d\omega\ \frac{f(\omega)\cdot(\omega-\omega_\mathrm{a})}{(\omega-\omega_\mathrm{a})^2+\epsilon^2}=&\int_{\omega_\mathrm{a}-\delta}^{\omega_\mathrm{a}+\delta} d\omega\ \frac{f(\omega)\cdot(\omega-\omega_\mathrm{a})}{(\omega-\omega_\mathrm{a})^2+\epsilon^2}+\\&+\int_a^{\omega_\mathrm{a}-\delta} d\omega\ \frac{f(\omega)\cdot(\omega-\omega_\mathrm{a})}{(\omega-\omega_\mathrm{a})^2+\epsilon^2}+\int_{\omega_\mathrm{a}+\delta}^b d\omega\ \frac{f(\omega)\cdot(\omega-\omega_\mathrm{a})}{(\omega-\omega_\mathrm{a})^2+\epsilon^2}\end{aligned} \tag{4.29}$$

where δ is assumed to be small and we take the limit $\delta\to 0$. Then, the second line is just the definition of Cauchy's principal value, so

$$P\int_a^b d\omega\ \frac{f(\omega)\cdot(\omega-\omega_\mathrm{a})}{(\omega-\omega_\mathrm{a})^2+\epsilon^2}\equiv\int_a^{\omega_\mathrm{a}-\delta} d\omega\ \frac{f(\omega)\cdot(\omega-\omega_\mathrm{a})}{(\omega-\omega_\mathrm{a})^2+\epsilon^2}+\int_{\omega_\mathrm{a}+\delta}^b d\omega\ \frac{f(\omega)\cdot(\omega-\omega_\mathrm{a})}{(\omega-\omega_\mathrm{a})^2+\epsilon^2} \tag{4.30}$$

For the integral including the singularity at $\omega=\omega_\mathrm{a}$ in the first line we note, that as we take the limit of $\delta\to 0$, the function $f(\omega)$ becomes constant over the integration interval, as the integration interval shrinks to an arbitrarily small size. Therefore, we pull the function $f(\omega)$ in front of the integral and replace ω with ω_a. However, the remaining integrand is odd with respect to the center of the integration interval, meaning the integral vanishes. In conclusion, the first term on the right hand side of equation 4.28 is Cauchy's principal value. The second term can be simplified as follows: As we eventually want to take the limit of $\epsilon\to 0$ and the term has a factor ϵ, the only contribution comes from the small integration interval around $\omega=\omega_\mathrm{a}$. Once again, we can pull our function $f(\omega)$ in front of the integral and replace ω by ω_a. The remaining integral is trivial

$$\epsilon\int_a^b d\omega\ \frac{f(\omega)}{(\omega-\omega_\mathrm{a})^2+\epsilon^2}\approx\epsilon f(\omega_\mathrm{a})\int_a^b d\omega\ \frac{1}{(\omega-\omega_\mathrm{a})^2+\epsilon^2} \tag{4.31}$$

$$= \epsilon f(\omega_\mathrm{a}) \cdot \frac{1}{\epsilon} \arctan\Big(\frac{\omega - \omega_\mathrm{a}}{\epsilon}\Big)\Big|_{\omega=a}^{\omega=b}$$

where in the last step the ϵ cancels. In the limit of $\epsilon \to 0$ we find

$$\lim_{\epsilon\to 0} \epsilon \int_a^b d\omega \; \frac{f(\omega)}{(\omega-\omega_\mathrm{a})^2+\epsilon^2} \approx f(\omega_\mathrm{a}) \cdot \lim_{\epsilon\to 0} \arctan\Big(\frac{\omega - \omega_\mathrm{a}}{\epsilon}\Big)\Big|_{\omega=a}^{\omega=b} = f(\omega_\mathrm{a}) \cdot \pi. \quad (4.32)$$

Collecting all the previous results, we end up with

$$\lim_{\epsilon\to 0} \int_a^b d\omega \; \frac{f(\omega)}{(\omega-\omega_\mathrm{a}) \pm i\epsilon} = P \int_a^b d\omega \; \frac{f(\omega)}{(\omega-\omega_\mathrm{a})} \mp i\pi f(\omega_\mathrm{a}). \quad (4.33)$$

For a more rigorous treatment, one has to use methods of complex integration which has been done e.g. in [30] (p. 102-106). Omitting all the integrals in equation 4.33, we are left with

$$\lim_{\epsilon\to 0} \; \frac{f(\omega)}{(\omega-\omega_\mathrm{a}) \pm i\epsilon} = P \; \frac{f(\omega)}{(\omega-\omega_\mathrm{a})} \mp i\pi f(\omega_\mathrm{a}) \cdot \delta(\omega-\omega_\mathrm{a}). \quad (4.34)$$

Of course, this expression only makes sense as an integrand in an integral over ω, but this is precisely the case in equation 4.13. Putting this expression back into equation 4.26 with $f(\omega) = e^{\pm i(\omega-\omega_\mathrm{a})t}$ and $f(\omega_\mathrm{a}) = 1$

$$\lim_{\epsilon\to 0} \int_0^t dt' e^{\pm i(\omega-\omega_\mathrm{a})(t-t')-\epsilon(t-t')} = \pm i\Big(P \; \frac{1}{(\omega-\omega_\mathrm{a})} \mp i\pi\cdot\delta(\omega-\omega_\mathrm{a})\Big) = \pm iP \; \frac{1}{(\omega-\omega_\mathrm{a})} + \pi\delta(\omega-\omega_\mathrm{a}) \quad (4.35)$$

leaves us with the desired result, the so-called Sokhotski-Plemelj theorem.

5 The cumulant expansion

Now that we know the set of differential equations that governs the dynamics of atoms coupled to electromagnetic fields, we proceed to (at least numerically) solve them. However, as we want to study collective effects, we immediately run into a big problem: if N is the number of atoms in our system, then the dimension of the Hilbert space is 2^N, even for the simplest case of two-level atoms. Just storing the state of such a highly dimensional system is extremely challenging: We need the complex amplitudes of the state for all possible 2^N basis states. Even if a single amplitude only needed 1 Byte (depending on the required precision, 16 Byte is more realistic), for a rather small system of $N = 50$ atoms we would already need 2^{50} Bytes, which is 1 PetaByte. This exponential scaling cannot be handled by just building bigger computers. Each additional atom doubles the necessary size of the Hilbert space. Soon the state vector requires more bits than atoms in the universe. If we want to simulate as many as hundreds of thousands of atoms, we have to find a way to handle this problem.

One big simplification arises due to the symmetric nature of the processes: If atoms are indistinguishable, e.g. if they are close together like in the Dicke Superradiance, then this ensemble can only occupy the symmetric subspace of the whole space, as the state has to be the same if we exchange any pair of particles. This severely reduces the number of accessible states, in fact, this symmetric subspace only contains $N + 1$ states and is equivalent to the Dicke ladder or the rightmost column of the Dicke Triangle [36]. Yet, if we divide the whole ensemble of atoms into subensembles, each subensemble only occupying such a symmetric subspace, the dimensions of the Hilbert space size still scales like

$$\dim\mathcal{H} = \prod_{i}^{n}(N_i + 1) \tag{5.1}$$

with n being the number of ensembles and N_i the number of atoms in the i-th ensemble. The system size still scales exponentially with the number of subensembles. In order to handle this, we use to following simplification: Instead of simulating the dynamics of the operators (in the Heisenberg picture), we are only interested in the expectation

value of a finite set of operators. This allows us to simplify the differential equation from an operator equation to a c-number equation. Let us try this for a simple case of atoms collectively interacting via an electromagnetic field. The master equation in this case reads

$$\dot{\rho} = i[\rho, \sum_{j \neq k} \Omega_{jk} \hat{\sigma}_j^+ \hat{\sigma}_k^-] + \sum_{jk} \frac{\Gamma_{jk}}{2} \Big(2\hat{\sigma}_j^- \rho \hat{\sigma}_k^+ - \hat{\sigma}_j^+ \hat{\sigma}_k^- \rho - \rho \hat{\sigma}_j^+ \hat{\sigma}_k^- \Big). \tag{5.2}$$

In order to find a differential equation for the expectation value of an operator $\hat{O}$ we write down

$$\frac{d}{dt}\langle \hat{O} \rangle = \frac{d}{dt} \mathrm{Tr}\{\hat{O}\hat{\rho}(t)\} = \mathrm{Tr}\{\hat{O}\frac{d}{dt}\hat{\rho}(t)\}. \tag{5.3}$$

In the Schroedinger picture, the operators are time independent and we are allowed to pull the time derivative inside the trace, as both operations are linear. For the time derivative of $\hat{\rho}(t)$ we insert the above master equation. Using the invariance of the trace under cyclic permutation and common commutation relations, one can derive a differential equation for the expectation value of the operator $\hat{O}$. Let's say we are interested in the excited state population, so we set $\hat{O} = \hat{\sigma}_i^{ee}$. In the simplest case of independent emitters, i.e. $\Omega_{jk} = 0$ and $\Gamma_{jk} = \delta_{jk}$, one arrives at the simple formula

$$\frac{d}{dt}\langle \hat{\sigma}_i^{ee} \rangle = -\Gamma_{ii} \langle \hat{\sigma}_i^{ee} \rangle \tag{5.4}$$

This is just an exponential decay with rate Γ_{ii} as we expected according to our previous results in the Wigner-Weisskopf approach. If the system gets more complicated, e.g. the atoms couple to each other, then the equations for the expectation values of operators get more complicated too. As an example, take the Dicke superradiance with $\Omega_{jk} = 0$ and $\Gamma_{jk} = \Gamma$. This particular setup can be achieved by putting atoms sufficiently close together in free space, or having atoms along a one dimensional fiber, with a distance of a multiple of a wavelength between each pair of atoms. Then the equation reads

$$\frac{d}{dt}\langle \hat{\sigma}_i^{ee} \rangle = -\Gamma_{ii} \langle \hat{\sigma}_i^{ee} \rangle - \sum_{i \neq k}^{N} \frac{\Gamma_{ik}}{2} (\langle \hat{\sigma}_i^+ \hat{\sigma}_k^- \rangle + \langle \hat{\sigma}_i^- \hat{\sigma}_k^+ \rangle). \tag{5.5}$$

In order to solve this differential equation, we also need to derive an equation for the expectation value of the operator product $\langle \hat{\sigma}_i^+ \hat{\sigma}_k^- \rangle$, which in turn may depend on expectation values of further operator products and so on. If one derives all these equations, e.g. for a finite system of two-level atoms, one arrives at the same

dimensionality as in the case for the full master equation. However, here comes the cumulant expansion into play: At some point we will truncate this expansion by approximating higher-order operator products by a combination of lower-order operator products, where we define the number of operators as the order. Then the resulting closed set of differential equations has a (much) lower dimensionality, allowing us to numerically integrate these equations. This concept of truncating was first introduced by R. Kubo in [37]. N. G. van Kampen has given a more hands-on approach in [38]. As deriving the equations by hand can be tedious, the julia-package QuantumCumulants.jl has simplified this step and also allows a direct numerical implementation. In the corresponding article [39] the authors also provide a short review of the method:

The joint cumulant, denoted by $\langle\bullet\rangle_{\mathrm{c}}$, of a product of order n of the operators $\hat{X}_1, \hat{X}_2, ..., \hat{X}_n$ is given by [37]:

$$\langle \hat{X}_1 \hat{X}_2 ... \hat{X}_n \rangle_{\mathrm{c}} = \sum_{p \in P(\mathcal{I})} (|p|-1)!(-1)^{|p|-1} \prod_{B \in p} \langle \prod_{i \in B} \hat{X}_i \rangle. \tag{5.6}$$

Here, $\mathcal{I} = 1, 2, ..., n$, $P(\mathcal{I})$ is the set of all partitions of $\mathcal{I}$ and $|p|$ denotes the length of the partition p while B runs over the blocks of each partition. The joint cumulant of order n is then given by one term of order n and other terms with order $< n$. Rearranging this equation allows us to express this one term of order n using only terms of lower order than n and the joint cumulant. Theorem I in [37] states, that the joint cumulant of a set of operators is zero, if any one (or any subset) of them is statistically independent of the others. As the joint cumulant can be thought of as a measure of correlation of operators, we assume, that it is zero [39] and neglect it. In turn, this allows us to express terms of order n only by terms with lower order by

$$\langle \hat{X}_1 \hat{X}_2 ... \hat{X}_n \rangle = \sum_{p \in P(\mathcal{I}) \backslash \mathcal{I}} (|p|-1)!(-1)^{|p|-1} \prod_{B \in p} \langle \prod_{i \in B} \hat{X}_i \rangle. \tag{5.7}$$

where $P(\mathcal{I})\backslash\mathcal{I}$ is the set of all partitions of $\mathcal{I}$ except $\mathcal{I}$ itself. Using this formula, we are able to express expectation values of operator products of order n as a sum of expectation values of operator products of lower order. This approximation allows us to truncate the derivation of expectation values of new operators and then close the set of differential equations in order to numerically integrate the set. As we introduced an approximation when we set the joint cumulant to zero, we should check if this is actually valid for our system. This can be numerically involved depending on system

size and expansion order, as the proper way to do this is to actually compute the joint cumulant.

However, for some systems it might be possible to check the agreement between expansion orders and the full master equation for a low number of atoms to provide an insight into the necessary expansion order to capture the relevant system dynamics. As it turns out, the so-called mean field ($n = 1$) is often not enough, as here we neglect all correlations between particles. Going to the second order, $n = 2$, already allows us to describe lots of systems sufficiently accurately. In the case of Dicke Superradiance, chapter 8 looks further into the details. As we need the expansions for second order $n = 2$ and third order $n = 3$ frequently, let us state them explicitly here

$$\langle \hat{X}_1 \hat{X}_2 \rangle = \langle \hat{X}_1 \rangle \langle \hat{X}_2 \rangle \tag{5.8a}$$

$$\langle \hat{X}_1 \hat{X}_2 \hat{X}_3 \rangle = \langle \hat{X}_1 \hat{X}_2 \rangle \langle \hat{X}_3 \rangle + \langle \hat{X}_1 \hat{X}_3 \rangle \langle \hat{X}_2 \rangle + \langle \hat{X}_1 \rangle \langle \hat{X}_2 \hat{X}_3 \rangle - 2 \langle \hat{X}_1 \rangle \langle \hat{X}_2 \rangle \langle \hat{X}_3 \rangle \tag{5.8b}$$

The cumulant expansion allows us to go from the exponential scaling for independent emitters of 2^N to a polynomial scaling N^2, N^3 etc. for second order and third order respectively. The price we have to pay is that the results are now approximate. Together with the grouping of indistinguishable atoms into subensembles, the cumulant expansion allows us to simulate the dynamics of hundreds of thousands of atoms sufficiently accurate, such that we find the processes that govern the collective dynamics of such big atomic ensembles.

6 Publication

The author of this thesis carried out the theoretical analysis as well as all analytical and numerical calculations presented in this work. C. Hotter and D. Plankensteiner provided helpful discussions and support in the interpretation of the results and H. Ritsch had the idea and was responsible for the supervision of this work. The first draft was written by the author of this thesis and later improved upon by the other authors.

Open Research Europe 4:8 (2024)

Threshold studies for a hot beam superradiant laser including an atomic guiding potential

M. Fasser, C. Hotter, D. Plankensteiner, and H. Ritsch

Background: Recent theoretical predictions hint at an implementation of a superradiant laser based on narrow optical clock transitions by using a filtered thermal beam at high density. Corresponding numerical studies give encouraging results but the required very high densities are sensitive to beam collimation errors and inhomogeneous shifts. Here we present extensive numerical studies of threshold conditions and the predicted output power of such a superradiant laser involving realistic particle numbers and velocities along the cavity axis. Detailed studies target the threshold scaling as a function of temperature as well as the influence of eliminating the hottest part of the atomic distribution via velocity filtering and the benefits of additional atomic beam guiding.

Methods: Using a cumulant expansion approach allows us to quantify the significance of atom-atom and atom-field correlations in such configurations. We predict necessary conditions to achieve a certain threshold photon number depending on the atomic temperature and density.

Results: In particular, we show that the temperature threshold can be significantly increased by using more atoms. Moreover, a velocity filter removing very fast atoms has only almost negligible influence despite their phase perturbing properties. On the positive side an additional conservative optical guiding towards cavity mode antinodes leads to significantly lower threshold and higher average photon number.
Conclusions: Interestingly we see that higher order atom-field and direct atom-atom quantum correlations play only a minor role in the laser dynamics, which is a bit surprising in the superradiant regime.

6.1 Introduction

Ever since the demonstration of the superior operation of an optical atomic clock [40–42] with respect to microwave implementations people started wondering about a possible active clock implementation in form of a superradiant laser [22, 43–58]. In analogy to the very successful hydrogen micro-maser technology [59] such an active device in principle promises at least similar stability and accuracy at a reduced technical cost and fragility. Here an implementation based on a dilute gas of cold clock atoms within a high-Q optical cavity was predicted to be a very promising path to go [44]. As a particular example, model setups based on a beam of inverted ultracold atoms traversing an optical resonator [60–62] were predicted to yield unprecedented stability and accuracy. However, as the operating optical wavelength ($\sim$ 500 nm) is several orders of magnitude shorter than the typical maser lines ($\sim$ 20 cm), the resulting technological challenges are similarly larger.

Already the construction of a suitable beam source is virtually equivalent to operating a continuous atom laser [63, 64] and thus poses a way more challenging task than its microwave analog. As the cavity mode volume is also way smaller the atoms have to be tightly confined before sending them through the resonator. Yet another problem is creating atomic inversion with minimal perturbation [65]. Despite intense efforts which recently lead to amazing technical advancements on guided atom beams [66–69] and pulsed superradiant lasing [20, 70–76], a fully continuous operating device [22, 48] has not been realized.

In recent calculations it was pointed out that a high precision could already be achieved using a much hotter atomic ensemble with a sufficiently high intra-cavity density [62, 77–79]. Here the sheer number of contributing atoms allows to cross the

laser threshold inducing an efficient collective synchronization process towards a very narrow effective linewidth. This approach at least in principle requires significantly less components and would allow for a rather compact setup involving only a beam oven, an optical resonator and a pump laser to create inversion. The precise conditions for a concrete setup, however, cannot be reliably analytically predicted and thus require large scale numerical simulations [62]. Here we set up a framework for such simulations which can deal with realistically large atom numbers and velocities. This allows to identify the minimal operating conditions and study the influence of extra elements as velocity filters or guiding potentials.

6.2 Methods: Theoretical Model

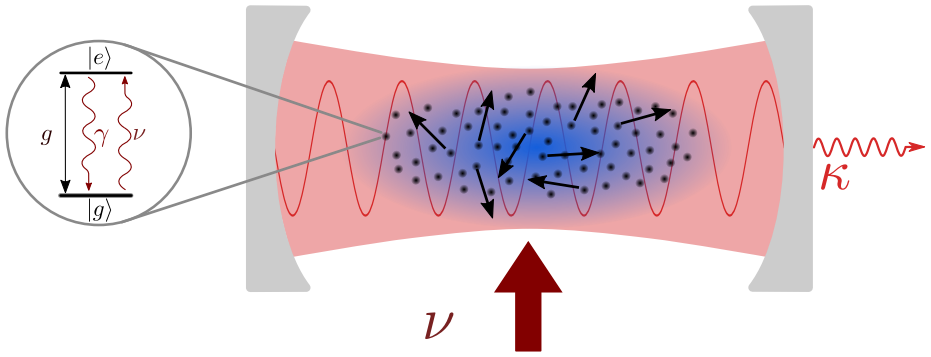

Figure 6.1: *Schematic of the system.* Atoms are incoherently pumped with rate ν and couple to an optical cavity. The clusters move according to a Gaussian velocity distribution with standard deviation σ_v, which relates to a certain temperature T. This motion is included along the cavity axis with a position dependent coupling strength g. The atoms decay with the rate γ and the photons leak out of the cavity with a rate κ.

We consider an ensemble of N two-level atoms with a transition frequency of ω_a coupled to a single mode cavity with resonance frequency ω_c, see Fig. 6.1. The coherent dynamics of this system is governed by the Tavis Cummings Hamiltonian, which in the rotating frame of the atomic transition frequency ω_a reads

$$H = \Delta a^\dagger a + \sum_{j=1}^{N} g(x_j)(a^\dagger \sigma_j^{\mathrm{ge}} + \sigma_j^{\mathrm{eg}} a), \tag{6.1}$$

with the atomic transition operator of the j-th atom $\sigma_j^{\mathrm{ge}} = |g\rangle_j\langle e|$, the cavity photon creation (annihilation) operator $a^\dagger$ (a), and the cavity-atom detuning $\Delta = \omega_\mathrm{c} - \omega_\mathrm{a}$. Atoms at a position x along the cavity axis couple to the cavity according to the mode function $g \cdot f(x) = g \cdot \cos(2\pi x/\lambda)$, where g is the maximal cavity coupling strength and λ the wavelength of the cavity photons. The motion of the atoms is treated classically by an initial atomic velocity drawn from a Gaussian distribution with width σ_v corresponding to a temperature T. In the beginning we treat freely moving atoms, later on we investigate the influence of an external optical potential. In both cases the atomic motion is fully determined by the initial velocity and position.

Additional to the coherent dynamics we need to account for the dissipative processes, which are described by Liouvillian term $\mathcal{L}[\rho]$ in the master equation for the system density matrix ρ

$$\dot{\rho} = i[\rho, H] + \mathcal{L}[\rho]. \tag{6.2}$$

In the Born-Markov approximation the Liouvillian super-operator for a jump operator J_i with a corresponding rate Γ_i can be written in Lindblad form as

$$\mathcal{L}[\rho] = \sum_i \frac{\Gamma_i}{2}\left(2J_i\rho J_i^\dagger - J_i^\dagger J_i\rho - \rho J_i^\dagger J_i\right). \tag{6.3}$$

The considered dissipative processes are listed in table 6.1, including cavity photon losses, individual spontaneous decay as well as incoherent pumping of the two-level atoms.

As we want to simulate systems with up to one million atoms, we cannot solve the full master equation due to exponential scaling of the size of the Hilbert space with the particle number. To this end we employ a mean field approach for operator averages. For a non-explicitly time-dependent operator $\mathcal{O}$ we can calculate the time-evolution

Table 6.1: *Dissipative Processes.* The system features a damped cavity mode, atomic decay and an incoherent pump.

i	c_i	Γ_i	Description
1	a	κ	cavity photon losses
2	σ_j^{ge}	γ	decay from $\|2\rangle_j$ to $\|1\rangle_j$
3	σ_j^{eg}	ν	excitation of the j-th atom

of its expectation value as

$$\frac{\mathrm{d}}{\mathrm{d}t}\langle\mathcal{O}\rangle = \mathrm{Tr}\{\mathcal{O}\dot{\rho}\} = i\langle[H,\mathcal{O}]\rangle + \langle\bar{\mathcal{L}}[\mathcal{O}]\rangle \tag{6.4}$$

with

$$\bar{\mathcal{L}}[\mathcal{O}] = \sum_i \frac{\Gamma_i}{2}\left(2J_i^\dagger \mathcal{O} J_i - J_i^\dagger J_i \mathcal{O} - \mathcal{O} J_i^\dagger J_i\right), \tag{6.5}$$

where we inserted the master equation (6.2) into Eq. (6.4) and used the cyclic property of the trace. To truncate the set of equations we approximate higher order quantum correlations with the cumulant expansion method [37, 80].

The first order approximation (mean field) is sufficient to accurately describe our system (see Appendix), the corresponding set of equations is

$$\dot{\langle a\rangle} = -\left(\frac{\kappa}{2} + i\Delta\right)\langle a\rangle - ig\sum_m f(x_m)\langle\sigma_m^{\mathrm{ge}}\rangle \tag{6.6a}$$

$$\dot{\langle\sigma_m^{\mathrm{ge}}\rangle} = -\frac{\gamma+\nu}{2}\langle\sigma_m^{\mathrm{ge}}\rangle + 2igf(x_m)(\langle\sigma_m^{\mathrm{ee}}\rangle - \frac{1}{2})\langle a\rangle \tag{6.6b}$$

$$\dot{\langle\sigma_m^{\mathrm{ee}}\rangle} = -(\gamma+\nu)\langle\sigma_m^{\mathrm{ee}}\rangle + igf(x_m)(\langle a\rangle^*\langle\sigma_m^{\mathrm{ge}}\rangle - \langle\sigma_m^{\mathrm{eg}}\rangle^*\langle a\rangle) + \nu, \tag{6.6c}$$

where the last two equations exist for each atom from $m = 1$ to N. The number of equations in this approximation scales linearly with the atom number N. Still, to simulate a system with several hundred thousand atoms we need further approximations. To this end, we assume that groups of K atoms behave in a sufficiently identical way, such that we can describe them with the same equations. This means, we group atoms into clusters. For the set of equations in 6.6, this means that the index m now runs only from $m = 1$ to the number of clusters N_{Cl}, but the source term $-ig\sum_m f(x_m)\langle\sigma_m^{\mathrm{ge}}\rangle$ in Eq. (6.6a) gets enhanced by the clustersize K. In the following, we use a clusternumber of $N_{\mathrm{Cl}} = 400$, which is a good compromise between simulating the real setup and still having a feasible computation time (see Appendix).

6.3 Photon number dependence on temperature

First, we investigate the influence of the atom number N and the temperature T on the steady state photon number. The results in mean field (for a comparison to higher orders see Appendix) are depicted in Fig. 6.2. Unsurprisingly, we always end up with the highest number of photons for the lowest temperature. The drop-

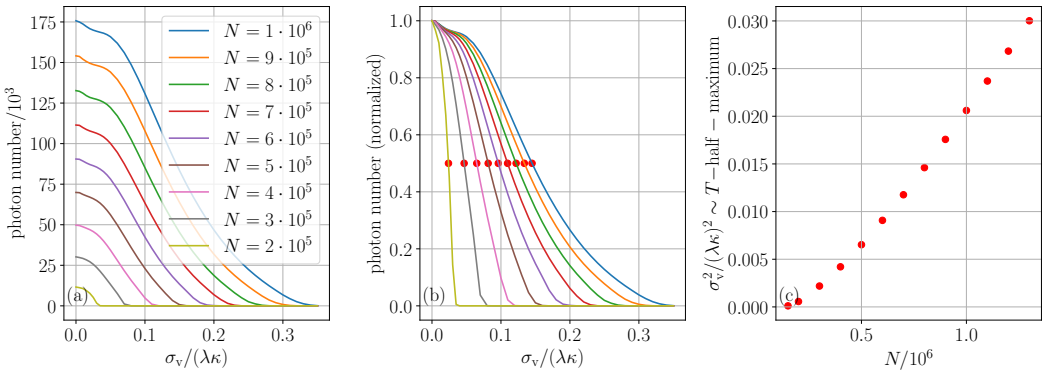

Figure 6.2: *Photon number dependence on temperature and atom number.* (a) steady state photon number (mean field, see Appendix for comparison to higher orders) as a function of the standard deviation of the velocity distribution σ_v for different atom numbers. (b) Photon number normalized to $\sigma_v = 0$ (maximum). The red dots indicate the value at which the curves have dropped to half of their initial value. After normalizing, the curves do not longer align, hinting to a nonlinear relation between atom and photon number. (c) Dependence of the threshold value of the velocity spread $\sigma_v^2 \sim T$ on the number of atoms. Larger atom numbers allow for larger possible values of σ_v, while maintaining a lot of photons inside the cavity. The parameters are $\nu = 0.5$, $\Delta = 0$, $g = 0.00136$ and $\kappa = 1$. We neglect γ since it is much smaller than ν, see Eq. (6.6).

off of the photon number for higher temperature can be explained by the Doppler effect, as higher velocities of the individual atoms lead to them being shifted out of resonance. Comparing each curve to the others, we can investigate the significant influence of the atom number on the photon number: Higher atom numbers yield higher photon numbers. While this is not surprising, the crucial aspect of this result becomes apparent, when we normalize the curves to their photon number value for zero temperature (Fig. 6.2(b)): The lacking coincidence of the curves hints to a nonlinear relation between atoms and photons. However, for low atom numbers we see the curves dropping to virtually 0 photons as early as for $\sigma_v/(\lambda\kappa) \approx 0.05$, whereas for higher atom numbers such a temperature has hardly any effect on the photon number. For example, for 10^6 atoms there are still approximately 95% of the photons at zero temperature in the cavity. The red dots indicate the points, at which the photon number has dropped to half their maximal value at zero temperature for each individual curve. These values are depicted in Fig. 6.2(c), they initially follow a quadratic relation, while for higher atom numbers the relation seems linear. From that graph we can clearly see, that using higher atom numbers allows a higher temperature while still having a decent

amount of photons inside the cavity. This could be beneficial to experimental setups, where it is generally difficult to cool the atoms down to low temperature. However, it remains to be seen what this means to the linewidth of the outcoming photons, as higher temperature usually leads to Doppler broadening of the linewidth.

6.4 Adding a velocity filter

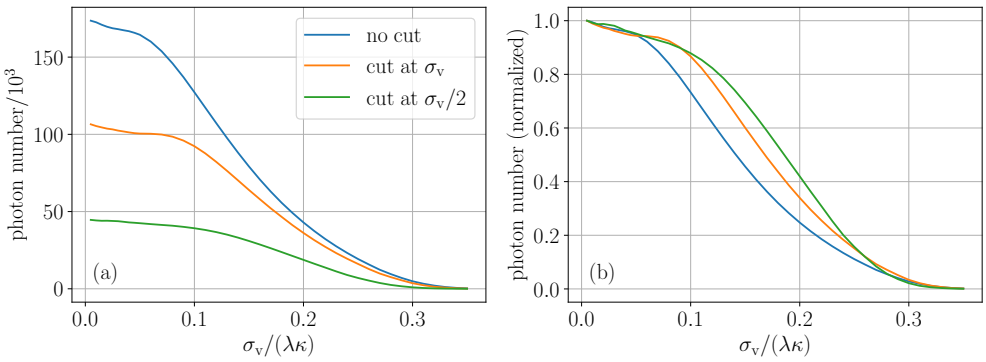

Figure 6.3: *Photon number for different velocity cutoffs.* (a) Mean steady state photon number. (b) Normalized to maximum photon number. Cutting off the the high velocity part of the distribution always yields a smaller steady state photon number, but it remains at a high level for increasing σ_v. We only depict the results in mean field, as the results in mixed order almost perfectly align. The parameters are the same as in Fig. 6.2.

An interesting idea is to consider a cutoff in the velocity distribution for the atoms. Experimentally, this may be achieved by using a velocity filter for the atomic beam to get rid of the atoms with very high velocity, creating a smaller but colder ensemble. This could be more advantageous than trying to narrow the velocity distribution by cooling, as cooling the atoms proposes an experimental challenge. To simulate such a filter, we start with the same number of atoms as before, but exclude all atoms from the dynamics with velocities higher than the cutoff. We depict the results in Fig. 6.3 for a cutoff at σ_v ($\approx 68\%$ slowest atoms) and at $\sigma_v/2$ ($\approx 38\%$ slowest atoms). To compare, we also depict the previous results without cutoff. In Fig. 6.3(a) the steady state photon number is shown for the different cutoffs. By cutting off the high velocity part of the atomic distribution, we lose only fast atoms, but it always leads to a decrease in photon number. A velocity filter therefore only reduces the photon number. It might still be useful with respect to the linewidth, which is not calculated at this

point.

However, the photon number seems to be more stable with increasing temperature, which can be seen in Fig. 6.3(b), where we normalize the graphs to their highest photon number (at zero temperature). While the photon number significantly drops already for low temperature (e.g. $\sigma_\mathrm{v} \approx 0.1$) for the uncut case, it stays relatively stable for the other cases, where we exclude the fast atoms.

In summary, including a velocity filter will negatively affect the photon number, but allow it to stay at a relatively stable value for low temperatures. However, it remains to be seen what effect such a velocity filter has on the linewidth of the atoms. In general, one would expect a velocity filter to be beneficial for the linewidth reduction, as the excluded, fast atoms increase the linewidth by means of the Doppler effect.

6.5 Dynamics including an optical lattice potential

So far, we assumed that the atoms move freely without any potential. After some time at non-zero temperature, the atoms will be randomly distributed over the mode function. To compare that situation to the zero-temperature case with non-moving atoms, we always place the atoms equidistantly distributed over the mode function. Therefore, the differences in photon number stem from the movement of the atoms itself, not from the somewhat artificial location of atoms on the mode function. The coupling between atoms and cavity field can be controlled (at least for low temperature) by including an optical lattice potential, as the atoms are trapped at the potential minimums. Aligning these potential minimums with the anti-nodes of the mode function leads to enhanced coupling compared to the random sampling of the mode function in the case where atoms move freely. The potential $V(x)$ has the form $V(x) = \Delta E \cdot \cos^2(\frac{4\pi}{\lambda_\mathrm{latt}} x)$ with spatial periodicity λ_latt and energy barrier ΔE. By using the Hamiltonian formalism one ends up with two linear differential equations of first order for each cluster. These additional equations can simply be added to the equations in the mean field (6.6) for simulation purposes. To keep the computation time low, we now simulated only $N_\mathrm{Cl} = 100$ clusters instead of 400 and only averaged over 10 trajectories instead of 50.
For the optimal case, we assume an optical potential with exactly half the wavelength of the mode function, that way the minima of the optical potential are situated at the maximum values of $|f(x_m)|$. The results of such a simulation are depicted in Fig. 6.4(a).

To compare to the previous results, we include the graph that we already calculated, which is the result for an energy barrier of $\Delta E = 0$. The energy is expressed in terms of the recoil energy $E_{\mathrm{rec}} = \frac{\hbar^2 k^2}{2m}$, where $k = 2\pi/\lambda$, v_{rec} is the associated recoil velocity and m is the mass of the atoms. To get exemplary values for these energy scales we use the ^{40}Ca intercombination line between $^1\mathrm{S}_0$ and $^3\mathrm{P}_1$ with $\lambda = 657\,\mathrm{nm}$ and $\Gamma = 2\pi \cdot 375\,\mathrm{Hz}$, the cavity linewidth is $\kappa = 2\pi \cdot 120\,\mathrm{kHz}$. To compare the two energy scales of the energy barrier and the velocity of the atoms, we color the data points according to the fraction of trapped atoms at each particular energy barrier and velocity. For high energy barriers and low velocities we have a lot of trapped atoms, these data points are colored blue, whereas for low energy barriers and high velocities almost no atoms are trapped, these points are colored yellow. As we can see from Fig. 6.4, the results change significantly by including a barrier. Let us first look at the case of low velocities/low temperatures: When the barrier is sufficiently high, then almost all the atoms are trapped at the antinodes of the mode function, leading to high coupling between atoms and cavities and eventually to higher photon number. For higher velocities/temperature, the number of photons stays significantly above the comparison graph for no energy barrier. On the one hand, this is because there are still atoms, that are trapped near the antinode of the mode function. On the other hand, there is a different effect at play, of which we can get a better insight when choosing the wavelength of the lattice slightly different from the wavelength of the mode function. Such a system may be of interest, as there usually is a mismatch between the effective optical lattice periodicity and the optical wavelength.
The results can be seen in Fig. 6.4(b), where we chose $\lambda_{\mathrm{latt}} = 0.99\,\lambda$. Note, how the results converge for very low temperature, regardless of the value of the energy barrier ΔE. This means, that the coupling is the same as in the barrierless case, where we distributed the atoms equidistantly over the mode function. So by choosing the wavelength of the optical lattice only slightly different to the wavelength of the mode function, we once again sample an average over the mode function, as long as the atoms sit on sufficiently many sites. Therefore the whole advantage of keeping atoms near the antinode of the mode function disappears and the coupling between the atoms and the cavity is the same compared to the coupling in the barrierless case. However, increasing the temperature, we still see a significant difference: Even though the average coupling is the same, the photon number is much higher. The atoms are decelerated, whenever they go over a potential barrier, yielding a reduced average velocity, which in turn decreases the Doppler effect and increases the photon number.

In summary, for low velocities/temperatures, the change in photon number depends

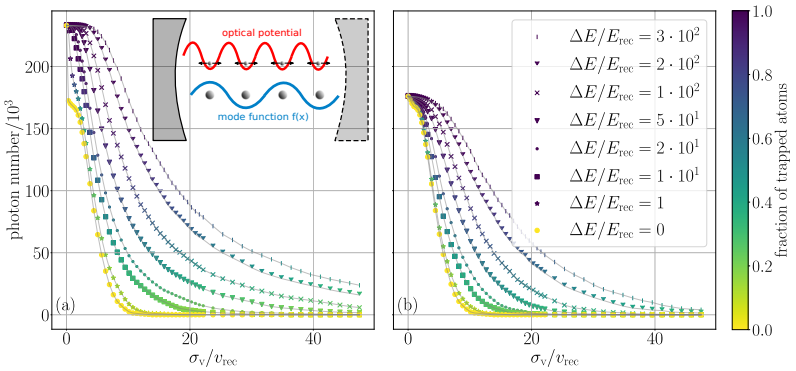

Figure 6.4: *Quasi-steady state photon number including a optical lattice potential with wavelength* $\lambda_{\text{latt}} = 0.5\,\lambda$ *(a) and* $\lambda_{\text{latt}} = 0.99\,\lambda$ *(b) with varying energy barriers.* The color of the data points indicates the fraction of trapped atoms, where at blue most of the atoms are trapped, while at yellow most of the atoms can escape their trap. (a) $\lambda_{\text{latt}} = 0.5\,\lambda$: Due to the choice of λ_{latt}, for low temperatures most of the atoms are trapped at the antinode of the mode-function, leading to a higher atom-cavity coupling and higher photon number. For higher temperatures, most of the atoms escape their trap, but the photon number stays significantly above the barrierless case. This is due to the energy barriers, which slow the atoms down, yielding lower Doppler effect and therefore higher photon number. (b) $\lambda_{\text{latt}} = 0.99\,\lambda$: For low temperatures the results coincide, regardless of the chosen energy barrier. This means, that the atom-cavity coupling is the same as in the barrierless case, where we distributed the atoms equidistantly over a mode function. For higher temperatures, most of the atoms escape their trap, but the photon number behaves similarly to the case with $\lambda_{\text{latt}} = 0.5\,\lambda$. Once again, the atoms get slowed by the barrier, eventually leading to significantly higher photon number compared to the barrierless case. The parameters are the same as in Fig. 6.2.

mostly on the change of coupling of the atoms, which again depends on the location of the minima of the optical potential compared to the antinodes of the mode function. For higher velocities/temperatures, the other effect of having a lower average velocity due to the barriers comes also into play. The lower average velocity leads to a decreased Doppler effect and therefore a significant increase of photon number.

6.6 Conclusions

We studied incoherently pumped two-level-atoms inside a single mode cavity. In particular, we investigated the influence of temperature on the photon number. For high temperatures, where the atoms are fast, the photon number is suppressed because of the Doppler effect. However, we saw that increasing the atom number, to get sufficient collective atom-cavity-coupling, can compensate this suppression. Including a velocity filter leads to a lower amount of atoms participating in the dynamics and therefore, as the number of atoms is a significant parameter, to a lower photon number. We plan to calculate the spectrum to see if excluding the fast atoms has a decreasing effect on the linewidth.

With an optical lattice potential the coupling between the atoms and the cavity field can be controlled. For low temperatures (compared to the energy barrier), most atoms are trapped and the atom-cavity coupling (and in consequence the photon number) can be engineered. However, for high temperatures, even though most of the atoms are not trapped, the photon number significantly increases compared to the situation without a potential. In some cases, where virtually no photons are generated anymore for a certain σ_v without the potential, we still have a macroscopic photon occupation number, even if σ_v is 4 times as high, by including the optical potential. Therefore including an optical potential becomes very beneficial for higher temperatures.

6.7 Appendix

6.7.1 Equations in higher orders

As mentioned in the main text, for our parameter regime the physics is accurately described by mean field. To verify this, we derive the equations for higher orders in the cumulant expansion and compare the numerical results with the mean field. For second order, one derives equations for two-operator averages. These will depend on other averages of two-operator and three-operator products. In order to close the set of differential equations one needs to derive equations for the two-operator averages and approximate the three-operator averages according to [37]

$$\langle abc\rangle \approx \langle ab\rangle\langle c\rangle + \langle ac\rangle\langle b\rangle + \langle cb\rangle\langle a\rangle - 2\langle a\rangle\langle b\rangle\langle c\rangle. \tag{6.7}$$

Using the phase invariance of the system [44,80] one ends up with the set of equations in second order of the cumulant expansion:

$$\langle \dot{a^\dagger a}\rangle = -\Big(\kappa - 2i\Delta\Big)\langle a^\dagger a\rangle + igK\sum_m f(x_m)(\langle a\sigma_m^{\mathrm{eg}}\rangle - \langle a^\dagger\sigma_m^{\mathrm{ge}}\rangle) \tag{6.8a}$$

$$\begin{aligned}\langle a^\dagger\dot{\sigma_m^{\mathrm{ge}}}\rangle =& -\Big(\frac{\gamma+\kappa+\nu}{2} - i\Delta\Big)\langle a\sigma_m^{\mathrm{eg}}\rangle + igf(x_m)(\langle\sigma_{\mathrm{m}}^{\mathrm{ee}}\rangle - \langle a^\dagger a\rangle) + ig\sum_{j=1}^{N} f(x_j)\langle\sigma_j^{\mathrm{eg}}\sigma_m^{\mathrm{ge}}\rangle \\ &+ 2igf(x_m)\langle a^\dagger a\rangle\langle\sigma_m^{\mathrm{ee}}\rangle\end{aligned} \tag{6.8b}$$

$$\langle\dot{\sigma_m^{\mathrm{ee}}}\rangle = igf(x_m)(\langle a^\dagger\sigma_m^{\mathrm{ge}}\rangle - \langle a\sigma_m^{\mathrm{eg}}\rangle) - (\gamma+\nu)\langle\sigma_m^{\mathrm{ee}}\rangle + \nu \tag{6.8c}$$

$$\begin{aligned}\langle\dot{\sigma_k^{\mathrm{ge}}\sigma_l^{\mathrm{eg}}}\rangle =& -(\nu+\gamma)\langle\sigma_k^{\mathrm{ge}}\sigma_l^{\mathrm{eg}}\rangle - igf(x_k)\langle a\sigma_l^{\mathrm{eg}}\rangle + igf(x_l)\langle a\sigma_k^{\mathrm{eg}}\rangle - \nu\langle\sigma_k^{\mathrm{ge}}\sigma_l^{\mathrm{eg}}\rangle \\ &+ 2igf(x_k)\langle\sigma_k^{\mathrm{ee}}\rangle\langle a\sigma_j^{\mathrm{eg}}\rangle - 2igf(x_l)\langle\sigma_j^{\mathrm{ee}}\rangle\langle a\sigma_k^{\mathrm{eg}}\rangle.\end{aligned} \tag{6.8d}$$

The advantage of this second order is, that we can include atom-field and atom-atom correlations, however, we pay the price in form of a higher computation time, as the number of equations now scales quadratically with the cluster number instead of linearly as above. The terms involving two atom operators $\langle\sigma_i\sigma_j\rangle$ are responsible for the quadratic scaling, as both i and j are between 1 and N. In an attempt to take the advantage of the upsides of both first order and second order, we approximate two-operator products if they both are atom operators by splitting them, but keep the correlations between atom and field, we call this particular truncation "mixed order":

$$\langle\dot{a}\rangle = -\Big(\frac{\kappa}{2} - i\Delta\Big)\langle a\rangle - K\cdot ig\sum_m f(x_m)\langle\sigma_m^{\mathrm{ge}}\rangle \tag{6.9a}$$

$$\langle\dot{a^\dagger a}\rangle = -\Big(\kappa - 2i\Delta\Big)\langle a^\dagger a\rangle + igK\sum_m f(x_m)(\langle a\sigma_m^{\mathrm{eg}}\rangle - \langle a^\dagger\sigma_m^{\mathrm{ge}}\rangle) \tag{6.9b}$$

$$\langle\dot{aa}\rangle = -\Big(\kappa - 2i\Delta\Big)\langle aa\rangle - 2igK\sum_m f(x_m)\langle a\sigma_m^{\mathrm{ge}}\rangle \tag{6.9c}$$

$$\begin{aligned}\langle a\dot{\sigma_m^{\mathrm{eg}}}\rangle =& -\Big(\frac{\gamma+\kappa+\nu}{2} - i\Delta\Big)\langle a\sigma_m^{\mathrm{eg}}\rangle + igf(x_m)\langle a^\dagger a\rangle - ig\sum_{j=1}^{N_{\mathrm{Cl}}}\sum_{i=1}^{K} f(x_j)\langle\sigma_m^{\mathrm{eg}}\sigma_{j,i}^{\mathrm{ge}}\rangle \\ &- 2igf(x_m)\langle a^\dagger a\sigma_m^{\mathrm{ee}}\rangle\end{aligned} \tag{6.9d}$$

$$\begin{aligned}\langle a\dot{\sigma_m^{\mathrm{ge}}}\rangle =& -\Big(\frac{\gamma+\kappa+\nu}{2} - i\Delta\Big)\langle a\sigma_m^{\mathrm{ge}}\rangle - igf(x_m)\langle aa\rangle - ig\sum_{j=1}^{N_{\mathrm{Cl}}}\sum_{i=1}^{K} f(x_j)\langle\sigma_m^{\mathrm{ge}}\sigma_{j,i}^{\mathrm{ge}}\rangle \\ &+ 2igf(x_m)\langle aa\sigma_m^{\mathrm{ee}}\rangle\end{aligned} \tag{6.9e}$$

$$\langle \dot{\sigma_m^{\mathrm{ee}}} \rangle = igf(x_m)(\langle a^\dagger \sigma_m^{\mathrm{ge}} \rangle - \langle a \sigma_m^{\mathrm{eg}} \rangle) - (\gamma + \nu)\langle \sigma_m^{\mathrm{ee}} \rangle + \nu \tag{6.9f}$$

$$\langle \dot{\sigma_m^{\mathrm{ge}}} \rangle = -\frac{\gamma + \nu}{2}\langle \sigma_m^{\mathrm{ge}} \rangle - igf(x_m)\langle a \rangle + 2igf(x_m)\langle a \sigma_m^{\mathrm{ee}} \rangle \tag{6.9g}$$

$$\begin{aligned}\langle \dot{a\sigma_m^{\mathrm{ee}}} \rangle = &-(\gamma + \nu)\langle a \sigma_m^{\mathrm{ee}} \rangle - \frac{\kappa}{2}\langle a \sigma_m^{\mathrm{ee}} \rangle + \nu \langle a \rangle - igf(x_m)\langle aa\sigma_m^{\mathrm{eg}} \rangle \\ &- ig \sum_{j=1}^{N_{\mathrm{Cl}}} \sum_{i=1}^{K} f(x_m)\langle \sigma_m^{\mathrm{ee}} \sigma_{j,i}^{\mathrm{ge}} \rangle + igf(x_j)\langle a^\dagger a \sigma_m^{\mathrm{ge}} \rangle.\end{aligned} \tag{6.9h}$$

For the sake of better readability we refrain from carrying out all the expansions of three-operator expectation values like $\langle aa\sigma_{\mathrm{m}}^{\mathrm{ee}} \rangle$. In order to end up with a closed set of equations, one needs to approximate the three-operator expectation values by two-operator expectation values according to Eq. (6.7). By neglecting the atom-atom correlations we get rid of the quadratic scaling, but we are still able to keep higher order correlations, namely the ones between atom and field.

Grouping the atoms into clusters is more involved in the second order and mixed order as opposed to first order, one has to carefully take into account for example the correlations within a cluster [56, 81].

6.7.2 Determining the steady state photon number

In order to study the photon number values depending on different parameters we initialize the set of differential equations with a certain parameter set and let the system evolve until it reaches its quasi-steady-state. The velocities are drawn from a Gaussian distribution with width σ_{v} corresponding to a temperature. We average over the photon number from the timepoint, at which the quasi-steady-state has been reached, see Fig. 6.5. Using more clusters leads to much smaller fluctuations, however, this also requires more computation time. Finding a compromise between high clusternumbers and reasonable computation time is discussed in the next section. Moreover, one can imagine that certain samples of the distribution exhibit special properties, in order to average them out we use 50 (unless indicated otherwise) different samples and also average over them.

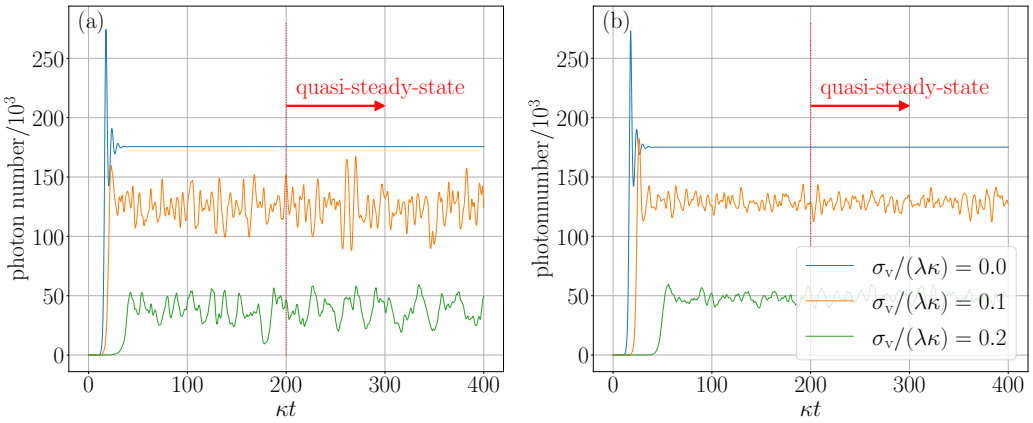

Figure 6.5: *Determining the steady state photon number.* Mean photon number time evolution for different σ_v with (a) 200 atom clusters and (b) 1000 atom clusters. After a certain time, the system reaches its quasi steady state. The fluctuations become smaller if we divide the velocity distribution into a larger number of atom clusters. The other parameters are the same as in Fig. 6.2 for $N = 10^6$.

6.7.3 Comparison expansion orders and number of clusters

Limited computation time forces us to make compromises, as both higher expansion orders and higher number of clusters describe the physical reality better, but also require more computation time.

In the following we compare the results for different expansion orders and number of cluster. In Fig. 6.6(a) the solid line depicts the first order, the dotted line mixed order and the dashed line represents the data in second order. We see that all three lines almost perfectly align. Therefore, using higher expansion orders does not lead to significant differences and the first order approximation captures the essential physics in our parameter regime.

In Fig. 6.6(b) we depict the results in first order for different clusternumbers ranging from $N_{\mathrm{Cl}} = 50$ to $N_{\mathrm{Cl}} = 1000$. Here we see, that varying the number of clusters N_{Cl} does have an influence on the results. We chose $N_{\mathrm{Cl}} = 400$, as the difference between choosing $N_{\mathrm{Cl}} = 400$ and as high as $N_{\mathrm{Cl}} = 1000$ is only marginal, while the computation time significantly increases.

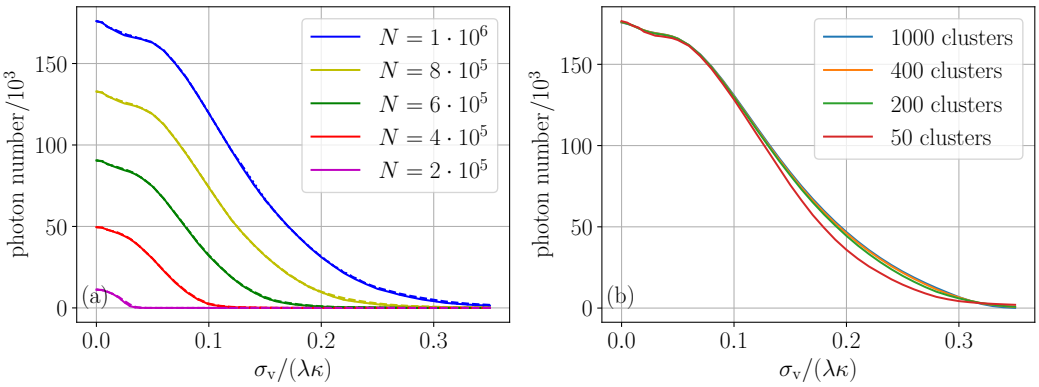

Figure 6.6: *Expansion orders and number of clusters.* (a) The solid line represents mean field, the dotted line is mixed order and the dashed line depicts the result in second order, we use $N_{\mathrm{Cl}} = 25$. The results for all orders agree very well. (b) The chosen number of clusters N_{Cl} makes a difference, especially for medium temperatures. However, increasing the number of clusters from $N_{\mathrm{Cl}} \approx 400$ has only a marginal effect on the results. The other parameters are the same as in Fig. 6.2 for $N = 10^6$.

Underlying data

Figshare: Superradiant_laser_Figures. `https://doi.org/10.6084/m9.figshare.c.6781920.v1` [82].
This project contains the following underlying data:

- Data used in Figures 2-6. All data are stored using DelimitedFiles.jl package in Julia.
- Data are stored together with the source code (see below), specific files to readout and plot the data are provided.

Data are available under the terms of the Creative Commons Zero "No rights reserved" data waiver (CC0 1.0 Public domain dedication).

Software availability

- Source code available from: https://github.com/martinf97/SRL_paper
- Archived source code at time of publication: https://doi.org/10.5281/zenodo.8232295 [83]

- License: Creative Commons Zero "No rights reserved" data waiver (CC0 1.0 Public domain dedication).

7 Publication

The author of this thesis carried out the theoretical analysis as well as most numerical calculations presented in this work. C. Hotter provided the idea, support in the development of code and the numerical results in the Appendix. L. Ostermann and H. Ritsch provided helpful discussions and support in the interpretation of the results. All authors contributed to the manuscript preparation.

Optica Quantum 2(6) pp. 397-403 (2024)

Subradiance and superradiant long-range excitation transport among quantum emitter ensembles in a waveguide

M. Fasser, L. Ostermann, H. Ritsch and C. Hotter

In contrast to free space, in waveguides the dispersive and dissipative dipole-dipole interactions among quantum emitters exhibit a periodic behavior over remarkably long distances. We propose a novel setup exploiting this long-range periodicity in order to create highly excited subradiant states and facilitate fast controlled collective energy transport amongst far-apart ensembles coupled to a waveguide. For sufficiently large ensembles collective superradiant emission into the fiber modes dominates over its free space counterpart. We show that for a large number of emitters a fast transverse coherent pulse can create almost perfect subradiant states with up to 50% excitation. On the other hand, for a coherent excitation of one sub-ensemble above an overall excitation fraction of 50% we find a nearly lossless and fast energy transfer to the ground state sub-ensemble. This transport can be enhanced or suppressed by controlling the positions of the ensembles relative to each other, while it can also be realized with a random position distribution. In the optimally enhanced case this fast transfer appears as superradiant emission with subsequent superabsorption, yet,

without a superradiant decay after the absorption. The highly excited subradiant states as well as the superradiant excitation transfer appear as suitable building blocks in applications like active atomic clocks, quantum batteries, quantum information protocols and quantum metrology procedures such as fiber-based Ramsey schemes.

7.1 Introduction

Spatial confinement of electromagnetic radiation field modes increases the atom-field coupling as well as the resulting dipole-dipole interaction between distant quantum emitters as the coupling is proportional to the field amplitude per photon generated by one emitter at the position of another. Extreme cases are optical resonators exhibiting quasi-uniform strong coupling over the entire mode volume [84] or single mode waveguides [85] such as optical fibers with weaker but close to infinite range interaction at their center.

As the atoms in a fiber are often distributed over large distances, their direct local interaction via free space is typically very small compared to the collective interaction mediated by the fiber [33]. Recent advances in fiber fabrication technology, laser cooling and manipulation of cold atomic ensembles allow for the implementation of such collective dynamics at unprecedented atom numbers [86–88]. While one typically first observes superradiant collective emission [2, 3] into the fiber [89–92], in this work we find that the opposite case of subradiance [36, 93–95] as well as superabsorption [11, 96, 97] can be implemented and reveals a plethora of novel physical phenomena and applications, especially in very large ensembles.

In addition to constituting a novel implementation of protected Ramsey spectroscopy [75, 98–100] we predict fast efficient long-distance collective energy transfer [101, 102] based on superradiance with subsequent superabsorption. This interplay between subradiant states with strongly reduced emission rates and the superradiant energy transfer can be exploited in quantum memories [6–10], quantum batteries [11–15, 103] and in order to remotely prepare perfectly inverted ensembles [104].

The manuscript has the following structure: after introducing our general model based on quantum emitter arrays with fiber-mediated effective dipole-dipole interactions we focus on the special case of two dilute ensembles. In order to treat a large number of emitters and high excitation manifolds we employ cumulant expansion equations up

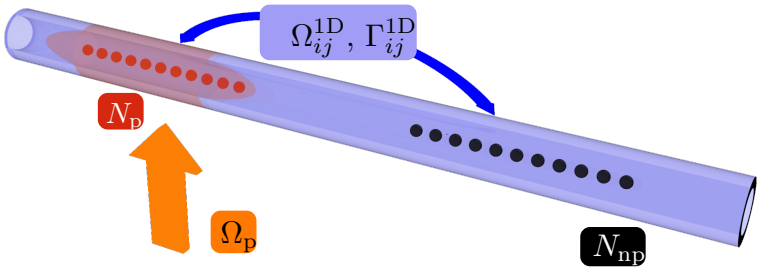

Figure 7.1: *Model.* Two ensembles of atoms coupled to a waveguide mode. Initially, only one ensemble with N_p atoms is pumped while the other with N_{np} atoms remains in the ground state. Below a certain pump threshold an almost perfectly subradiant state is created, while above this threshold a fast superradiant energy transfer from the pumped to the non-pumped ensemble takes place, where the energy is (super-)absorbed and remains in the second ensemble. Note that the two ensembles do not need to be spatially separated.

to second order to numerically study generic cases of the collective system dynamics, when only one of two ensembles is coherently pumped. We then analyze the transition from a subradiant collective decay blockade to a superradiant energy transfer between the two ensembles as a function of atom numbers, coupling conditions, and initial state.

7.2 Model

We consider N identical two-level emitters coupled to a single optical fiber mode, see fig. 7.1. The coupling rate of each emitter into the fiber is given by $\Gamma^{1D} = \Gamma \frac{k_0 \mu^2}{\epsilon_0 A} \chi$, which is determined by the free space decay rate Γ, the effective area A, the mode wavenumber k_0 and the normalization constant χ that accounts for the distribution of the electric field into the mode [33, 105]. The derivation of the collective couplings, dispersive and dissipative, is performed similarly to the calculations for 3D free space [32] but for only one propagation dimension and a refractive index larger than vacuum. The fiber is modeled as an infinitely extended cylinder. A detailed account of this can be found in the supplement of ref. [33] and references therein. In the rotating frame of the atomic transition frequency, the system is described by the Hamiltonian

$$H = \sum_{i \neq j}^{N} \Omega_{ij}^{1\mathrm{D}} \sigma_i^+ \sigma_j^- . \tag{7.1}$$

The waveguide-mediated dipole-dipole coupling rates are

$$\Omega_{ij}^{1\mathrm{D}}(x_{ij}) = \frac{\Gamma^{1\mathrm{D}}}{2} \sin\left(k_{\mathrm{eff}} x_{ij}\right), \tag{7.2}$$

where $x_{ij} = |x_i - x_j|$ is the distance between two emitters i and j, and k_{eff} denotes the effective wavenumber of the guided mode. The incoherent part describing the dissipative processes is accounted for by the Lindblad term

$$\mathcal{L}[\rho] = \frac{1}{2} \sum_{i,j}^{N} \Gamma_{ij}^{1\mathrm{D}} (2\sigma_i^- \rho \sigma_j^+ - \sigma_i^+ \sigma_j^- \rho - \rho \sigma_i^+ \sigma_j^-) \tag{7.3}$$

with the collective fiber-mediated decay rates

$$\Gamma_{ij}^{1\mathrm{D}}(x_{ij}) = \Gamma^{1\mathrm{D}} \cos\left(k_{\mathrm{eff}} x_{ij}\right). \tag{7.4}$$

We assume sufficiently large distances between the emitters such that we can neglect free space dipole-dipole interaction, which decreases as $1/x$ in the far field. Furthermore, we are only interested in time scales, where the individual free space spontaneous emission of the atoms is not relevant. This means our model holds for large dilute atomic clouds with sufficiently many atoms or high enough coupling efficiency to the waveguide. The open system can thus be described by the following master equation in the Born-Markov approximation [106]

$$\dot{\rho} = i[\rho, H] + \mathcal{L}[\rho]. \tag{7.5}$$

Since we aim at considering large systems with up to 10^6 emitters, where a full quantum simulation is by far out of reach, we will treat this problem in a second-order cumulant expansion [37, 80] which turns out to capture the dynamics remarkably well. A code example that automatically derives and numerically solves the corresponding equations is provided in Supplement 1.

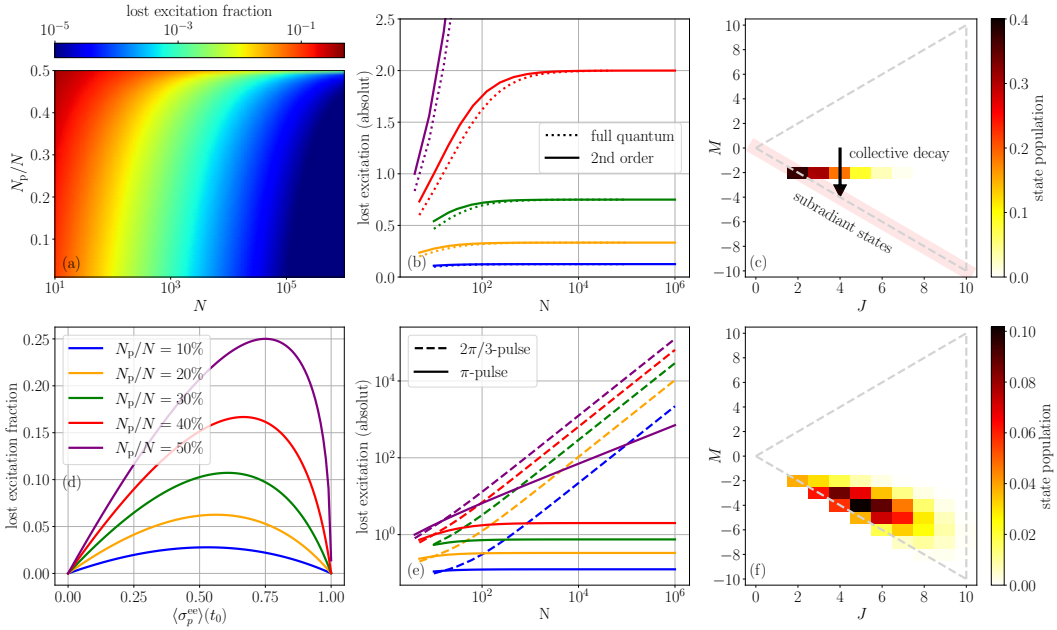

Figure 7.2: *Subradiant states.* (a) Percentage of lost excitation for a full excitation of the number of pumped atoms N_p. For large N the fraction of lost excitation approaches zero. (b) Absolute number of lost excitations for different fractions of pumped atoms N_p/N. Below the threshold, the number of lost excitations saturates to $N_\mathrm{p}/(N_\mathrm{np} - N_\mathrm{p})$. (d) Lost excitation fraction for coherent excitations to an initial excited state population of $\langle \sigma_\mathrm{p}^{ee} \rangle (t_0)$ for $N = 10^4$ atoms. Weaker coherent excitations can lead to more losses. (e) Lost excitation for an initial $2/3\pi$-pulse. It does not saturate for large N. (c) and (f) Population of the Dicke states for $N = 20$ atoms and an initial π-pulse and $2/3\pi$-pulse, respectively on $N_\mathrm{p} = 8$ atoms. In (c) the subradiant states (shaded red) and the collective decay (merely reducing M) are indicated.

7.3 Subradiant States

Subradiant states with respect to a single mode waveguide are of interest for various quantum technologies, in particular for controlled photon storage and release [10, 36]. However, deterministically and reliably creating such states is experimentally difficult. In ref. [36] the authors showed that quasi-localized dark states can be created by exciting a minority fraction of the emitters separated by multiples of half an effective wavelength $\lambda_\mathrm{eff}/2$. In this case, the coherent coupling between the emitters vanishes ($\Omega_{ij}^\mathrm{1D} = 0$), and the dynamics reduces to waveguide-mediated collective emission. The mere presence of the coupled emitters in the ground state inhibits the superradiant

decay of the excited fraction. So far only systems with a moderate number of emitters where a small fraction is fully excited have been considered. With a larger fraction of excited emitters the prepared states lose a certain amount of their excitation energy before the system becomes fully dark.

In the following, we analyze the corresponding dynamics in the limit of large numbers of emitters and investigate the scaling of the lost excitation fraction in the preparation process of these subradiant states via a sufficiently fast transverse coherent pumping. In the numerical simulation, we implement this by setting the corresponding initial state of the atoms. First, we assume a spacing of λ_{eff} between the emitters. The discrete translation symmetry of the model allows us to describe it with two collective spins only, a spin-$N_{\text{p}}/2$ for the pumped atoms and a spin-$N_{\text{np}}/2$ for the non-pumped atoms. In fig. 7.2a we show the percentage of lost excitation depending on the total number of emitters $N = N_{\text{p}} + N_{\text{np}}$ coupled to the waveguide and the fraction of fully excited atoms N_{p}/N. We observe that this percentage decreases with N. In particular, the suppression with growing N dominates over the increased losses for larger fractional excitations. This means, that the percentage of lost excitations can be made arbitrarily small for a sufficiently large number of emitters, up to the threshold for subradiance at $N_{\text{p}}/N = 50\%$.

The number of lost excitations and the subradiance threshold can be nicely understood by means of the Dicke states $|J, M\rangle$ [2], the eigenstates of the collective spin operators $J^z|J, M\rangle = M|J, M\rangle$ and $\mathbf{J}^2|J, M\rangle = J(J+1)|J, M\rangle$, with $0 \leq J \leq N/2$ and $|M| \leq J$. Figure 7.2c depicts the Dicke state representation for a full excitation of $N_{\text{p}} = 8$ atoms and $N = N_{\text{np}} + N_{\text{p}} = 20$. We obtain a distribution of Dicke states with a well-defined M quantum number corresponding to N_{p} excitations. Since the collective decay of a Dicke state appears as a reduction of M with J being unchanged ($J^-|J, M\rangle \rightarrow |J, M-1\rangle$), one finds that all states with $M = -J$ are fully subradiant. It is also clear that only subradiant states with $M \leq 0$ can exist, corresponding to $N_{\text{p}} \leq N/2$ [36, 75, 100, 107, 108]. The average lost excitations then correspond to the population of the state $|\psi\rangle$ times its excitation difference to the subradiant state with the same J quantum number to which it will decay, i.e. $\sum_{J,M} |\langle\psi|J, M\rangle|^2(M + J)$. In fig. 7.2b we show the total number of lost excitations for different fractions of pumped atoms N_{p}/N. We find that it converges to $N_{\text{p}}/(N_{\text{np}} - N_{\text{p}})$ for large N. The dotted lines correspond to calculations using the Dicke states, which perfectly agree with full quantum simulations (not shown). The solid lines are the results of the second-order cumulant expansions, which agree very well with the full quantum model, especially

for large N.

In fig. 7.2f we show the population of the Dicke states for an initial coherent excitation of $N_\mathrm{p} = 8$ atoms with a $2/3\pi$-pulse ($\langle\sigma_\mathrm{p}^{ee}\rangle(t_0) = 75\%$) and $N = 20$. Surprisingly, this state loses more excitations than with a π-pulse, although it is initially less excited. This is shown in Figure 7.2d and Figure 7.3c for different initial coherent excitations and the number of pumped emitters. Figure 7.2e depicts the lost excitation as a function of the atom number N for an initial $2/3\pi$-pulse. In this case, it does not saturate for large N. This means, for a spacing between the emitters in multiples of $d = \lambda_\mathrm{eff}$ this dark state preparation protocol works best when a fraction of the emitters are fully excited. For a coherent excitation, this requires an almost perfect π-pulse.

Another way of creating subradiant states is to use opposite phases such that the emitted radiation interferes destructively [75, 100, 109–111]. In a waveguide, this can be realized by a spacing of the atoms in multiples of $d = \lambda_\mathrm{eff}/2$. In fig. 7.3f we plot the percentage of lost excitation for this case. One can see that the lost excitation depends mainly on the initial excitation $\mathcal{E} = \langle\sigma_\mathrm{p}^{ee}\rangle(t_0) \cdot N_\mathrm{p}/N$. Below the threshold at $\mathcal{E} = 1/2$ the lost excitation fraction is very close to zero for a sufficiently large N, i.e. we can create subradiant states through an arbitrary coherent excitation almost without losing energy (for $\mathcal{E} < 1/2$).

7.4 Superradiance and Superabsorption

In the previous section, we have focused on the collective subradiant behavior of the emitters coupled to a waveguide. From the Dicke triangle representation, it is clear that such subradiant states can only exist for a total number of excitations below $N/2$ (corresponding to $M \leq 0$). In the following, we investigate the dynamics of total initial excitations above 50%. As before, we start by considering a spacing of multiples of λ_eff. In this case, we observe a fast excitation transfer from the initially fully excited to the non-excited ensemble facilitated by the collective decay via the shared bath, i.e. the waveguide [101, 102, 112]. In fig. 7.4a, we show a typical time evolution above the threshold ($\mathcal{E} > 1/2$, dashed lines), where we observe a superradiant decay of the initially excited ensemble and superabsorption in the initially non-excited ensemble. For comparison we have also plotted the behavior below the threshold ($\mathcal{E} < 1/2$, solid lines), where no energy transfer takes place.

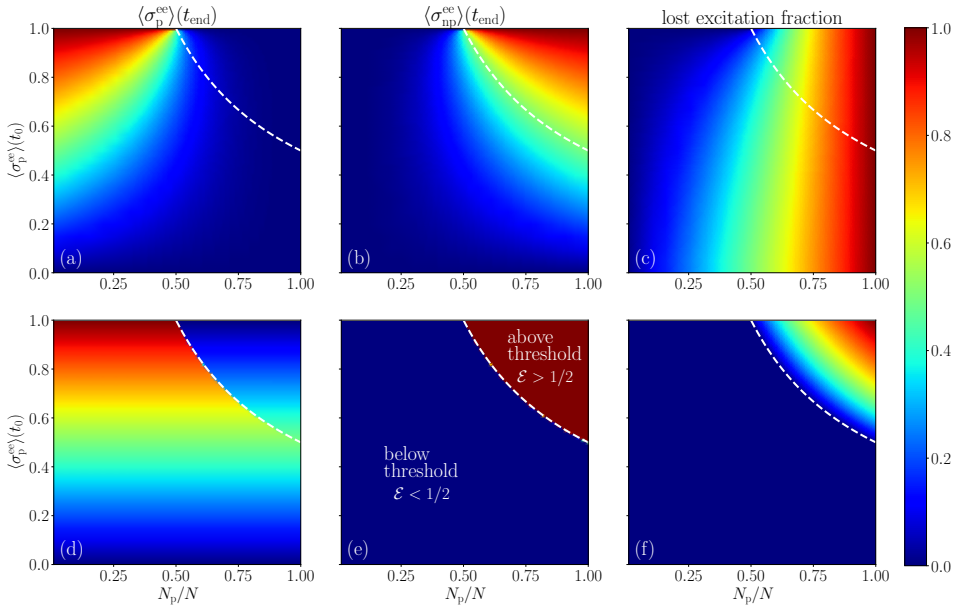

Figure 7.3: *Steady-State Population and Lost Excitation.* Scan over the fraction of pumped atoms N_p/N and the initial excited state population $\langle\sigma_p^{ee}\rangle(t_0)$ after a coherent excitation pulse. The upper panel depicts the case for an emitter spacing of $d = \lambda_{eff}$ ($\Gamma_{ij}^{1D} = \Gamma^{1D}$, symmetric decay rates) and the lower the one for $d = \lambda_{eff}/2$ ($\Gamma_{ij}^{1D} = \pm\Gamma^{1D}$, anti-symmetric decay rates). (a) and (d) show the steady-state population of the pumped atoms, (b) and (e) of the non-pumped atoms while (c) and (f) depict the fraction of lost excitations. The subradiant behavior and the energy transfer drastically improve for the anti-symmetric decay rates. For an initial full excitation, the behavior is the same for both cases. For the lower panel a threshold at $\mathcal{E} = 1/2$ (dashed white line) from subradiance to superradiance with subsequent superabsorption can be observed prominently. The chosen atom number in these scans is $N = 10^6$.

Superabsorption can be interpreted as the inverse process to superradiance [11, 96, 97]. Hence, the excitation is usually immediately reemitted after the rapid collective absorption, which makes it difficult to observe the phenomenon. In the two-ensemble case described above, however, the emitters are in a subradiant state after the absorption, which means it is not followed by superradiant emission. This should make it experimentally much more accessible and useful. Let us mention that in the effective waveguide description the term superabsorption refers to the fast absorption of virtual photons.

Similar to the subradiance described in the previous section we find that the superradi-

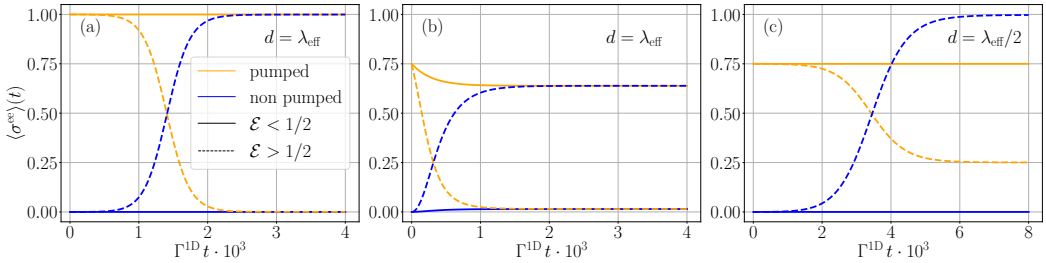

Figure 7.4: *Time Evolution.* (a) Subradiant behavior (solid lines) and superradiant energy transfer (dashed lines) for initially fully inverted pumped atoms. (b) Coherent excitation to 75% ($2/3\pi$-pulse) for symmetric decay rates ($d = \lambda_{\text{eff}}$), where subradiance and energy transfer are less optimal. (c) Anti-symmetric decay rates ($d = \lambda_{\text{eff}}/2$), featuring subradiance and the optimal energy transfer for arbitrary coherent excitations. The chosen atom number is $N = 10^4$, for $\mathcal{E} < 1/2$ ($\mathcal{E} > 1/2$) we use $N_{\text{p}} = 2 \cdot 10^3$ ($N_{\text{p}} = 8 \cdot 10^3$).

ance with subsequent superabsorption in the case of a spacing of multiples of λ_{eff} works well only if one ensemble is initially fully excited. Figure 7.4b shows the dynamics for a coherent excitation of the pumped ensemble to $\langle \sigma_{\text{p}}^{\text{ee}} \rangle (t_0) = 75\%$ ($2/3\pi$-pulse), where we notice that the energy transfer is not fully exciting the non-pumped ensemble above threshold ($\mathcal{E} > 1/2$, dashed lines). This can also be seen in the Scan 7.3b.

Again, in order to optimize this process such that it works well for arbitrary coherent excitations, we can use an emitter spacing of multiples of $\lambda_{\text{eff}}/2$. The resulting opposite phases in the collective decay lead to a sharp threshold at an initial excitation fraction of $\mathcal{E} = 1/2$. Below the threshold the system is subradiant and above we observe optimal superradiance from the pumped ensemble with subsequent superabsorption from the non-pumped ensemble. This is demonstrated in the time evolution in fig. 7.4c and scans in fig. 7.3d-f, the dashed line represents the threshold at 50% total excitation.

Comparing the results for λ_{eff} and $\lambda_{\text{eff}}/2$ spacing in fig. 7.3a-c and fig. 7.3d-f, respectively, we observe a profound difference in the threshold behavior for not completely inverted coherently excited ensembles.

In order to characterize the superradiant energy transfer fig. 7.5a depicts the atom number dependence of the time T_{sa} it takes the non-pumped ensemble to reach 95% of the final state excitation, i.e. $\langle \sigma_{\text{np}}^{ee} \rangle = 0.95 \cdot \langle \sigma_{\text{np}}^{ee} \rangle (t_{\text{end}})$. We find a scaling close to $T_{\text{sa}} \sim N^{-1}$ as for superradiant decay [2, 70, 72, 91]. For an initial excitation sufficiently above the threshold this scaling holds for any coherent excitation. Close to the

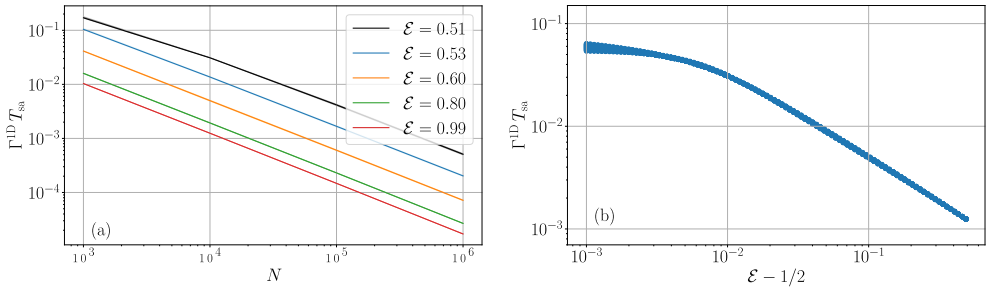

Figure 7.5: *Superabsorption Time Scale.* (a) Atom number scaling of the energy transfer time T_{sa} as approximately N^{-1} (b) Transfer time T_{sa} for different coherent excitations with the same initial excitation fraction $\mathcal{E} = \langle \sigma_{\mathrm{p}}^{ee} \rangle (t_0) N_{\mathrm{p}}/N$. Far above the threshold T_{sa} depends on $\mathcal{E}$ only. Close to the threshold, a full excitation of fewer emitters leads to a faster transfer than a smaller coherent excitation of more emitters. The number of atoms in (b) is $N = 10^4$.

threshold different coherent excitations with the same initial excitation fraction $\mathcal{E}$ can lead to a slightly different transfer duration T_{sa}. This can be seen in fig. 7.5b, where we plot $T_{\mathrm{sa}}(\mathcal{E})$ for different coherent excitations. In the vicinity of the threshold, the transfer is faster for a full excitation of fewer emitters (data points with smaller T_{sa}) than a smaller coherent excitation of more emitters with the same $\mathcal{E}$.

7.5 Uniform Distribution: Coherent Dipole-Dipole Interaction Effects

So far we have considered the special cases in which the emitters are located precisely at multiples of $\lambda_{\mathrm{eff}}/2$, where the coherent dipole-dipole interaction vanishes, i.e. $\Omega_{ij} = 0$ for all i and j. For a moderate number of emitters that can be positioned e.g. with optical tweezers or in the case of microwave waveguides this is experimentally feasible. However, for large atomic clouds that couple to an optical waveguide, all positions along the waveguide with respect to the periodic coupling are equally likely. In order to investigate the influence of the resulting coherent dipole-dipole interaction we sample the different positions. In particular, we use four equidistant positions with a spacing of $d = \lambda_{\mathrm{eff}}/4$ for the pumped and non-pumped ensemble. A comparison with six equidistant positions is shown in fig. 7.7a, b, d and e in Supplement 1, which underpins that four ensembles are sufficient for a qualitative description of the coherent

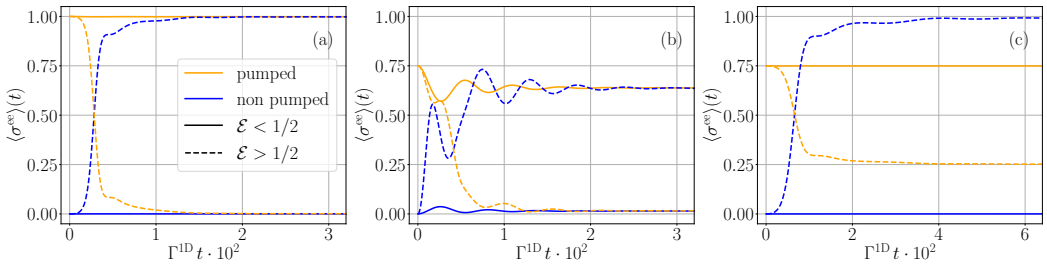

Figure 7.6: *Time Evolution including Coherent Dipole-Dipole Interaction.* Population of the pumped and non-pumped emitters. For an initial full excitation of the pumped ensemble (a), the dynamics are only slightly modified by the coherent interaction. In contrast the behavior for a coherent excitation to 75% changes significantly due to the coherent interaction (b). (c) shows that the optimal behavior can be recovered with a vanishing excitation phase in the pumped ensemble for coherent excitations. The atom numbers are the same as in Figure 7.4.

dipole-dipole interaction effects.

In fig. 7.6 we show the dynamics for $N = 10^4$ emitters for different cases. For a fully excited pumped ensemble (Figure 7.6a) the behavior below as well as above threshold is only weakly modified by the coherent dipole-dipole interaction. The slower overall dynamic mainly stems from the reduced incoherent rates. This has been tested by simulating the dynamics with incoherent rates Γ_{ij} corresponding to a spacing $d = \lambda_{\text{eff}}/4$ while neglecting the coherent interaction ($\Omega_{ij} = 0$), see fig. 7.7c and f in Supplement 1. In contrast, for an arbitrary coherent excitation, the subradiant and superabsorption features are strongly affected by the coherent dipole-dipole interaction. The dynamics for an initial coherent $2/3\pi$-pulse is shown in fig. 7.6b. We see that the behavior is not optimal, similar to the one with a spacing of $d = \lambda_{\text{eff}}$ (Figure 7.4). The coherent interaction seems to cancel the positive effect from the opposite phases of the collective decay rates.

The crucial difference in the above two cases is the initial coherence in the later one. This means an initial incoherent excitation to $\langle \sigma_{\text{p}}^{ee} \rangle (t_0) = 75\%$ should lead to the same optimal subradiant and superradiant transfer behavior. One way to approximately resemble an incoherent excitation is to excite ensembles with vanishing phases. In fig. 7.6c we show the dynamics for this case, where the pumped ensemble is divided into two sub-ensembles which are excited with opposite phases. This leads to an almost optimal behavior below and above the threshold. Note that for a large ensemble of

emitters an overall vanishing excitation phase is usually automatically given due to the position distribution. Additional imperfections such as differences in the atomic transition frequencies are discussed in Supplement 1. These results suggest that the phenomenon should be observable with two separated dilute clouds of atoms coupled to a waveguide.

7.6 Conclusions

We have shown a transition from sub- to superradiance with subsequent superabsorption for two ensembles of emitters coupled to a waveguide. The lost excitation for the subradiant states saturates for a large number of emitters. This allows for creating highly excited subradiant states with up to 50% excitations. Above the threshold, an efficient superradiant energy transfer between the two ensembles takes place [101, 102, 104, 112]. We were able to show that this process also works with a non-fully inverting coherent excitation of the pumped atoms by utilizing a vanishing phase. In addition, we demonstrated that the influence of the coherent waveguide-mediated dipole-dipole interaction can also be strongly suppressed with such a vanishing phase, which is usually automatically given for large atomic ensembles. This insight is crucial for experimental implementations with large dilute ensembles. The necessary operating conditions are within reach of current experimental setups [90, 113–115].

The efficiency of the process can be increased by optimizing the emitter positions, this can e.g. be realized with optical tweezers [116] or self-organization [117, 118]. The described mechanisms should also be valid for multi-mode waveguides as the fundamental mechanisms pertain while the interference of several modes leads to a mere modification in the periodicity of the couplings. In future work, it could be interesting to investigate potential retardation effects for widely separated ensembles, as well as the possibility of engineering the dissipation by detuning ensembles. We also want to mention that ensembles of emitters in a single-mode bad cavity, where the cavity field can be adiabatically eliminated, feature a similar collective dissipation with opposite phases. Yet, for a vanishing atom-cavity detuning the resulting effective equations for the atoms do not experience coherent dipole-dipole interaction terms [106, 108, 119]. This can be beneficial for the above-described phenomena. Of particular interest are ring cavities with a uniform coupling strength for all atoms [58].

Acknowledgments

The numerical simulations were performed with the open-source frameworks QuantumCumulants.jl [80] and QuantumOptics.jl [120]. M. F. and H. R. acknowledge funding from the Austrian Science Fund (FWF) Grant DOI 10.55776/W1259. M. F., L. O. and H. R. acknowledge the FET OPEN Network Cryst3 funded by the European Union (EU) via Horizon 2020.

Disclosures

The authors declare no conflict of interest.

Data availability

Data underlying the results presented in this paper are available in Ref [121].

7.7 Supplemental document

7.7.1 Simulation Code

The Julia code to derive and numerically solve the second-order cumulant equations can be found in the online documentation of the toolbox QuantumCumulants.jl [80]: `https://qojulia.github.io/QuantumCumulants.jl/stable/examples/waveguide/`. By setting $M_\mathrm{p} = 4$ and $M_\mathrm{np} = 4$ in the example one creates the 324 equations to reproduce the results in Figure 7.6a and b in the main text.

To verify the validity of the second-order cumulant expansion we perform a fourth-order simulation for the parameters in fig 7.4a, which shows almost no difference in the time evolution. With the above-mentioned program this can be done by setting $M_\mathrm{p} = 1$ and $M_\mathrm{np} = 1$, changing the order to order $= 4$, completing the system of equations with complete!(eqs) and setting the initial state of the pumped atoms to $\psi_\mathrm{np} = spindown(bs1)$. This will result in 209 equations, the derivation and the numerical simulation can take a few minutes.

7.7.2 Six vs. Four Subensembles

In fig. 7.7 we compare the time evolution including coherent dipole-dipole interaction for four and six different positions at $x_4 = \{0, 1, 2, 3\} \cdot \lambda_{\text{eff}}/4$ and $x_6 = \{0, 1, 2, 3, 4, 5\} \cdot \lambda_{\text{eff}}/6$, respectively. For the full excitation in fig. 7.7a and b the difference is barely visible. For an initial coherent excitation to 75% the oscillations are stronger, see Figure 7.7d and e. However, we expect the oscillations to damp out very quickly for more positions. Unfortunately, we cannot test this in the second-order cumulant expansion approach, since the number of coupled differential equations for the 2×6 spins is already 702. In fig. 7.7c we show the dynamics for each of the four ensembles. In fig. 7.7f we set the coherent dipole-dipole interaction to zero, and see that this only slightly changes the dynamics.

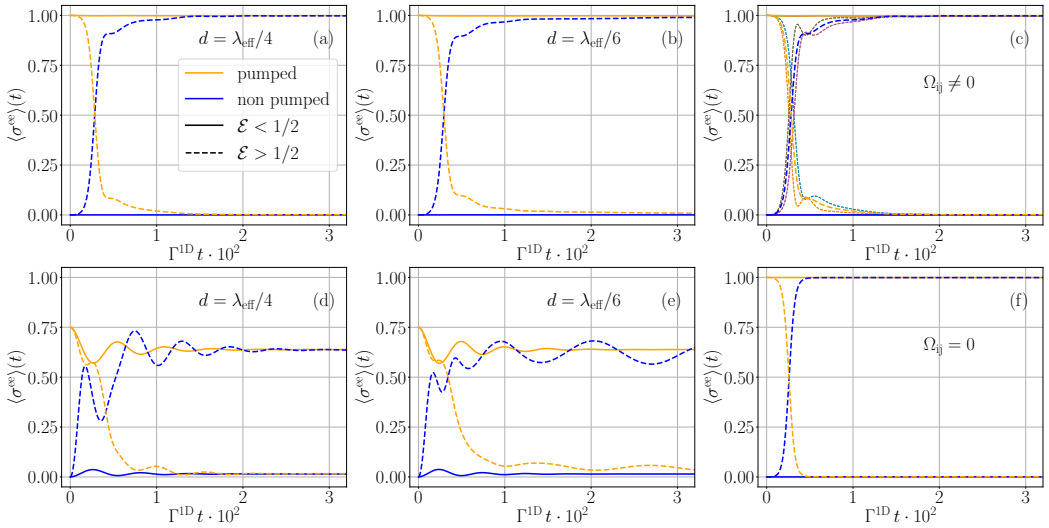

Figure 7.7: *Coherent Dipole-Dipole Interaction Effects.* (a) and (d) Time evolution above and below the threshold for an initial π-pulse and $2/3\pi$-pulse excitation, respectively. These plots are the same as in Figure 7.6a and b in the main text for four positions with a spacing of $d = \lambda_{\text{eff}}/4$. (b) and (e) Comparison to six sub-ensembles with a spacing of $d = \lambda_{\text{eff}}/6$. The time evolution in (a) and (b) is almost identical, for (d) and (e) they agree qualitatively. In (c) we plot all trajectories of the different ensembles for the case presented in (a). In (f) we artificially set the coherent dipole-dipole interaction to zero. This reveals that the slower dynamic for the four positions can be traced back to the reduced collective decay rate.

7.7.3 Experimental imperfections

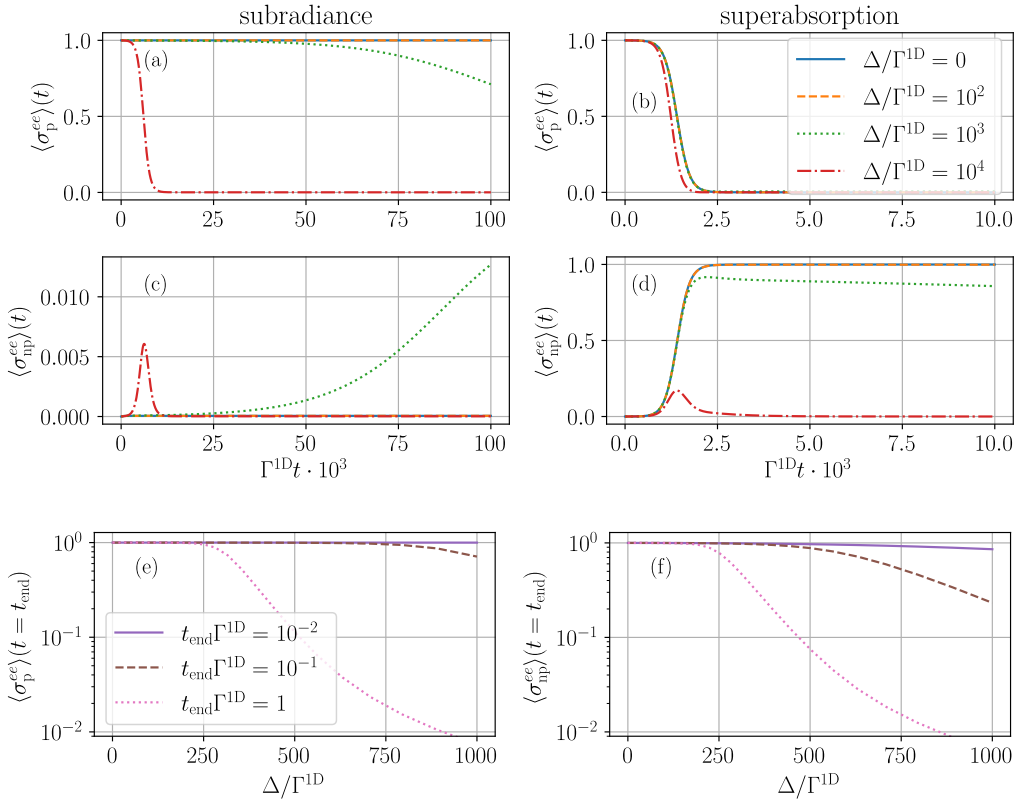

Figure 7.8: *Detuning Effects.* (a) - (d) Subradiance (left) and superabsorption (right) time evolution of the excited state population of the pumped and non-pumped atoms for different detunings. (e) and (f) Detuning dependence of the final excited state population of the pumped (subradiance) and non-pumped (superabsorption) atoms for different times t_{end}. The parameters are the same as in fig. 7.4a of the main text. The legend in (b) applies to (a)-(d) and the legend in (e) also applies to (f).

A typical experimental imperfection is an inhomogeneous atomic transition frequency, which can e.g. be caused by motion or electric and magnetic field gradients. For our setup, we can investigate the effect of such frequency differences in the (simple) extreme case, when the pumped and non-pumped atoms have a detuning Δ. We include this in our model with an additional Hamiltonian term

$$H_\Delta = \Delta \sum_{i=1}^{N_{np}} \sigma_i^{ee}. \tag{7.6}$$

Here, the sum involves all atoms in the non-pumped ensemble. Note, however, that we could also introduce a detuning of the pumped atoms. In fig. 7.8 we show the influence of such a detuning on the subradiance (left) and superradiant energy transfer (right). The excited state population time evolutions in Fig. 7.8a-d show that the subradiance (a, c) and superabsorption (b, d) are very robust to such frequency differences Δ for long time scales. Fig. 7.8e and fig. 7.8f verify this, where we plot the final excited state population of the pumped $\langle\sigma_{\mathrm{p}}^{ee}\rangle$ and non-pumped $\langle\sigma_{\mathrm{np}}^{ee}\rangle$ atoms for different times t_{end} in the subradiance and superabsorption case, respectively. We can see that large detunings, here $\Delta/\Gamma^{1\mathrm{D}} > 200$, only become relevant at long time scales ($t_{\mathrm{end}}\Gamma^{1\mathrm{D}} = 1$). Individual atomic decay into free space reduces the excited state population independently. This means we need to consider processes that happen in a time frame much shorter than the natural excited state lifetime of the atoms. The same applies to individual dephasing.

8 Publication

The author of this thesis carried out the numerical calculations presented in this work. C. Genes and H. Ritsch provided the idea, and supported, together with R. Holzinger, the interpretation of the results. All authors contributed to the manuscript preparation.

Photonics 12(10), 996 (2025)

Benchmarking the Cumulant Expansion Method Using Dicke Superradiance

M. Fasser, C. Genes, H. Ritsch and R. Holzinger

Collective superradiant decay of a tightly packed inverted quantum emitter ensemble is among the most intensely studied phenomena in quantum optics. Since the seminal work of Dicke more than half a century ago, a plethora of theoretical calculations in quantum many-body physics have followed. Widespread experimental efforts range from the microwave to the X-ray regime. Nevertheless, accurate calculations of the time dynamics of the superradiant emission pulse still remain a challenging task requiring approximate methods for large ensembles. Here, we benchmark the cumulant expansion method for describing collective superradiant decay against a newly found exact solution. The application of two variants of the cumulant expansion exhibits reliable convergence of time and magnitude of the maximum emission power with increasing truncation order. The long-term population evolution is only correctly captured for low emitter numbers, where an individual spin-based cumulant expansion proves more reliable than the collective spin-based variant. Surprisingly, odd orders show unphysical behavior [122]. At sufficiently high spin numbers, both chosen cumulant methods agree, but still fail to reliably converge to the numerically exact result. Generally, on longer time scales the expansions substantially overestimate

the remaining population. While numerically fast and efficient, cumulant expansion methods need to be treated with sufficient caution when used for long-time evolution or reliably finding steady states.

8.1 Introduction

Quantum many-body problems rarely allow for full analytical solutions and are typically also prohibitively difficult to solve numerically. A plethora of expansion methods has thus been developed to study them approximately. In particular, when convergence to their classical counterparts is expected in the large-number limit, the first quantum corrections to appear are of central interest. Beyond a 1st order expansion [123], the quantum cumulant expansion is one of the most widely used methods for studying the influence of quantum correlations in many-body physics [38]. It has proven very successful in studies of photon statistics and quantum correlations in various light sources, beginning with the first successful model description of a laser and even non-classical light sources such as few-photon emitters [124]. Despite its success in solving concrete practical problems, hardly any detailed studies of its convergence when applying higher-order expansions exist [125, 126]. Mostly, second-order calculations, which include pair correlations, have proven sufficient. Systematic numerical studies in this direction are often hampered by a lack of analytically solvable, nonlinear, and nontrivial many-body dynamics models, in which convergence could be studied thoroughly and quantitatively.

Luckily, many decades after the prediction of superradiance [2, 3, 127] and clear experimental evidence [128], a tractable analytical solution for the seminal problem of free space Dicke superradiance has been recently put forward [129, 130]. This new analytic form of the solution beyond the single spin quantum Rabi model [131] allows to obtain highly accurate solutions for very large atom numbers, way beyond any direct numerical solution of the master equation. As high-order correlations build up during the time evolution of superradiant decay, this gives an ideal reference frame for a systematic test of the cumulant expansion for high quantum emitter numbers.

Recent experiments in free-space atomic arrays and waveguided platforms have heightened the interest in collective light–matter effects relevant to (driven) superradiance. In this context, cumulant (cluster) expansions provide a microscopically based yet tractable framework for modeling higher-order correlations. Recent experimental

works [92, 132–136] employed cumulant-based expansions to theoretically model driven superradiant dynamics. This experimental progress further motivates our work of benchmarking cumulant truncations against the exact master equation numerics. Here we can use the established quantum cumulant approach [80] to generate high-order expansions and study the convergence of key quantities, such as the peak emitted power or the time of maximum emission, as well as higher-order photon correlations. While no quantum entanglement builds up in pure superradiant decay [137], a closely related recent study exhibited the buildup of dipole correlations, particularly in the early phase of superradiance [138]. This shows the need for higher-order corrections beyond a field expansion, which misses all correlations. The early time phase correlation buildup starting from a random first emission event typically leads to a significant variance of the time when the intensity maximum occurs, if one unravels the evolution in single wavefunction trajectories [139]. Alternative approaches to modeling collective light–matter dynamics include phase-space techniques such as the truncated Wigner approximation [140], stochastic wavefunction/quantum-trajectory (MCWF) simulations [141], exact diagonalization for small ensembles, and tensor-network/MPS methods [142] that are most effective in (quasi) 1D or weakly entangled regimes. Cumulant (cluster) expansions occupy a complementary niche: they retain operator correlations up to a chosen order, exploit permutation symmetry when present, and scale favorably with system size, yielding analytic insight and computationally efficient predictions for early-time, low-order observables.

Interestingly, while most of the individual stochastic trajectories exhibit highly nonclassical, entangled intermediate states [143], this property is completely washed out by ensemble averaging. Efforts to reproduce the vanishing trajectory-averaged entanglement using a stochastic unraveling thus prove numerically very intensive. The buildup of spin correlations, however, appears automatically when evaluating the second-order cumulant as introduced below. A comparison of the exact result with the predictions of a truncated cumulant expansion can then reveal the importance of even higher-order correlations.

This work is organized as follows: After introducing the Dicke model and the resulting master equation in both the individual and collective bases, we define and present the two corresponding forms of the cumulant expansion in the two operator basis sets. As the first test, we study the convergence of a cumulant expansion of the collective Spin operators to the exact results for increasing expansion order. For smaller numbers of atoms, we then study the convergence properties of an individual spin-based expansion,

which becomes exact once the expansion order reaches the number of spins. We then compare the two expansion methods for larger ensembles, followed by a more detailed analysis of how the error scales with the number of atoms and the expansion order for both methods.

8.2 Theoretical description

8.2.1 Quantum Master equation

The Dicke superradiance problem involves finding the density operator ρ which satisfies the following master equation in Lindblad form (in an interaction picture where the trivial action of the free Hamiltonian is removed):

$$\begin{aligned}\frac{d}{dt}\rho(t) &= \Gamma \sum_{n,m=1}^{N} \Big[\sigma_n \rho \sigma_m^\dagger - \frac{1}{2}\big(\sigma_n^\dagger \sigma_m \rho - \rho \sigma_n^\dagger \sigma_m\big)\Big] \\ &= \Gamma\Big[S\rho S^\dagger - \frac{1}{2}\big(S^\dagger S\rho - \rho S^\dagger S\big)\Big],\end{aligned} \tag{8.1}$$

where $\sigma_n = |e_n\rangle\langle g_n|$ is the jump operator for emitter n and $S = \sum_n \sigma_n$ is the symmetric jump operator in the Dicke basis [2]. Note that besides the number of emitters N, we are left with only one parameter Γ, the spontaneous decay rate of a single two-level emitter, which simply sets the time scale.

We will calculate the averaged total emitted power and excited state population, given by (setting $\hbar = 1$)

$$P_{\text{out}} = \Gamma \sum_{n,m=1}^{N} \langle \sigma_n^\dagger \sigma_m \rangle = \Gamma \langle S^\dagger S \rangle, \quad n_{\text{ex}} = \sum_{n=1}^{N} \langle \sigma_n^{ee} \rangle, \tag{8.2}$$

as a figure of merit using both the full master equation in the symmetric Dicke subspace and using the cumulant expansion method, explained below. The total excited state population n_{ex} in Eq. 8.2 tracks how much population resides in the excited state during the dissipative time evolution.

8.2.2 Equations of motion for expectation values of operators

Let us further define a general operator $\mathcal{O}$ with expectation value $\langle\mathcal{O}\rangle(t) = \mathrm{Tr}\{\mathcal{O}\rho(t)\}$. Then, its dynamics are given by

$$\frac{d}{dt}\langle\mathcal{O}\rangle = \Gamma \sum_{n,m=1}^{N} \big\langle \sigma_n^\dagger \mathcal{O}\sigma_m - \frac{1}{2}\{\sigma_n^\dagger\sigma_m, \mathcal{O}\}\big\rangle. \tag{8.3}$$

Throughout this work we assume, that the system is initialized in the uncorrelated product state $|\psi_0\rangle = \prod_{n=1}^{N} |e_n\rangle$ and using Eq. 8.3 we start noticing that $\langle\sigma_n\rangle = 0$, $\langle\sigma_n\sigma_m^{ee}\rangle = 0$, $\langle\sigma_n^\dagger\sigma_m^\dagger\sigma_k\rangle = 0$ (for $n \neq m \neq k$) and so forth, namely terms $\sigma_a^\dagger\sigma_b$ have to appear simultaneously. We are interested in the time evolution of the system operators, which leads to a coupled set of equations with increasing order in the operator correlations, namely

$$\{\langle\sigma_n^{ee}\rangle, \langle\sigma_n^\dagger\sigma_m\rangle, \langle\sigma_n^{ee}\sigma_m^{ee}\rangle, \langle\sigma_n^\dagger\sigma_m\sigma_k^{ee}\rangle, \langle\sigma_n^{ee}\sigma_m^{ee}\sigma_k^{ee}\rangle, ...\}, \tag{8.4}$$

where $n \neq m \neq k$. The computational complexity of the coupled set of equations scales polynomially with correlation order r as $\sim \mathcal{O}(N^r)$. In order to obtain a closed set of equations and render the system numerically tractable, the correlations have to be truncated, which can be done systematically using the cumulant expansion method [37], explained in the next section.

8.3 Cumulant Expansion Method

In order to stop the hierarchy of equations above from expanding and close the system of equations, we need to apply a systematic cumulant expansion on the operator averages. The cumulant (cluster) expansion rewrites moments of spin operators in terms of operator correlators ("cumulants"), which quantify correlations beyond products of lower-order moments. Truncating at order k (i.e., setting all cumulants of order $> k$ to zero) closes the equations of motion for cumulants up to that order: k=1 is 1st order (mean field); k=2 retains pair correlations and already captures the collective build-up underlying the superradiant pulse; higher k include three- and four-body effects but may become numerically challenging and, if pushed too far, can yield unphysical behavior [122]. The approximation is most reliable when correlations remain moderate or approximately Gaussian (early times, large N, near-symmetric

states), while accuracy degrades for long-time/steady-state properties and high-order observables. We employ both individual-operator and collective-spin formulations: the former resolves site-to-site structure, the latter exploits permutation symmetry in the Dicke limit. In the following sections we compare each truncation directly to the exact dynamics based on the master equation and quantify errors.

In order to obtain a closed set of equations, only correlations up to a certain order are considered, while all higher-order correlations are expanded in terms of lower orders. This approximation can be computed in a systematic fashion, using the cumulant expansion. The joint cumulant of an Mth-order correlation $\langle\hat{\mathcal{O}}_1...\hat{\mathcal{O}}_M\rangle$ can be expressed as an alternate sum of products of their expectation values and is compactly written as [37]

$$\kappa(\hat{\mathcal{O}}_1,...,\hat{\mathcal{O}}_M)=\sum_P(|P|-1)!(-1)^{|P|-1}\prod_{B\in P}\Big\langle\prod_{i\in B}\hat{\mathcal{O}}_i\Big\rangle \tag{8.5}$$

where P runs through the list of all partitions of $\{1,...,M\}$, B runs through the list of all blocks of the partition P and $|P|$ is the number of parts in the partition. An approximation can be made by setting $\kappa(\hat{\mathcal{O}}_1,...,\hat{\mathcal{O}}_M)=0$, which allows to express $\langle\hat{\mathcal{O}}_1...\hat{\mathcal{O}}_M\rangle$ with correlations of order $M-1$ and lower. For instance, the expansion of expectation values involving three operators reads

$$\begin{aligned}\langle\hat{\mathcal{O}}_1\hat{\mathcal{O}}_2\hat{\mathcal{O}}_3\rangle\approx{}&\langle\hat{\mathcal{O}}_1\rangle\langle\hat{\mathcal{O}}_2\hat{\mathcal{O}}_3\rangle+\langle\hat{\mathcal{O}}_2\rangle\langle\hat{\mathcal{O}}_1\hat{\mathcal{O}}_3\rangle\\&+\langle\hat{\mathcal{O}}_3\rangle\langle\hat{\mathcal{O}}_1\hat{\mathcal{O}}_2\rangle-2\langle\hat{\mathcal{O}}_1\rangle\langle\hat{\mathcal{O}}_2\rangle\langle\hat{\mathcal{O}}_3\rangle.\end{aligned} \tag{8.6}$$

This introduces some error, as all higher-order correlations are neglected. In the following sections, we will quantitatively analyze this error based on the truncation order and number of emitters.

8.4 Benchmarking cumulant expansion convergence

Let us now proceed to test the accuracy and convergence of the cumulant expansion approximation with the exact master equation using superradiant decay as a benchmark. We note, that the primary goal is to test the convergence of higher order cumulant orders with exact numerics in the context of strongly correlated systems, and not provide accurate predictions of Dicke superradiance. In this section we test this for increasing cumulant expansion orders, i.e., setting the Mth-order cumulant to zero for increasing M.

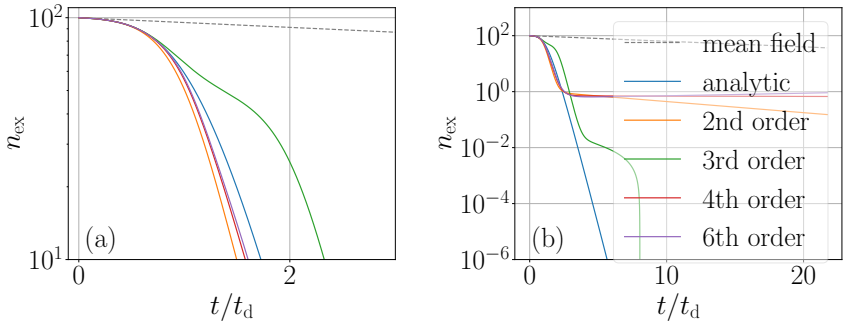

Figure 8.1: *Comparison of numerically exact prediction of the time evolution of the upper state population (blue line) to the approximate results using increasing cumulant expansion orders for N=100 spins.* In (a) we show a zoom-in of (b) at shorter time scales. While for short times up to the point of maximum emission, predictions agree quite accurately and converge with order, the long-term evolution strongly differs from the exact result with the 3rd-order (green) exhibiting a very large, even qualitatively wrong, deviation from the quantum evolution based on exact numerics (blue). The uppermost (dashed) line depicts the first-order solution, which completely misses superradiance. Here mean field refers to a 1st order cumulant expansion.

Before going into details, however, let's note that in the chosen Dicke limit [3] of all atoms well within a cubic wavelength and neglecting dipolar energy shifts, there is actually only a single interesting physical parameter, namely the total atom number N entering the exact dynamics. The other free parameter Γ is the single-atom decay rate (proportional to the square of the dipole moment), which only fixes the overall time scale. It does not change the results in any other way. Of course, for any finite extent or nonspherical shape of the cloud as well as for any imperfect excitation of the ensemble, many more details of the geometry will enter [144]. While these corrections will somewhat change the actual numbers, we will ignore them here for the sake of clarity of the arguments.

8.4.1 Time evolution

Let us start with a comparison of the predicted time evolution of the full ensemble and use key quantities as the total remaining excited state population as well as the momentarily emitted power in Eq. 8.2 for benchmarking the cumulant expansion versus the full density matrix evolution. In a first step, we choose only two representative

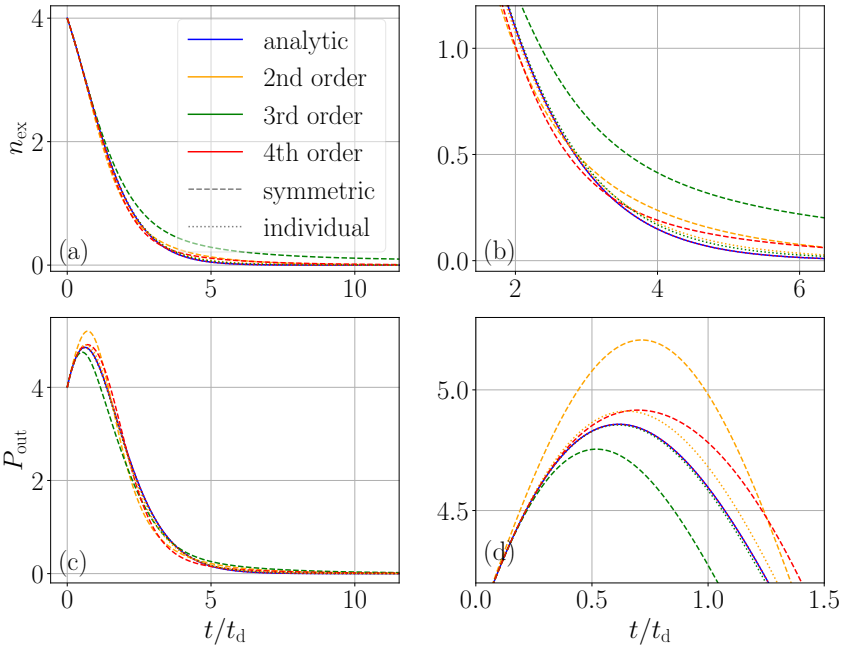

Figure 8.2: *Population decay and emission power for a small number of $N = 4$ atoms.* Numerically exact solution (blue) compared to approximations using different cumulant expansion orders based on a collective spin basis (dashed lines) and an individual spin basis (dotted lines). Here (b) is a zoom-in of (a) while (d) is a zoom-in of (c) at short times. Surprisingly, odd orders show even qualitative deviation from the exact result. As expected for an order equivalent to the spin number ($N = 4$), the individual cumulant expansion correctly reproduces the exact numerical solution. The collective spin-based cumulant expansion shows no convergence in this case.

system sizes from small ($N = 4$) to large ($N = 100$). In a further step below, we will then compare characteristic quantities as the time and magnitude of the maximal emitted power, as key average properties to characterize the reliability of the approximations over many orders of magnitude of atom numbers. In Fig. 8.1 we depict the population decay of an average-sized ensemble of $N = 100$ emitters in units of the analytically predicted time of maximal emission power, t_d. On the left, we show the evolution till the time where 90% of the atoms have decayed, comparing different expansion orders. Note, that $t_d = \ln N/(N\Gamma)$ is the delayed time, when the superradiant peak emission approximatiely occurs [3] and plot the time evolution in units of t_d. We only find a quantitatively good agreement for times before maximum

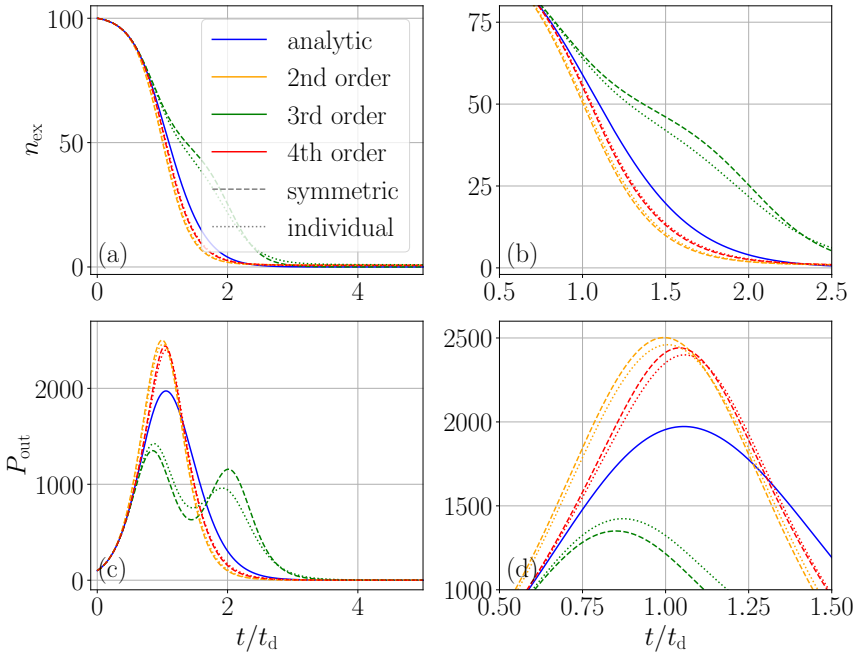

Figure 8.3: *Population evolution (upper plots) and emission rate (lower plots) for $N = 100$ atoms calculated using exact numerics (solid blue) and different expansion orders (yellow:2, green:3, red:4).* On the right side in (b) and (d), we depict a zoomed portions around the time of maximal emission. Odd orders soon even qualitatively deviate from the exact results. The difference between a collective spin-based expansion (dashed lines) and an individual spin-based cumulant expansion (dotted lines) here for a larger $N = 100$ is significantly smaller as compared to the few spins $N = 4$ case above.

emission. Strong deviation from the exact results appears in particular for odd orders at later times. Let us add here that the 1st expansion fails from the beginning, as it simply reproduces individual (exponential) decay with no buildup of collective dynamics. This is shown in the straight uppermost dashed line. We see that in this time range, even orders slowly converge to the exact result, already diverging by about 10% for the prediction of the time when only 10% of the initial population is left in the ensemble.

For longer times, where the remaining population has decayed to less than one percent, the cumulant expansion simply fails to correctly reproduce the decay process. Somewhat surprisingly, no convergence towards the exact dynamics appears even for higher-order calculations. The predicted decay curves from the truncated expansion

generally exhibit a rather nonphysical long-lived population fraction.

It is well known that the cumulant expansion approximation of interacting spins becomes exact when the order reaches the number of spins [37]. Hence, in the next step, we look at the small number of only 4 spins to study the cumulant convergence as shown in Fig 8.2. Indeed, the 4th-order represented by exactly the same set of coupled equations used above for the case of $N = 100$ now behaves indistinguishably from the exact result based on solving the full master equation. Again, as above, the 3rd-order expansion exhibits a worse agreement than the 2nd-order. Interestingly, the individual spin-based expansion here converges very well and way better than the symmetric collective approach.

As we will see below in more detail, the convergence difference between individual and collective spin cumulants strongly reduces with sample size, but while the two methods converge to each other, they still significantly deviate from the exact numerical result. In Fig. 8.3 we highlight this for the case of $N = 100$ emitters. While the two approaches only differ on a few percent level at a later time, there are even qualitative deviations from the exact dynamics. In particular, we see a clearly nonphysical double peak structure in the emission power depicted on the lower left for the 3rd-order cumulant expansion. On the lower left (zoomed plot), we see a better agreement of the various approaches at least until the time of maximum emission. It remains a bit unclear to us where this curious behavior originates, but it seems to be related to the crossing of the equator in the Bloch sphere, where dynamics change from synchronization to dephasing of the individual spins. Geometrically on the Bloch sphere, inhomogeneous frequency shifts (e.g., disorder- or dipole-interaction-induced) generate azimuthal phase diffusion of individual spins; the collective transverse magnetization $\langle S^{\dagger} \rangle$ then dephases as the enclosed phase area grows, diminishing the macroscopic dipole that drives superradiance. This “phase–area” picture is standard in cooperative emission and explains how dephasing suppresses cooperativity [3, 32]. This might lead to erroneous three-spin correlations, which need non-trivial four-spin correlations as correction factors. Overall, it is a strong reminder that the cumulant expansion beyond second order needs to be taken with great care.

8.4.2 Peak emission time and power

After highlighting some key properties of the time evolution, we now come to a more systematic quantitative analysis of the system size scaling. For this, we choose two

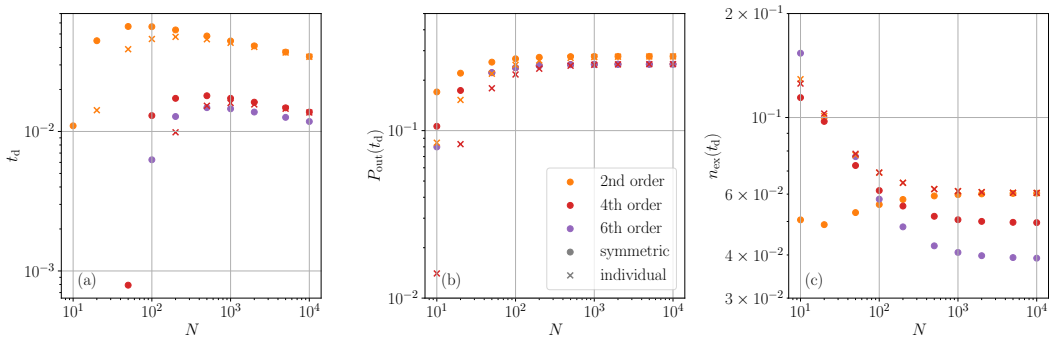

Figure 8.4: *Relative error of increasing cumulant expansion orders compared to the full quantum time evolution (based on exact numerics using the master equation) for the characteristic quantities of superradiance as the time t_d of maximal emission (left), the maximal emission power (middle), and the average atomic population at the power maximum (right).* One generally finds deviations at the percent level with some improvement with expansion order from 2nd-order (orange), via fourth order (red) to 6th-order (purple). The individual operator-based expansions (crosses) are more reliable than the collective operator cumulants (dots), in particular at small system sizes.

central observables in the dynamics, namely time and power of the maximum emission peak. This allows us to compare the quantitative accuracy of various orders of our two cumulant approaches (individual or collective spin basis) as a function of system size N. In Fig. 8.4 on the left, we plot the relative deviation of the predicted time of maximum emission from the exact value. It appears promising that already the second order cumulant expansion yields results accurate to better than 5%, which somewhat slowly improves with emitter number. The 4th-order is more accurate and converges towards a 1% error for large ensembles. Again, the individual operator-based expansions behave consistently superior, particularly for smaller N.

The prediction for maximal power shown in the middle is somewhat less accurate and converges only to the few percent level for large N. Surprisingly, higher-order corrections do not substantially improve the prediction.

Looking at the remaining upper state population at maximum emission time plotted in the right panel of Fig. 8.4, we find a similar percent level accuracy. However, in this case, we find significant improvement for larger ensembles, and a higher-order expansion significantly improves the prediction. As already seen in the time evolution plots in Figs. 8.1-8.3, the third order turns out to be very unreliable even at this rather

short evolution time. Again, a second-order expansion using individual operators turns out to be a fairly good and reliable approximation over all system sizes.

In summary, we see that the quality and usefulness of the cumulant expansions strongly depend on the targeted observable and deteriorate for longer time scales. In general, going beyond the second order is hardly worth the effort, as some minor improvements come with a much more complex set of equations to solve. On the other hand, several important quantities, such as intensity correlations or spectra, require higher-order observables anyway. The rather poor long-time behaviors also hint that steady state calculations can be rather problematic, even if one finds a numerical solution of the nonlinear coupled set of equations.

8.5 Conclusions

It is well known that for the perfectly inverted initial state, i.e., all emitters in the excited state, in the Dicke model, a 1st cumulant expansion completely fails, as no coherence dipole-dipole correlations are accounted for [33]. Here, we have demonstrated that a second-order cumulant expansion produces a fairly reliable approximation to the full superradiant decay, in particular, for higher atom numbers and up to intermediate timescales. Surprisingly, higher-order expansions generally only lead to minor improvements even in the best case. Actually, the third-expansion often exhibits physically incorrect oscillatory solutions on intermediate timescales [122]. Interestingly, two possible variants of the cumulant expansion, based either on individual atomic spin operators or, alternatively, on the collective spin basis, lead to different predictions beyond 1st order cumulant expansion. For not too large numbers, the first case of using a many-particle cumulant expansion leads to significantly higher accuracy and even converges to the exact result when the order approaches the particle number. Fortunately, the differences between the two basis models vanish in the large N limit. Future work will involve systematic benchmarks of equal-time spin–spin quantum correlations of higher orders and in particular two-time/intensity correlations $g^{(2)}(0)$, important to characterize the correlated emission process [145]. In summary, we find that a cumulant expansion to second order can capture a large part of the deviation from classical to quantum dynamics, while the usefulness of higher-order expansions is rather limited. In particular, due to the much larger number of equations to be solved, the extra effort barely pays off. Of course, fourth-order expansions are still required to obtain higher-order correlation functions such as the $g^2(0)$-function for

intensity correlations. These results, however, should be interpreted with caution.

Acknowledgments

We thank Klemens Hammerer for helpful comments and suggestions. Numerical calculations were performed based on the QuantumCumulants.jl [80] package. We acknowledge support from the (FWF) doctoral college DK-ALM W1259-N2 and the COE1 QuantA. CG acknowledges financial support from the Max Planck Society and the Deutsche Forschungsgemeinschaft (DFG, German Research Foundation) – Project-ID 429529648 – TRR 306 QuCoLiMa.

9 Publication

A. Bychek carried out the numerical calculations presented in this work. H. Ritsch, I. Vyborni, S. Yelin and K. Hammerer provided the idea and supervision. The author of this thesis was mainly responsible for the analytic calculations and results presented in the chapter about emission spectrum for two emitters. All authors contributed to the manuscript preparation.

arXiv:2607.06556 (2026)

Continuous Narrow-Linewidth Superradiance in Waveguide-QED

A. Bychek, M. Fasser, I. Vybornyi, K. Hammerer, S. Yelin, H. Ritsch, R. Holzinger

Superradiant lasers promise continuous, narrow-linewidth coherent emission at the bare atomic transition frequency, enabling frequency references of exceptional precision. Recent experiments have advanced the field, but achieving truly continuous operation remains technically challenging. Here we propose an alternative route to an active optical frequency reference with fewer emitters using all-to-all dipole-dipole interactions mediated by a nanophotonic waveguide. We show that selectively pumping only a sub-ensemble of emitters, rather than the full ensemble, substantially improves emission characteristics. The collective interactions with unpumped emitters provide narrowband frequency selection and establish an effective feedback mechanism analogous to the role of a macroscopic cavity. We find directional superradiant emission with strongly phase-synchronized emitter correlations and a narrow output spectrum close to the bare emitter resonance. Our results demonstrate a strong metrological gain from selective partial pumping of quantum emitters with the second-order intensity correlation $g^{(2)}(0) \simeq 1$, indicating reduced equal-time intensity fluctuations, and

open a route to waveguide-based optical frequency references using small clock-atom ensembles for chip-scale precision metrology.

9.1 Introduction

Optical atomic clocks achieve exceptional precision by referencing light to long-lived atomic transitions allowing unprecedented accuracy and stability in measuring time and frequency [146, 147]. Recently, there has been a growing number of theoretical and experimental studies focused on the development of an *active* optical frequency reference, in which the atoms themselves continuously generate a narrow-linewidth optical signal whose frequency remains tied to the bare atomic transition [20, 22, 44–46, 48, 57, 71, 77, 148–151]. Such a source should combine high photon flux, long temporal coherence, and minimal frequency shifts from the clock transition. Collective radiative effects provide a natural mechanism for enhancing useful optical signals. Since Dicke's original work on superradiant spontaneous emission [2, 3], it has been understood that ensembles of quantum emitters can radiate cooperatively through collective dipole–dipole exchange, producing emission rates and field correlations inaccessible to independent atoms. This makes superradiance a powerful resource for generating macroscopic coherence and collective light emission in driven-dissipative many-body systems [133, 152–155]. For metrological applications, however, the central challenge is not simply to produce a transient superradiant burst, but to harness superradiance as a *continuous narrow-linewidth resource*, where pumping, dissipation, and collective synchronization are balanced in a nonequilibrium steady state without destroying atomic coherence.

A particularly compelling approach to this idea is a *superradiant laser*, where an ensemble of incoherently pumped atomic emitters radiates into a lossy cavity mode in the bad-cavity regime [20, 22, 44, 46, 48, 50, 52, 56, 57, 65, 71, 77, 148–151, 156, 157]. In this regime, optical coherence is stored predominantly in the atoms rather than in the cavity field, reducing the sensitivity of the emitted light to cavity-frequency fluctuations. Theory predicts steady-state superradiant emission with enhanced intensity compared to independent emitters and a spectral linewidth that can be below the natural single-emitter linewidth [44, 57]. These features make superradiant lasers promising candidates for active optical clocks and ultra-stable frequency references. At the same time, recent experimental advances have shown that their development still faces major technical challenges on the route to truly continuous operation, which

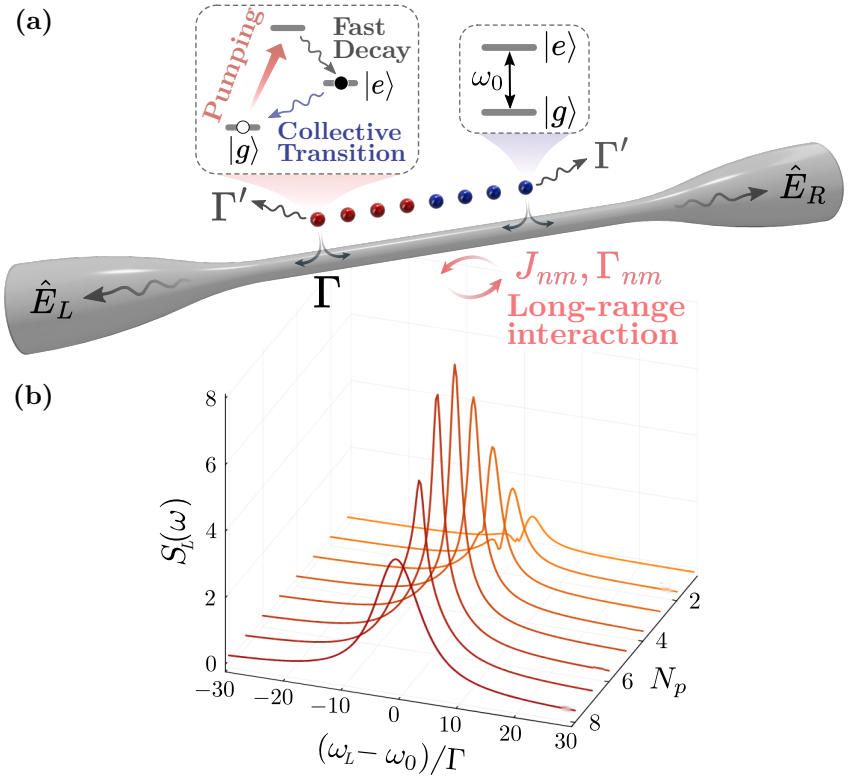

Figure 9.1: *Continuous narrow-linewidth collective emission.* **(a)** An ensemble of quantum emitters coupled to a single-mode waveguide reservoir. The emitters feature excited ($|e\rangle$) and ground ($|g\rangle$) states with coupling rates Γ to the resonant bidirectional waveguide mode and local loss with rates Γ' (both assumed to be identical for all emitters). A subset (in red) is incoherently pumped with rate R, with the rest (in blue) providing collective feedback, resulting in collective emission into left- and right-propagating electric fields. **(b)** Emission spectrum from $N = 8$ emitters into the left direction, presented for different numbers of pumped emitters N_p at rate $R = 5\Gamma$. The spectra show maximal spectral narrowing and peak height for pumped fractions near one-half of the emitters. Simulations are performed with the full solution of the master equation.

requires sufficiently large ensembles to be confined, pumped, and replenished while maintaining favorable collective coupling to the optical resonator. Current efforts focus on optical atomic conveyors or beams of excited atoms passing through an optical resonator [149, 156], as well as optimized multilevel pumping schemes using multiple repumping lasers [22, 65].

This raises a central question for precision metrology: can steady-state superradiant

emission be realized in a more compact, cavity-free architecture, with fewer emitters and without relying on a conventional optical resonator? This is directly relevant for frequency metrology and the development of transportable, chip-scale active atomic clocks [44, 57, 158]. Waveguide QED provides a particularly attractive platform in this context [159]. When ensembles of quantum emitters couple to a tightly confined one-dimensional guided mode, photons emitted by one emitter can be reabsorbed and reemitted by the others, generating position-dependent coherent emitter–emitter interactions and collective dissipation [159–162]. The relative phases of these interactions can be engineered through the emitter positions along the waveguide, enabling collective radiative states ranging from enhanced *superradiant* to strongly suppressed *subradiant* [105, 159], while simultaneously collecting the emitted light into directional guided modes [163].

In this work, we show that a small, partially pumped ensemble of identical quantum emitters coupled to a bidirectional 1D waveguide realizes a superradiant, narrow-linewidth light source with a single spectral line close to the emitter resonance frequency, as shown in Fig. 9.1(b). A key ingredient is *partial incoherent pumping* of the emitter ensemble [164, 165]. Throughout this work, we use *partial pumping* to denote spatially selective incoherent pumping: only a subset of emitters along the waveguide is optically pumped, while the remaining emitters are left unpumped. The pumped fraction provides broadband gain, which is amplified and spectrally filtered by the unpumped emitters. Thus, waveguide-mediated interactions are not only a mechanism for enhanced radiation, but a resource for producing metrologically useful continuous superradiance.

We analyze the steady-state emission properties using the quantum master equation for small system sizes, whereas for larger ensembles we employ a second-order cumulant expansion to capture both the buildup of collective correlations and superradiance as well as the emission spectrum [162]. Photon statistics in the emitted light provide complementary information about equal-time intensity fluctuations, quantified by the zero-delay second-order correlation function $g^{(2)}(0)$ [132]. This allows us to identify optimal emitter configurations, pump strengths, and pumped fractions that maximize the radiated power and minimize linewidth, and to assess their robustness against static positional disorder and inhomogeneous frequency broadening.

9.2 Theoretical description

We consider N *identical* two-level quantum emitters at positions $\{x_n\}$, with resonance frequency ω_0, coupled to a single-mode, bidirectional waveguide reservoir with rate Γ, and subject to decay into free space outside the resonant waveguide mode with rate Γ', as illustrated schematically in Fig. 9.1(a). A subset $\mathcal{P} \subset \{1, \ldots, N\}$ consisting of $N_p = |\mathcal{P}|$ emitters is incoherently pumped with rate R, while the remaining emitters are unpumped. After tracing out the electromagnetic field and applying the Born–Markov and rotating-wave approximations, the dynamics of the reduced emitter density matrix $\hat{\rho}$ are governed by the Lindblad master equation [159, 160, 166, 167]:

$$\dot{\hat{\rho}} = -\frac{i}{\hbar}\big[\hat{H}, \hat{\rho}\big] + \mathcal{L}_\Gamma\big[\hat{\rho}\big] + \mathcal{L}_\mathrm{R}\big[\hat{\rho}\big] + \mathcal{L}_\mathrm{fs}\big[\hat{\rho}\big], \tag{9.1}$$

with coherent exchange described by the Hamiltonian,

$$\hat{H}/\hbar = \sum_{n,m=1}^{N} J_{nm}\, \hat{\sigma}_n^\dagger \hat{\sigma}_m = \sum_{n>m} \frac{J_{nm}}{2}\big(\hat{\sigma}_n^x \hat{\sigma}_m^x + \hat{\sigma}_n^y \hat{\sigma}_m^y\big), \tag{9.2}$$

in a frame rotating at frequency ω_0 and with the coherent exchange rate $J_{nm} = \frac{\Gamma}{2}\sin(k|x_n - x_m|)$. Here, $\hat{\sigma}_n = |g\rangle_n\langle e|_n$ denotes the Pauli lowering operator of emitter n, and using $\hat{\sigma}_n = \frac{1}{2}(\hat{\sigma}_n^x - i\hat{\sigma}_n^y)$, the coherent part forms an XY spin model without on-site interaction due to $J_{nn} = 0$.

Collective dissipation into the waveguide, incoherent pumping and free-space decay are described by the Lindbladian superoperators:

$$\mathcal{L}_\Gamma[\hat{\rho}] = \sum_{n,m=1}^{N} \frac{\Gamma_{nm}}{2}\Big(2\hat{\sigma}_n\hat{\rho}\hat{\sigma}_m^\dagger - \hat{\sigma}_n^\dagger\hat{\sigma}_m\hat{\rho} - \hat{\rho}\hat{\sigma}_n^\dagger\hat{\sigma}_m\Big), \tag{9.3a}$$

$$\mathcal{L}_\mathrm{R}[\hat{\rho}] = \sum_{n\in\mathcal{P}} \frac{R}{2}\Big(2\hat{\sigma}_n^\dagger\hat{\rho}\hat{\sigma}_n - \hat{\sigma}_n\hat{\sigma}_n^\dagger\hat{\rho} - \hat{\rho}\hat{\sigma}_n\hat{\sigma}_n^\dagger\Big), \tag{9.3b}$$

$$\mathcal{L}_\mathrm{fs}[\hat{\rho}] = \sum_{n=1}^{N} \frac{\Gamma'}{2}\Big(2\hat{\sigma}_n\hat{\rho}\hat{\sigma}_n^\dagger - \hat{\sigma}_n^\dagger\hat{\sigma}_n\hat{\rho} - \hat{\rho}\hat{\sigma}_n^\dagger\hat{\sigma}_n\Big). \tag{9.3c}$$

Collective dissipation between emitters n and m occurs with rates $\Gamma_{nm} = \Gamma\cos(k|x_n - x_m|)$ at the emitter resonance frequency ω_0, where $k = \omega_0/v_g$ is the guided-mode wavevector and v_g is the group velocity of the propagating waveguide photons [160]. The collective rates are governed by the Green's tensor for a one-dimensional photonic

environment evaluated at ω_0 via [168]

$$\frac{3\pi\Gamma}{k}\,\mathbf{d}^*\cdot\mathbf{G}(x_n,x_m,\omega_0)\cdot\mathbf{d}=-\frac{i\Gamma}{2}\exp\big(ik|x_n-x_m|\big), \tag{9.4}$$

where $\mathbf{d}$ is the transition dipole moment of the two-level emitters (using $\mu_0\omega_0^2|\mathbf{d}|^2/\hbar = 3\pi\Gamma/k$). Furthermore, we assume a bidirectional (non-chiral) waveguide model such that the relative phases between emitters depend on the absolute value of the relative positions, i.e. relative phase $k|x_n-x_m|$ (mod 2π). Radiative decay into the waveguide mode competes with free-space losses and results in a coupling efficiency quantified by $\beta=\Gamma/(\Gamma+\Gamma')\leq 1$ [159]. We note that, in the superradiant regime, collective emission into the guided mode becomes the dominant mechanism driving the atomic dynamics, surpassing competing dissipative processes.

Although the waveguide-mediated couplings are controlled by the propagation phase $k|x_n-x_m|$, the physical emitter separations can be chosen much larger than the resonant wavelength. For an equidistant chain we write the nearest-neighbor spacing as

$$a=a_0+\delta a,\qquad a_0=\ell\lambda_0,\qquad \ell=0,1,2,\ldots, \tag{9.5}$$

so that $ka=2\pi\ell+k\delta a$ and all collective waveguide couplings depend only on the residual phase $\phi=k\delta a$. We therefore assume $a_0\gg\lambda_0$ such that free-space dipole-dipole interactions can be neglected, while δa determines the waveguide-mediated coherent and dissipative couplings. As a remark, we note that the collective dissipative couplings can be written in the form

$$\Gamma_{nm}=\Gamma\big[\cos(kx_n)\cos(kx_m)+\sin(kx_n)\sin(kx_m)\big],$$

as elements of a collective dissipation matrix, which has rank at most two [105]. Generically, it admits two non-zero eigenvalues $\Gamma_\pm$ satisfying $\Gamma_++\Gamma_-=N\Gamma$, while the rank reduces to one in the special case $kx_n=2\pi\ell_n$ with $\ell_n=0,1,2,\ldots$. Physically, this is because a bidirectional 1D waveguide has only two independent radiative output channels: left- and right-propagating modes. Accordingly, $\mathcal{L}_\Gamma[\hat\rho]$ can be represented by two collective jump operators or, equivalently, by the two directional input-output operators. These representations are related by linear combinations, but the directional output fields are, in general, not identical to the eigenstates of the collective dissipation matrix.

We follow the standard input–output treatment from Refs. [160, 169] for the left- and

right-propagating electromagnetic fields, $\hat{a}_{L/R}(t) = \hat{a}_{L/R,\mathrm{in}}(t) + \sum_j e^{\pm ikx_j}\sqrt{\Gamma/2}\,\hat{\sigma}_j(t)$ [160]. For a single guided mode in units of the group velocity v_g (set to unity below), the positive-frequency components of the fields in the far field to the right/left of the emitter ensemble read

$$\hat{E}_{L/R} = i\sqrt{\Gamma/2}\sum_{n=1}^{N} e^{\pm ikx_n}\hat{\sigma}_n. \tag{9.6}$$

Here, we have omitted the input fields $\hat{E}_{\mathrm{in}}$ appearing in the input–output relations. In our setup the guided modes are assumed to be initially in the vacuum state, and we evaluate normally ordered output-field observables, for which the vacuum input contributes only quantum noise and does not affect the quantities considered below. We therefore use Eq. (9.6) throughout this work as the radiated field exiting the waveguide through the left- and right-propagating output fields.

9.2.1 Figures of merit

We characterize the steady-state emission properties by analyzing the following:

(i) Emitted field intensity. A central signature of steady-state superradiance is a superlinear (up to quadratic) scaling of the emitted intensity with the emitter number N [2, 133]. The radiated steady-state field intensity (or power divided by $\hbar\omega_0$) into the waveguide reads

$$I_{\mathrm{L/R}} = \langle \hat{E}^{\dagger}_{\mathrm{L/R}}\hat{E}_{\mathrm{L/R}}\rangle = \frac{\Gamma}{2}\sum_{n,m=1}^{N} e^{\pm ik(x_m - x_n)}\langle \hat{\sigma}^{\dagger}_n\hat{\sigma}_m\rangle. \tag{9.7}$$

Independent emission yields $I_{\mathrm{L/R}} \propto N\Gamma$, whereas phase-synchronized emission leads to superlinear scaling of the emitted intensity with N.

(ii) Spectral properties of the emitted light. A further figure of merit is a narrow, well-resolved emission line with full width at half maximum (FWHM) centered close to the bare emitter frequency ω_0. The normally ordered, steady-state emission spectra in the left/right directions are defined by

$$S_{\mathrm{L/R}}(\omega) = 2\,\mathrm{Re}\left[\int_0^{\infty} d\tau\, e^{\mathrm{i}\omega\tau}\,\langle \hat{E}^{\dagger}_{\mathrm{L/R}}(t_{\mathrm{ss}}+\tau)\,\hat{E}_{\mathrm{L/R}}(t_{\mathrm{ss}})\rangle\right], \tag{9.8}$$

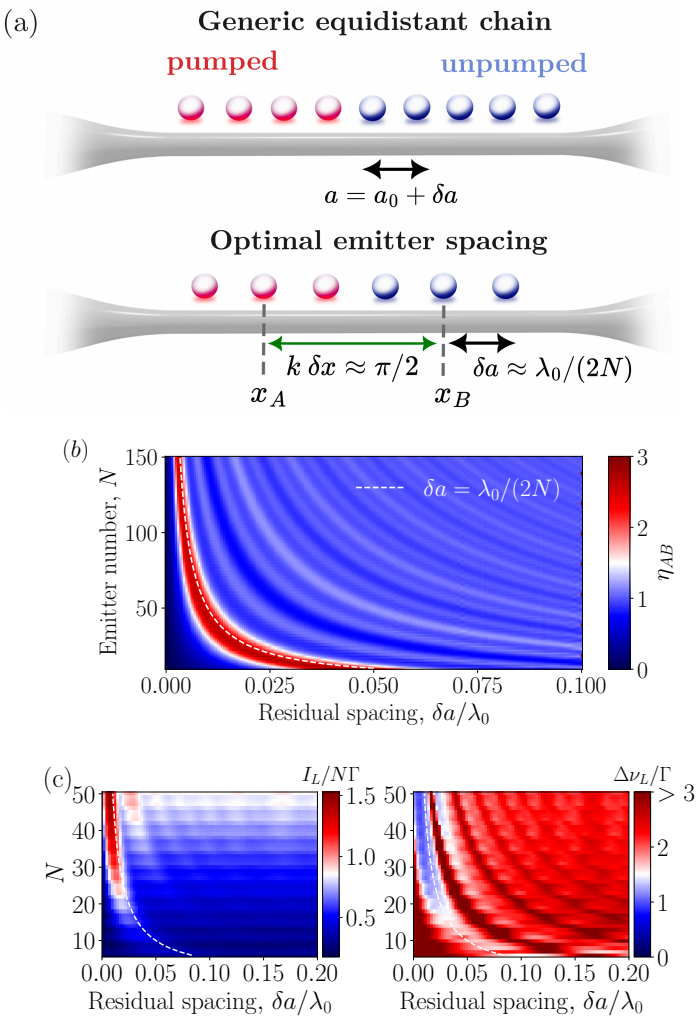

Figure 9.2: *Optimal emitter spacing and emission properties of a regular chain under incoherent pumping of its left half:* **(a)** Sketch of a chain with nearest-neighbor emitter spacing $a = a_0 + \delta a$, where $a_0 = \ell\lambda_0$ is an integer-wavelength offset. For an optimized emitter spacing, center-to-center residual phase is approximately $k\delta x \approx \pi/2$ between the two sub-ensemble centers. **(b)** The ratio of coherent versus dissipative coupling between the pumped (A) and unpumped (B) ensembles is quantified by the parameter η_{AB} defined in Eq. (9.12) and plotted as a function of the residual spacing δa and total emitter number N. For $N_p = N/2$, the optimal residual spacing follows $\delta a \approx \lambda_0/(2N)$ (white dashed line) corresponding to a residual phase $k\delta a \approx \pi/N$. **(c)** The numerical results for the steady-state emission intensity (I_L) and spectral linewidth ($\Delta\nu_L$) exhibit optimal values when η_{AB} is maximal (white dashed line). Simulations are based on the second-order cumulant approach. Parameters: $R = 10\Gamma, \Gamma' = 0$.

where t_{ss} denotes the simulation time at which the system is observed to have reached steady state.

(iii) Photon statistics. Finally, we characterize the photon statistics of the emitted field via the equal-time, zero-delay intensity correlation function

$$g^{(2)}_{\mathrm{L/R}}(0) = \frac{\left\langle \left(\hat{E}^{\dagger}_{\mathrm{L/R}}(t_{\mathrm{ss}})\right)^2 \left(\hat{E}_{\mathrm{L/R}}(t_{\mathrm{ss}})\right)^2 \right\rangle}{\left\langle \hat{E}^{\dagger}_{\mathrm{L/R}}(t_{\mathrm{ss}}) \hat{E}_{\mathrm{L/R}}(t_{\mathrm{ss}}) \right\rangle^2}, \tag{9.9}$$

which probes equal-time intensity fluctuations of the left- and right-going output fields. Values $g^{(2)}_{\mathrm{L/R}}(0)=1$ correspond to Poissonian photon statistics, $g^{(2)}_{\mathrm{L/R}}(0)>1$ to photon bunching (super-Poissonian statistics), and $g^{(2)}_{\mathrm{L/R}}(0)<1$ to photon antibunching (sub-Poissonian statistics). In our system, $g^{(2)}_{\mathrm{L/R}}(0)$ complements the intensity scaling and linewidth by quantifying the strength of equal-time intensity fluctuations in the directional output fields.

9.2.2 Optimal atomic emitter spacing

In physical implementations, the emitters do not need to be separated by subwavelength distances, since the coherent and dissipative waveguide-mediated couplings depend only on the residual phase $\phi = k\delta a$. In this work, we divide the chain into a pumped ensemble $A = \{1, \ldots, N_p\}$ followed by an unpumped ensemble $B = \{N_p + 1, \ldots, N\}$. To characterize how the passive ensemble interacts with a given pumped emitter $n \in A$, we introduce the local phase sum

$$r_n = \sum_{j \in B} \exp\big[ik(x_j - x_n)\big] = \sum_{j=N_p+1}^{N} \exp\big[i\phi(j-n)\big], \tag{9.10}$$

where the integer-wavelength part of the spacing drops out of the phase factor. For an equidistant chain, this geometric series can be evaluated in closed form as

$$r_n = \exp\left[i\phi\left(\frac{3N}{4} + \frac{1}{2} - n\right)\right] \frac{\sin(N\phi/4)}{\sin(\phi/2)}. \tag{9.11}$$

The prefactor in Eq. (9.11) is the propagation phase from emitter n to the center of the passive ensemble, while the common amplitude factor describes the coherent addition of all contributions from ensemble B. The relative propagation phase therefore controls

whether the inter-ensemble coupling is predominantly coherent or dissipative.

To quantify this, we define the accumulated coherent and dissipative inter-ensemble contributions and their ratio as

$$J_{AB} = \sum_{n \in A} \left| \Im r_n \right|, \; \Gamma_{AB} = \sum_{n \in A} \left| \Re r_n \right|, \quad \eta_{AB} \equiv \frac{J_{AB}}{\Gamma_{AB}}. \tag{9.12}$$

The ratio η_{AB} is a measure for how strongly coherent exchange dominates over dissipative coupling between the pumped and passive halves.

In Fig. 9.1(b), we observe that the improved emission characteristics are obtained when the pumped and unpumped sub-ensembles are of comparable size. In the following, we focus on the representative case where the first half of the emitters is incoherently pumped, while the second half remains unpumped (more general pumped fractions are discussed in the Supplemental Material). In the half-pumped case, the common amplitude factor in Eq. (9.11) cancels in η_{AB}, so that the optimization is governed purely by the phase profile across the pumped ensemble.

The analytical results presented in Fig. 9.2(b) indicate that η_{AB} is maximized close to

$$\phi_{\text{opt}} = k\delta a_{\text{opt}} \approx \frac{\pi}{N}. \tag{9.13}$$

For $k = 2\pi/\lambda_0$, this corresponds to a residual spacing $\delta a_{\text{opt}} \approx \lambda_0/(2N)$, and therefore to an actual emitter spacing

$$a_{\text{opt}} = a_0 + \delta a_{\text{opt}} = \ell\lambda_0 + \frac{\lambda_0}{2N}. \tag{9.14}$$

This agrees well with the residual spacing at which the steady-state directional emission is maximal and the spectral linewidth is minimal, shown in Fig. 9.2(c).

This optimum admits a simple geometric interpretation in terms of the phase difference between the centers of the two ensembles. The center positions of the pumped and passive halves are

$$x_A = a\left(\frac{N}{4} + \frac{1}{2}\right), \qquad x_B = a\left(\frac{3N}{4} + \frac{1}{2}\right), \tag{9.15}$$

so that their center-to-center separation is $x_B - x_A = Na/2$. Since the integer-wavelength part contributes only an integer multiple of 2π to the inter-emitter phases, the relevant reduced center-to-center phase is $k(x_B - x_A) \equiv N\phi/2 \pmod{\pi}$. At

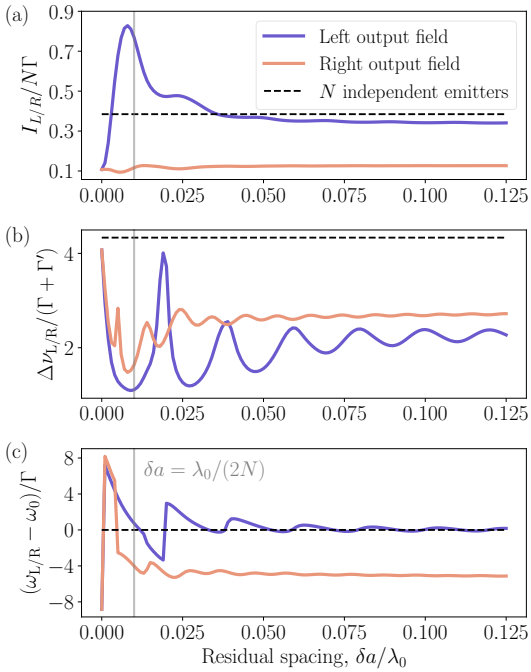

Figure 9.3: *Emission into left- and right-propagating waveguide modes.* Emerging left/right asymmetry of steady-state emission properties for varying residual nearest-neighbor phase $k\delta a$. **(a)** Normalized steady-state photon emission $I_{L/R}$ is enhanced into the left and strongly suppressed into the right-propagating direction. **(b)** Full width at half maximum $\Delta\nu_{L/R}$ of the spectral peak in units of the emitter spectral linewidth $\Gamma + \Gamma'$ decreases strongly toward the left output at optimal spacing. **(c)** The spectral peak position $\omega_{L/R}$ is close to the emitter's natural frequency for left propagation and strongly shifted for right propagation. Parameters: $N_p = N/2$, $N = 50$, $R = 10\Gamma$, $\Gamma' = 2\Gamma$.

the optimal residual phase $\phi_{\text{opt}} = \pi/N$, this becomes $k(x_B - x_A) = \pi/2 \pmod{\pi}$. Thus, the optimal spacing corresponds to an approximate quarter-wave phase shift between the centers of the pumped and passive halves, which suppresses the net dissipative inter-ensemble coupling while enhancing the coherent exchange responsible for collective feedback and narrow-linewidth superradiant emission.

9.3 Steady-state results

We now turn to the steady-state emission properties of a partially pumped emitter chain coupled to a single-mode waveguide reservoir. In the following, we calculate

the dynamics and steady-state properties using a second-order cumulant expansion approach [37, 170] that retains two-body correlations, see the Supplemental Material for details. In related physical models, this approach has captured the steady-state emission properties quite well and shown good agreement with the exact solution of the master equation [164, 170]. The central observables are the directional photon emission $I_{L/R}$, the spectral linewidth $\Delta\nu_{L/R}$, the frequency shift $\omega_{L/R} - \omega_0$ of the spectral peak from the emitter resonance, and the equal-time intensity correlation $g^{(2)}_{L/R}(0)$.

Figure 9.2 and the ratio in Eq. (9.12) first identify the geometric condition under which the pumped and unpumped parts of the chain are predominantly coupled via coherent interaction. At the optimal residual spacing $\delta a_{\mathrm{opt}} \simeq \lambda_0/(2N)$ the net dissipative coupling between the two ensembles is suppressed while the coherent exchange remains large. The steady-state emission and spectral linewidth properties in Fig. 9.2(c) show that this geometric optimum coincides with enhanced directional emission and a reduced spectral linewidth.

The same partial-pumping geometry also produces a pronounced left–right asymmetry in the emitted field. Although the waveguide reservoir itself is reciprocal and bidirectional, the partial pumping pattern is not invariant under inversion of the chain. In combination with the propagation phases in the directional output operators, this produces different left- and right-propagating steady-state fields. As shown in Fig. 9.3, photon emission is strongly enhanced in the left-propagating field and suppressed in the opposite direction. This asymmetry arises from the combination of spatially selective partial pumping and coherent waveguide-mediated exchange [171]. The coherent couplings J_{nm} create imaginary, phase-dependent inter-emitter coherences, which enter the directional intensities with opposite propagation phases. Consequently, the collectively emitted field interferes constructively in one propagation direction and destructively in the other. Importantly, the bright left-propagating field is also the spectrally useful one: its emission peak remains close to the bare emitter frequency ω_0, whereas the weak right-propagating component is strongly frequency shifted. We therefore focus on the left-propagating output in the following, since it simultaneously combines the desired emission properties.

Next, we fix the residual phase $k\delta a = \pi/5$ and show the scaling of emission properties with the total emitter number in Fig. 9.4. For sufficiently strong pumping, the steady-state photon emission I_L increases with N and reaches values above the N independent-emitter level, demonstrating superradiant enhancement. At the same

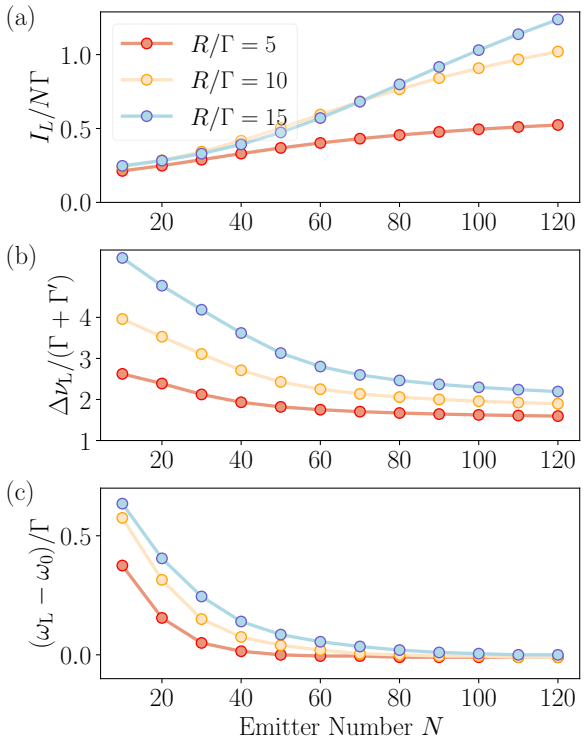

Figure 9.4: *Equidistant emitter chain.* The emission properties are shown for the left-propagating field as a function of the total emitter number N for three different pumping rates. **(a)** The photon emission rate I_L shows an increase and saturation above $N\Gamma$ for sufficient pumping rates. **(b)** The spectral linewidth $\Delta\nu_L$ shows a decrease and eventual saturation above $\Gamma+\Gamma'$. **(c)** The spectral peak position ω_L approaches the natural emitter frequency ω_0 for increasing N. Parameters: $N_p = N/2$, $k\delta a = \pi/5$, $\Gamma' = 3\Gamma$.

time, the linewidth decreases with increasing N and saturates on a scale set by the total single-emitter linewidth $\Gamma + \Gamma'$. The spectral peak position also moves toward the bare transition frequency. Thus, even for a fixed waveguide phase, increasing the number of emitters improves the three relevant properties of the emitted light: brightness, linewidth, and reduced shift of the spectral peak position. The saturation visible at large N, however, indicates that a fixed residual phase and pumping rate do not maintain the optimal feedback condition as the total emitter number changes.

In Fig. 9.5, we instead consider the optimized configuration, where the residual emitter spacing is chosen according to $k\delta a = \pi/N$ and the pumping rate is scaled with N. In this case the quarter-wave phase relation between the pumped and passive halves is

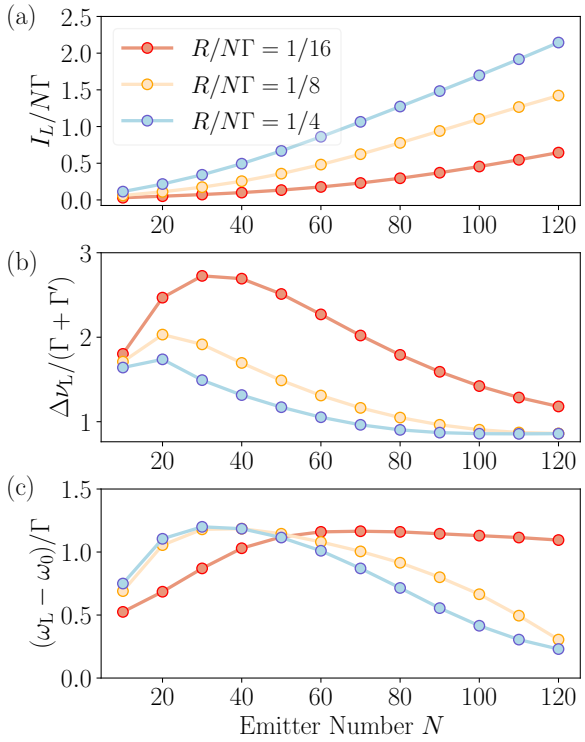

Figure 9.5: *Optimal emitter spacing.* Emission characteristics are shown for the left-propagating field as a function of the total emitter number N for N-dependent pumping rates. **(a)** The steady-state emission rate I_L exhibits a quadratic scaling $I_L \sim \Gamma N^2$. **(b)** The full width at half maximum $\Delta\nu_\mathrm{L}$ of the spectral peak in units of $\Gamma + \Gamma'$ shows a decrease and eventually decreases below the single-emitter linewidth $\Gamma + \Gamma'$. **(c)** The spectral peak position ω_L approaches the natural emitter frequency ω_0 for increasing N. Parameters: $N_p = N/2$, $k\delta a = \pi/N$, $\Gamma' = 3\Gamma$.

maintained as N increases. The resulting emission shows the characteristic signatures of steady-state superradiance: the photon emission scales quadratically, $I_L \sim N^2\Gamma$, the linewidth decreases toward values below the total single-emitter linewidth $\Gamma + \Gamma'$, and the spectral peak approaches the bare emitter resonance frequency ω_0.

Finally, Fig. 9.6 characterizes the photon statistics of the emitted field. We apply a fourth-order cumulant expansion of the equations of motion to account for the higher-order correlations entering $\langle(\hat{E}^\dagger)^2\hat{E}^2\rangle$ in Eq. (9.9). To derive and solve the resulting large systems of nonlinear differential equations, we employ an automated procedure based on a cumulant generating function [37] with details of this approach to be published in future work. For the optimized configuration, within the computationally

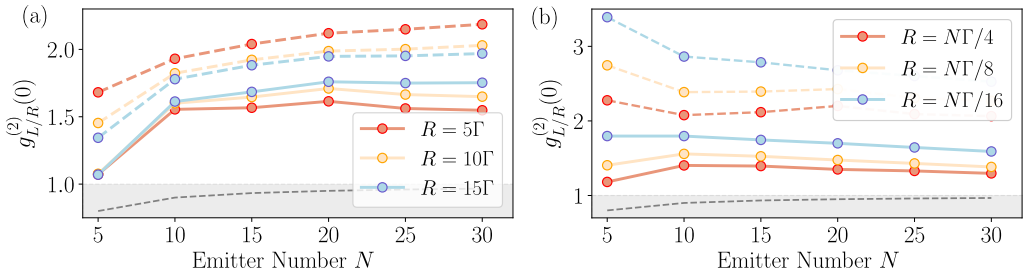

Figure 9.6: *Second-order correlation.* $g^{(2)}(0)$ of the left (solid line) and right (dashed line) propagating fields as a function of N. **(a)** For an equidistant chain with residual phase $k\delta a = \pi/5$ and $R/\Gamma = 5, 10, 15$. **(b)** For $k\delta a = \pi/N$ according to Eq. (9.12) and $R/N\Gamma = 1/16, 1/8, 1/4$. The left-propagating output approaches the Poissonian value from above for $k\delta a = \pi/N$, while the fixed-spacing geometry remains bunched over the range shown. In both cases $g^{(2)}(0)$ stays below the thermal value 2, indicating reduced equal-time intensity fluctuations compared with strongly bunched light. Simulations are performed using a fourth-order cumulant expansion of the equations of motion. Gray dashed lines show $g^{(2)}(0)$ for N independent emitters. Further parameters: $N_p = N/2$, $\Gamma' = 0$.

accessible system sizes, $g^{(2)}_L(0)$ approaches the Poissonian value from above, while the fixed-spacing configuration remains more strongly bunched. The approach of $g^{(2)}_L(0)$ toward unity indicates reduced equal-time intensity fluctuations. Together with the narrow emission spectrum and superlinear intensity scaling, this behavior is consistent with the buildup of superradiance with a stationary laser-like output field rather than independent broadband fluorescence.

9.3.1 Metrological performance

A central motivation for narrow-linewidth superradiant emission is its use as an active optical frequency reference. In such a device, the emitted field should ideally combine three properties: a substantial photon flux, which reduces photon shot noise in the detected signal, a narrow linewidth, which increases the coherence time and improves the frequency resolution, and a small frequency shift from the bare atomic transition. The last property ensures that the output field remains close in frequency to the atomic reference rather than to geometry- or interaction-induced collective modes [44, 57, 158].

To quantify these requirements in a single parameter, we introduce the metrological

parameter

$$M_{L/R} \equiv \frac{I_{L/R}\Gamma}{\Delta\nu_{L/R}^2 + 4(\omega_{L/R} - \omega_0)^2}. \tag{9.16}$$

Here, $I_{L/R}$ is the field intensity emitted into the left- or right-propagating mode, $\Delta\nu_{L/R}$ is the full width at half maximum of the corresponding emission spectrum, and $\omega_{L/R} - \omega_0$ quantifies the frequency shift away from the bare emitter resonance. The additional factor of Γ makes $M_{L/R}$ dimensionless, since $I_{L/R}$, Γ, $\Delta\nu_{L/R}$, and $\omega_{L/R} - \omega_0$ are all expressed as rates or frequencies. The structure of Eq. (9.16) is motivated by shot-noise-limited frequency readout [57, 158]. Here, the frequency uncertainty scales approximately as the spectral linewidth divided by the square root of the detected photon number, i.e. brighter emission and narrower linewidth directly improve the short-term frequency stability. In addition, a frequency reference should be accurate: the spectral maximum should remain close to the atomic transition frequency ω_0. The term $4(\omega_{L/R} - \omega_0)^2$ in Eq. (9.16) therefore penalizes frequency shifts. Large values of $M_{L/R}$ thus identify emission that is simultaneously bright, spectrally narrow, and weakly shifted from the atomic reference frequency.

As a benchmark, we compare the collective emission to N independent incoherently pumped emitters. For a single independent emitter, the steady-state photon flux into one propagation direction is

$$I_{L/R}^{\mathrm{ind}} = \frac{1}{2} I_{\mathrm{ind}} = \frac{1}{2} \frac{R\Gamma}{\Gamma + \Gamma' + R}, \tag{9.17}$$

where the factor $1/2$ reflects symmetric emission into the left- and right-propagating waveguide modes. The corresponding linewidth is power broadened by the incoherent pumping and reads $\Delta\nu_{\mathrm{ind}} = \Gamma + \Gamma' + R$. For N independent emitters, the intensity grows only linearly with N, while the linewidth is unchanged. In the absence of frequency shifts, the independent-emitter metrological parameter is therefore

$$M_{L/R}^{\mathrm{ind}} = N \frac{R\Gamma^2}{2(\Gamma + \Gamma' + R)^3}. \tag{9.18}$$

In the strong-pumping limit $R \gg \Gamma + \Gamma'$, one obtains $M_{L/R}^{\mathrm{ind}} \sim N\Gamma^2/(2R^2)$ for fixed pump rate and $M_{L/R}^{\mathrm{ind}} \sim 1/N$ for pump rates proportional to N, as seen in Fig. 9.7. Increasing the pump rate in an independent-emitter ensemble thus increases the photon flux only at the cost of strong power broadening, lowering the metrological figure of merit.

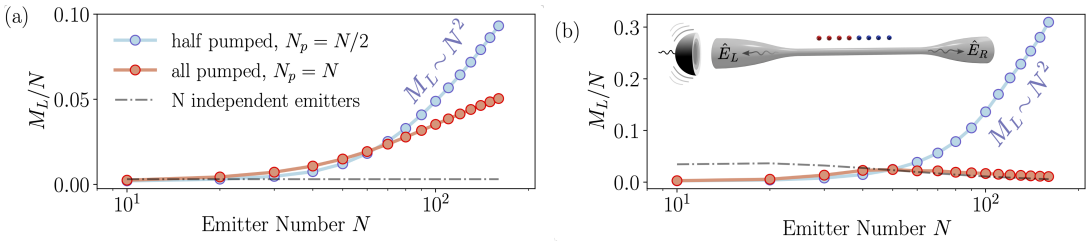

Figure 9.7: *Metrological performance.* Comparison of the metrological parameter M_L in Eq. (9.16) in the left waveguide output field. We consider partial pumping (leftmost $N_p = N/2$ emitters) and all emitters pumped ($N_p = N$) as a function of N. **(a)** Equidistant chain with residual phase $k\delta a = \pi/5$ and $R = 15\Gamma$. **(b)** Optimal residual spacing $k\delta a = \pi/N$ and pump rate $R = N\Gamma/16$. The gray dashed line shows M_L for N independent emitters. Partial pumping shows the best metrological performance according to the heuristic parameter M_L and fares substantially better for optimal emitter spacing. $\Gamma' = \Gamma$ in both plots.

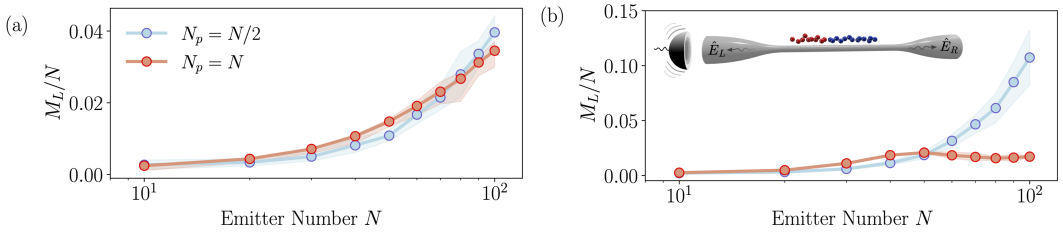

Figure 9.8: *Metrological performance under imperfections.* We show the disorder-averaged scaling of M_L with the total emitter number N in the presence of static positional disorder and inhomogeneous transition frequencies, modeled as described in the main text. **(a)** Pumping rate $R = 15\Gamma$. **(b)** Pumping rate $R = N\Gamma/16$. Partial pumping shows superior metrological performance and retains an approximately quadratic scaling with N. Parameters in both plots: initial residual spacing $\delta a = 0$, $\Gamma' = \Gamma$, disorder strengths $\sigma_a = \lambda_0/4$, $\sigma_\omega = \Gamma$, averaged over 50 random realizations for each curve.

The partially pumped ensemble with waveguide-mediated interactions behaves qualitatively differently. In the collective regime, the left-propagating photon flux is enhanced superlinearly, and for the optimized configuration approaches the superradiant scaling $I_L \propto N^2\Gamma$. At the same time, the linewidth remains on the order of, or below, the single-emitter decay scale, and the spectral maximum stays close to the bare transition, $\Delta\nu_L,\ |\omega_L - \omega_0| \lesssim \Gamma$. Consequently, Eq. (9.16) yields a quadratic enhancement,

$$M_L \sim N^2, \tag{9.19}$$

as shown in Fig. 9.7. This scaling expresses the metrological advantage of the partially pumped collective system: the waveguide-mediated interactions generate a bright output field without the severe power broadening that would occur for independent emitters and without the frequency shift that appears when all collectively interacting emitters are pumped. The unpumped part of the emitter chain therefore acts as a collective frequency-selective resonator, enabling narrow-line photon emission that remains tied to the atomic transition frequency, reminiscent of a conventional superradiant laser model [44, 48].

In Fig. 9.8, we test the robustness of this metrological enhancement by including static positional and frequency disorder [171]. For an equidistant chain we write the emitter positions as $x_n = n(a_0 + \delta a) + \xi_n$, where ξ_n are random displacements drawn from a normal distribution with standard deviation σ_a. The positional disorder ξ_n therefore randomizes the residual propagation phases entering the waveguide-mediated couplings. Inhomogeneous transition frequencies are given by $\omega_n = \omega_0 + \Delta_n$ with standard deviation σ_ω. In the frame rotating at the mean transition frequency ω_0, the additional Hamiltonian reads $\hat{H}_\Delta/\hbar = \sum_{n=1}^{N} \Delta_n \hat{\sigma}_n^\dagger \hat{\sigma}_n$. This term produces the detuning contribution $i(\Delta_n - \Delta_m)\langle \hat{\sigma}_n^\dagger \hat{\sigma}_m \rangle$ in the equations of motion for the optical coherences, see the Supplemental Material for details. For each value of N, the metrological figure of merit is averaged over independent disorder realizations.

The disorder-averaged results show that the metrological advantage of partial pumping persists beyond ideal emitter chains. Even for strong phase disorder, with $\sigma_a = \lambda_0/4$ corresponding to a waveguide phase uncertainty $k\sigma_a = \pi/2$, and in the presence of inhomogeneous transition frequencies with $\sigma_\omega = \Gamma$, the partially pumped configuration retains $M_L \sim N^2$ and outperforms uniformly pumped chains. This indicates that the underlying gain–resonator mechanism with the active-passive ensemble structure holds even in the presence of disorder.

9.4 Conclusions

As a key result, our study shows that the presence of unpumped emitters in an ensemble with all-to-all waveguide-mediated interactions not only strongly enhances collective emission into the fundamental guided mode, but also narrows the spectral linewidth while reducing frequency shifts. The observed improvement in the emitted light properties results from the dipole-dipole coupling of two sub-ensembles of comparable size: the incoherently pumped ensemble allows for the transfer of excitation and gain, while the unpumped sub-ensemble amplifies the emission and provides collective frequency-selective feedback. At the example of a 1D chain of quantum emitters, we show that the maximized ratio of coherent dipole-dipole exchange versus dissipative coupling between the pumped and unpumped sub-ensembles provides the optimal emitter configuration that realizes the desired regime of superradiant, narrow-linewidth emission close to the bare atomic resonance. The emitted light exhibits a strong asymmetry of emission properties in the pumped-emitter direction, and features reduced equal-time intensity fluctuations with $g^{(2)}(0) \simeq 1$. In contrast to conventional superradiant lasing in optical cavities, where the superradiant lasing threshold occurs only at large emitter numbers [44, 57], our results point to continuous narrowband superradiance even for small numbers of emitters. This setup thus appears to be a promising candidate for a waveguide-based active optical frequency reference with small clock-atom ensembles.

For instance, based on existing photonic microcell technology [172, 173], the system should have greatly reduced technical complexity when compared to passive optical clock designs or cavity-based superradiant lasers. Due to the periodicity of the emitter couplings to a waveguide mode the requirement on tight atomic positioning needed for strong dipole-dipole interactions in free space can be lifted, such that the atoms no longer need to be trapped at sub-wavelength distances. Thus, emitters can be arbitrarily placed with separations that exceed the resonant wavelength because the interaction strengths depend solely on the relative phase. This makes waveguide systems particularly beneficial for precise atomic positioning in experiments using neutral atoms trapped near optical nanofibers with optical lattices [174] and reconfigurable tweezer arrays [175]. At the same time, an experimental realization will require sufficient waveguide coupling efficiency, spatially selective repumping, suppression or calibration of light shifts stemming from the pumping and trapping of atoms, and precise control over emitter positions. These requirements are demanding but realistic

in view of rapid progress in waveguide QED platforms. Importantly, our results show that the superradiant, narrow-linewidth emission enabled by the active-passive ensemble structure persists even under strong positional disorder and moderate frequency broadening. In this regime, partial pumping continues to outperform the fully pumped configuration, demonstrating that the advantage does not rely on a perfectly ordered emitter geometry.

Acknowledgments

This research was funded in whole or in part by the Austrian Science Fund (FWF) QuantA 10.55776/COE1 (A.B., R.H., H.R.), and 10.55776/ESP3246525 (A.B.). M.F. acknowledges funding from the Austrian Science Fund (FWF) Grant DOI 10.55776/W1259 and from the FET OPEN Network Cryst3 funded by the European Union (EU) via Horizon 2020. S.F.Y. would like to acknowledge NSF via the CUA PFC (PHY-2317134) and AFOSR through FA9550-24-1-0311. I.V. and K.H. acknowledge support from DFG through the Collaborative Research Center SFB1227 (DQ-mat Project-ID 274200144) and from the Federal Ministry for Research, Technology and Space (BMFTR) Germany through project ATIQ.

9.5 Supplemental Material

9.5.1 Quantum master equation

We model N identical two-level emitters at positions $\{x_n\}$ coupled to a single guided mode of a bidirectional one-dimensional waveguide. In the laboratory frame, the total Hamiltonian in frequency units is [159, 160]

$$\hat{H}/\hbar = \sum_{n=1}^{N} \omega_0 \hat{\sigma}_n^\dagger \hat{\sigma}_n + \sum_{\mu=L,R} \int d\omega\, \omega\, \hat{b}_\mu^\dagger(\omega)\hat{b}_\mu(\omega) + \sum_{n,\mu} \int d\omega \left[g_\omega e^{i s_\mu k_\omega x_n} \hat{b}_\mu(\omega)\hat{\sigma}_n^\dagger + \text{H.c.} \right], \tag{9.20}$$

where $\hat{\sigma}_n = |g\rangle_n\langle e|_n$, $\hat{b}_\mu(\omega)$ annihilates a left- or right-propagating waveguide photon, and $s_R = +1$, $s_L = -1$.

Tracing out the waveguide in the Born–Markov and rotating-wave approximations, assuming vacuum input, a linearized dispersion relation around ω_0, and negligible retardation across the array, yields a Markovian master equation for the reduced

emitter density matrix. In a frame rotating at ω_0, it takes the form

$$\dot{\rho} = -\frac{i}{\hbar}\left[\hat{H}_{\mathrm{wg}}, \rho\right] + \mathcal{L}_{\Gamma}[\rho] + \mathcal{L}_{\mathrm{R}}[\rho] + \mathcal{L}_{\mathrm{fs}}[\rho]. \tag{9.21}$$

The waveguide-mediated coherent exchange is

$$\hat{H}_{\mathrm{wg}}/\hbar = \sum_{n,m=1}^{N} J_{nm}\hat{\sigma}_n^{\dagger}\hat{\sigma}_m, \tag{9.22}$$

while collective dissipation into the guided mode is described by

$$\mathcal{L}_{\Gamma}[\rho] = \sum_{n,m=1}^{N} \frac{\Gamma_{nm}}{2}\left(2\hat{\sigma}_n\rho\hat{\sigma}_m^{\dagger} - \hat{\sigma}_n^{\dagger}\hat{\sigma}_m\rho - \rho\hat{\sigma}_n^{\dagger}\hat{\sigma}_m\right). \tag{9.23}$$

For a bidirectional, nonchiral waveguide one obtains

$$J_{nm} - \frac{i}{2}\Gamma_{nm} = -\frac{i\Gamma}{2}e^{ik|x_n - x_m|}. \tag{9.24}$$

The absolute value in the phase reflects the fact that photons can propagate in both directions with equal amplitude [168]. In addition to the guided-mode dynamics, we include local incoherent pumping and parasitic free-space decay as independent Markovian channels,

$$\mathcal{L}_{\mathrm{R}}[\rho] = \sum_{n\in N_p} \frac{R}{2}\left(2\hat{\sigma}_n^{\dagger}\rho\hat{\sigma}_n - \hat{\sigma}_n\hat{\sigma}_n^{\dagger}\rho - \rho\hat{\sigma}_n\hat{\sigma}_n^{\dagger}\right), \tag{9.25}$$

$$\mathcal{L}_{\mathrm{fs}}[\rho] = \sum_{n=1}^{N} \frac{\Gamma'_n}{2}\left(2\hat{\sigma}_n\rho\hat{\sigma}_n^{\dagger} - \hat{\sigma}_n^{\dagger}\hat{\sigma}_n\rho - \rho\hat{\sigma}_n^{\dagger}\hat{\sigma}_n\right). \tag{9.26}$$

Here, $\mathcal{L}_{\mathrm{R}}$ models spatially selective incoherent repumping, while $\mathcal{L}_{\mathrm{fs}}$ accounts phenomenologically for radiative loss outside the guided mode. Throughout this work, we assume weak frequency dependence of the waveguide coupling around ω_0, negligible retardation on the scale of the emitter dynamics, and emitter separations large enough that direct free-space dipole-dipole interactions can be neglected.

9.5.2 Waveguide phase optimization

In the ideal bidirectional waveguide model, the collective couplings depend only on phase differences along the waveguide, rather than on bare distances. For an

equidistant chain with positions $x_n = (n-1)a$, we write the physical nearest-neighbor spacing as

$$a = a_0 + \delta a, \qquad a_0 = \ell\lambda_0, \qquad \ell \in \mathbb{N}. \tag{9.27}$$

The integer-wavelength part a_0 can be chosen large enough to suppress direct free-space dipole-dipole interactions, while the residual spacing δa fixes the relevant waveguide phase

$$\phi \equiv k\delta a = ka \pmod{2\pi}. \tag{9.28}$$

The waveguide-mediated couplings then read

$$J_{nm} = \frac{\Gamma}{2}\sin\big(|n-m|\phi\big), \qquad \Gamma_{nm} = \Gamma\cos\big(|n-m|\phi\big). \tag{9.29}$$

To understand the optimal emitter spacing under partial pumping, consider a contiguous pumped ensemble $A = \{1, \ldots, N_p\}$ followed by an unpumped ensemble $B = \{N_p + 1, \ldots, N\}$. The collective coupling between the two parts is governed by the complex phase sum

$$K_{AB}(\phi) \equiv \sum_{n\in A}\sum_{j\in B} e^{i\phi(j-n)}. \tag{9.30}$$

Its real and imaginary parts determine the net dissipative and coherent inter-ensemble couplings,

$$\Sigma_\Gamma^{AB} = \Gamma\,\mathrm{Re}\,K_{AB}, \qquad \Sigma_J^{AB} = \frac{\Gamma}{2}\,\mathrm{Im}\,K_{AB}. \tag{9.31}$$

For an equidistant chain this sum can be evaluated exactly as

$$K_{AB}(\phi) = e^{iN\phi/2}\,\frac{\sin(N_p\phi/2)\,\sin[(N-N_p)\phi/2]}{\sin^2(\phi/2)}. \tag{9.32}$$

The half-pumped case, $N_p = N/2$, is particularly transparent. Equation (9.32) reduces to

$$K_{AB}(\phi) = e^{iN\phi/2}\left[\frac{\sin(N\phi/4)}{\sin(\phi/2)}\right]^2. \tag{9.33}$$

Hence the net dissipative coupling between the pumped and passive halves vanishes whenever $\cos(N\phi/2) = 0$, that is $\phi = (2r+1)\pi/N$ for $r = 0, 1, 2, \ldots$.

The smallest positive solution $\phi = \pi/N$ corresponds to purely coherent coupling between the pumped and passive halves while keeping the coherent exchange large. In

terms of the residual spacing this gives

$$\delta a_{\mathrm{opt}} = \frac{\phi_{\mathrm{opt}}}{k} = \frac{\lambda_0}{2N}. \tag{9.34}$$

Thus the corresponding physical spacing may be chosen as

$$a_{\mathrm{opt}} = a_0 + \delta a_{\mathrm{opt}} = \ell\lambda_0 + \frac{\lambda_0}{2N}, \tag{9.35}$$

with ℓ large enough to suppress direct free-space interactions. For other contiguous pumped fractions, the same ensemble-sum analysis applies, although the precise optimum depends on $f = N_p/N$, the optimal nearest-neighbor phase remains of order $\phi_{\mathrm{opt}} \sim 1/N$.

This should be contrasted with the uniformly pumped chain. When all emitters are pumped, there is no active-passive ensemble structure, and the natural optimum is the fully phase-matched Dicke-like limit $\phi = 0$ modulo 2π, for which $J_{nm} = 0$ and $\Gamma_{nm} = \Gamma$ for all emitter pairs. In that case all emitters radiate into the same bright collective mode.

The same geometric idea extends to non-equidistant chains. For arbitrary emitter positions, the relevant quantity is still the inter-ensemble phase sum

$$K_{AB} = \sum_{n\in A}\sum_{j\in B} e^{ik(x_j - x_n)}. \tag{9.36}$$

The analogue of the equidistant optimum is therefore not a specific spacing, but the condition

$$\mathrm{Re}\, K_{AB} \approx 0, \qquad |\mathrm{Im}\, K_{AB}| \text{ large}, \tag{9.37}$$

i.e. suppressed net dissipative coupling together with strong coherent exchange between pumped and passive emitters. For two ensembles of spatially disordered emitters centered around $\bar{x}_A$ and $\bar{x}_B$, one may write approximately

$$K_{AB} \approx N_A N_B\, e^{ik(\bar{x}_B - \bar{x}_A)} F_A^*(k) F_B(k), \tag{9.38}$$

where

$$F_A(k) = \frac{1}{N_A}\sum_{n\in A} e^{ik(x_n - \bar{x}_A)}, \qquad F_B(k) = \frac{1}{N_B}\sum_{j\in B} e^{ik(x_j - \bar{x}_B)} \tag{9.39}$$

are structural form factors describing the internal phase matching within each cloud.

If $|F_A|$ and $|F_B|$ are close to unity, the same mechanism as above is recovered: a quarter-wave phase difference between the cloud centers,

$$k(\bar{x}_B - \bar{x}_A) \approx \frac{\pi}{2} \ (\mathrm{mod}\ \pi), \tag{9.40}$$

suppresses the net dissipative inter-cloud coupling while maximizing the coherent exchange.

9.5.3 Equations of motion and observables

Second-order cumulant expansion

Using the full quantum master equation to describe the system dynamics leads to a number of coupled equations that grows exponentially with the atom number, which restricts exact numerical simulations to relatively small ensembles. To access larger emitter numbers, we employ a cumulant expansion method [37, 162, 170]. In this approach, one derives equations of motion for operator expectation values from the quantum Langevin or Heisenberg equations and truncates the resulting hierarchy by factorizing higher-order correlators in terms of lower-order ones.

The emitter frequencies can be inhomogeneously broadened, leading to a decay rate Γ_n into the waveguide mode, incoherent pumping occurs with rate R_n and the emitters can decay with rate Γ'_n into free space. In realistic setups, local Stark shifts, Doppler shifts, or other sources of disorder can lead to a distribution of transition frequencies $\omega_n = \omega_0 + \Delta_n$. As long as this inhomogeneous broadening is weak compared to the relevant collective rates, $|\Delta_n| \ll \Gamma_n, J_{nm}$, we can work in a frame rotating at the mean frequency ω_0 and neglect the detunings Δ_n, while retaining the resulting emitter-dependent decay rates Γ_n that sample the frequency-dependent waveguide density of states.

Throughout, we assume that all emitters are initially prepared in the ground state, such that $\langle \hat{\sigma}_n^{ee} \rangle = 0$, $\langle \hat{\sigma}_n^\dagger \hat{\sigma}_m \rangle = 0$, and $\langle \hat{\sigma}_n^{ee} \hat{\sigma}_m^{ee} \rangle = 0$ at $t = 0$ for all n, m. We then truncate the hierarchy at second order, so that only three types of correlators acquire non-zero expectation values during the evolution, namely $\langle \hat{\sigma}_n^{ee} \rangle$, $\langle \hat{\sigma}_n^\dagger \hat{\sigma}_m \rangle$, and $\langle \hat{\sigma}_n^{ee} \hat{\sigma}_m^{ee} \rangle$.

This yields a closed set of coupled differential equations for the second-order cumulants:

$$\begin{aligned}
\frac{d}{dt}\langle\hat{\sigma}_n^{ee}\rangle &= -(\Gamma_n+\Gamma'_n+R_n)\langle\hat{\sigma}_n^{ee}\rangle + 2\sum_{k\neq n}^{N}\Re\Big\{g_{nk}\langle\hat{\sigma}_k^{\dagger}\hat{\sigma}_n\rangle\Big\} + R_n \\
\frac{d}{dt}\langle\hat{\sigma}_n^{\dagger}\hat{\sigma}_m\rangle &= -\left(\frac{\Gamma_n+\Gamma'_n+R_n+\Gamma_m+\Gamma'_m+R_m}{2} - i\big(\Delta_n-\Delta_m\big)\right)\langle\hat{\sigma}_n^{\dagger}\hat{\sigma}_m\rangle \\
&\quad + 2\Gamma_{nm}\langle\hat{\sigma}_n^{ee}\hat{\sigma}_m^{ee}\rangle + g_{nm}\langle\hat{\sigma}_m^{ee}\rangle + g_{nm}^{*}\langle\hat{\sigma}_n^{ee}\rangle \\
&\quad - \sum_{k\neq n,m}^{N}\Big(g_{km}^{*}\langle\hat{\sigma}_n^{\dagger}\hat{\sigma}_k\rangle\big(2\langle\hat{\sigma}_m^{ee}\rangle-1\big) + g_{kn}\langle\hat{\sigma}_k^{\dagger}\hat{\sigma}_m\rangle\big(2\langle\hat{\sigma}_n^{ee}\rangle-1\big)\Big) \\
\frac{d}{dt}\langle\hat{\sigma}_n^{ee}\hat{\sigma}_m^{ee}\rangle &= -(\Gamma_n+\Gamma'_n+R_n+\Gamma_m+\Gamma'_m+R_m)\langle\hat{\sigma}_n^{ee}\hat{\sigma}_m^{ee}\rangle + R_n\langle\hat{\sigma}_m^{ee}\rangle + R_m\langle\hat{\sigma}_n^{ee}\rangle \\
&\quad + 2\sum_{k\neq n,m}^{N}\Re\Big\{g_{km}\langle\hat{\sigma}_n^{ee}\rangle\langle\hat{\sigma}_k^{\dagger}\hat{\sigma}_m\rangle + g_{kn}\langle\hat{\sigma}_m^{ee}\rangle\langle\hat{\sigma}_k^{\dagger}\hat{\sigma}_n\rangle\Big\},
\end{aligned} \tag{9.41}$$

with $n \neq m$ and where we defined the collective dipole-dipole couplings $g_{nm} = iJ_{nm} - \Gamma_{nm}/2$ with

$$J_{nm} = \frac{\sqrt{\Gamma_n\Gamma_m}}{2}\sin(k|x_n - x_m|), \qquad \Gamma_{nm} = \sqrt{\Gamma_n\Gamma_m}\cos(k|x_n - x_m|). \tag{9.42}$$

Emission spectrum

The directional emission spectrum in the main text can be written as

$$S_{L/R}(\omega) = \Gamma\,\mathrm{Re}\left[\sum_{n,m=1}^{N} e^{\pm ik(x_m-x_n)}\int_0^{\infty} d\tau\, e^{i\omega\tau}G_{nm}(\tau)\right], \tag{9.43}$$

where

$$G_{nm}(\tau) \equiv \Big\langle\hat{\sigma}_n^{\dagger}(t_{\mathrm{ss}}+\tau)\hat{\sigma}_m(t_{\mathrm{ss}})\Big\rangle. \tag{9.44}$$

Within the second-order cumulant approximation, these two-time correlators are evaluated using the quantum regression theorem together with the same truncation used for the equal-time cumulants. Writing

$$p_n^{\mathrm{ss}} = \langle\hat{\sigma}_n^{ee}\rangle_{\mathrm{ss}}, \qquad C_{nm}^{\mathrm{ss}} = \langle\hat{\sigma}_n^{\dagger}\hat{\sigma}_m\rangle_{\mathrm{ss}}, \tag{9.45}$$

the regression equations read

$$\frac{d}{d\tau}G_{nm}(\tau) = -\frac{\Gamma_n + \Gamma'_n + R_n}{2}\, G_{nm}(\tau) - \sum_{k\neq n} g_{kn}\big(2p_n^{\mathrm{ss}} - 1\big)\, G_{km}(\tau), \tag{9.46}$$

with initial condition

$$G_{nm}(0) = C_{nm}^{\mathrm{ss}}. \tag{9.47}$$

Equivalently, for each fixed m one may write Eq. (9.46) in matrix form as

$$\dot{\mathbf{G}}^{(m)}(\tau) = \mathbf{M}_{\mathrm{ss}}\mathbf{G}^{(m)}(\tau), \qquad \mathbf{G}^{(m)}(0) = \mathbf{C}^{\mathrm{ss}}_{\cdot m}, \tag{9.48}$$

where

$$(\mathbf{M}_{\mathrm{ss}})_{nk} = -\frac{\Gamma_n + \Gamma'_n + R_n}{2}\delta_{nk} - (1-\delta_{nk})\, g_{kn}\big(2p_n^{\mathrm{ss}} - 1\big). \tag{9.49}$$

The spectrum is then obtained from the Laplace transform

$$\tilde{\mathbf{G}}^{(m)}(\omega) \equiv \int_0^\infty d\tau\, e^{i\omega\tau}\mathbf{G}^{(m)}(\tau) = -\big(\mathbf{M}_{\mathrm{ss}} + i\omega\mathbf{1}\big)^{-1}\mathbf{G}^{(m)}(0), \tag{9.50}$$

which yields

$$S_{L/R}(\omega) = \Gamma\,\mathrm{Re}\left[\sum_{n,m=1}^{N} e^{\pm ik(x_m - x_n)}\tilde{G}_{nm}(\omega)\right]. \tag{9.51}$$

In practice, we first solve the steady-state second-order cumulant equations for p_n^{ss} and C_{nm}^{ss}, then construct $\mathbf{M}_{\mathrm{ss}}$ and evaluate the above linear response for each frequency ω.

As a useful benchmark, consider N independent incoherently pumped emitters, for which all off-diagonal couplings vanish, $g_{nm} = 0$ for $n \neq m$, and

$$C_{nm}^{\mathrm{ss}} = \delta_{nm}p_e, \qquad p_e = \frac{R}{\Gamma + \Gamma' + R}. \tag{9.52}$$

Equation (9.46) then reduces to

$$G_{nm}(\tau) = \delta_{nm}\, p_e\, e^{-(\Gamma+\Gamma'+R)\tau/2}, \tag{9.53}$$

so that the left- and right-going spectra are identical and Lorentzian,

$$S_{L/R}^{\mathrm{ind}}(\omega) = N\,\frac{\Gamma}{2}\,p_e\,\frac{\Gamma + \Gamma' + R}{\omega^2 + [(\Gamma + \Gamma' + R)/2]^2}. \tag{9.54}$$

Thus, the independent-emitter reference has full width at half maximum

$$\Delta\nu_{\mathrm{ind}} = \Gamma + \Gamma' + R. \tag{9.55}$$

In the absence of free-space loss, $\Gamma' = 0$, this reduces to $\Delta\nu_{\mathrm{ind}} = \Gamma + R$.

Second-order correlation function

We expand the numerator of the second-order correlation function $g^{(2)}(0)$ from the main text in terms of lower-order cumulants. Starting from the directional output field

$$\hat{E}_{\mathrm{L/R}} = i\sqrt{\frac{\Gamma}{2}}\sum_{n=1}^{N} e^{\pm ikx_n}\hat{\sigma}_n, \tag{9.56}$$

the four-point correlator entering $g^{(2)}(0)$ is

$$\left\langle \hat{E}^{\dagger}_{\mathrm{L/R}}\hat{E}^{\dagger}_{\mathrm{L/R}}\hat{E}_{\mathrm{L/R}}\hat{E}_{\mathrm{L/R}}\right\rangle = \left(\frac{\Gamma}{2}\right)^2 \sum_{n,m,o,p=1}^{N} e^{\pm ik(x_o+x_p-x_n-x_m)}\langle\hat{\sigma}^{\dagger}_n\hat{\sigma}^{\dagger}_m\hat{\sigma}_o\hat{\sigma}_p\rangle. \tag{9.57}$$

We employ a fourth-order cumulant expansion for smaller emitter numbers to capture the effect of these four-point correlators. Since $g^{(2)}_{L/R}(0)$ probes equal-time intensity fluctuations, values approaching unity should be interpreted as reduced intensity noise. Temporal phase coherence is instead inferred from the first-order field correlation and the corresponding spectral narrowing.

9.5.4 Emission spectrum for two emitters

For two emitters the set of differential equations in second order is already exact. For such a small system we calculate the spectrum analytically. Here we consider pumping only the first atom and we investigate how the couplings modify the spectrum. It is important to note that the following calculations are done with a general Γ_{12} and J_{12}; the results therefore also apply to couplings mediated by any setup (e.g. atoms in free space), not just in the case of a waveguide. In other environments apart from a waveguide, one might be able to access more of the parameter region of Γ_{12} and J_{12}, whereas in the waveguide the propagation phase fixes both coupling rates.
The necessary correlation functions for obtaining the spectrum are $G_{11}(\tau)$, $G_{12}(\tau)$, $G_{21}(\tau)$ and $G_{22}(\tau)$. The necessary steady-state values can be derived from a set

of equations containing $\langle\sigma_1^{\mathrm{ee}}\rangle$, $\langle\sigma_2^{\mathrm{ee}}\rangle$, $\langle\sigma_1^\dagger\sigma_2\rangle$, $\langle\sigma_1\sigma_2^\dagger\rangle$ and $\langle\sigma_1^{\mathrm{ee}}\sigma_2^{\mathrm{ee}}\rangle$. The Quantum-Fluctuation-Regression Theorem allows us to find equations of motion for $G_{ij}(\tau) = \sigma_i^\dagger(\tau)\sigma_j(0)$ from the equations of $\sigma_i^\dagger$: Starting from the equations of motion for $\langle\sigma_i^\dagger\rangle$

$$\frac{d}{dt}\begin{pmatrix}\langle\sigma_1^\dagger(\tau)\rangle\\ \langle\sigma_2^\dagger(\tau)\rangle\end{pmatrix} = \underbrace{\begin{pmatrix}-\frac{\Gamma+R}{2} & -(iJ_{12}-\Gamma_{12}/2)\cdot\sigma_{1,ss}^{\mathrm{z}}\\ -(iJ_{12}-\Gamma_{12}/2)\cdot\sigma_{2,ss}^{\mathrm{z}} & -\frac{\Gamma}{2}\end{pmatrix}}_{=:M}\cdot\begin{pmatrix}\langle\sigma_1^\dagger(\tau)\rangle\\ \langle\sigma_2^\dagger(\tau)\rangle\end{pmatrix}, \tag{9.58}$$

the Quantum Fluctuation Regression Theorem allows us to insert the operator $\sigma_j(0)$ into the expectation values, such that we end up with a system of equations

$$\frac{d}{dt}y(\tau) = M\cdot y(\tau) \tag{9.59}$$

with $y = (G_{1j}, G_{2j})^T$. Defining the Laplace transform $x(s) = \mathcal{L}(y(\tau))$, we note that the spectrum is given by $S(\omega) = 2\Re x(i\omega)$, as the Fourier transform and the Laplace transform are equivalent at $s = i\omega$. In order to find $x(i\omega)$, we use the Laplace transform to convert the set of differential equations (9.59) into a set of algebraic equations:

$$(i\omega - M)\cdot x(i\omega) = y(0) \tag{9.60}$$

which can be easily solved. The solution to $(i\omega - M)^{-1} := A$ is given by

$$A_{11} = \frac{2(\Gamma+2i\omega)}{(\Gamma+2i\omega)(R+\Gamma+2i\omega) - \sigma_{1,ss}^{\mathrm{z}}\sigma_{2,ss}^{\mathrm{z}}(\Gamma_{12}-2iJ_{12})^2} \tag{9.61a}$$

$$A_{12} = \frac{2\sigma_{1,ss}^{\mathrm{z}}(\Gamma_{12}-2iJ_{12})}{(\Gamma+2i\omega)(R+\Gamma+2i\omega) - \sigma_{1,ss}^{\mathrm{z}}\sigma_{2,ss}^{\mathrm{z}}(\Gamma_{12}-2iJ_{12})^2} \tag{9.61b}$$

$$A_{21} = \frac{2\sigma_{2,ss}^{\mathrm{z}}(\Gamma_{12}-2iJ_{12})}{(\Gamma+2i\omega)(R+\Gamma+2i\omega) - \sigma_{1,ss}^{\mathrm{z}}\sigma_{2,ss}^{\mathrm{z}}(\Gamma_{12}-2iJ_{12})^2} \tag{9.61c}$$

$$A_{22} = \frac{2(R+\Gamma+2i\omega)}{(\Gamma+2i\omega)(R+\Gamma+2i\omega) - \sigma_{1,ss}^{\mathrm{z}}\sigma_{2,ss}^{\mathrm{z}}(\Gamma_{12}-2iJ_{12})^2} \tag{9.61d}$$

and $y(0)$ can be determined from the steady state values of the corresponding operators. In conclusion, the full spectrum is then given by $S(\omega) = 2\Re s(\omega)$

$$\begin{aligned} s(\omega) = {} & A_{11}\cdot\Big(\Gamma\langle\sigma_1^{\mathrm{ee}}\rangle_{\mathrm{ss}} + \Gamma_{12}\langle\sigma_1^\dagger\sigma_2\rangle_{\mathrm{ss}}\Big) + \\ & A_{12}\cdot\Big(\Gamma\langle\sigma_1\sigma_2^\dagger\rangle_{\mathrm{ss}} + \Gamma_{12}\langle\sigma_2^{ee}\rangle_{\mathrm{ss}}\Big) + \\ & A_{21}\cdot\Big(\Gamma_{12}\langle\sigma_1^{ee}\rangle_{\mathrm{ss}} + \Gamma\langle\sigma_1^+\sigma_2\rangle_{\mathrm{ss}}\Big) + \end{aligned} \tag{9.61e}$$

$$A_{22} \cdot \Big(\Gamma_{12} \langle \sigma_1 \sigma_2^\dagger \rangle_{\mathrm{ss}} + \Gamma \langle \sigma_2^{ee} \rangle_{\mathrm{ss}} \Big),$$

where the steady state values stem from the term $y(0)$. The only thing left to do is find analytic expressions for the steady state values: From the cumulant expansion one gets a set of differential equations in the form of

$$\dot{\mathbf{y}} = \tilde{M} \cdot \mathbf{y} + \mathbf{x} \tag{9.62}$$

where

$$\mathbf{y} = \begin{pmatrix} \langle \sigma_1^{\mathrm{ee}} \rangle \\ \langle \sigma_2^{\mathrm{ee}} \rangle \\ \langle \sigma_1^\dagger \sigma_2 \rangle \\ \langle \sigma_1 \sigma_2^\dagger \rangle \\ \langle \sigma_1^{\mathrm{ee}} \sigma_2^{\mathrm{ee}} \rangle \end{pmatrix} \qquad \mathbf{x} = \begin{pmatrix} R \\ 0 \\ 0 \\ 0 \\ 0 \end{pmatrix}$$

In steady state, we require $\dot{\mathbf{y}}_{\mathrm{ss}} = 0$, therefore we have for $\mathbf{y}_{ss}$

$$\mathbf{y}_{ss} = -\tilde{M}^{-1} \cdot \mathbf{x} \tag{9.63}$$

with the matrix $\tilde{M}$

$$\tilde{M} = \begin{pmatrix} -\Gamma - R & 0 & -i \cdot J_{12} - \Gamma_{12}/2 & i \cdot J_{12} - \Gamma_{12}/2 & 0 \\ 0 & -\Gamma & i \cdot J_{12} - \Gamma_{12}/2 & -i \cdot J_{12} - \Gamma_{12}/2 & 0 \\ -i \cdot J_{12} - \Gamma_{12}/2 & i \cdot J_{12} - \Gamma_{12}/2 & -\Gamma - R/2 & 0 & 2 \cdot \Gamma_{12} \\ i \cdot J_{12} - \Gamma_{12}/2 & -i \cdot J_{12} - \Gamma_{12}/2 & 0 & -\Gamma - R/2 & 2 \cdot \Gamma_{12} \\ 0 & R & 0 & 0 & -2\Gamma - R \end{pmatrix}. \tag{9.64}$$

Inverting this matrix one arrives at the steady state values for the expectation values:

$$\langle \sigma_1^{\mathrm{ee}} \rangle_{\mathrm{ss}} = \frac{R(R+2\Gamma)\left(R^2\Gamma + 4R\Gamma^2 + 4\Gamma^3 + 3R\Gamma_{12}^2 - 2\Gamma\Gamma_{12}^2 + 4(R+2\Gamma)J_{12}^2\right)}{\Gamma(R+\Gamma)(R+2\Gamma)^3 + (R+2\Gamma)\left(3R^2 - 4\Gamma^2\right)\Gamma_{12}^2 + 4\left((R+2\Gamma)^3 + 4(R-2\Gamma)\Gamma_{12}^2\right)J_{12}^2} \tag{9.65a}$$

$$\langle \sigma_2^{\mathrm{ee}} \rangle_{\mathrm{ss}} = \frac{R(R+2\Gamma)^2\left(\Gamma_{12}^2 + 4J_{12}^2\right)}{\Gamma(R+\Gamma)(R+2\Gamma)^3 + (R+2\Gamma)\left(3R^2 - 4\Gamma^2\right)\Gamma_{12}^2 + 4\left((R+2\Gamma)^3 + 4(R-2\Gamma)\Gamma_{12}^2\right)J_{12}^2} \tag{9.65b}$$

$$\langle \sigma_1^+ \sigma_2^- \rangle_{\mathrm{ss}} = -\frac{R(\Gamma_{12} + 2iJ_{12})\left(\Gamma(R+2\Gamma)^2 + 4i(R-2\Gamma)\Gamma_{12}J_{12}\right)}{\Gamma(R+\Gamma)(R+2\Gamma)^3 + (R+2\Gamma)\left(3R^2 - 4\Gamma^2\right)\Gamma_{12}^2 + 4\left((R+2\Gamma)^3 + 4(R-2\Gamma)\Gamma_{12}^2\right)J_{12}^2} \tag{9.65c}$$

$$\langle\sigma_1^-\sigma_2^+\rangle_{\mathrm{ss}} = -\frac{R(\Gamma_{12}-2iJ_{12})\left(\Gamma(R+2\Gamma)^2-4i(R-2\Gamma)\Gamma_{12}J_{12}\right)}{\Gamma(R+\Gamma)(R+2\Gamma)^3+(R+2\Gamma)\left(3R^2-4\Gamma^2\right)\Gamma_{12}^2+4\left((R+2\Gamma)^3+4(R-2\Gamma)\Gamma_{12}^2\right)J_{12}^2} \tag{9.65d}$$

$$\langle\sigma_1^{\mathrm{ee}}\sigma_2^{\mathrm{ee}}\rangle_{\mathrm{ss}} = \frac{R^2(R+2\Gamma)\left(\Gamma_{12}^2+4J_{12}^2\right)}{\Gamma(R+\Gamma)(R+2\Gamma)^3+(R+2\Gamma)\left(3R^2-4\Gamma^2\right)\Gamma_{12}^2+4\left((R+2\Gamma)^3+4(R-2\Gamma)\Gamma_{12}^2\right)J_{12}^2}. \tag{9.65e}$$

Inserting these expressions into Eq. (9.61e), one arrives at an analytic expression for the spectrum depending only on the system parameters Γ, Γ_{12}, J_{12} and R. The full expression is rather lengthy, but one can do more analytic work in some limiting cases. For $\Gamma_{12} = J_{12} = 0$, one arrives at the spectrum for independent atoms.

Narrowing of the spectrum due to J_{12} ($\Gamma_{12} = 0$)

Particularly interesting is the case for $\Gamma_{12} = 0$, which we analyze further. In the waveguide, this happens when the propagation phase between the emitters satisfies $kd = \pi/2 + q\pi$, or equivalently $d = (q+1/2)\lambda_0/2$ with $q \in \mathbb{N}$, then also the coupling rate J_{12} is fixed to $J_{12} = \Gamma/2$. To make the following calculations more versatile, we consider a general J_{12}.
The integer part of this distance may be chosen large enough to suppress direct free-space interactions. In this case we have no collective dissipative cross terms, so we distinguish between the spectrum of the pumped atom and the spectrum of the unpumped atom. Simplifying the above equations yields

$$S_{1,2}(\omega) = 2\cdot\frac{2R\Gamma}{(R+2\Gamma)\cdot(R\Gamma+\Gamma^2+4J_{12}^2)}\cdot\frac{a_{1,2}+4\omega^2 b_{1,2}}{(4\omega^2+c)^2+d} =: K\cdot\frac{a_{1,2}+4\omega^2 b_{1,2}}{(4\omega^2+c)^2+d} \tag{9.66}$$

with

$$a_1(R,\Gamma,J_{12}) = (\Gamma^2(R+2\Gamma)+4\,J_{12}^2\Gamma(1+\sigma_1^z))\cdot(R\Gamma+\Gamma^2+4\,J_{12}^2\sigma_1^z\sigma_2^z) \tag{9.67a}$$
$$b_1(R,\Gamma,J_{12}) = \Gamma(R+\Gamma)(R+2\Gamma)+4J_{12}^2(\Gamma(1-\sigma_1^z)+R) \tag{9.67b}$$
$$a_2(R,\Gamma,J_{12}) = 4J_{12}^2(R+\Gamma(1-\sigma_2^z))\cdot(R\Gamma+\Gamma^2+4\,J_{12}^2\sigma_1^z\sigma_2^z) \tag{9.67c}$$
$$b_2(R,\Gamma,J_{12}) = 4J_{12}^2\Gamma(1+\sigma_2^z) \tag{9.67d}$$
$$c(R,\Gamma,J_{12}) = \Gamma R+\Gamma^2-4\,J_{12}^2\sigma_1^z\sigma_2^z+R^2/2 \tag{9.67e}$$
$$d(R,\Gamma,J_{12}) = -\frac{1}{4}(R+2\Gamma)^2(R^2-16\,J_{12}^2\sigma_1^z\sigma_2^z), \tag{9.67f}$$

where the index $1,2$ indicates the spectrum of the first (pumped) atom and the second (unpumped) atom. For the full spectrum, use $a = a_1 + a_2$ and $b = b_1 + b_2$. Approximating the spectrum by making use of the Taylor expansion up to second order

$$S_{1,2}(\omega) \approx S_{1,2}(0) + \frac{1}{2}\omega^2 \cdot \underbrace{K \cdot \left(\frac{8\, b_{1,2}}{c^2+d} - \frac{16\, a_{1,2}\, c}{(c^2+d)^2}\right)}_{=:C} + O(\omega^4) \tag{9.68}$$

also allows us to read off the curvature C of the spectrum at $\omega = 0$. Since the spectrum is symmetric, this approximation is correct up to fourth order. In Fig. 9.9 we depict the normalized curvature $\tilde{C} = \frac{C}{S(0)}$ for different pumping strengths R and coupling rates J_{12}. From Eq. (9.66) we can also determine the FWHM by starting from

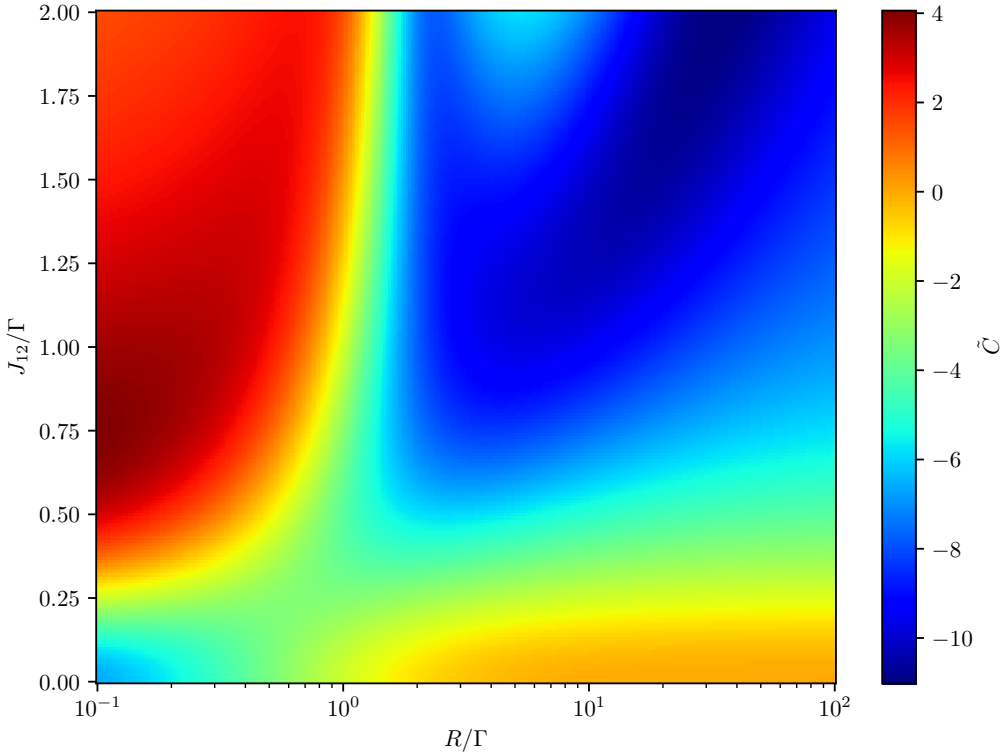

Figure 9.9: *Scan of the normalized curvature $\tilde{C}$ at $\omega = 0$ for varying pumping strength R and coupling rate J_{12}. All values can be calculated analytically.* Positive curvature (red) means that there is a dip in the spectrum at $\omega = 0$, whereas negative curvature (blue) indicates a peak in the spectrum. For $R > \Gamma$, increasing the coupling rate J_{12} leads to a narrowing of the peak. The coupling to the unpumped atom mediated by the waveguide therefore leads to a spectrum with a narrower peak.

$$\frac{a_{1,2} + 4\omega^2 b_{1,2}}{(4\omega^2 + c)^2 + d} = \frac{a_{1,2}}{c^2 + d}\frac{1}{2}. \tag{9.69}$$

The solutions of this equation read

$$(\omega^2)_\pm = \frac{-ac + b(c^2 + d)}{4a} \pm \frac{1}{32a}\sqrt{64a^2(c^2 + d) + (8ac - 8b(c^2 + d))^2}. \tag{9.70}$$

We disregard the solution with the minus, so the solution for the FWHM is then, because of symmetry, given by

$$\text{FWHM} = 2 \cdot \sqrt{(\omega^2)_+}. \tag{9.71}$$

Altogether we arrive at

$$\text{FWHM} = \sqrt{\frac{1}{a}} \cdot \sqrt{-ac + b(c^2 + d) + 1/8\sqrt{64a^2(c^2 + d) + (8ac - 8b(c^2 + d))^2}}. \tag{9.72}$$

Armed with the analytic expression for the full spectrum, the spectra of the individual atoms, their curvature and FWHM, we now investigate the influence of the coupling mediated through the waveguide on the spectra in Fig. 9.10. The spectrum of the pumped atom (a) gets power broadened, while the spectrum of the unpumped atom (c) is narrow. The sum of these spectra is depicted in (c). Comparing the full spectrum of both atoms (c) to the spectrum of an independent pumped atom in (d), the significant narrowing of the peak becomes apparent.

Independent emitters ($J_{12} = 0$, $\Gamma_{12} = 0$)

For independent emitters the above equations simplify further to

$$S(\omega) = \frac{2R\Gamma}{(R + \Gamma)^2} \cdot \frac{1}{1 + (\frac{2\omega}{R+\Gamma})^2}. \tag{9.73}$$

Here we have $\omega_{\max} = 0$ and for the FWHM linewidth we get power broadening,

$$\Delta\omega = \Gamma + R. \tag{9.74}$$

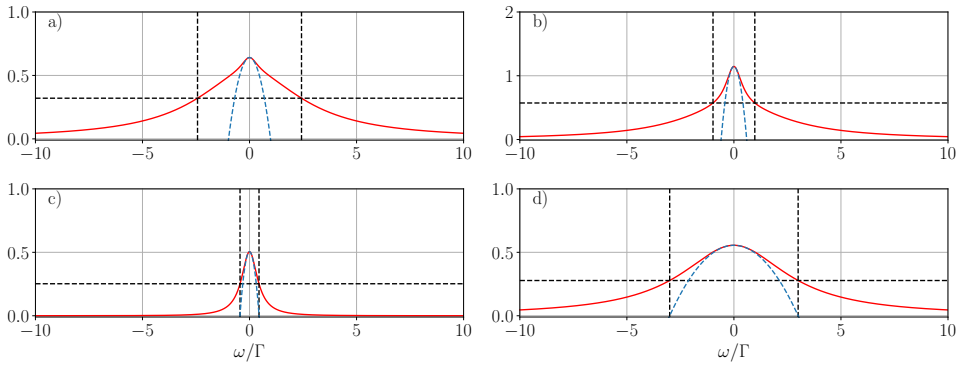

Figure 9.10: *Analytic spectra (red), Full Width at Half Maximum (black dashed) and Taylor approximation up to second order (blue dashed) of the spectra of two emitters with propagation phase $kd = \pi/2$ modulo π. All plotted graphs are described by analytic functions.* In (a) we plot the spectrum of the pumped atom, while in (c) the spectrum of the unpumped atom is depicted. Panel (b) shows the total spectrum, while in (d) the spectrum of an independent atom is plotted. The spectrum of the pumped atom in (a) is broadened by power, whereas the spectrum of the unpumped atom in (c) is narrow. Since the total spectrum is just a sum of the individual contributions ($\Gamma_{12} = 0$), we get a broader background from the pumped atom with a small peak from the unpumped atom. Comparing this total spectrum to the spectrum of a pumped atom without the coupling J_{12} in (d), we clearly notice the narrowing of the peak.

10 Ongoing work

The author of this thesis carried out most of the analytical and all the numerical calculations presented in this work. Sofia Ribeiro supervised the work and provided the idea and support in the interpretation of the results. Both authors contributed to the manuscript preparation.

Molecular Aggregation Dynamics inside picocavities

M. Fasser, S. Ribeiro

We study the aggregation dynamics of nonpolar molecules confined in picocavities, where strongly anisotropic electromagnetic fields reshape intermolecular interactions and orientational relaxation. Using an effective model that combines anisotropic Lennard-Jones interactions, Langevin dissipation, and cavity-induced coupling to molecular transition dipoles, we compare free-space aggregation with confinement-modified behavior. In free space, the dynamics relax toward ordered chains via a competition between dispersion forces, thermal fluctuations, and viscous damping, and exhibit a clear separation between rapid intra-cluster ordering and slower inter-cluster recombination. Under cavity confinement, the structured field generates configuration-dependent forces that can reorient molecules, localize clusters, and open confinement-dependent aggregation pathways. We show that the steady-state orientational order and aggregation patterns depend sensitively on the misalignment between dispersion- and cavity-coupled dipoles and on the spatial anisotropy of the cavity field, giving rise to partially aligned and frustrated configurations with no free-space analogue. These results identify concrete parameter regimes in which picocavity confinement qualitatively alters nanoscale aggregation and suggest polarization- and orientation-sensitive observables for future experiments in strongly confined plasmonic environments.

10.1 Introduction

Nonpolar molecules confined in picocavities – subnanometer gaps formed at metallic junctions – provide a versatile platform for nanoscale light-matter interactions relevant to nanophotonics, surface-enhanced Raman spectroscopy (SERS), and plasmonics [176–179]. Such gaps support highly localized, strongly anisotropic electromagnetic fields generated by plasmonic resonances [180, 181], which can modify molecular properties and interactions at the subnanometer scale [182–185]. Recent tip-enhanced Raman experiments have demonstrated single-molecule sensitivity in picocavities [181], underscoring their potential for probing molecular dynamics under extreme confinement.

In bulk phases, the aggregation of nonpolar molecules is governed primarily by van der Waals interactions and is often described using Lennard-Jones (LJ) potentials [186–188]. The resulting dynamics reflect a balance among attractive dispersion forces, thermal fluctuations, and solvent-mediated dissipation [189]. Under picocavity confinement, geometric constraints and spatially varying electromagnetic fields reshape the effective intermolecular potential landscape, and can thereby alter aggregation kinetics, cluster stability, and the accessible orientational configurations relative to free space. In particular, field anisotropy and confinement-dependent changes in interaction depth may favor molecular arrangements that are not readily realized without the cavity.

Although nonpolar molecules possess no permanent ground-state dipole, their transition dipole moments couple to localized optical near fields [190], enabling strong light-matter interactions and, in some regimes, hybridized states with mixed photonic and molecular character [191, 192]. Electromagnetic confinement has been shown to perturb chemical reactivity and intermolecular forces [193, 194] and to alter local energy landscapes [195]. How such field-induced effects compete with van der Waals attraction, thermal motion, and solvent viscosity in determining aggregation pathways and steady states remains an open theoretical question.

In this work, we develop an effective theoretical framework to investigate the aggregation of nonpolar molecules inside picocavities. Intermolecular forces are modeled by anisotropic LJ potentials, environmental effects enter through a Langevin description of temperature and solvent viscosity, and electromagnetic confinement is captured by coupling molecular transition dipole moments to a localized cavity mode that is treated semiclassically and adiabatically eliminated to yield a configuration-dependent mean field. Within this common framework, we compare aggregation dynamics in free

space and under cavity confinement using combined analytical and numerical analysis.

Beyond providing a minimal model, we identify three main trends. First, strong field confinement together with controlled misalignment between the dispersion-induced and cavity-coupled dipoles generates frustrated, partially ordered steady states with no analogue in free space. Second, in the strongly overdamped regime, the dynamics exhibit a clear separation between rapid intra-cluster ordering and slower inter-cluster recombination, clarifying how dissipation and temperature shape aggregation pathways. Third, we systematically map the steady-state van der Waals-induced orientational order parameter S_{vdW} as a function of cavity strength, spatial confinement, and dipole misalignment, and connect these trends to experimentally relevant observables such as orientational order, clustering behavior, and polarization-dependent spectroscopic response.

The paper proceeds as follows. In Sec. 10.2, we introduce the effective model based on an anisotropic Lennard-Jones interaction and a Langevin description of dissipation and thermal fluctuations. In Sec. 10.3, we extend this framework to include a localized cavity mode, treated semiclassically and adiabatically eliminated to yield a configuration-dependent field acting on the molecular coordinates, and we account for possible misalignment between the dispersion-induced and cavity-coupled dipoles. Section 10.4 uses numerical simulations to compare aggregation dynamics in free space and under cavity confinement, analyzing how temperature, viscosity, confinement strength, and dipole misalignment shape clustering and orientational order. Finally, Sec. 10.5 discusses experimental scenarios and potential applications of cavity-modified aggregation before we summarize our main conclusions in Sec. 10.6.

10.2 Theoretical Framework and Intermolecular Interaction Potentials

We consider a one-dimensional chain of N nonpolar molecules with centers located along the z axis and separated by distances r_{ij}. Each molecule is modeled as a rigid diatomic rotor composed of two point masses, m_1 and m_2, connected by a bond of fixed length R. The molecular orientation is specified by the spherical angles $\theta_i \in [0, \pi]$ and $\phi_i \in [0, 2\pi]$, which define the direction of the molecular axis (see Fig. 10.1). Translational motion is restricted to the chain direction.

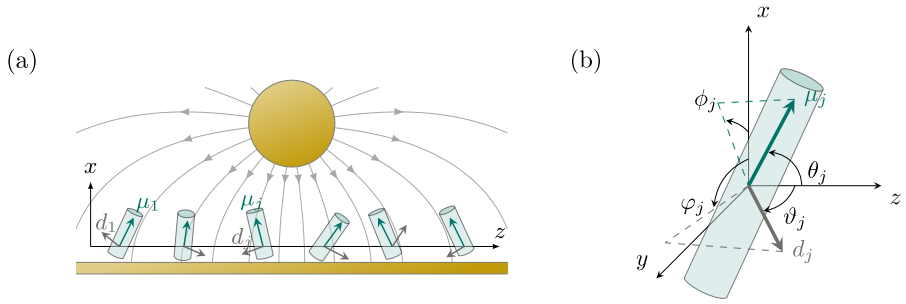

Figure 10.1: (a) Schematic of a one-dimensional molecular chain inside a cavity formed by a metal nanoparticle above a planar surface (not to scale). (b) The transition dipole $\mathbf{d}_j$ and the induced dipole $\boldsymbol{\mu}_j$ are represented in spherical coordinates. The molecular orientation is specified by the polar and azimuthal angles.

The rotational kinetic energy of molecule i is

$$K_i^{\mathrm{rot}} = \frac{1}{2} I\omega^2 = \frac{I}{2}\left(\dot{\theta}_i^2 + \dot{\phi}_i^2 \sin^2\theta_i\right), \tag{10.1}$$

where ω_i is the angular velocity and I is the moment of inertia about an axis perpendicular to the molecular bond. For a diatomic molecule with masses m_1 and m_2, one has

$$I = \frac{R^2 m_1 m_2}{m_1 + m_2},$$

For equal masses, $m_1 = m_2 = M$, this reduces to $I = MR^2/2$, corresponding to a linear rigid rotor. Since the molecule is symmetric about its bond axis, rotation around this axis does not change its orientation, and the two angles (θ_i, ϕ_i) are sufficient to describe its rotational state.

The translational kinetic energy along the chain axis is

$$K_i^{\mathrm{trans}} = \frac{1}{2} m\, \dot{z}_i^2, \tag{10.2}$$

where $m = m_1 + m_2$ is the total molecular mass. In the present model, the z_i coordinates may be treated as either fixed or dynamical variables, depending on the level of translational freedom included in the simulation.

We model intermolecular interactions using an effective anisotropic Lennard-Jones

(LJ) potential [186, 196], which combines short-range steric repulsion with orientation-dependent attraction,

$$U_{ij} = \frac{C_{12}}{(z_i - z_j)^{12}} - \frac{C_6}{(z_i - z_j)^6} f_{ij}^2, \tag{10.3}$$

with

$$f_{ij} = \sin\theta_i \sin\theta_j \cos(\phi_i - \phi_j) - 2\cos\theta_i \cos\theta_j. \tag{10.4}$$

The coefficient C_6 is treated as a constant parameter in this work, and temperature effects are introduced only through thermal fluctuations and solvent-mediated dissipation in the equations of motion. The repulsive term is included phenomenologically in the standard LJ form to capture short-range exclusion.

The angular factor f_{ij} is motivated by the tensor structure of the dipole-dipole interaction. For dipoles separated along the chain axis, $\hat{\mathbf{r}} = \hat{\mathbf{z}}$, the contraction $\boldsymbol{\mu}_i \cdot \boldsymbol{\mu}_j - 3(\boldsymbol{\mu}_i \cdot \hat{\mathbf{r}})(\boldsymbol{\mu}_j \cdot \hat{\mathbf{r}})$ reduces to $\sin\theta_i \sin\theta_j \cos(\phi_i - \phi_j) - 2\cos\theta_i \cos\theta_j$, which we square to obtain the effective anisotropy f_{ij}^2 in Eq.(10.3). In this sense, Eq.(10.3) represents a minimal anisotropic Lennard-Jones potential that inherits its orientational dependence from the dipolar tensor, rather than a full microscopic dispersion calculation.

In contrast to models for polar molecules, we do not include a separate permanent dipole-dipole term $\propto r^{-3}$, because the nonpolar systems of interest do not possess permanent ground-state dipoles. The leading orientational dependence of the effective dispersion interaction is instead encoded in f_{ij} in Eq. (10.3). The resulting potential is intended to describe intermolecular separations of a few ångströms around the LJ minimum, where short-range repulsion and dispersion dominate, rather than the very short-range chemical-bonding regime or the asymptotic C_6/r^6 tail. Accordingly, the parameters and angular dependence should be viewed as representative of a broad class of nonpolar systems, designed to capture qualitative orientational preferences and aggregation pathways under confinement, rather than as a quantitatively accurate fit for a particular molecule.

In this effective description, the dipole vectors that motivate the anisotropy enter only implicitly through f_{ij}; we do not introduce an additional dynamical variable for the dispersion dipole $\boldsymbol{\mu}$ beyond the molecular orientation angles, but instead encode its effect directly in the orientation-dependent Lennard-Jones interaction.

The Lagrangian for the N-molecule system in the absence of external fields is then

$$\begin{aligned} L &= K - U \\ &= \frac{1}{2}\sum_{i=1}^{N}\left\{m\dot{z}_i^2 + I\left(\dot{\theta}_i^2 + \dot{\phi}_i^2\sin^2\theta_i\right)\right\} \\ &\quad + \sum_{i<j}^{N}\left\{\frac{C_6}{(z_i - z_j)^6}\left[\sin\theta_i\sin\theta_j\cos(\phi_i - \phi_j)\right.\right. \\ &\quad \left.\left. -2\cos\theta_i\cos\theta_j\right]^2 - \frac{C_{12}}{(z_i - z_j)^{12}}\right\}. \end{aligned} \tag{10.5}$$

10.2.1 Equations of Motion with Dissipation and Stochastic Forces

The system dynamics follow from the Euler-Lagrange equations [197, 198]

$$\frac{d}{dt}\frac{\partial L}{\partial \dot{q}_i} - \frac{\partial L}{\partial q_i} = Q_i, \tag{10.6}$$

where q_i denotes a generalized coordinate and Q_i represents nonconservative forces [199]. Dissipation is incorporated phenomenologically through a Rayleigh dissipation function $\mathcal{F}$, yielding

$$\frac{d}{dt}\frac{\partial L}{\partial \dot{q}_i} - \frac{\partial L}{\partial q_i} = -\frac{\partial \mathcal{F}}{\partial \dot{q}_i}. \tag{10.7}$$

We model the surrounding medium as a viscous environment that gives rise to translational and rotational drag. Under Stokes flow, the dissipation functions are taken as

$$\mathcal{F}_{\text{trans}} = \frac{m\gamma_z}{2}\dot{z}_i^2 \tag{10.8}$$

$$\mathcal{F}_{\text{rot}} = \frac{I\gamma_\theta}{2}\,\dot{\theta}_i^2 + \frac{I\gamma_\phi}{2}\sin^2\theta_i\,\dot{\phi}_i^2. \tag{10.9}$$

where γ_z, $\gamma\theta$, and γ_ϕ are friction coefficients. The corresponding frictional forces are

$$-\frac{\partial \mathcal{F}_{\text{trans}}}{\partial \dot{z}_i} = -m\gamma_z\,\dot{z}_i, \tag{10.10}$$

$$-\frac{\partial \mathcal{F}_{\text{rot}}}{\partial \dot{\theta}_i} - \frac{\partial \mathcal{F}_{\text{rot}}}{\partial \dot{\phi}_i} = -I\gamma_\theta\,\dot{\theta}_i - I\gamma_\phi\sin^2\theta_i\,\dot{\phi}_i. \tag{10.11}$$

Thermal fluctuations are incorporated by adding Gaussian white noise terms consistent with the fluctuation-dissipation theorem [199, 200]. The resulting stochastic contributions are (defining $\kappa_z = m\gamma_z$, $\kappa_\theta = I\gamma_\theta$ and $\kappa_\phi = I\gamma_\phi$),

$$-\frac{\partial \mathcal{F}}{\partial \dot{z}_i} = -\kappa_z \, \dot{z}_i + \eta_z(t), \tag{10.12}$$

$$-\frac{\partial \mathcal{F}}{\partial \dot{\theta}_i} = -\kappa_\theta \, \dot{\theta}_i + \eta_\theta(t), \tag{10.13}$$

$$-\frac{\partial \mathcal{F}}{\partial \dot{\phi}_i} = -\kappa_\phi \sin^2\theta_i \, \dot{\phi}_i + \eta_\phi(t), \tag{10.14}$$

where $\langle \eta_a(t) \rangle = 0$ for $a \in z, \theta, \phi$, and the noise correlators satisfy

$$\left\langle \eta_z(t)\eta_z(t') \right\rangle = 2\kappa_z \, k_\mathrm{B} T \delta(t - t') \tag{10.15}$$

$$\left\langle \eta_\theta(t)\eta_\theta(t') \right\rangle = 2\kappa_\theta \, k_\mathrm{B} T \delta(t - t') \tag{10.16}$$

$$\left\langle \eta_\phi(t)\eta_\phi(t') \right\rangle = 2\kappa_\phi \, k_\mathrm{B} T \delta(t - t'), \tag{10.17}$$

where k_B is Boltzmann's constant and T is the absolute temperature. In the numerical implementation, the effective translational damping depends on the molecular orientation relative to the chain axis, so that $\kappa_z = \kappa_z(\theta)$. The stochastic equations are therefore interpreted in the Stratonovich sense [201].

The resulting equations of motion are

$$\dot{z}_i = \frac{p_{z_i}}{m}, \tag{10.18a}$$

$$\dot{\theta}_i = \frac{p_{\theta_i}}{I}, \tag{10.18b}$$

$$\dot{\phi}_i = \frac{p_{\phi_i}}{I \sin^2\theta_i}, \tag{10.18c}$$

$$\dot{p}_{z_i} = \sum_{i<j}^{N} \left\{ -\frac{6C_6}{(z_i - z_j)^7} \left[\sin\theta_i \sin\theta_j \cos(\phi_i - \phi_j) - 2\cos\theta_i \cos\theta_j \right]^2 + \frac{12C_{12}}{(z_i - z_j)^{13}} \right\} + \eta_z(t) - \kappa_z(\theta)\dot{z}_i, \tag{10.18d}$$

$$\dot{p}_{\theta_i} = I\dot{\phi}_i^2 \sin\theta_i \cos\theta_i + \sum_{i<j}^{N} \left\{ \frac{2C_6}{(z_i - z_j)^6} \left[\cos\theta_i \sin\theta_j \cos(\phi_i - \phi_j) + 2\sin\theta_i \cos\theta_j \right] \times \left[\sin\theta_i \sin\theta_j \cos(\phi_i - \phi_j) - 2\cos\theta_i \cos\theta_j \right] \right\} + \eta_\theta(t) - \kappa_\theta \dot{\theta}_i, \tag{10.18e}$$

$$\dot{p}_{\phi_i} = -\sum_{i<j}^{N} \frac{2C_6}{(z_i - z_j)^6} \sin\theta_i \sin\theta_j \sin(\phi_i - \phi_j) \left[\sin\theta_i \sin\theta_j \cos(\phi_i - \phi_j) - 2\cos\theta_i \cos\theta_j\right] + \eta_\phi(t) - \kappa_\phi \sin^2\theta_i \, \dot{\phi}_i. \tag{10.18f}$$

At finite temperature, the dynamics are governed by stochastic differential equations.

Modeling assumptions and scope

Before turning to the full equations of motion, it is useful to summarize the main modeling choices and their intended scope. First, the intermolecular forces are described by an effective anisotropic Lennard-Jones potential rather than by explicit many-body electronic-structure calculations. This coarse-grained description captures short-range steric repulsion and the leading orientational tendencies of dispersion forces, which are the dominant ingredients for aggregation and orientational ordering on the nanometer scale. It does not include explicit many-body dispersion corrections or chemistry-specific interaction details.

Second, each molecule is treated as a rigid rotor with its center of mass constrained to move along a single spatial direction. This one-dimensional, rigid-rotor description is motivated by the strong geometric confinement in picocavities and is intended as a minimal framework for studying how orientation and clustering respond to electromagnetic confinement, rather than a full three-dimensional description of molecular motion.

Third, environmental effects are incorporated through a Langevin description with orientationally dependent friction and thermal noise. In this approach, the molecular surroundings act as a viscous reservoir that sets damping rates and temperature, while microscopic solvent and substrate degrees of freedom are integrated out and are not modeled explicitly.

Finally, the dynamics are classical or semiclassical at the level of the molecular coordinates: we follow many-body configurations and relaxation pathways over picosecond timescales, rather than quantum coherence or photon statistics. In particular, we do not attempt a fully quantum treatment of the cavity field or polaritonic excitations; instead, in Sec. 10.3 the cavity is treated as a strongly damped semiclassical mode that is adiabatically eliminated to yield configuration-dependent mean forces.

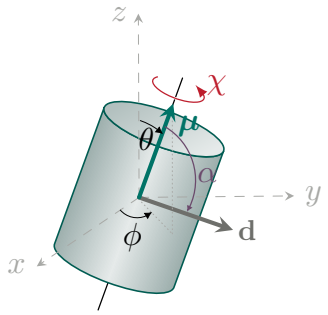

Figure 10.2: *Schematic representation of a rigid molecular rotor with Euler angles* (θ, ϕ, χ). The vector $\boldsymbol{\mu}$ denotes the molecular symmetry axis, while $\mathbf{d}$ is the transition dipole coupled to the cavity field. The angle α quantifies the fixed misalignment between the two dipoles.

These assumptions define the regime of validity of the model: they neglect explicit many-body dispersion, material-specific electronic structure, and coherent cavity-QED dynamics, and should be interpreted as providing qualitative trends for how strong electromagnetic confinement affects orientation, clustering, and relaxation pathways of nonpolar molecules, rather than quantitative predictions for particular chemical species.

10.3 Modeling Nonpolar Molecule-Cavity Interactions

We now consider how picocavity confinement modifies the aggregation dynamics. Picocavities confine electromagnetic fields to nanoscale volumes, producing strong local field enhancement and, in turn, strong light-matter coupling. Throughout this work, we focus on a representative geometry consisting of a metallic nanoparticle above a planar metallic surface.

Although nonpolar molecules do not possess a permanent ground-state dipole moment, they can interact with light through transition dipole moments associated with electronic or vibrational excitations (see Fig. 10.1). In the present model, this coupling is treated within an effective classical-Lagrangian framework, with the cavity field entering as an additional dynamical coordinate.

In principle, a nanophotonic picocavity supports quantized electromagnetic modes and can enter regimes of strong or ultrastrong light-matter coupling. In this work, we do not attempt to describe polariton formation, photon statistics, or coherent Rabi

dynamics. Instead, we are interested in how the average cavity field and its spatial confinement modify the effective interaction landscape governing slow aggregation and orientational relaxation. Throughout, we assume that electronic excitations are not coherently populated on the aggregation timescale – either because the system is driven off resonance or because excitation and dephasing processes act rapidly – so that the cavity effectively acts as a structured environment generating configuration-dependent mean forces on the molecular coordinates. We therefore represent the relevant cavity mode as a single harmonic oscillator and subsequently eliminate its fast oscillatory dynamics to obtain a quasi-static, configuration-dependent field amplitude acting on the molecular coordinates. This semiclassical treatment is appropriate when molecular reorientation and aggregation occur on timescales that are long compared with the optical period and cavity damping time, so that quantum fluctuations of the field mainly renormalise the effective potential rather than generating long-lived light-matter coherence.

We represent a single cavity mode as a harmonic oscillator [202]

$$\hat{H}_{\mathrm{HO}} = \frac{1}{2} m_{\mathrm{cav}} \dot{\mathcal{Q}}^2 + \frac{1}{2} m_{\mathrm{cav}} \omega_c^2 \mathcal{Q}^2. \tag{10.19}$$

where m_{cav} is a formal mass parameter introduced to reproduce the classical oscillator form, and $\mathcal{Q}$ denotes the cavity mode amplitude. The corresponding Lagrangian is

$$\mathcal{L}_{\mathrm{HO}} = \frac{1}{2} m_{\mathrm{cav}} \dot{\mathcal{Q}}^2 - \frac{1}{2} m_{\mathrm{cav}} \omega_c^2 \mathcal{Q}^2. \tag{10.20}$$

Within the quantized-field picture, the electric field in a cavity of effective mode volume V may be written as

$$\mathbf{E}(\mathbf{r}, t) = \mathcal{E}_0 (a + a^\dagger) \mathbf{u}(\mathbf{r}) \tag{10.21}$$

where $\mathcal{E}_0 = \sqrt{\frac{\hbar \omega_c}{2 \varepsilon_0 V}}$ is the field amplitude, ω_c is the cavity resonance frequency, and $\mathbf{u}(\mathbf{r})$ the normalized mode function. Identifying $\mathcal{Q} \propto (a + a^\dagger)$, we write

$$\mathbf{E}(\mathcal{Q}) = \mathcal{E}_0 \mathcal{Q} \hat{e}, \tag{10.22}$$

where $\hat{e}$ is the polarization unit vector. Matching the oscillator energy to the field

energy yields

$$\frac{1}{2}m_{\mathrm{cav}}\omega_c^2\mathcal{Q}^2 \sim \frac{\varepsilon_0}{2}E^2V, \tag{10.23}$$

which gives the effective scaling

$$m_{\mathrm{cav}} = \frac{\hbar}{2\omega_c}. \tag{10.24}$$

The light-matter interaction energy is taken as

$$V_{\mathrm{int}} = -\mathbf{d}\cdot\mathbf{E}(\mathbf{r},t), \tag{10.25}$$

so that for a single mode

$$\mathbf{E}(\mathbf{r},t) = \mathcal{E}_0(\mathbf{r})\,\mathcal{Q}(t)\,\hat{e}. \tag{10.26}$$

For a highly confined picocavity formed by a metallic nanoparticle above a planar surface [181, 190, 191, 203–206], we use a Gaussian mode profile,

$$\mathbf{E}\,(x,\,r) = E_{\max}\exp\left(-\frac{r^2}{w_r^2} - \frac{x^2}{w_x^2}\right)\hat{x}, \tag{10.27}$$

where x is the gap direction and r is the lateral distance from the cavity center. The maximum field amplitude is

$$E_{\max} = \sqrt{\frac{2\hbar\omega}{\varepsilon_0\pi^{3/2}w_r^2w_x}}. \tag{10.28}$$

A molecule at position (x_0, r_0) interacts with this field through

$$V_{\mathrm{int}} = -\mathbf{d}\cdot[\mathcal{E}_0(\mathbf{r})\,\mathcal{Q}(t)\hat{e}] = -g(\mathbf{r},\,\vartheta)\mathcal{Q}(t) \tag{10.29}$$

with coupling coefficient

$$g(\mathbf{r},\,\vartheta) = \mathcal{E}_0(\mathbf{r})\,\mathbf{d}(\vartheta)\cdot\hat{e}. \tag{10.30}$$

The interaction Lagrangian for N molecules is then

$$\mathcal{L}_{\text{int}} = \sum_{i=1}^{N} g_i(\mathbf{r}_i,\, \vartheta_i)\, \mathcal{Q}. \tag{10.31}$$

The full cavity-coupled Lagrangian is

$$\mathcal{L}_{\text{cav}} = \frac{1}{2} m_{\text{cav}} \dot{\mathcal{Q}}^2 - \frac{1}{2} m_{\text{cav}} \omega_c^2 \mathcal{Q}^2 + \sum_{i=1}^{N} g_i(\mathbf{r}_i,\, \vartheta_i) \mathcal{Q}. \tag{10.32}$$

Here, $\mathcal{Q}(t)$ is the cavity mode amplitude. In the parameter regime considered here, the cavity oscillation time is short compared with the molecular rearrangement time. We therefore treat the cavity mode in a semiclassical and effectively adiabatic approximation, and average over the rapid oscillations to obtain a quasi-static field amplitude used in the molecular equations of motion. Further details are given in Appendix 10.7.1.

To account for possible misalignment between the dipole responsible for van der Waals interactions and the transition dipole that couples to the cavity, we introduce a fixed angle α. This breaks the cylindrical symmetry of the molecule and introduces an additional rotational degree of freedom χ around the molecular axis (see Fig. 10.2). The kinetic energy associated with this rotation is

$$K_\chi = \frac{1}{2} I_\chi \dot{\chi}^2. \tag{10.33}$$

The corresponding Langevin equations are

$$\dot{\chi} = \frac{p_{\chi_i}}{I_\chi}, \tag{10.34a}$$

$$\dot{p}_{\chi_i} = +\eta_\chi(t) - \kappa_\chi \dot{\chi}, \tag{10.34b}$$

and the noise correlator is given by

$$\left\langle \eta_\chi(t) \eta_\chi(t') \right\rangle = 2\kappa_\chi\, k_{\text{B}} T \delta(t - t'). \tag{10.35}$$

For slender molecules, rotational friction about the symmetry axis is typically weaker than that for rotations perpendicular to the axis, so κ_χ is expected to be smaller than κ_θ and κ_ϕ.

The induced dipole moment is written as

$$\boldsymbol{\mu} = (\cos\phi\sin\theta,\, \sin\phi\sin\theta,\, \cos\theta)^{\mathrm{T}}. \tag{10.36}$$

If the cavity dipole lies in the plane defined by $\boldsymbol{\mu}$ and the z axis, the reference configuration $\chi = 0$ is

$$\boldsymbol{d}_{\chi=0} = (\cos\phi\sin(\theta+\alpha),\, \sin\phi\sin(\theta+\alpha), \cos(\theta+\alpha))^{\mathrm{T}}. \tag{10.37}$$

For a general rotation by χ about $\boldsymbol{\mu}$, Rodrigues' rotation formula gives

$$\mathbf{d} = \mathbf{d}_{\chi=0}\cos\chi + \boldsymbol{\mu}\times\mathbf{d}_{\chi=0}\sin\chi + \boldsymbol{\mu}\,(\boldsymbol{\mu}\cdot\mathbf{d}_{\chi=0})\,(1-\cos\chi)\,. \tag{10.38}$$

In this construction, the vector $\boldsymbol{\mu}$ represents an effective dipole associated with the anisotropic dispersion interaction encoded in the LJ-potential, while $\mathbf{d}$ denotes a transition dipole moment coupled to the cavity field. These two dipoles need not be collinear for a generic molecule: the tensor structure of dispersion and the symmetry of a particular optical transition can select different molecular axes. The fixed angle α thus parameterizes a possible misalignment between the axis that optimises van der Waals attraction and the axis that couples most strongly to the cavity mode. The additional rotational degree of freedom χ describes rotation about the molecular symmetry axis and allows us to resolve how the cavity torque competes with the orientational preferences imposed by the anisotropic LJ interaction.

The relative angle between the two dipoles remains fixed at α, since $\boldsymbol{\mu}\cdot\mathbf{d} = \cos\alpha$ for all θ, ϕ, and χ. The x component of $\mathbf{d}$ is then

$$\frac{d_x}{d_0} = \sin(\theta+\alpha)\cos\phi\cos\chi - \sin\alpha\sin\chi\sin\phi + \sin\theta\,\cos\phi\,\cos\alpha\,(1-\cos\chi)\,.$$

Using Eq. (10.32), the cavity equation of motion is

$$\ddot{\mathcal{Q}} = -\omega_c^2\mathcal{Q} + 2\frac{\omega}{\hbar}\sum_{i=1}^{N} g_i(\mathbf{r}_i,\, \vartheta_i). \tag{10.39}$$

In the parameter regime considered here, the cavity mode oscillates much faster than the molecular degrees of freedom. Writing the field coordinate as $\mathcal{Q}(t) = \mathrm{Re}\left[\tilde{\mathcal{Q}}(t)e^{-i\omega_c t}\right]$ with a slowly varying envelope and neglecting $\ddot{\tilde{\mathcal{Q}}}$ and $\dot{\tilde{\mathcal{Q}}}$ relative to $\omega_c\dot{\tilde{\mathcal{Q}}}$ and $\omega_c^2\tilde{\mathcal{Q}}$, the envelope follows the instantaneous molecular configuration.

Averaging over times long compared with $2\pi/\omega_c$ but short compared with the molecular rearrangement time then yields a quasi-static effective coordinate

$$\mathcal{Q}_{\text{eff}} = \frac{E_{\max}}{\hbar\omega} \times \sum_{i=1}^{N} d_x(\theta_i, \phi_i, \chi_i) \exp\left(-\frac{z_i^2}{w_r^2} - \frac{x_h^2}{w_x^2}\right). \tag{10.40}$$

which is used in the molecular equations of motion (see Appendix 10.7.1 for details and a discussion of the timescale hierarchy). In this work, we neglect explicit cavity-loss and noise terms in the equations of motion and treat the cavity as a strongly damped, semiclassical mode that follows the slow molecular dynamics adiabatically. Physically, radiative and ohmic losses set a cavity damping rate κ_c that is large compared with the molecular reorientation and aggregation rates in the parameter regime considered, so that the cavity field relaxes rapidly to a configuration-dependent mean value. As a result, the role of the cavity is captured by the quasi-static coordinate $\mathcal{Q}_{\text{eff}}$ and its associated mean forces on the molecular coordinates, rather than by resolving cavity fluctuations or coherent field dynamics. This mean-force picture differs from cavity-QED and polaritonic-chemistry approaches that track coherent excitations and polariton formation [182, 191, 192], and is instead tailored to overdamped, picosecond aggregation dynamics.

The cavity also contributes additional terms to the equations of motion for p_{z_i}, p_{θ_i}, p_{ϕ_i}, and p_{χ_i} through the derivatives of $\mathcal{L}_{\text{cav}}$ with respect to the corresponding coordinates. For completeness, the derivatives of the cavity field profile and the dipole projection are

$$\begin{aligned}
\frac{\partial E_{\text{x}}(x,y,z)}{\partial z} &= E_{\max} \exp\left(-\frac{z^2}{w_{\text{r}}^2} - \frac{x_h^2}{w_{\text{x}}^2}\right) \frac{-2z}{w_{\text{r}}^2}, \\
\frac{1}{d_0}\frac{\partial}{\partial\theta}(d_{\text{x}}) &= \cos(\theta+\alpha)\cos\phi\cos\chi + \cos\theta\cos\phi\cos\alpha(1-\cos\chi), \\
\frac{1}{d_0}\frac{\partial}{\partial\phi}(d_{\text{x}}) &= -\sin(\theta+\alpha)\sin\phi\cos\chi - \sin\alpha\sin\chi\cos\phi - \sin\theta\sin\phi\cos\alpha(1-\cos\chi), \\
\frac{1}{d_0}\frac{\partial}{\partial\chi}(d_{\text{x}}) &= -\sin(\theta+\alpha)\cos\phi\sin\chi - \sin\alpha\cos\chi\sin\phi + \sin\theta\cos\phi\sin\chi\cos\alpha.
\end{aligned}$$

Combining the free-space dynamics with the cavity-induced terms yields the full stochastic equations of motion inside the picocavity.

$$\dot{z}_i = \frac{p_{z_i}}{m}, \tag{10.41a}$$

$$\dot{\theta}_i = \frac{p_{\theta_i}}{I}, \tag{10.41b}$$

$$\dot{\phi}_i = \frac{p_{\phi_i}}{I \sin^2\theta_i}, \tag{10.41c}$$

$$\dot{\chi}_i = \frac{p_\chi}{I_\chi}, \tag{10.41d}$$

$$\begin{aligned}\dot{p}_{z_i} = &\sum_{i<j}^{N} \left\{ -\frac{6C_6}{(z_i - z_j)^7} \left[\sin\theta_i \sin\theta_j \cos(\phi_i - \phi_j) - 2\cos\theta_i \cos\theta_j\right]^2 + \frac{12C_{12}}{(z_i - z_j)^{13}} \right\} \\ &+ \eta_z(t) - \kappa_z(\theta)\dot{z}_i + \mathcal{Q}_{\text{eff}}\, \mathcal{E}_0(\mathbf{r}_i) \frac{-2z_i}{w_{\text{r}}^2}\, d_0 \Big(\sin(\theta_i + \alpha)\cos\phi_i \cos\chi_i \\ &- \sin\alpha \sin\chi_i \sin\phi_i + \sin\theta_i \cos\phi_i (1 - \cos\chi_i)\cos\alpha \Big),\end{aligned} \tag{10.41e}$$

$$\begin{aligned}\dot{p}_{\theta_i} = &I\dot{\phi}_i^2 \sin\theta_i \cos\theta_i + \sum_{i<j}^{N} \left\{ \frac{2C_6}{(z_i - z_j)^6} \left[\cos\theta_i \sin\theta_j \cos(\phi_i - \phi_j) + 2\sin\theta_i \cos\theta_j\right] \right. \\ &\left. \times \left[\sin\theta_i \sin\theta_j \cos(\phi_i - \phi_j) - 2\cos\theta_i \cos\theta_j\right] \right\} + \eta_\theta(t) - \kappa_\theta \dot{\theta}_i \\ &+ \mathcal{Q}_{\text{eff}}\, \mathcal{E}_0(\mathbf{r}_i)\, d_0 \Big(\cos(\theta_i + \alpha)\cos\phi_i \cos\chi_i + \cos\theta_i \cos\phi_i (1 - \cos\chi_i)\cos\alpha \Big),\end{aligned} \tag{10.41f}$$

$$\begin{aligned}\dot{p}_{\phi_i} = &-\sum_{i<j}^{N} \frac{2C_6}{(z_i - z_j)^6} \sin\theta_i \sin\theta_j \sin(\phi_i - \phi_j) \left[\sin\theta_i \sin\theta_j \cos(\phi_i - \phi_j) - 2\cos\theta_i \cos\theta_j\right] \\ &+ \eta_\phi(t) - \kappa_\phi \sin^2\theta_i\, \dot{\phi}_i + \mathcal{Q}_{\text{eff}}\, \mathcal{E}_0(\mathbf{r}_i)\, d_0 \Big(-\sin(\theta_i + \alpha)\sin\phi_i \cos\chi_i \\ &- \sin\alpha \sin\chi_i \cos\phi_i - \sin\theta_i \sin\phi_i (1 - \cos\chi_i)\cos\alpha \Big),\end{aligned} \tag{10.41g}$$

$$\begin{aligned}\dot{p_{\chi_i}} = &\eta_\chi(t) - \kappa_\chi \dot{\chi} + \mathcal{Q}_{\text{eff}}\, \mathcal{E}_0(\mathbf{r}_i)\, d_0 \Big(-\sin(\theta_i + \alpha)\cos\phi_i \sin\chi_i \\ &- \sin\alpha \cos\chi_i \sin\phi_i + \sin\theta_i \cos\phi_i \sin\chi_i \cos\alpha \Big),\end{aligned} \tag{10.41h}$$

with

$$\mathcal{E}_0(\mathbf{r}) = E_{\max} \exp\left(-\frac{z^2}{w_r^2} - \frac{x_h^2}{w_x^2} \right),$$

$$\mathcal{Q}_{\text{eff}} = \frac{E_{\max}}{\hbar\omega} \sum_{i=1}^{N} d_x(\theta_i, \phi_i, \chi_i)\, \exp\left(-\frac{z_i^2}{w_r^2} - \frac{x_h^2}{w_x^2} \right).$$

In the special case $\alpha = 0$, the equations simplify, χ decouples, and the interaction reduces to coupling between the cavity field and the projection of the molecular axis along the cavity polarization. The corresponding interaction potential for molecule i

becomes

$$V_{\mathrm{int}_i} = -d_0 \cos\phi_i \sin\theta_i E_{\max} \mathcal{Q} \times \exp\left(-\frac{z_i^2}{w_{\mathrm{r}}^2} - \frac{x_h^2}{w_{\mathrm{x}}^2}\right) \tag{10.42}$$

The resulting simplified equations retain the same structure as Eq. (10.18), with cavity-induced forces and torques added to the translational and rotational equations. This simplified limit is useful for assessing the relative role of confinement and dipole alignment in the aggregation dynamics.

The alignment of the transition dipole with the cavity field determines the strength of the coupling. In general, dipoles tend to orient along the local field direction because this minimizes the interaction energy. In a picocavity, where the field is highly anisotropic, only certain molecular orientations couple strongly to the mode. This orientation selectivity can modify the aggregate structure and is relevant for spectroscopic observables, including tip-enhanced Raman spectroscopy and single-molecule fluorescence, where field alignment plays an important role.

10.4 Numerical Results

10.4.1 Simulation Parameters for Experimentally Relevant Conditions

We choose simulation parameters to be broadly consistent with experimentally accessible molecular and picocavity scales. The Lennard-Jones (LJ) parameters are taken from representative molecular values of water [207], while the cavity parameters are selected to reflect strong but plausible confinement in plasmonic nanocavity platforms [206]. The goal is to explore the qualitative impact of confinement on aggregation dynamics within a controlled effective model.

To anchor the effective model in experimentally relevant ranges, Table 10.1 summarizes the main simulation parameters alongside representative molecular and cavity scales.

The intrinsic LJ timescale is set by the molecular mass, interaction depth, and length scale. For a particle of mass m interacting via a LJ potential with depth ε and length scale σ, a natural time unit is

$$\tau_{\mathrm{LJ}} = \sigma\sqrt{\frac{m}{\varepsilon}}. \tag{10.43}$$

Quantity	Simulation value	Representative experimental scale
LJ depth ε	$10 - 100$ meV	dispersion well depths for small organics
LJ length σ	$3 - 5$ Å	molecular diameters (e.g. water, benzene)
Intrinsic time τ_{LJ}	$0.4 - 2.2$ ps	vibrational / librational timescales
Transition dipole d_0	$1 - 2$ D	allowed electronic / vibrational transitions
Peak field $E_{\max}$	5×10^8 V/m	near-field in sub-nm plasmonic gaps
Interaction scale $d_0 E_{\max}$	$50 - 400$ meV	cavity-induced torque comparable to LJ depth

Table 10.1: Representative mapping between simulation parameters and experimental scales.

Using the representative values of σ and ε in Table 10.1, this yields characteristic times in the sub-picosecond to few-picosecond range [see Appendix 10.7.2].

Friction coefficients and Stokes scaling for cylindrical molecules

We include solvent effects phenomenologically through Langevin friction and noise, with effective translational and rotational friction coefficients chosen to be consistent with continuum Stokes hydrodynamics for rigid cylindrical rods of length L and radius a (aspect ratio $p = L/2a$). For a slender cylinder in a Newtonian fluid of viscosity η, the drag coefficients are [208]

$$\gamma_{\parallel} \simeq \frac{2\pi\eta L}{\ln p - 0.20}, \tag{10.44}$$

I	meV·ps^2	2.0
m	meV·Å^{-2} · ps^2	2.0
C_6	meV·Å^6	1.2×10^4
C_{12}	meV·Å^{12}	2.0×10^7
Energy unit	meV	1.602×10^{-22} J
Time unit	ps	10^{-12} s
Distance unit	Å	10^{-10} m

Table 10.2: Molecular parameters used for the numerical simulations.

$$\gamma_\perp \simeq \frac{4\pi\eta L}{\ln p + 0.84}, \tag{10.45}$$

$$\gamma_r^\perp \simeq \frac{\pi\eta L^3}{3(\ln p - 0.66)}. \tag{10.46}$$

Here $\gamma_\parallel$ and $\gamma_\perp$ denote translational friction coefficients parallel and perpendicular to the molecular axis, while $\gamma_r^\perp$ corresponds to rotational friction about axes perpendicular to the rod. Rotation about the molecular symmetry axis (χ) is associated with a smaller friction coefficient $\gamma_r^\parallel \sim \pi\eta a^2 L$.

Because translational motion is restricted to the cavity axis (z direction), the effective translational friction depends on the molecular orientation relative to this axis. We use the interpolating form

$$\gamma_z(\theta) = \gamma_\parallel \cos^2\theta + \gamma_\perp \sin^2\theta. \tag{10.47}$$

For the numerical work, we approximate this by fixing $\gamma_\perp/\gamma_\parallel = 9$, so that

$$\gamma_z = \bar{\gamma}_z \left(0.1\cos^2\theta + 0.9\sin^2\theta\right). \tag{10.48}$$

This approximation captures the expected orientational dependence of drag without materially affecting the qualitative behavior discussed below.

Within our Langevin formulation [Eqs. (10.12)–(10.14)], the dissipative coefficients are related to the damping rates by

$$\kappa_z = m\bar{\gamma}_z,$$
$$\kappa_\theta = I_\theta \gamma_\theta,$$

$$\kappa_\phi = I_\phi \gamma_\phi,$$
$$\kappa_\chi = I_\chi \gamma_\chi,$$

with κ_z measured in $\left[\text{meV} \cdot \text{Å}^{-2} \cdot \text{ps}\right]$ and $\kappa_{\theta,\phi,\chi}$ in $[\text{meV} \cdot \text{ps}]$. We identify the effective damping rates with hydrodynamic estimates as

$$\bar{\gamma}_z \approx \gamma_\parallel / m,$$
$$\gamma_\theta = \gamma_\phi \approx \gamma_r^\perp / I,$$
$$\gamma_\chi \approx \gamma_r^\parallel / I_\chi,$$

so that $\kappa_\chi \ll \kappa_\theta \approx \kappa_\phi$, reflecting the weaker resistance to rotation about the molecular axis.

For representative molecular dimensions $L \sim 1 - 2$ nm and $a \sim 0.2 - 0.3$ nm, together with a water-like viscosity $\eta \sim 10^{-3}\,\text{Pa}\,\text{s}$, the Stokes-Tirado relations yield friction coefficients of order [208]

$$\kappa_z \sim 500 - 700\,\text{meV}\,\text{Å}^{-2}\,\text{ps},$$
$$\kappa_\theta \sim \kappa_\phi \sim 600 - 800\,\text{meV}\,\text{ps}.$$

These values correspond to translational diffusion constants $D = k_B T/\gamma \sim 10^{-10} - 10^{-9}\,\text{m}^2\,\text{s}^{-1}$ at room temperature, which are representative of small organic molecules in liquid environments.

For cryogenic picocavities (5–100 K), continuum hydrodynamics is no longer reliable; dissipation then arises from weak environmental couplings such as phonons, residual gas, and cavity-modified radiative damping [209]. In this regime, the friction coefficients are treated as effective phenomenological parameters, with noise amplitudes fixed by the fluctuation-dissipation relation at temperature T. The same damping parameters are used in the free-space and cavity calculations for consistency.

To model this low-temperature regime, we use representative friction values

$$\kappa_z = 200 - 400\ \text{meV}\,\text{Å}^{-2}\,\text{ps},$$
$$\kappa_\theta = \kappa_\phi = 500 - 1500\ \text{meV}\,\text{ps},$$
$$\kappa_\chi = 100 - 200\ \text{meV}\,\text{ps},$$

where the smaller value of κ_χ reflects weaker environmental coupling for rotation about

the molecular axis. These parameters are chosen to place the system in a strongly damped regime while keeping the dynamics numerically stable and comparable in scale to the intermolecular interaction energies in Table 10.2.

The associated momentum relaxation times are

$$\tau_{\text{trans}} = \frac{m}{\kappa_z} \sim 0.005 - 0.01 \text{ ps},$$
$$\tau_{\text{rot}} = \frac{I}{\kappa_\theta} \sim 0.001 - 0.004 \text{ ps},$$
$$\tau_\chi = \frac{I_\chi}{\kappa_\chi} \sim 0.01 \text{ ps}.$$

These times are much shorter than the intrinsic LJ timescale τ_{LJ}, indicating that momentum relaxes rapidly and that aggregation proceeds in a strongly damped regime dominated by conservative forces and thermal fluctuations [see Appendix 10.7.2]. For comparison, typical nanoplasmonic picocavities operate at optical frequencies $\omega_c \sim 10^{15}$ s^{-1}, corresponding to sub-femtosecond oscillation periods and cavity damping times that are orders of magnitude shorter than both τ_{LJ} and the picosecond-scale configurational relaxation times considered here, so that the cavity mode remains the fastest degree of freedom in the problem.

The corresponding translational diffusion coefficients are

$$D = \frac{k_B T}{\kappa_z} \sim 5 \times 10^{-12} - 5 \times 10^{-10} \,\text{m}^2\,\text{s}^{-1}$$

for $T = 5 - 100$ K. These values are consistent with slow nanoscale transport and support the use of a strongly damped Langevin description. Exploring underdamped or more weakly damped regimes, in which inertial effects and oscillatory relaxation become important, would be a natural extension of this work but lies beyond the strongly overdamped aggregation dynamics considered here.

Picocavity parameters and light-matter coupling

To investigate the role of electromagnetic confinement, we consider a linearly polarized cavity field along the x axis. Molecular centers are fixed at $x = x_h$ and $y = 0$, so that

κ_z	meV·Å^{-2} · ps	200
κ_θ	meV·ps	500
κ_ϕ	meV·ps	500
κ_χ	meV·ps	100

Table 10.3: Parameters used for the numerical simulations.

only the x component of the molecular dipole couples to the cavity field,

$$V_{\text{int}} = -d_x\, E_{\max} \exp\left[-\frac{z^2}{w_r^2} - \frac{x_h^2}{w_x^2}\right] \mathcal{Q}(t),$$

where $d_x = \mathbf{d} \cdot \hat{x} = n_x^{\mathbf{d}} d_0$ and $\mathcal{Q}(t)$ is the cavity mode coordinate.

We characterize the cavity by three parameters: the peak field amplitude $E_{\max}$, the transverse confinement length w_r, and the longitudinal confinement length w_x. At fixed $E_{\max}$, decreasing w_r drives the field from a weakly varying background toward a strongly localized picocavity profile.

For representative molecules, we take $d_0 \sim 2.0$ Åe (approximately 1 Debye), so that $d_0 E_{\max}$ sets the scale of the cavity-induced interaction. To obtain a meaningful competition between cavity alignment and intermolecular interactions, this scale should be comparable to the LJ depth while remaining below the regime in which the cavity force trivially dominates the molecular dynamics. Experiments on plasmonic picocavities have reported transverse near-field strengths approaching 1.9×10^9 V/m in sub-nanometer gaps [210], and theoretical studies of picocavity field profiles emphasize confinement below 1 nm^3 [211]. The representative values $E_{\max} \sim 5 \times 10^8$ V/m and $w_r, w_x \sim$ a few ångströms used here correspond to such strongly confined gaps and yield interaction scales $d_0 E_{\max} \sim 50 - 400$ meV, i.e., torques comparable to the LJ energy scale that should be observable through polarization- and orientation-sensitive spectroscopies rather than as a purely perturbative effect.

10.4.2 Discussion

The numerical simulations are initialized from random positions and orientations, with random number seeds fixed to facilitate reproducibility and direct comparison between

parameter regimes. At $T = 0$ K, all molecules start from rest and the dynamics are driven entirely by deterministic forces. At $T > 0$ K, initial velocities are sampled from a Maxwell-Boltzmann distribution,

$$P(v) = \sqrt{\frac{m}{2\pi k_{\mathrm{B}} T}} \exp\left(-\frac{m v^2}{2 k_{\mathrm{B}} T}\right), \tag{10.49}$$

with zero mean and variance $k_B T/m$.

To keep the discussion focused on aggregation rather than collision-dominated transport, we primarily consider low temperatures. In this regime, molecular motion remains close to local potential minima and the trajectories probe relaxation within the interaction landscape rather than high-energy collision processes. At higher temperatures, additional thermally activated rearrangements can occur, but these lie beyond the regime emphasized in the present work.

Unless otherwise stated, all simulations were performed using the numerical parameters listed in Table 10.2 and 10.3. In all stochastic realizations, the molecules were initially placed at random positions along the z-axis, and their initial velocities were randomly sampled from the distribution corresponding to the specified temperature.

Details of the numerical integration scheme and convergence tests are provided in Appendix 10.7.3.

10.4.3 Aggregation in Free Space

We first analyze molecular dynamics in free space, where motion is governed by the LJ interaction, dissipation, and thermal fluctuations. The interaction potential depends on both intermolecular separation and relative dipole orientation, and equilibrium configurations correspond to minima of the effective potential.

Figure 10.3 shows that, in free space, an initially disordered chain of nonpolar molecules rapidly relaxes into a compact, head-to-tail aggregate at the LJ minimum, with orientational alignment along the chain axis. As illustrated in Fig. 10.3(a), four representative relative orientations can be identified: head-to-tail (i), head-to-head (ii), and side-by-side parallel (iii) or anti-parallel (iv); in the parameter regime studied here, the dynamics relax toward the global minimum (i)/(ii), while side-by-side configurations remain energetically disfavored and are not populated in the low-temperature trajectories.

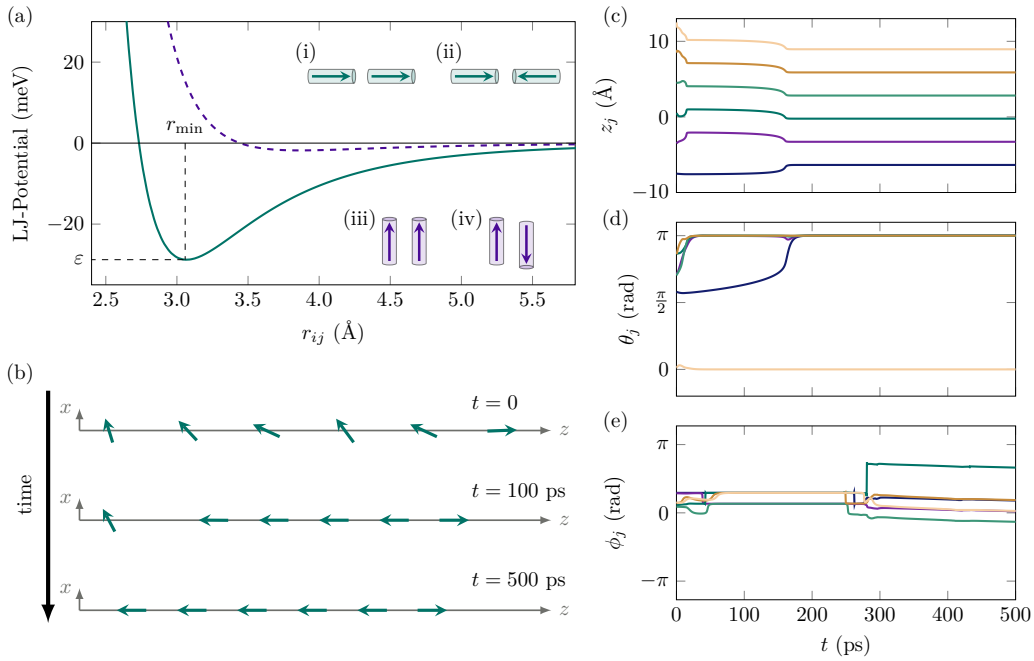

Figure 10.3: *Free-space aggregation of an $N = 6$ molecular chain.* (a) Lennard-Jones potential [Eq. (10.3)] for two dipoles in representative orientations: (i) $\theta_i = \theta_j = 0$ and (ii) $\theta_i = 0$, $\theta_j = \pi$ (solid green curve), and (iii) $\theta_i = \theta_j = \pi/2$ and (iv) $\theta_i = \pi/2$, $\theta_j = -\pi/2$ (dashed purple curve). After relaxation, the dipoles predominantly adopt configurations (i) and (ii), corresponding to $\varepsilon = -28.79$ meV and $r_{\min} = 3.058$ Å. (b) Representative aggregate of $N = 6$ molecules, showing dipole orientations and molecular positions at $t = 0$, 100, and 500 ps. (c) Representative molecular trajectories z_i as a function of time for molecules initially randomly placed along the z-axis, with zero velocity and $T = 0$. (d) Time evolution of the polar angles θ_j and (e) the azimuthal angles ϕ_j. Unless otherwise stated, all simulations were performed using the numerical parameters listed in Table 10.2 and 10.3.

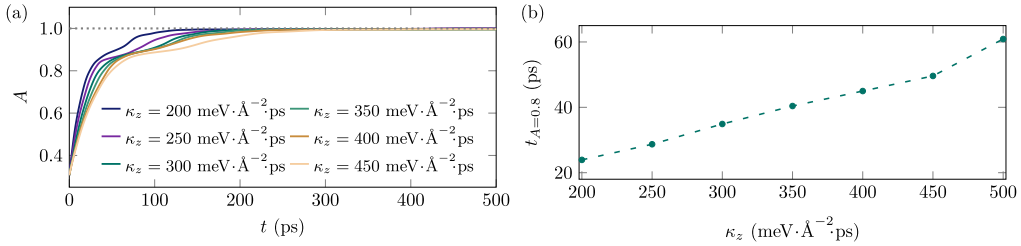

Figure 10.4: *Effect of solvent viscosity on orientational dynamics.* (a) Time evolution of the orientational order parameter A during aggregation for different values of κ_z in a system of $N = 6$ molecules. The rotational friction coefficients κ_θ and κ_ϕ were varied proportionally so that the ratios listed in Table 10.3 were maintained. (b) Time required to reach $A = 0.8$ as a function of κ_z. Results averaged over 11 independent random seeds.

At zero temperature, the final molecular orientation is determined by the initial polar angle: if $\theta_{\text{initial}} < \pi/2$, the molecule relaxes to $\theta_{\text{final}} \to 0$; if $\theta_{\text{initial}} > \pi/2$, $\theta_{\text{final}} \to \pi$. Once a molecule aligns along the z axis, the azimuthal angle becomes irrelevant. Figure 10.3(b)-(e) shows representative trajectories for $N = 6$ molecules, relaxing into a stable one-dimensional chain with mean separation [$\langle r_{ij} \rangle = 3.06$ Å] close to the LJ minimum.

To quantify orientational ordering, we monitor the alignment parameter

$$A(t) = \frac{3\langle \cos^2 \theta(t) \rangle - 1}{2}. \tag{10.50}$$

The quantity $A(t)$ approaches unity for strong alignment along the chain axis. Because the dynamics are stochastic, $A(t)$ generally fluctuates below the ideal limit. In the following, values $A \gtrsim 0.8$ indicate strong alignment, while $A \gtrsim 0.9$ corresponds to near-perfect ordering in the sense of this model.

The solvent viscosity controls the rate at which the system relaxes. Larger friction suppresses translational motion and increases the time needed to reach the steady state, whereas lower friction allows faster rearrangement. Figure 10.4 demonstrates that increasing translational friction slows aggregation: weak damping accelerates relaxation relative to the nearly conservative limit, while sufficiently large damping leads to slow, transport-limited aggregation and an optimal intermediate damping that minimizes the time required to reach a given orientational order.

Temperature plays a dual role: it increases mobility but also enhances fluctuations

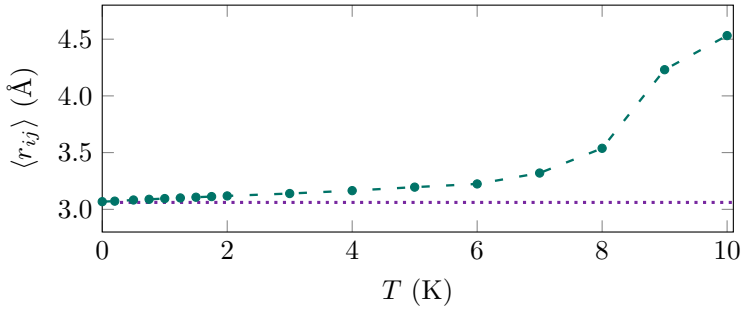

Figure 10.5: *Average intermolecular distance $\langle r_{ij} \rangle$ as a function of temperature T in a system of $N = 6$ molecules.* The dashed line marks the LJ equilibrium separation $r_{\min} = 3.06$ Å. The reported values correspond to time averages over the final stable aggregate. Results averaged over 7 independent random seeds, where aggregation to a single cluster is obtained.

that destabilize the ordered aggregate. At low temperatures, aggregates are more compact and more stable; as temperature increases, the mean intermolecular spacing grows and orientational order decreases, reflecting the competition between energetic stabilization and thermal agitation. Figure 10.5 shows that higher temperature leads to more expanded aggregates, with mean intermolecular distances increasing above the LJ minimum as thermal fluctuations compete with dispersion. Figure 10.6 reveals that orientational order is maximal at low temperature and degrades as T increases, with an intermediate range where thermal motion initially facilitates alignment (shortening the time to reach $A = 0.8$) before ultimately hindering sustained ordering once fluctuations become too strong.

Analysis of Cluster Alignment and Aggregation Dynamics

To examine multi-cluster dynamics, we next consider two initially separated molecular clusters [see Fig. 10.7, where $d > r_{\min}$]. The evolution proceeds in two stages: rapid intra-cluster reorientation followed by slower inter-cluster recombination. The first stage reflects local relaxation within each cluster and occurs on a timescale of order 100 ps. The second stage depends more strongly on the initial separation and relative orientation of the clusters and may lead either to coalescence into a single aggregate or to long-lived metastable multi-cluster configurations.

This separation of timescales is represented in Fig. 10.7. For favorable initial configurations, the ordered clusters attract each other and merge into a larger aggregate;

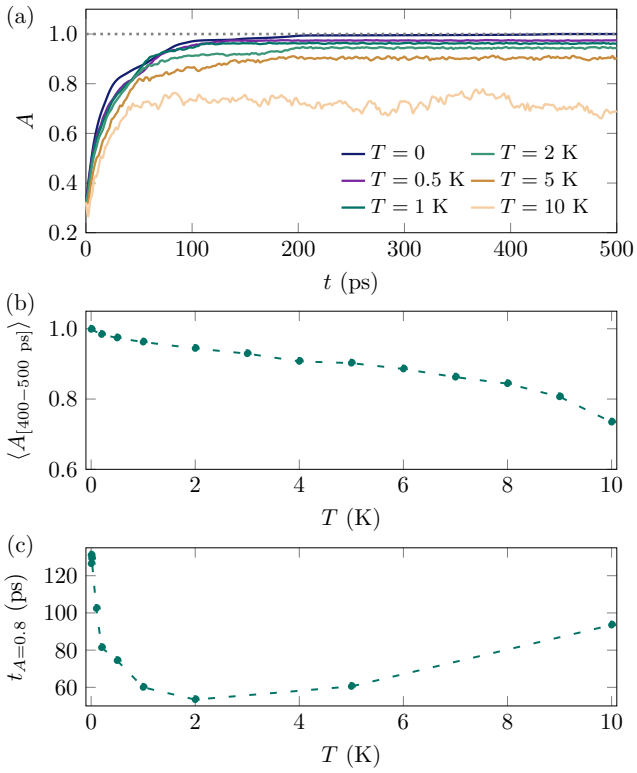

Figure 10.6: *Effects of temperature on orientational dynamics.* (a) Time evolution of the order parameter A for different temperatures in a system of $N = 6$ molecules. (b) Time-averaged A over the interval 400-500 ps, as a function of temperature. Results in (a) and (b) are averaged over 11 independent random seeds. (c) Time required to reach $A = 0.8$ as a function of temperature. In (c), we set a single seed where simulations started from the same initial molecular positions and orientations, while the initial velocities were randomly assigned according to the specified temperature.

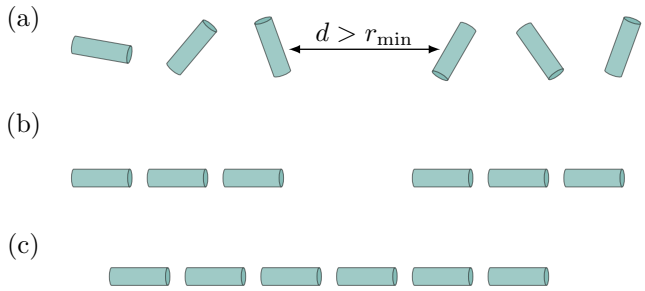

Figure 10.7: *Schematic aggregation dynamics for two molecular clusters initially separated by a distance $d > r_{\min}$.* (a) Initial state. (b) Rapid intra-cluster alignment. (c) Slower cluster recombination into a single aggregate.

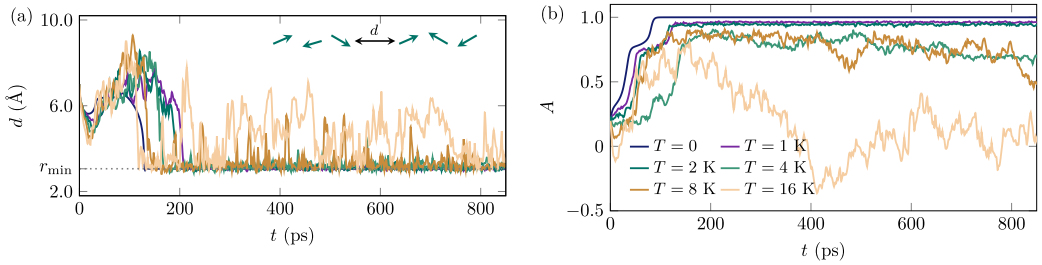

Figure 10.8: *Temperature dependence of the aggregation dynamics* for an $N = 6$ molecular system initially arranged as two three-molecule clusters, where the initial intercluster separation satisfied $d \equiv r_4 - r_3 \gg r_{\text{av}}$. (a) Intercluster separation d as a function of time for different temperatures. (b) Orientational order parameter A during aggregation.

for less favorable configurations, recombination is delayed and the system remains trapped in a metastable state over the observation window.

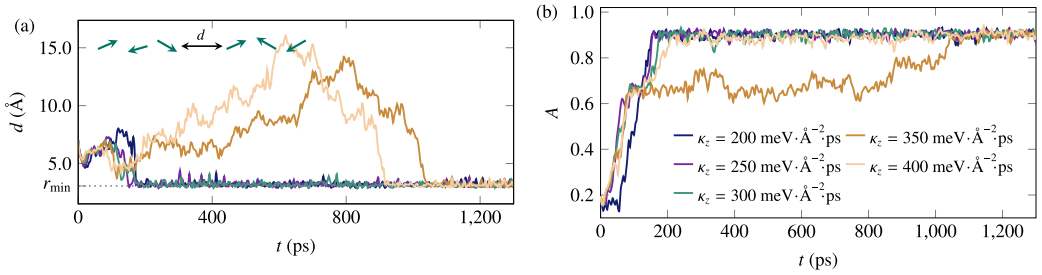

Figure 10.9: *Effect of solvent viscosity on cluster aggregation dynamics* at $T = 5$ K in a system of $N = 6$ molecules initially arranged as two separated three-molecule clusters, where the initial intercluster separation satisfied $d \equiv r_4 - r_3 \gg r_{\text{av}}$. Results are shown for different values of the translational friction coefficient κ_z. The rotational friction coefficients κ_θ and κ_ϕ were varied proportionally so that the ratios listed in Table 10.3 were maintained. (a) Intercluster separation d as a function of time. (b) Orientational order parameter A during aggregation.

Figure 10.8 illustrates this two-stage aggregation process as a function of temperature: fast intra-cluster ordering is present across the range considered, while higher temperatures prolong the recombination time and weaken sustained cluster-cluster attraction. Figure 10.9 shows that increasing viscosity similarly slows cluster recombination while leaving the rapid intra-cluster ordering largely intact. Larger friction increases the recombination time, whereas lower friction allows faster translational motion and shorter

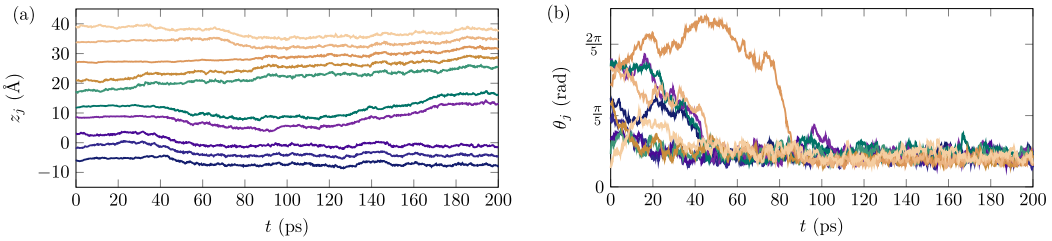

Figure 10.10: *Aggregation dynamics of an $N = 10$ molecular system at $T = 5$ K with random initial intermolecular separations.* The initial positions satisfy $r_{ij} > r_{\min}$. (a) Time evolution of intermolecular distances z_i, showing rapid formation of multiple clusters followed by long-lived metastable configurations. (b) Time evolution of the polar angle $\theta_j(t)$.

recombination times; at sufficiently low viscosity, rotational motion becomes underdamped and the orientational order parameter exhibits oscillatory relaxation. These results show that solvent-mediated dissipation controls both orientational relaxation and aggregation kinetics in the free-space case.

Finally, Fig. 10.10 highlights that, for $N = 10$, the system quickly forms multiple clusters that persist for long times before merging. The early-time dynamics are dominated by rapid local ordering, while the late-time evolution reflects slower motion between clusters, consistent with a rugged free-energy landscape containing multiple shallow minima separated by barriers.

10.4.4 Aggregation Under Cavity Confinement

We now turn to the effect of cavity confinement on aggregation. Unless stated otherwise, the cavity calculations are performed at $T = 0$ K with $N = 10$ molecules [system with $L_{\text{chain}} \approx 30$ Å]. In this regime, the cavity field introduces additional position-dependent forces and torques through the coupling of the molecular transition dipoles to the local electric field. Figure 10.11 illustrates how an inhomogeneous cavity field restructures both positions and orientations, generating spatially heterogeneous aggregates in which molecules in high-field regions align more strongly with the cavity polarization.

To characterize the orientational dynamics, we monitor two order parameters. The first is the time-dependent alignment parameter defined in Eq. (10.50) which measures alignment of the molecular axes with the van der Waals (chain) axis and approaches

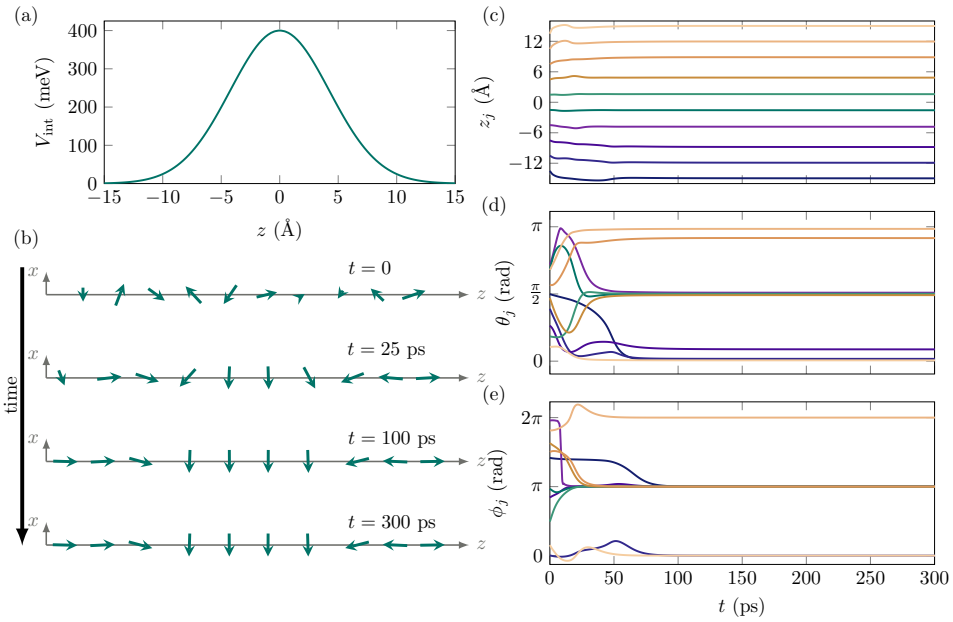

Figure 10.11: (a) Cavity potential V_{int} for $d_0 E_{\max} = 400$ meV, with $w_r = 6$ Å. (b) Representative molecular configuration in a system containing $N = 10$ molecules at $t = 0$, 25, 100, 500 ps for $T = 0$. (c) Representative molecular trajectories z_i. (d) Time evolution of the polar angles θ_j. (e) Time evolution of the azimuthal angles ϕ_j.

unity for strong alignment. The second is the steady-state van der Waals-induced orientational order parameter

$$S_{\text{vdW}} = \frac{1}{N} \sum_{N} \langle |\hat{\boldsymbol{\mu}}_j \cdot \hat{e}_{\text{vdW}}| \rangle = \frac{1}{N} \sum_{N} \langle |\cos \theta_j| \rangle \tag{10.51}$$

where $\hat{\boldsymbol{\mu}}_j$ is the unit vector along the molecular axis of molecule j, $\hat{\mathbf{e}}_{\text{vdW}}$ is the z-axis direction, and θ_j is the angle between these two vectors. Here, $S_{\text{vdW}} \approx 1$ indicates an LJ-dominated state with alignment along the chain axis, $S_{\text{vdW}} \approx 0$ corresponds to a cavity-dominated state with dipoles aligned predominantly along the cavity polarization, and intermediate values signal frustrated, partially ordered configurations.

Both quantities have direct experimental analogues. The buildup or loss of $A(t)$ would manifest as changes in polarization-resolved line shapes and dichroic signals in ultrafast pump-probe or single-molecule fluorescence measurements, while S_{vdW} is related to the distribution of molecular orientations and can in principle be inferred

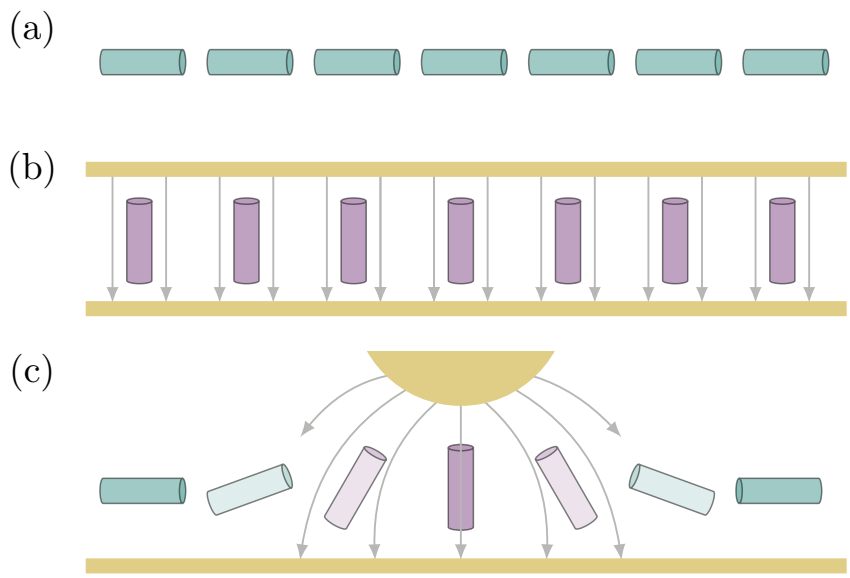

Figure 10.12: *Schematic of molecular dipole orientations under different electromagnetic confinement conditions.* (a) In the absence of cavity confinement, orientations are governed by intermolecular LJ interactions. (b) In a uniform cavity field, dipoles tend to align along the field polarization direction. (c) In an anisotropic cavity, position-dependent field gradients produce spatially dependent orientations.

from polarization-dependent tip-enhanced Raman spectra or other orientation-sensitive probes in picocavities. In the following, we use $A(t)$ to characterize alignment kinetics and S_{vdW} to distinguish LJ-dominated, cavity-dominated, and frustrated partially ordered steady states.

Aligned dipoles $\alpha = 0$

We first consider the simplest case in which the dipole responsible for van der Waals interactions is aligned with the transition dipole that couples to the cavity field ($\alpha = 0$). Figure 10.12 summarizes the three relevant confinement regimes: no cavity, a uniform cavity field, and an anisotropic cavity field.

In the uniform-field case, the cavity induces a collective reorientation of the dipoles as the coupling strength is increased. Figure 10.13 shows a crossover of the steady-state order parameter S^{ss}_{vdW} from values near unity in the LJ-dominated regime to values close to zero in the cavity-dominated regime as $d_0 E_{\max}$ increases. This behavior reflects

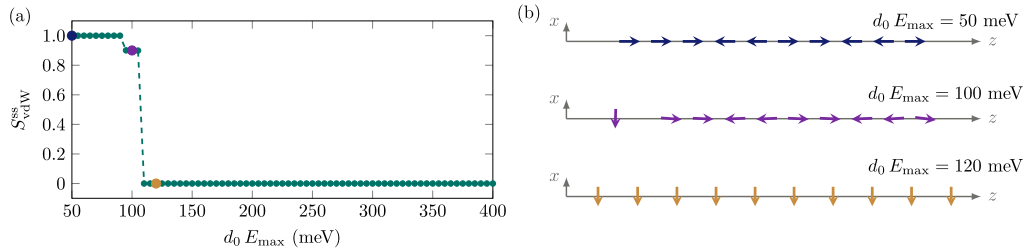

Figure 10.13: *Collective dipole alignment in a uniform cavity field for an ensemble of $N = 10$ molecules prepared in an aligned-dipole configuration ($\alpha = 0$) at $T = 0$.* (a) Steady-state orientational order parameter S^{ss}_{vdW} as a function of the cavity-coupling strength d_0E_{max}. (b) Representative steady-state molecular orientations for $d_0E_{max} = 50$, 100, and 120 meV.

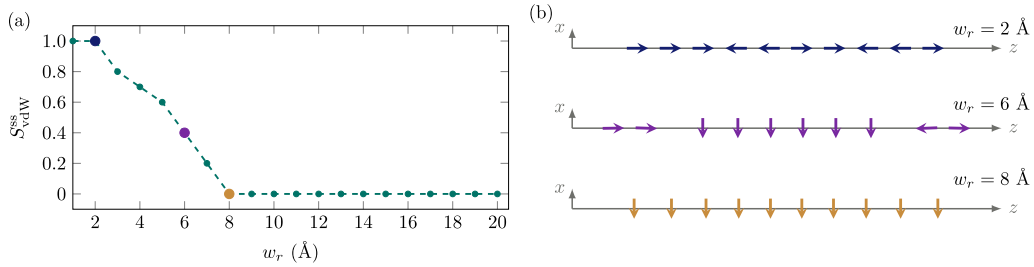

Figure 10.14: *Collective dipole alignment in an anisotropic cavity field for an ensemble of $N = 10$ molecules initially prepared in an aligned-dipole configuration ($\alpha = 0$) at $T = 0$.* (a) Steady-state orientational order parameter S^{ss}_{vdW} as a function of transverse confinement length w_r where we fixed $d_0E_{max} = 500$ meV. (b) Representative steady-state molecular orientations for $w_r = 2$, 6, and 8 meV.

a transition from chain-aligned ordering along the aggregation axis to alignment along the cavity polarization axis.

The same trend can be characterized in terms of confinement length. Figure 10.14 demonstrates that tightening the transverse confinement w_r enhances cavity control over orientation, driving a similar crossover even at fixed coupling strength. In this case S^{ss}_{vdW} decreases smoothly with decreasing w_r, showing no sharp threshold-like collective reorientation; both stronger coupling and stronger spatial confinement favor alignment with the cavity field.

In an anisotropic field, the cavity intensity varies across the mode volume, so the torque acting on each molecule depends on its position. As a result, the aggregate

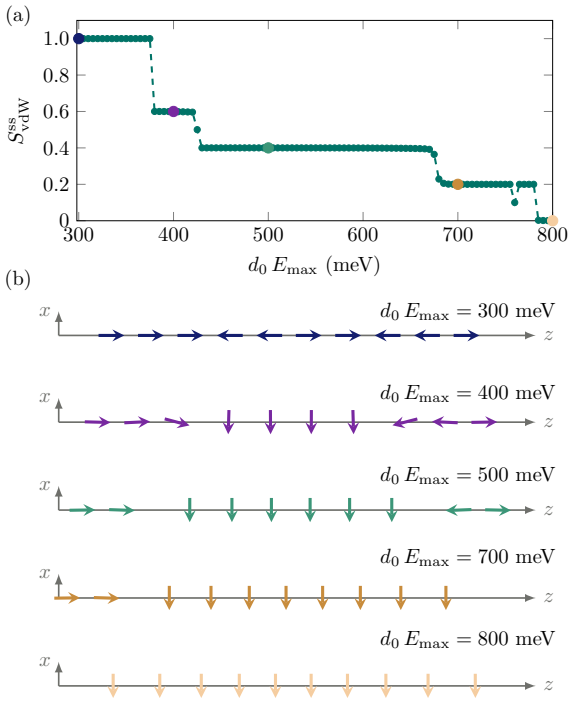

Figure 10.15: *Collective dipole alignment in an anisotropic cavity field for an ensemble of $N = 10$ molecules initially prepared in an aligned-dipole configuration ($\alpha = 0$) at $T = 0$.* (a) Steady-state orientational order parameter $S^{\mathrm{ss}}_{\mathrm{vdW}}$ as a function of the cavity-coupling strength $d_0 E_{\mathrm{max}}$ for a transverse confinement length $w_r = 6$ Å. (b) Representative steady-state molecular orientations for $d_0 E_{\mathrm{max}} = 300$, 400, 500, 700, and 800 meV.

becomes spatially heterogeneous: molecules in regions of stronger field align more strongly with the cavity polarization, whereas those in weaker-field regions retain a more van der Waals-like orientation. Figure 10.15 shows that in such an anisotropic cavity, increasing $d_0 E_{\mathrm{max}}$ induces a sequence of threshold-like reorientation events, with coexisting LJ- and cavity-aligned regions; a series of abrupt reductions in S^{ss}_{vdW} marks these collective reorientation transitions.

Misaligned dipoles $\alpha \neq 0$

We now turn to the more general case in which the van der Waals dipole $\boldsymbol{\mu}$ and the cavity-coupled transition dipole $\mathbf{d}$ are misaligned by a fixed angle $\alpha \neq 0$. Figure 10.16 demonstrates that misalignment between the dispersion and cavity dipoles frustrates

cavity-induced ordering and stabilizes partially aligned steady states over a broad parameter range. For small misalignment angles, the cavity-induced behavior remains qualitatively similar to the aligned case. As α increases, however, the competition between cavity-induced torques and intermolecular ordering becomes stronger, and larger fields are required to obtain comparable reorientation. Beyond a critical misalignment, the system no longer reaches a fully cavity-aligned state in the parameter range considered, and partially aligned configurations persist. This trend is visible both as a function of coupling strength and as a function of confinement length. In the anisotropic case, the effect of misalignment is more pronounced, since field gradients amplify the position dependence of the torque, and the resulting steady states often contain coexisting cavity-dominated and van der Waals-dominated regions. At $T = 0$ K, the frustrated configurations we observe are long-lived steady states of the overdamped dynamics rather than short-lived transients: once formed, they persist over the full simulation window without further large-scale rearrangements. At finite temperature (not shown here), noise leads to slow fluctuations around these configurations, so the reported values of $S^{\mathrm{ss}}_{\mathrm{vdW}}$ should be interpreted as averages over an ensemble of noise realizations rather than strictly single-trajectory fixed points.

Overall, the cavity results show that electromagnetic confinement can modify aggregation pathways and steady-state orientations in a manner that depends sensitively on field strength, spatial confinement, and dipole misalignment. Within the model studied here, uniform cavities favor smooth, global reorientation, while anisotropic fields generate spatially inhomogeneous aggregates. The main effect of misalignment is to reduce the efficiency of cavity-induced alignment and to promote frustrated or partially aligned states. These results provide a model-based description of how picocavity confinement can influence the aggregation of nonpolar molecules and identify the parameters that control the crossover between van der Waals-dominated and cavity-dominated behavior.

10.5 Experimental Feasibility and Potential Applications

The aggregation behavior predicted in this work arises from the interplay between van der Waals interactions, thermal fluctuations, dissipation, and cavity-mediated electromagnetic confinement. While direct observation of nonpolar molecular aggregation in picocavities remains experimentally challenging, several platforms may provide access to the relevant physics, either through plasmonic nanocavities or through analog

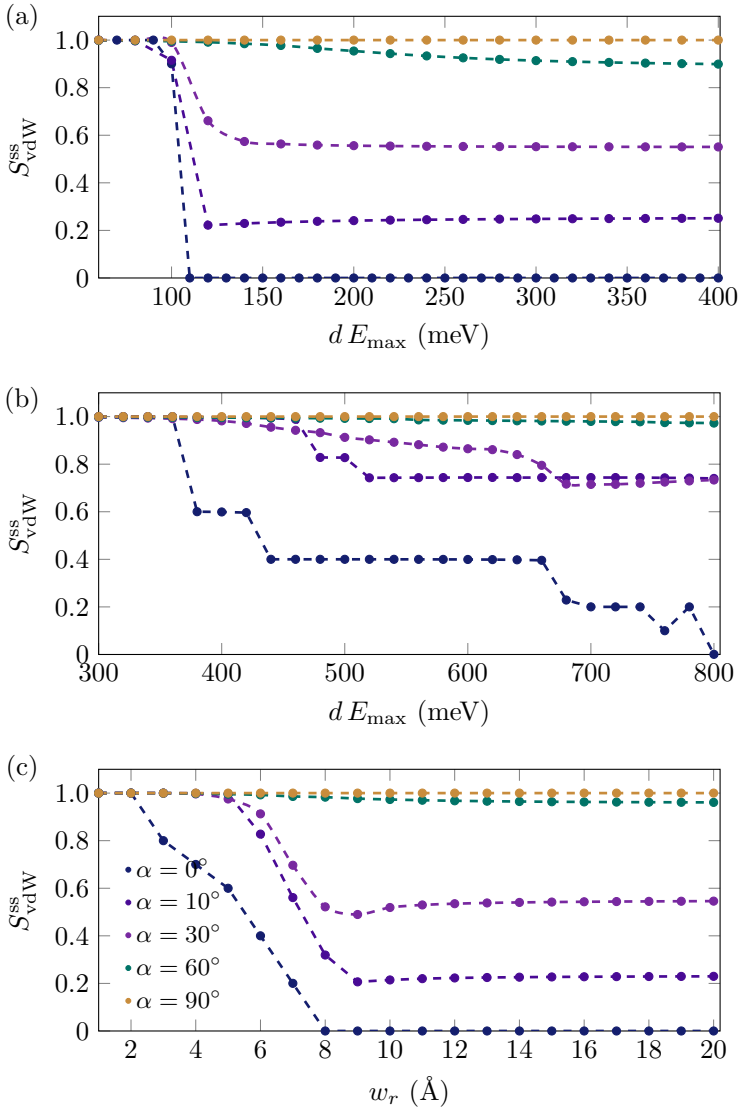

Figure 10.16: *Steady-state van der Waals-induced orientational order parameter* S^{ss}_{vdW} *of an ensemble of* $N = 10$ *molecules, at* $T = 0$ *K, prepared in different misaligned-dipole configurations* α. Results are shown for (a) an isotropic cavity as a function of cavity coupling, (b) an anisotropic cavity with fixed transverse confinement $w_r = 6$Å, and (c) as a function of w_r for fixed $d_0 E_{\mathrm{max}} = 500$ meV.

quantum-simulation systems.

10.5.1 Nanocavity Platforms

Plasmonic picocavities, formed, for example, between metallic tips and planar substrates or in nanoparticle junctions, can confine electromagnetic fields to sub-nanometer volumes with large local field enhancements [191,206]. Among the platforms considered here, such nanocavities most directly realize the conditions assumed in our model: strong subnanometer confinement, large field gradients, and coupling of nonpolar molecules to localized transition dipoles. For sufficiently strong and spatially varying confinement, the resulting field gradients may bias molecular orientations and modify the effective aggregation landscape in a manner consistent with the trends discussed in Sec. 10.4.

Potential observables include changes in vibrational or electronic spectroscopy, polarization-dependent response, and shifts in the distribution of molecular orientations. Time-resolved optical methods, including ultrafast pump-probe spectroscopy [212, 213] and tip-enhanced Raman spectroscopy [214, 215], can in principle probe such effects on femtosecond to picosecond timescales by monitoring polarization-resolved line shapes and intensity fluctuations. At present, their main value is in constraining the parameter regime in which cavity-modified aggregation could be observed, rather than in providing a direct measurement of the full many-body dynamics.

In the language of our model, experimental signatures would appear as changes in the orientational order parameters $A(t)$ and $S_{\mathrm{vdW}}^{\mathrm{ss}}$, inferred from polarization-resolved TERS, single-molecule fluorescence, or pump-probe measurements.

10.5.2 Ultracold Atomic and Molecular Analogs

A complementary route is offered by quantum simulation with ultracold atoms or molecules trapped in optical lattices, tweezer arrays, or related geometries [216, 217]. These systems allow the interaction strength, confinement geometry, and dissipation to be tuned with high precision, making them useful analogs of the effective aggregation problem considered here. In particular, ultracold polar molecules such as NaCs, RbCs, and CaF [218–221] or Rydberg-dressed atoms [222] provide controllable long-range interactions that can mimic aspects of the effective intermolecular forces in our model, albeit with a different microscopic origin (electrostatic dipole-dipole or Rydberg van

der Waals interactions rather than dispersion).

In these platforms, time-of-flight imaging, fluorescence microscopy, or state-resolved spectroscopy can be used to track clustering, orientational ordering, or rearrangement dynamics [223,224]. Although they are not literal realizations of picocavity aggregation, such analog systems offer a controlled setting in which to explore how tunable long-range interactions and confinement can give rise to clustering and ordering phenomena analogous to those captured by our effective model.

10.5.3 Transition Dipole Orientations in nonpolar Molecules

Even in molecules without permanent dipole moments, optical transitions are associated with well-defined transition dipole moments determined by molecular symmetry and selection rules. In symmetric molecules such as homonuclear diatomics or aromatic species, the permanent dipole vanishes while the transition dipole orientation remains fixed by the character of the relevant electronic or vibrational transition. For example, in benzene, the $\pi \rightarrow \pi^*$ transition of E_{1u} symmetry produces a transition dipole predominantly in the molecular plane, whereas in naphthalene different transitions can be oriented along distinct molecular axes [225–227].

This orientation dependence is relevant because cavity coupling depends on the projection of the transition dipole onto the local field polarization. In a strongly confined picocavity, spatially varying fields may therefore select particular molecular orientations and influence which configurations are most strongly coupled. Within the model studied here, such symmetry-determined transition dipoles provide concrete realizations of the misalignment angle α and suggest specific transitions and polarization geometries for which cavity-modified aggregation effects could be most pronounced in polarization-sensitive spectroscopic measurements.

10.5.4 Applications

The trends identified here suggest several possible directions in which cavity-modified aggregation could be relevant. In nanocatalysis, field-induced reorientation may influence the accessibility and dwell times of reactive configurations in confined environments. In molecular optomechanics and nanophotonics, the collective motion of molecular assemblies coupled to confined modes could underpin field-responsive, reconfigurable materials based on spatially ordered aggregates. In all such scenarios,

the most immediate signatures are expected in polarization- and orientation-sensitive spectroscopies, which probe changes in local order and clustering rather than directly imaging individual trajectories.

Overall, the framework developed here provides a basis for assessing how confinement, dissipation, and dipole orientation can influence molecular aggregation. The most immediate experimental relevance is likely to come from spectroscopic signatures of reorientation and clustering rather than direct imaging of the full many-body dynamics, although analogue platforms may help to benchmark the underlying mechanisms in a more controlled setting.

10.6 Conclusions

In this work, we developed a minimal effective framework for the aggregation dynamics of nonpolar molecules under simultaneous geometric and electromagnetic confinement. The model combines anisotropic Lennard-Jones interactions, Langevin dissipation, and cavity-induced coupling to molecular transition dipoles, allowing a direct comparison between free-space aggregation and picocavity-modified behavior within a single setting.

Within the free-space model, aggregation is governed by the competition between attractive dispersion forces, thermal fluctuations, and viscous damping. Our simulations clarify how, in the strongly damped regime, configurational relaxation dominates over inertial effects: increasing friction slows aggregation despite rapid momentum relaxation, while increasing temperature both enhances mobility and destabilizes orientational order, leading to larger mean intermolecular separations.

When cavity coupling is included, the structured electromagnetic field reshapes the effective interaction landscape and alters both the spatial organization and orientational ordering of the molecules. The cavity field biases aggregates toward field-aligned configurations, and the steady states depend sensitively on coupling strength, confinement length, and the relative orientation of the dispersion-induced and cavity-coupled dipoles. For aligned dipoles, we find a crossover from Lennard-Jones-dominated chain alignment to cavity-dominated, field-aligned structures. For misaligned dipoles, the competition between van der Waals and cavity-induced torques leads instead to frustrated, partially ordered configurations that have no analogue in standard LJ+Langevin aggregation; in our overdamped, low-temperature regime these appear

as long-lived steady states (or noise-averaged steady states), not as transient artifacts.

Taken together, our results highlight three main physical trends. First, strong electromagnetic confinement and controlled dipole misalignment generate frustrated, partially ordered steady states, extending conventional LJ-based aggregation models to regimes where cavity-induced torques and van der Waals forces compete on comparable footing. Second, the dynamics exhibit a clear separation between rapid intra-cluster ordering and slower inter-cluster recombination in the strongly overdamped regime, providing a concrete characterization of aggregation pathways in terms of distinct configurational timescales. Third, the steady-state van der Waals-induced orientational order parameter S_{vdW} is highly sensitive to cavity strength, confinement length, and dipole misalignment, offering a direct bridge between the effective model and polarization- and orientation-sensitive observables in nanophotonic experiments.

In contrast to most cavity-QED and polaritonic-chemistry studies, which focus on coherent excitations, polariton formation, or modifications of reaction barriers, the present work addresses how picocavity fields modify slow, overdamped aggregation and orientational relaxation through configuration-dependent mean forces. Likewise, while SERS and picocavity experiments have established single-molecule sensitivity and field localization, our results provide a concrete, dynamical picture of how such confined fields can reorganize nonpolar aggregates and generate frustrated steady states. Within this scope, the most direct experimental signatures of the predicted behavior are expected in changes to orientational order, clustering, and polarization-dependent spectroscopic response rather than in direct imaging of individual trajectories.

The framework developed here is intentionally minimal: it treats molecules as classical rigid rotors interacting via effective anisotropic Lennard-Jones potentials and coupled to a semiclassical cavity mode that is adiabatically eliminated to yield configuration-dependent forces. As such, the predictions should be interpreted as qualitative trends for how strong electromagnetic confinement can influence molecular orientation, clustering, and relaxation pathways, rather than as material-specific benchmarks. A more complete description would incorporate explicit many-body electronic structure, a microscopic bath model for dissipation, and, where appropriate, a fully quantum treatment of the cavity field and molecular excitations capable of capturing coherent polariton formation and nonclassical field statistics beyond the mean-force picture adopted here.

Nevertheless, the present approach identifies the key parameters – confinement strength,

field anisotropy, and dipole misalignment – that control the crossover between van der Waals-dominated and cavity-dominated aggregation. It is readily adaptable to other platforms with tunable interactions and reconfigurable geometries, ranging from field-structured molecular assemblies near nanophotonic structures to related long-range interacting systems, and thus provides a starting point for systematic studies of aggregation and ordering in strongly confined electromagnetic environments.

Acknowledgments

SR would like to acknowledge financial support from the Max Planck Society. MF acknowledges funding from the Austrian Science Fund (FWF) Grant DOI 10.55776/W1259 and from the FET OPEN Network Cryst3 funded by the European Union (EU) via Horizon 2020.

Data Availability

The data that support the findings of this article are openly available at [228]. The repository includes the basic simulation code for the aggregation without the cavity, for the aggregation including the cavity with aligned dipoles and for the aggregation including the cavity with misaligned dipoles. Moreover, the underlying data for the figures is included and labeled appropriately.

10.7 Appendix

10.7.1 Effective potential

In the cavity-coupled equations of motion, the field coordinate $\mathcal{Q}(t)$ evolves at the cavity frequency ω_c, whereas the molecular coordinates $z_i(t)$, $\theta_i(t)$, $\phi_i(t)$, and $\chi_i(t)$ vary on much slower timescales. In the parameter regime considered here, this separation of timescales allows the cavity mode to be treated in a semiclassical and effectively adiabatic manner. Rather than resolving the full fast oscillatory dynamics at every step, we derive a quasi-static expression for the cavity amplitude that depends on the instantaneous molecular configuration.

We begin from the cavity equation of motion obtained from Eq. (10.41),

$$\ddot{\mathcal{Q}}(t) + \omega_c^2 \mathcal{Q}(t) = \frac{2\omega_c E_{\max}}{\hbar} \sum_{i=1}^{N} d_x(\theta_i, \phi_i, \chi_i)\, f(z_i), \tag{10.52}$$

where

$$f(z_i) = \exp\left[-\frac{z_i^2}{w_r^2} - \frac{x_h^2}{w_x^2}\right]. \tag{10.53}$$

The cavity coordinate may be written as a rapidly oscillating part multiplied by a slowly varying envelope. A convenient representation is

$$\mathcal{Q}(t) = \tilde{\mathcal{Q}}(t)\, e^{i\omega t}, \tag{10.54}$$

where $\tilde{\mathcal{Q}}(t)$ varies slowly compared with $e^{-i\omega_c t}$. This decomposition is standard in rotating-wave and adiabatic-elimination treatments.

Substituting into the equation of motion gives

$$\ddot{\tilde{\mathcal{Q}}} - 2i\omega_c \dot{\tilde{\mathcal{Q}}} = \frac{2\omega_c E_{\max}}{\hbar} \sum_{i=1}^{N} d_x(\theta_i, \phi_i, \chi_i)\, f(z_i), e^{i\omega_c t}. \tag{10.55}$$

Because the molecular coordinates evolve slowly on the cavity timescale, the envelope $\tilde{\mathcal{Q}}(t)$ may be taken to vary slowly compared with the carrier oscillation. We therefore neglect $\ddot{\tilde{\mathcal{Q}}}$ relative to $2i\omega_c \dot{\tilde{\mathcal{Q}}}$, which yields the first-order approximation

$$\dot{\tilde{\mathcal{Q}}} \simeq -\frac{iE_{\max}}{\hbar} \sum_{i=1}^{N} d_x(\theta_i, \phi_i, \chi_i)\, f(z_i), e^{i\omega_c t}. \tag{10.56}$$

Integrating over times long compared with the optical period $2\pi/\omega_c$ but short compared with the molecular rearrangement time allows us to separate the fast cavity oscillations from the slow molecular motion. Writing the cavity coordinate as

$$\mathcal{Q}(t) = \mathrm{Re}\left[\tilde{\mathcal{Q}}(t) e^{-i\omega_c t}\right],$$

with a slowly varying envelope $\tilde{\mathcal{Q}}(t)$, we neglect $\ddot{\tilde{\mathcal{Q}}}$ and $\dot{\tilde{\mathcal{Q}}}$ compared with $\omega_c \dot{\tilde{\mathcal{Q}}}$ and $\omega_c^2 \tilde{\mathcal{Q}}$.

To leading order, the envelope then follows the instantaneous molecular configuration,

$$\tilde{\mathcal{Q}}(t) \simeq \frac{E_{\max}}{\hbar\omega_c} \sum_{i=1}^{N} d_x(\theta_i, \phi_i, \chi_i), f(z_i),$$

so that averaging over the rapid optical oscillations removes the carrier phase and leaves the quasi-static contribution

$$\mathcal{Q}_{\text{eff}} = \frac{E_{\max}}{\hbar\omega_c} \sum_{i=1}^{N} d_x(\theta_i, \phi_i, \chi_i)\, f(z_i). \tag{10.57}$$

This expression is the effective cavity coordinate used in the main text. It captures the leading-order influence of the cavity field on the molecular dynamics while filtering out the fast oscillatory component that is not resolved on the aggregation timescale. In the derivation above, an explicit cavity-loss term $\kappa_c\dot{\mathcal{Q}}$ and associated noise have been omitted from Eq. (10.52). Their main effect in the strongly damped regime of interest would be to set the relaxation time with which the cavity amplitude approaches $\mathcal{Q}\text{eff}(t)$ and to add fast fluctuations around this mean value. For typical nanoplasmonic picocavities, the corresponding damping time κ_c^{-1} is orders of magnitude shorter than the Lennard-Jones, rotational, and aggregation timescales (see Sec.IV and Appendix 10.7.2), so that these fluctuations average out on the times of interest. Within the present mean-force description, we therefore retain only the quasi-static, configuration-dependent cavity coordinate $\mathcal{Q}\text{eff}(t)$ and neglect explicit loss and noise in the cavity sector.

In this approximation, the cavity-induced interaction may be viewed as a quasi-static potential generated by the instantaneous molecular configuration. Substituting $\mathcal{Q}_{\text{eff}}$ into the molecular equations of motion yields the effective cavity forces used in Secs. 10.4 and 10.5.

The validity of this effective description relies on a clear separation of timescales between the cavity mode and the molecular degrees of freedom. Typical nanoplasmonic picocavities operate at optical frequencies $\omega_c \sim 10^{15}$ s^{-1}, corresponding to oscillation periods $T_c = 2\pi/\omega_c \lesssim 10^{-14}$ s. For quality factors $Q_c \sim 10 - 50$, the cavity damping rate is $\kappa_c \simeq \omega_c/Q_c \sim 2 \times 10^{13} - 10^{14}$ s^{-1}, so that the cavity field decays on timescales $\kappa_c^{-1} \sim 10^{-14} - 10^{-13}$ s. By contrast, the intrinsic Lennard-Jones timescale τ_{LJ}, set by the molecular mass, interaction depth, and length scale (Sec. 10.2), lies in the range $\tau_{\text{LJ}} \sim 0.4 - 2$ ps for the parameters in Table 10.2. The momentum-relaxation times

associated with the chosen friction coefficients (Table 10.3) are

$$\tau_{\text{trans}} = \frac{m}{\kappa_z} \sim 5 \times 10^{-15} - 10^{-14}\,\text{s},$$
$$\tau_{\text{rot}} = \frac{I}{\kappa_{\theta,\phi}} \sim 10^{-15} - 4 \times 10^{-15}\,\text{s},$$

while the configurational relaxation and aggregation processes observed in the simulations occur over tens to hundreds of picoseconds (Sec.10.4). Thus,

$$T_c,\ \kappa_c^{-1} \ll \tau_{\text{rot}}, \qquad \tau_{\text{trans}} \ll \tau_{\text{LJ}} \ll \tau_{\text{agg}},$$

where τ_{agg} denotes the characteristic aggregation time. Within this hierarchy, the cavity amplitude $\mathcal{Q}(t)$ is the fastest degree of freedom in the problem and relaxes rapidly to the configuration-dependent value $\mathcal{Q}_{\text{eff}}(t)$, justifying its adiabatic elimination.

If this separation of timescales were not satisfied – for example, in regimes of very low cavity loss, resonant coherent driving, or long-lived polaritonic excitations – a more complete quantum treatment of the coupled light-matter dynamics would be required, including coherent Rabi oscillations and photon statistics. In the parameter ranges explored here, we remain in the opposite, strongly damped limit, in which the cavity primarily acts as a structured environment generating configuration-dependent mean forces on the classical molecular coordinates.

10.7.2 Relaxation Time and the Role of Friction

To understand the interplay between inertia and friction in molecular dynamics, consider a damped harmonic oscillator

$$m\ddot{x} + \kappa\dot{x} + kx = 0, \tag{10.58}$$

where m is the mass (inertia), κ is the friction coefficient, k is the stiffness (curvature of the potential), and $x(t)$ is the displacement from equilibrium. It is possible to define the natural (undamped) frequency and damping rate,

$$\omega_0 = \sqrt{\frac{k}{m}}, \qquad \gamma = \frac{\kappa}{m}. \tag{10.59}$$

Thus, the equation becomes

$$\ddot{x} + \gamma\dot{x} + \omega_0^2 x = 0. \tag{10.60}$$

The different regimes are defined by the relative magnitude of γ and ω_0.

1. Underdamped Regime ($\gamma < 2\omega_0$): Friction is weak compared to inertia. The system oscillates while slowly losing energy,

$$x(t) = Ae^{-\gamma t/2}\cos(\omega t + \phi), \tag{10.61}$$

with $\omega = \sqrt{\omega_0^2 - \gamma^2/4}$. The amplitude decays on the timescale

$$\tau_{\text{amp}} = \frac{2}{\gamma} = \frac{2m}{\kappa}. \tag{10.62}$$

Physically, inertia dominates short-time dynamics, allowing oscillations (overshoot), while friction slowly removes energy. Increasing κ (friction) shortens τ_{amp}, damping oscillations faster.

2. Critically Damped Regime ($\gamma = 2\omega_0$): This is the boundary between oscillatory and non-oscillatory motion – the system returns to equilibrium *as fast as possible without oscillating*. This regime represents optimal damping.

3. Overdamped Regime ($\gamma > 2\omega_0$): Friction dominates inertia, suppressing oscillations. In the strong damping limit $\gamma \gg \omega_0$, the inertial term $m\ddot{x}$ is negligible, and the dynamics reduce to

$$\kappa\dot{x} + kx = 0, \tag{10.63}$$

and the solution is purely exponential,

$$x(t) = x_0 e^{-t/\tau_{\text{overdamped}}}, \tag{10.64}$$

with the configurational relaxation time

$$\tau_{\text{overdamped}} = \frac{\kappa}{k}. \tag{10.65}$$

Here, motion is dominated by viscous drag; increasing friction slows down the relaxation to equilibrium.

Two distinct relaxation timescales must be distinguished

(a) Momentum Relaxation: If the stiffness $k = 0$, the system describes pure velocity damping

$$m\dot{v} = -\kappa v, \tag{10.66}$$

with solution

$$v(t) = v_0 e^{-t/\tau_{\text{momentum}}}, \quad \tau_{\text{momentum}} = \frac{m}{\kappa}. \tag{10.67}$$

Increasing friction κ decreases τ_{momentum}, meaning momentum relaxes faster.

(b) Configurational (Position) Relaxation Time: In the overdamped regime relevant for strongly damped aggregation,

$$\tau_{\text{config}} = \frac{\kappa}{k}. \tag{10.68}$$

Here, larger friction κ increases τ_{config}, slowing down how fast the particle approaches equilibrium.

Summary of physical meaning:

- τ_{momentum} governs how quickly velocities thermalize; typically very short (~ 0.005 ps in our system).
- τ_{config} governs the timescale of structural rearrangements (aggregation) and can be much longer (picoseconds), controlled by friction and potential curvature.
- Large friction thus causes *fast* velocity relaxation but *slow* configurational relaxation.
- This explains why increasing friction κ reduces momentum relaxation time but increases aggregation time, resolving the apparent paradox.

Connection to our simulations: For our representative parameters $\kappa_z = 200$ meV Å^{-2} ps, $\kappa_\theta = \kappa_\phi = 500$ meV ps, and $\kappa_\chi = 100$ meV ps, the momentum relaxation times are

$$\tau_{\text{trans}} = \frac{m}{\kappa_z} \sim 0.01 \text{ ps},$$

$$\tau_{\text{rot}} = \frac{I}{\kappa_\theta} \sim 0.004 \text{ ps},$$
$$\tau_\chi = \frac{I_\chi}{\kappa_\chi} \sim 0.01 \text{ ps},$$

much shorter than the intrinsic Lennard-Jones oscillation timescale $\tau_{\text{LJ}} \sim 0.4 - 2.2$ ps. This places the system in the strongly overdamped regime: molecules do not oscillate inertially but rapidly equilibrate velocities, while configurational rearrangements and aggregation occur on the picosecond timescale, primarily governed by conservative intermolecular forces and thermal fluctuations.

Thus, our simulations connect the general relaxation picture to physically meaningful aggregation dynamics under cryogenic picocavity conditions, capturing both the fast momentum equilibration and slower configurational relaxation. This framework clarifies the roles of friction and inertia in nanoscale molecular aggregation under confinement.

10.7.3 Numerical methodology and convergence

The equations of motion [Eqs. (10.18) and (10.41)] were integrated using the `DifferentialEquations.jl` package in Julia. At zero temperature ($T = 0$), the deterministic equations were solved using adaptive Runge-Kutta methods. For the cavity calculations, when there is a misalignment between the van der Waals dipole $\boldsymbol{\mu}$ and the cavity-coupled dipole $\mathbf{d}$ ($\alpha \neq 0$), we employed the fifth-order Tsitouras solver (`Tsit5`), while the remaining deterministic simulations used the default adaptive ODE solver. At finite temperature ($T > 0$), the stochastic equations were integrated using the adaptive stochastic Runge-Kutta solver `SOSRA`. In all cases, the numerical integration employed adaptive timestep control based on local error estimation, while the solution was recorded at uniform intervals of 0.1 ps for deterministic simulations and 0.5 ps for stochastic simulations.

Typical simulation times ranged from 500 ps for the $N = 6$ chains to $1 - 2$ ns for the $N = 10$ cavity runs, ensuring that the observables reached their steady-state values on the timescales of interest. For each parameter set, the reported quantities were averaged over 7-11 independent noise realizations and random initial configurations.

The numerical convergence of the simulations was verified by repeating representative calculations with more stringent integration settings and by comparing the resulting steady-state observables. No statistically significant differences were observed within

the reported numerical accuracy. System-size effects were assessed by comparing $N = 6$ and $N = 10$ chains: while the detailed cluster structure and aggregation timescales differ, the separation between fast intra-cluster ordering and slower inter-cluster recombination, as well as the LJ-dominated, cavity-dominated, and frustrated regimes identified by S_{vdW}, remain qualitatively unchanged.

11 Conclusions and Outlook

In this thesis, I investigated the collective dynamics of quantum emitters interacting via a photonic mode of a cavity or a waveguide. To this end, I started by introducing a proper quantum description of atoms, the electromagnetic field and their interaction. We understood the spontaneous emission using the Wigner-Weisskopf ansatz and Fermi's Golden rule. Armed with this knowledge, we derived the equations governing the dynamics of atoms coupled to a waveguide. These equations eventually allow us to investigate quantum emitter ensembles coupled to a waveguide.

The first project in my thesis focused on atoms in a cavity, constituting a superradiant laser. In particular, we looked at the influence of temperature on the photon numbers. Due to the Doppler effect, the resonance of fast atoms is shifted and the effective coupling is suppressed. One can overcome this by increasing the collective atom-cavity-coupling, but there are limits to this increase. Searching for further handles to up the laser power, we included a velocity filter for fast atoms. As the fast atoms get filtered, only slow atoms take part in the dynamics. However, as this also reduces the total number of atoms, the photon numbers are suppressed. Another idea is to include an optical guiding potential. For low temperatures (compared to the energy barrier) the atoms get trapped between the potential barriers, increasing the effective coupling and therefore the photon numbers. Even for high temperatures one sees a significant increase in photon numbers, in some cases including an optical lattice potential enables a macroscopic photon occupation number, even when there was virtually no photon without the optical potential. While the velocity filter did not lead to an increase in photon numbers, the optical potential is a useful tool enabling high photon numbers even for high temperatures.

Then we switched our attention to atoms in a waveguide. We showed, that using the distance between atoms and different pumping schemes one can engineer the radiation properties of ensembles of atoms in waveguides, enabling us to create highly excited subradiant states with up to 50% excitation. Above a well-defined threshold, the ensemble becomes superradiant, allowing for a fast transition from sub-

to superradiance with subsequent superabsorption by another ensemble of emitters. Using a vanishing phase, coherent waveguide-mediated dipole-dipole interaction can be strongly suppressed, allowing for experimental implementations with large dilute ensembles. Future work could focus on retardation effects for widely separated ensembles or detuning ensembles to influence the dissipation.

As the previous work heavily relied on the cumulant expansion method, we investigated this approximation in further detail using the example of Dicke superradiance. We demonstrated, that a second-order cumulant expansion captures the dynamics fairly reliably, however, for low atomic numbers and on long timescales the cumulant expansion has its limitations. Higher orders only lead to minor improvements, while odd orders often exhibit oscillatory solutions that are physically incorrect. In particular, we investigated the difference in the cumulant expansion based on the individual spin operators and based on the collective spin operators. For a low number of atoms, the expansion based on individual operators produces significantly better results and even converges to the exact result when the expansion order approaches the particle number. The difference between these two expansions disappears in the large N limit. Future work could involve benchmarks of equal-time spin-spin quantum correlations of higher orders, e.g. intensity correlations or compare and contrast the cumulant expansion method with different approximations such as a truncated Wigner approximation or using Matrix Product states.

Then we went back to atoms coupled to a waveguide and investigated the spectrum of the radiation. Here we saw how the presence of unpumped emitters in an ensemble narrows the spectral linewidth while reducing frequency shifts. In the example of only two atoms one can derive analytic expressions for the spectrum to retrace the narrowing of the linewidth. The pumped ensemble transfers the excitation and the unpumped ensemble provides frequency-selective feedback. These results point to continuous narrowband superradiance even for small number of emitters and suggest this setup as a promising candidate for active optical frequency reference with small clock-atom ensembles.

In the last project we studied the aggregation of nonpolar molecules in a cavity. To this end, we developed a toy model including anisotropic Lennard-Jones interactions, Langevin dissipation and cavity-induced coupling to molecular transition dipoles. Without the cavity, the aggregation is governed by attractive dispersion forces, thermal fluctuations and viscous damping. Including the cavity, the electromagnetic field reshapes the effective interaction landscape opening up new aggregation pathways.

With confinement strength, field anisotropy and dipole misalignment as key parameters, one can control the crossover between van der Waals-dominated and cavity dominated aggregation. A natural idea is to extend this work to polar molecules, where one permanent dipole moment governs both intermolecular dipole-dipole forces as well as the coupling to an external electric field. Ultracold polar molecules then provide a highly controllable platform for studying the aggregation of molecules.

Taken together, this thesis underlines the importance of collective dynamics of quantum emitter arrays interacting via photonic modes. In a cavity these collective dynamics enable the system to work as a superradiant laser, this kind of laser is insensitive to cavity mirror fluctuations, which are limiting the linewidth of conventional lasers. Coupling the atoms via a waveguide mode allows us to engineer their radiation rates and a fast transition between subradiant and superradiant behavior, these essential building blocks unlock applications such as quantum batteries or quantum memories. Looking at the spectrum of atoms in a waveguide, by partially pumping the ensembles we can achieve continuous narrowband superradiance with a low number of emitters. Here, the presence of an unpumped ensemble is crucial. Moreover, the collective coupling of molecules to a picocavity reshapes intermolecular interactions and opens new pathways of aggregation.

However, the accurate simulation of such systems remains difficult, as the size of the Hilbert space scales exponentially with emitter number and approximations such as the cumulant expansion method have their limitations. Nevertheless, future research will find ways to push the boundaries to further our understanding of collective quantum dynamics among quantum emitters.

Bibliography

[1] A. Einstein, "Emission and absorption of radiation in quantum theory," *Verhandlungen der Deutschen Physikalischen Gesellschaft*, vol. 18, pp. 318–323, 1916.

[2] R. H. Dicke, "Coherence in spontaneous radiation processes," *Phys. Rev.*, vol. 93, pp. 99–110, Jan 1954.

[3] M. Gross and S. Haroche, "Superradiance: An essay on the theory of collective spontaneous emission," *Physics Reports*, vol. 93, no. 5, pp. 301–396, 1982.

[4] M. Moreno-Cardoner, D. Plankensteiner, L. Ostermann, D. E. Chang, and H. Ritsch, "Subradiance-enhanced excitation transfer between dipole-coupled nanorings of quantum emitters," *Phys. Rev. A*, vol. 100, p. 023806, Aug 2019.

[5] M. Moreno-Cardoner, R. Holzinger, and H. Ritsch, "Efficient nano-photonic antennas based on dark states in quantum emitter rings," *Opt. Express*, vol. 30, pp. 10779–10791, Mar 2022.

[6] R. Zhao, Y. O. Dudin, S. D. Jenkins, C. J. Campbell, D. N. Matsukevich, T. A. B. Kennedy, and A. Kuzmich, "Long-lived quantum memory," *Nature Physics*, vol. 5, pp. 100–104, Dec. 2008.

[7] B. Zhao, Y.-A. Chen, X.-H. Bao, T. Strassel, C.-S. Chuu, X.-M. Jin, J. Schmiedmayer, Z.-S. Yuan, S. Chen, and J.-W. Pan, "A millisecond quantum memory for scalable quantum networks," *Nature Physics*, vol. 5, pp. 95–99, Dec. 2008.

[8] A. I. Lvovsky, B. C. Sanders, and W. Tittel, "Optical quantum memory," *Nature Photonics*, vol. 3, pp. 706–714, Dec. 2009.

[9] D. Plankensteiner, L. Ostermann, H. Ritsch, and C. Genes, "Selective protected state preparation of coupled dissipative quantum emitters," *Scientific Reports*, vol. 5, nov 2015.

[10] A. Asenjo-Garcia, M. Moreno-Cardoner, A. Albrecht, H. J. Kimble, and D. E.

Chang, "Exponential improvement in photon storage fidelities using subradiance and "selective radiance" in atomic arrays," *Phys. Rev. X*, vol. 7, p. 031024, Aug 2017.

[11] J. Q. Quach, K. E. McGhee, L. Ganzer, D. M. Rouse, B. W. Lovett, E. M. Gauger, J. Keeling, G. Cerullo, D. G. Lidzey, and T. Virgili, "Superabsorption in an organic microcavity: Toward a quantum battery," *Science Advances*, vol. 8, no. 2, p. eabk3160, 2022.

[12] D. Ferraro, M. Campisi, G. M. Andolina, V. Pellegrini, and M. Polini, "High-power collective charging of a solid-state quantum battery," *Phys. Rev. Lett.*, vol. 120, p. 117702, Mar 2018.

[13] F. Pirmoradian and K. Mølmer, "Aging of a quantum battery," *Phys. Rev. A*, vol. 100, p. 043833, Oct 2019.

[14] J. Q. Quach and W. J. Munro, "Using dark states to charge and stabilize open quantum batteries," *Phys. Rev. Appl.*, vol. 14, p. 024092, Aug 2020.

[15] G. Ferioli, A. Glicenstein, L. Henriet, I. Ferrier-Barbut, and A. Browaeys, "Storage and release of subradiant excitations in a dense atomic cloud," *Phys. Rev. X*, vol. 11, p. 021031, May 2021.

[16] T.-X. Zhu, X. Liu, Z.-Q. Zhou, and C.-F. Li, "Remote quantum networks based on quantum memories," *Nanophotonics*, vol. 14, no. 11, pp. 1975–1992, 2025.

[17] C. W. Gardiner and P. Zoller, *The Quantum World of Ultra-Cold Atoms and Light, Book II: The Physics of Quantum-Optical Devices*. Cold Atoms, London: Imperial College Press, 2015.

[18] C. W. Gardiner and P. Zoller, *The Quantum World of Ultra-Cold Atoms and Light, Book I: Foundations of Quantum Optics*. Cold Atoms, London and Singapore: Imperial College Press, 2014.

[19] T. Fliessbach, *Elektrodynamik: Lehrbuch zur Theoretischen Physik 2*. Berlin, Heidelberg: Springer-Verlag, 2012.

[20] M. A. Norcia, M. N. Winchester, J. R. K. Cline, and J. K. Thompson, "A cold-strontium laser in the superradiant crossover regime," *Phys. Rev. X*, vol. 6, p. 011025, 2016.

[21] M. A. Norcia and J. K. Thompson, "Strong coupling on a forbidden transition in

strontium and nondestructive atom counting," *Phys. Rev. A*, vol. 93, p. 023804, Feb 2016.

[22] S. L. Kristensen, E. Bohr, J. Robinson-Tait, T. Zelevinsky, J. W. Thomsen, and J. H. Müller, "Subnatural linewidth superradiant lasing with cold sr 88 atoms," *Physical Review Letters*, vol. 130, no. 22, p. 223402, 2023.

[23] D. J. Griffiths and D. F. Schroeter, *Introduction to Quantum Mechanics*. Cambridge University Press, third ed., 2018.

[24] N. Pucker and C. B. Lang, *Mathematische Methoden der Physik*. Berlin, Heidelberg: Springer, 2016.

[25] C. C. Gerry and P. L. Knight, *Introductory Quantum Optics*. Cambridge, UK: Cambridge University Press, 2005.

[26] J. J. Sakurai, *Modern Quantum Mechanics*. Addison-Wesley Publishing Company, 1994.

[27] D. J. Griffiths, *Introduction to electrodynamics*. Pearson, 2013.

[28] H. B. G. Casimir, "On the attraction between two perfectly conducting plates," *Indag. Math.*, vol. 10, no. 4, pp. 261–263, 1948.

[29] D. A. Steck, *Quantum and Atom Optics*. available online, 2007.

[30] G. Grübl, *Mathematische Methoden der Theoretischen Physik 2*. Oxford, UK: Oxford University Press, 2019.

[31] V. Weisskopf and E. Wigner, "Berechnung der natürlichen Linienbreite auf Grund der Diracschen Lichttheorie," *Zeitschrift fur Physik*, vol. 63, pp. 54–73, Jan. 1930.

[32] Z. Ficek and R. Tanaś, "Entangled states and collective nonclassical effects in two-atom systems," *Physics Reports*, vol. 372, no. 5, pp. 369–443, 2002.

[33] L. Ostermann, C. Meignant, C. Genes, and H. Ritsch, "Super- and subradiance of clock atoms in multimode optical waveguides," *New Journal of Physics*, vol. 21, p. 025004, feb 2019.

[34] G. Lindblad, "On the generators of quantum dynamical semigroups," *Communications in Mathematical Physics*, vol. 48, pp. 119–130, Jun 1976.

[35] H.-P. Breuer and F. Petruccione, *The theory of open quantum systems*. Innsbruck,

Österreich: Springer, 2002.

[36] R. Holzinger, R. Gutiérrez-Jáuregui, T. Hönigl-Decrinis, G. Kirchmair, A. Asenjo-Garcia, and H. Ritsch, "Control of localized single- and many-body dark states in waveguide qed," *Phys. Rev. Lett.*, vol. 129, p. 253601, Dec 2022.

[37] R. Kubo, "Generalized cumulant expansion method," *Journal of the Physical Society of Japan*, vol. 17, no. 7, pp. 1100–1120, 1962.

[38] N. G. van Kampen, "A cumulant expansion for stochastic linear differential equations," *Physica*, vol. 74, no. 2, pp. 215–238, 1974.

[39] D. Plankensteiner, C. Hotter, and H. Ritsch, "Quantumcumulants. jl: A julia framework for generalized mean-field equations in open quantum systems," *Quantum*, vol. 6, p. 617, 2022.

[40] M. Takamoto, F.-L. Hong, R. Higashi, and H. Katori, "An optical lattice clock," *Nature*, vol. 435, no. 7040, pp. 321–324, 2005.

[41] B. Bloom, T. Nicholson, J. Williams, S. Campbell, M. Bishof, X. Zhang, W. Zhang, S. Bromley, and J. Ye, "An optical lattice clock with accuracy and stability at the 10- 18 level," *Nature*, vol. 506, no. 7486, pp. 71–75, 2014.

[42] A. D. Ludlow, M. M. Boyd, J. Ye, E. Peik, and P. O. Schmidt, "Optical atomic clocks," *Reviews of Modern Physics*, vol. 87, no. 2, p. 637, 2015.

[43] F. Haake, M. I. Kolobov, C. Fabre, E. Giacobino, and S. Reynaud, "Superradiant laser," *Phys. Rev. Lett.*, vol. 71, pp. 995–998, Aug 1993.

[44] D. Meiser, J. Ye, D. R. Carlson, and M. J. Holland, "Prospects for a millihertz-linewidth laser," *Phys. Rev. Lett.*, vol. 102, p. 163601, 2009.

[45] J. Chen, "Active optical clock," *Chinese Science Bulletin*, vol. 54, no. 3, pp. 348–352, 2009.

[46] D. Meiser and M. J. Holland, "Steady-state superradiance with alkaline-earth-metal atoms," *Phys. Rev. A*, vol. 81, p. 033847, 2010.

[47] D. Meiser and M. Holland, "Intensity fluctuations in steady-state superradiance," *Physical Review A*, vol. 81, no. 6, p. 063827, 2010.

[48] J. G. Bohnet, Z. Chen, J. M. Weiner, D. Meiser, M. J. Holland, and J. K. Thompson, "A steady-state superradiant laser with less than one intracavity

photon," *Nature*, vol. 484, no. 7392, pp. 78–81, 2012.

[49] V. Vuletic, "An almost lightless laser," *Nature*, vol. 484, no. 7392, pp. 43–44, 2012.

[50] T. Maier, S. Kraemer, L. Ostermann, and H. Ritsch, "A superradiant clock laser on a magic wavelength optical lattice," *Optics express*, vol. 22, no. 11, pp. 13269–13279, 2014.

[51] Y. Zhang, Y.-X. Zhang, and K. Mølmer, "Monte-carlo simulations of superradiant lasing," *New Journal of Physics*, vol. 20, p. 112001, nov 2018.

[52] K. Debnath, Y. Zhang, and K. Mølmer, "Lasing in the superradiant crossover regime," *Physical Review A*, vol. 98, no. 6, p. 063837, 2018.

[53] C. Hotter, D. Plankensteiner, L. Ostermann, and H. Ritsch, "Superradiant cooling, trapping, and lasing of dipole-interacting clock atoms," *Optics express*, vol. 27, no. 22, pp. 31193–31206, 2019.

[54] A. Gogyan, G. Kazakov, M. Bober, and M. Zawada, "Characterisation and feasibility study for superradiant lasing in 40ca atoms," *Opt. Express*, vol. 28, pp. 6881–6892, Mar 2020.

[55] Y. Zhang, C. Shan, and K. Mølmer, "Ultranarrow superradiant lasing by dark atom-photon dressed states," *Physical Review Letters*, vol. 126, no. 12, p. 123602, 2021.

[56] A. Bychek, C. Hotter, D. Plankensteiner, and H. Ritsch, "Superradiant lasing in inhomogeneously broadened ensembles with spatially varying coupling," *Open Research Europe*, vol. 1, p. 73, 2021.

[57] G. A. Kazakov, S. Dubey, A. Bychek, U. Sterr, M. Bober, and M. Zawada, "Ultimate stability of active optical frequency standards," *Phys. Rev. A*, vol. 106, p. 053114, 2022.

[58] J. Zhang, T. Shi, J. Miao, and J. Chen, "The development of active optical clock," *AAPPS Bulletin*, vol. 33, no. 1, p. 10, 2023.

[59] H. M. Goldenberg, D. Kleppner, and N. F. Ramsey, "Atomic hydrogen maser," *Phys. Rev. Lett.*, vol. 5, pp. 361–362, Oct 1960.

[60] G. A. Kazakov and T. Schumm, "Active optical frequency standard using sequential coupling of atomic ensembles," *Physical Review A*, vol. 87, no. 1,

p. 013821, 2013.

[61] G. A. Kazakov and T. Schumm, "Active optical frequency standards using cold atoms: Perspectives and challenges," in *2014 European Frequency and Time Forum (EFTF)*, pp. 411–414, 2014.

[62] M. Tang, S. A. Schäffer, and J. H. Müller, "Prospects of a superradiant laser based on a thermal or guided beam of ^{88}Sr," *Phys. Rev. A*, vol. 106, p. 063704, Dec 2022.

[63] T. Salzburger and H. Ritsch, "Atom-photon pair laser," *Phys. Rev. A*, vol. 75, p. 061601, Jun 2007.

[64] M. Holland, K. Burnett, C. Gardiner, J. I. Cirac, and P. Zoller, "Theory of an atom laser," *Phys. Rev. A*, vol. 54, pp. R1757–R1760, Sep 1996.

[65] C. Hotter, D. Plankensteiner, G. Kazakov, and H. Ritsch, "Continuous multi-step pumping of the optical clock transition in alkaline-earth atoms with minimal perturbation," *Optics Express*, vol. 30, no. 4, pp. 5553–5568, 2022.

[66] S. Bennetts, C.-C. Chen, B. Pasquiou, and F. Schreck, "Steady-state magneto-optical trap with 100-fold improved phase-space density," *Phys. Rev. Lett.*, vol. 119, p. 223202, Dec 2017.

[67] C.-C. Chen, S. Bennetts, R. G. Escudero, B. Pasquiou, and F. Schreck, "Continuous guided strontium beam with high phase-space density," *Phys. Rev. Applied*, vol. 12, p. 044014, Oct 2019.

[68] R. G. Escudero, C.-C. Chen, S. Bennetts, B. Pasquiou, and F. Schreck, "Steady-state magneto-optical trap of fermionic strontium on a narrow-line transition," *Phys. Rev. Res.*, vol. 3, p. 033159, Aug 2021.

[69] C.-C. Chen, R. González Escudero, J. Minář, B. Pasquiou, S. Bennetts, and F. Schreck, "Continuous bose–einstein condensation," *Nature*, vol. 606, no. 7915, pp. 683–687, 2022.

[70] M. A. Norcia, M. N. Winchester, J. R. Cline, and J. K. Thompson, "Superradiance on the millihertz linewidth strontium clock transition," *Science advances*, vol. 2, no. 10, p. e1601231, 2016.

[71] M. A. Norcia, J. R. K. Cline, J. A. Muniz, J. M. Robinson, R. B. Hutson, A. Goban, G. E. Marti, J. Ye, and J. K. Thompson, "Frequency measurements

of superradiance from the strontium clock transition," *Phys. Rev. X*, vol. 8, p. 021036, 2018.

[72] T. Laske, H. Winter, and A. Hemmerich, "Pulse delay time statistics in a superradiant laser with calcium atoms," *Physical Review Letters*, vol. 123, no. 10, p. 103601, 2019.

[73] S. A. Schäffer, M. Tang, M. R. Henriksen, A. A. Jørgensen, B. T. Christensen, and J. W. Thomsen, "Lasing on a narrow transition in a cold thermal strontium ensemble," *Physical Review a*, vol. 101, no. 1, p. 013819, 2020.

[74] M. Tang, S. A. Schäffer, A. A. Jørgensen, M. R. Henriksen, B. T. Christensen, J. H. Müller, and J. W. Thomsen, "Cavity-immune spectral features in the pulsed superradiant crossover regime," *Physical Review Research*, vol. 3, no. 3, p. 033258, 2021.

[75] C. Hotter, L. Ostermann, and H. Ritsch, "Cavity sub- and superradiance for transversely driven atomic ensembles," *Phys. Rev. Res.*, vol. 5, p. 013056, Jan 2023.

[76] E. Bohr, S. L. Kristensen, C. Hotter, S. A. Schäffer, J. Robinson-Tait, J. W. Thomsen, T. Zelevinsky, H. Ritsch, and J. H. Müller, "Collectively enhanced ramsey readout by cavity sub-to superradiant transition," *arXiv preprint arXiv:2306.12544*, 2023.

[77] H. Liu, S. B. Jäger, X. Yu, S. Touzard, A. Shankar, M. J. Holland, and T. L. Nicholson, "Rugged mhz-linewidth superradiant laser driven by a hot atomic beam," *Physical Review Letters*, vol. 125, no. 25, p. 253602, 2020.

[78] S. B. Jäger, H. Liu, A. Shankar, J. Cooper, and M. J. Holland, "Regular and bistable steady-state superradiant phases of an atomic beam traversing an optical cavity," *Phys. Rev. A*, vol. 103, p. 013720, Jan 2021.

[79] S. B. Jäger, H. Liu, J. Cooper, T. L. Nicholson, and M. J. Holland, "Superradiant emission of a thermal atomic beam into an optical cavity," *Phys. Rev. A*, vol. 104, p. 033711, Sep 2021.

[80] D. Plankensteiner, C. Hotter, and H. Ritsch, "Quantumcumulants.jl: A julia framework for generalized mean-field equations in open quantum systems," 2021.

[81] M. Fasser, "Simulating a superradiant laser based on a thermal atomic beam," Master's thesis, University of Innsbruck, Innsbruck, Austria, 3 2022.

[82] M. Fasser, "Superradiant_laser_figures," *Figshare*, https://doi.org/10.6084/m9.figshare.c.6781920.v1, 2023.

[83] M. Fasser, "Srl_paper," *Zenodo*, https://doi.org/10.5281/zenodo.8232295, 2023.

[84] D. S. Dovzhenko, S. V. Ryabchuk, Y. P. Rakovich, and I. R. Nabiev, "Light–matter interaction in the strong coupling regime: configurations, conditions, and applications," *Nanoscale*, vol. 10, no. 8, pp. 3589–3605, 2018.

[85] A. González-Tudela, A. Reiserer, J. J. García-Ripoll, and F. J. García-Vidal, "Light–matter interactions in quantum nanophotonic devices," *Nature Reviews Physics*, vol. 6, pp. 166–179, Jan. 2024.

[86] L. Ruks, X. Xu, R. Ohta, W. J. Munro, and V. M. Bastidas, "Coherent response of inhomogeneously broadened and spatially localized emitter ensembles in waveguide qed," *Phys. Rev. A*, vol. 109, p. 023706, Feb 2024.

[87] J. Chen, Y. Luo, J. Luo, H. Huang, H. Cheng, G.-s. Liu, L. Chen, Z. Chen, and Y. Chen, "Magnetic-field-assisted optical fiber quantum temperature sensor with enhanced sensitivity," *Optics Letters*, vol. 49, p. 1421, Mar. 2024.

[88] D. Ribezzo, M. Zahidy, G. Lemmi, A. Petitjean, C. De Lazzari, I. Vagniluca, E. Conca, A. Tosi, T. Occhipinti, L. K. Oxenløwe, A. Xuereb, D. Bacco, and A. Zavatta, "Quantum key distribution over 100 km of underwater optical fiber assisted by a fast-gated single-photon detector," *Phys. Rev. Appl.*, vol. 20, p. 044052, Oct 2023.

[89] A. Goban, C.-L. Hung, J. D. Hood, S.-P. Yu, J. A. Muniz, O. Painter, and H. J. Kimble, "Superradiance for atoms trapped along a photonic crystal waveguide," *Phys. Rev. Lett.*, vol. 115, p. 063601, Aug 2015.

[90] S. Okaba, D. Yu, L. Vincetti, F. Benabid, and H. Katori, "Superradiance from lattice-confined atoms inside hollow core fibre," *Communications Physics*, vol. 2, Oct. 2019.

[91] R. Pennetta, M. Blaha, A. Johnson, D. Lechner, P. Schneeweiss, J. Volz, and A. Rauschenbeutel, "Collective radiative dynamics of an ensemble of cold atoms coupled to an optical waveguide," *Phys. Rev. Lett.*, vol. 128, p. 073601, Feb 2022.

[92] C. Liedl, F. Tebbenjohanns, C. Bach, S. Pucher, A. Rauschenbeutel, and P. Schneeweiss, "Observation of superradiant bursts in a cascaded quantum

system," *Phys. Rev. X*, vol. 14, p. 011020, Feb 2024.

[93] A. Albrecht, L. Henriet, A. Asenjo-Garcia, P. B. Dieterle, O. Painter, and D. E. Chang, "Subradiant states of quantum bits coupled to a one-dimensional waveguide," *New Journal of Physics*, vol. 21, p. 025003, feb 2019.

[94] M. Zanner, T. Orell, C. M. F. Schneider, R. Albert, S. Oleschko, M. L. Juan, M. Silveri, and G. Kirchmair, "Coherent control of a multi-qubit dark state in waveguide quantum electrodynamics," *Nature Physics*, vol. 18, pp. 538–543, Mar. 2022.

[95] A. Tiranov, V. Angelopoulou, C. J. van Diepen, B. Schrinski, O. A. D. Sandberg, Y. Wang, L. Midolo, S. Scholz, A. D. Wieck, A. Ludwig, A. S. Sørensen, and P. Lodahl, "Collective super- and subradiant dynamics between distant optical quantum emitters," *Science*, vol. 379, pp. 389–393, Jan. 2023.

[96] K. D. B. Higgins, S. C. Benjamin, T. M. Stace, G. J. Milburn, B. W. Lovett, and E. M. Gauger, "Superabsorption of light via quantum engineering," *Nature Communications*, vol. 5, Aug. 2014.

[97] D. Yang, S.-h. Oh, J. Han, G. Son, J. Kim, J. Kim, M. Lee, and K. An, "Realization of superabsorption by time reversal of superradiance," *Nature Photonics*, vol. 15, pp. 272–276, Mar. 2021.

[98] L. Ostermann, H. Ritsch, and C. Genes, "Protected state enhanced quantum metrology with interacting two-level ensembles," *Phys. Rev. Lett.*, vol. 111, p. 123601, Sep 2013.

[99] L. Ostermann, D. Plankensteiner, H. Ritsch, and C. Genes, "Protected subspace ramsey spectroscopy," *Phys. Rev. A*, vol. 90, p. 053823, Nov 2014.

[100] E. A. Bohr, S. L. Kristensen, C. Hotter, S. A. Schäffer, J. Robinson-Tait, J. W. Thomsen, T. Zelevinsky, H. Ritsch, and J. H. Müller, "Collectively enhanced ramsey readout by cavity sub- to superradiant transition," *Nature Communications*, vol. 15, Feb. 2024.

[101] Y. Hama, E. Yukawa, W. J. Munro, and K. Nemoto, "Negative-temperature-state relaxation and reservoir-assisted quantum entanglement in double-spin-domain systems," *Phys. Rev. A*, vol. 98, p. 052133, Nov 2018.

[102] Y. Hama, W. J. Munro, and K. Nemoto, "Relaxation to negative temperatures in double domain systems," *Phys. Rev. Lett.*, vol. 120, p. 060403, Feb 2018.

[103] J.-Y. Gyhm and U. R. Fischer, "Beneficial and detrimental entanglement for quantum battery charging," *AVS Quantum Science*, vol. 6, p. 012001, 01 2024.

[104] J. Dias, C. W. Wächtler, V. M. Bastidas, K. Nemoto, and W. J. Munro, "Reservoir-assisted energy migration through multiple spin domains," *Phys. Rev. B*, vol. 104, p. L140303, Oct 2021.

[105] S. Cardenas-Lopez, S. J. Masson, Z. Zager, and A. Asenjo-Garcia, "Many-body superradiance and dynamical mirror symmetry breaking in waveguide qed," *Phys. Rev. Lett.*, vol. 131, p. 033605, Jul 2023.

[106] C. Gardiner and P. Zoller, *Quantum noise: a handbook of Markovian and non-Markovian quantum stochastic methods with applications to quantum optics.* Springer Science & Business Media, New York, 2004.

[107] N. Shammah, S. Ahmed, N. Lambert, S. De Liberato, and F. Nori, "Open quantum systems with local and collective incoherent processes: Efficient numerical simulations using permutational invariance," *Phys. Rev. A*, vol. 98, p. 063815, Dec 2018.

[108] A. Shankar, J. T. Reilly, S. B. Jäger, and M. J. Holland, "Subradiant-to-subradiant phase transition in the bad cavity laser," *Phys. Rev. Lett.*, vol. 127, p. 073603, Aug 2021.

[109] K. E. Ballantine and J. Ruostekoski, "Subradiance-protected excitation spreading in the generation of collimated photon emission from an atomic array," *Phys. Rev. Res.*, vol. 2, p. 023086, Apr 2020.

[110] O. Rubies-Bigorda and S. F. Yelin, "Superradiance and subradiance in inverted atomic arrays," *Phys. Rev. A*, vol. 106, p. 053717, Nov 2022.

[111] Z. Yan, J. Ho, Y.-H. Lu, S. J. Masson, A. Asenjo-Garcia, and D. M. Stamper-Kurn, "Superradiant and subradiant cavity scattering by atom arrays," *Phys. Rev. Lett.*, vol. 131, p. 253603, Dec 2023.

[112] J. Dias, C. W. Wächtler, K. Nemoto, and W. J. Munro, "Entanglement generation between distant spins via quasilocal reservoir engineering," *Phys. Rev. Res.*, vol. 5, p. 043295, Dec 2023.

[113] S. Abend, B. Allard, A. S. Arnold, T. Ban, L. Barry, B. Battelier, A. Bawamia, Q. Beaufils, S. Bernon, A. Bertoldi, A. Bonnin, P. Bouyer, A. Bresson, O. S. Burrow, B. Canuel, B. Desruelle, G. Drougakis, R. Forsberg, N. Gaaloul, A. Gauguet,

M. Gersemann, P. F. Griffin, H. Heine, V. A. Henderson, W. Herr, S. Kanthak, M. Krutzik, M. D. Lachmann, R. Lammegger, W. Magnes, G. Mileti, M. W. Mitchell, S. Mottini, D. Papazoglou, F. Pereira dos Santos, A. Peters, E. Rasel, E. Riis, C. Schubert, S. T. Seidel, G. M. Tino, M. Van Den Bossche, W. von Klitzing, A. Wicht, M. Witkowski, N. Zahzam, and M. Zawada, "Technology roadmap for cold-atoms based quantum inertial sensor in space," *AVS Quantum Science*, vol. 5, Mar. 2023.

[114] A. Bertoldi, C.-H. Feng, D. S. Naik, B. Canuel, P. Bouyer, and M. Prevedelli, "Fast control of atom-light interaction in a narrow linewidth cavity," *Phys. Rev. Lett.*, vol. 127, p. 013202, Jun 2021.

[115] F. Melli, K. Vasko, L. Rosa, F. Benabid, and L. Vincetti, "Azimuthal fourier decomposition for loss analysis of hollow-core tube lattice fibers part i: Ideal fibers," *Results in Optics*, vol. 15, p. 100657, May 2024.

[116] G. Pesce, P. H. Jones, O. M. Maragò, and G. Volpe, "Optical tweezers: theory and practice," *The European Physical Journal Plus*, vol. 135, Dec. 2020.

[117] D. E. Chang, J. I. Cirac, and H. J. Kimble, "Self-organization of atoms along a nanophotonic waveguide," *Phys. Rev. Lett.*, vol. 110, p. 113606, Mar 2013.

[118] H. Ritsch, P. Domokos, F. Brennecke, and T. Esslinger, "Cold atoms in cavity-generated dynamical optical potentials," *Rev. Mod. Phys.*, vol. 85, pp. 553–601, Apr 2013.

[119] S. B. Jäger, T. Schmit, G. Morigi, M. J. Holland, and R. Betzholz, "Lindblad master equations for quantum systems coupled to dissipative bosonic modes," *Phys. Rev. Lett.*, vol. 129, p. 063601, Aug 2022.

[120] S. Krämer, D. Plankensteiner, L. Ostermann, and H. Ritsch, "Quantumoptics. jl: A julia framework for simulating open quantum systems," *Comp. Phys. Comm.*, vol. 227, pp. 109–116, 2018.

[121] M. Fasser, "Supporting data to research article," *Zenodo*, https://doi.org/10.5281/zenodo.11365844, 2024.

[122] M. Sánchez-Barquilla, R. E. F. Silva, and J. Feist, "Cumulant expansion for the treatment of light–matter interactions in arbitrary material structures," *The Journal of Chemical Physics*, vol. 152, p. 034108, 01 2020.

[123] N. N. Bogoliubov, *Problems of Dynamical Theory in Statistical Physics*. Oxford,

UK: Pergamon Press, 1960.

[124] R. Holzinger, M. Moreno-Cardoner, and H. Ritsch, "Nanoscale continuous quantum light sources based on driven dipole emitter arrays," *Applied Physics Letters*, vol. 119, p. 024002, 07 2021.

[125] L. Brey and R. E. Prange, "Cumulant expansion for the density matrix in quantum statistical mechanics," *Physical Review B*, vol. 30, no. 5, pp. 2581–2587, 1984.

[126] M. Kira and S. W. Koch, "Cluster-expansion representation in quantum optics," *Physical Review A*, vol. 73, no. 1, p. 013813, 2006.

[127] M. G. Benedict, A. M. Ermolaev, V. A. Malyshev, I. V. Sokolov, and E. D. Trifonov, *Super-radiance: Multiatomic Coherent Emission*. Series in Optics and Optoelectronics, Boca Raton: CRC Press, 1 ed., 1996.

[128] S. Roof, K. Kemp, M. Havey, and I. Sokolov, "Observation of single-photon superradiance and the cooperative lamb shift in an extended sample of cold atoms," *Physical review letters*, vol. 117, no. 7, p. 073003, 2016.

[129] R. Holzinger and C. Genes, "A compact analytical solution of the dicke superradiance master equation via residue calculus," *Zeitschrift für Naturforschung A*, vol. 80, no. 8, pp. 673–679, 2025.

[130] R. Holzinger, N. S. Bassler, J. Lyne, F. G. Jimenez, J. T. Gohsrich, and C. Genes, "Solving dicke superradiance analytically: A compendium of methods," 2025.

[131] D. Braak, "Integrability of the Rabi model," *Physical Review Letters*, vol. 107, no. 10, p. 100401, 2011.

[132] G. Ferioli, A. Glicenstein, I. Ferrier-Barbut, and A. Browaeys, "A non-equilibrium superradiant phase transition in free space," *Nature Physics*, vol. 19, no. 9, pp. 1345–1349, 2023.

[133] G. Ferioli, A. Glicenstein, F. Robicheaux, R. T. Sutherland, A. Browaeys, and I. Ferrier-Barbut, "Laser-driven superradiant ensembles of two-level atoms near dicke regime," *Phys. Rev. Lett.*, vol. 127, p. 243602, Dec 2021.

[134] F. Tebbenjohanns, C. D. Mink, C. Bach, A. Rauschenbeutel, and M. Fleischhauer, "Predicting correlations in superradiant emission from a cascaded quantum system," *Phys. Rev. A*, vol. 110, p. 043713, Oct 2024.

[135] G. Ferioli, I. Ferrier-Barbut, and A. Browaeys, "Emergence of second-order coherence in the superradiant emission from a free-space atomic ensemble," *Phys. Rev. Lett.*, vol. 134, p. 153602, Apr 2025.

[136] C. Bach, F. Tebbenjohanns, C. Liedl, P. Schneeweiss, and A. Rauschenbeutel, "Emergence of second-order coherence in superfluorescence," 2024.

[137] N. S. Bassler, "Absence of entanglement growth in dicke superradiance," *arXiv preprint arXiv:2504.13646*, 2025.

[138] X. H. Zhang, D. Malz, and P. Rabl, "Unraveling superradiance: entanglement and mutual information in collective decay," *arXiv preprint arXiv:2505.13401*, 2025.

[139] J. P. Clemens and H. Carmichael, "Stochastic initiation of superradiance in a cavity: an approximation scheme within quantum trajectory theory," *Physical review A*, vol. 65, no. 2, p. 023815, 2002.

[140] C. D. Mink and M. Fleischhauer, "Collective radiative interactions in the discrete truncated Wigner approximation," *SciPost Phys.*, vol. 15, p. 233, 2023.

[141] A. J. Daley, "Quantum trajectories and open many-body quantum systems," *Advances in Physics*, vol. 63, no. 2, pp. 77–149, 2014.

[142] J. I. Cirac, D. Pérez-García, N. Schuch, and F. Verstraete, "Matrix product states and projected entangled pair states: Concepts, symmetries, theorems," *Rev. Mod. Phys.*, vol. 93, p. 045003, Dec 2021.

[143] C. Hotter, A. Kosior, H. Ritsch, and K. Gietka, "Conditional atomic cat state generation via superradiance," *arXiv preprint arXiv:2410.11542*, 2024.

[144] A. Gorlach, A. Pizzi, K. Mølmer, J. Avron, M. Segev, and I. Kaminer, "Super-coherence: Harnessing long-range interactions to preserve collective coherence in disordered systems," 2025.

[145] R. Holzinger, O. Rubies-Bigorda, S. F. Yelin, and H. Ritsch, "Symmetry-based efficient simulation of higher-order coherences in quantum many-body superradiance," *Phys. Rev. Res.*, vol. 7, p. 033203, Aug 2025.

[146] E. Oelker, R. Hutson, C. Kennedy, L. Sonderhouse, T. Bothwell, A. Goban, D. Kedar, C. Sanner, J. Robinson, G. Marti, *et al.*, "Demonstration of 4.8× 10-17 stability at 1 s for two independent optical clocks," *Nature Photonics*, vol. 13,

no. 10, pp. 714–719, 2019.

[147] A. Aeppli, K. Kim, W. Warfield, M. S. Safronova, and J. Ye, "Clock with 8× 10-19 systematic uncertainty," *Physical Review Letters*, vol. 133, no. 2, p. 023401, 2024.

[148] D. Pan, B. Arora, Y.-m. Yu, B. Sahoo, and J. Chen, "Optical-lattice-based cs active clock with a continual superradiant lasing signal," *Physical Review A*, vol. 102, no. 4, p. 041101, 2020.

[149] F. Famà, S. Zhou, B. Heizenreder, M. Tang, S. Bennetts, S. B. Jäger, S. A. Schäffer, and F. Schreck, "Continuous cavity qed with an atomic beam," *Physical Review A*, vol. 110, no. 6, p. 063721, 2024.

[150] J. R. Cline, V. M. Schäfer, Z. Niu, D. J. Young, T. H. Yoon, and J. K. Thompson, "Continuous collective strong coupling of strontium atoms to a high finesse ring cavity," *Physical review letters*, vol. 134, no. 1, p. 013403, 2025.

[151] J. T. Reilly, S. B. Jäger, J. Cooper, and M. J. Holland, "Fully collective superradiant lasing with vanishing sensitivity to cavity length vibrations," *Physical Review Letters*, vol. 136, no. 14, p. 143803, 2026.

[152] M. Lei, R. Fukumori, J. Rochman, B. Zhu, M. Endres, J. Choi, and A. Faraon, "Many-body cavity quantum electrodynamics with driven inhomogeneous emitters," *Nature*, vol. 617, no. 7960, pp. 271–276, 2023.

[153] D. Goncalves, L. Bombieri, G. Ferioli, S. Pancaldi, I. Ferrier-Barbut, A. Browaeys, E. Shahmoon, and D. Chang, "Driven-dissipative phase separation in free-space atomic ensembles," *PRX Quantum*, vol. 6, p. 020303, Apr 2025.

[154] S. Cardenas-Lopez, E. Guardiola-Navarrete, and A. Asenjo-Garcia, "Emergent spin order and steady-state superradiance in one-dimensional baths," 2026.

[155] W. Kersten, N. de Zordo, O. Diekmann, E. S. Redchenko, A. N. Kanagin, A. Angerer, W. J. Munro, K. Nemoto, I. E. Mazets, S. Rotter, T. Pohl, and J. Schmiedmayer, "Self-induced superradiant masing," *Nature Physics*, vol. 22, pp. 158–163, 2026.

[156] V. M. Schäfer, Z. Niu, J. R. Cline, D. J. Young, E. Y. Song, H. Ritsch, and J. K. Thompson, "Continuous recoil-driven lasing and cavity frequency pinning with laser-cooled atoms," *Nature Physics*, vol. 21, no. 6, pp. 902–908, 2025.

[157] S. Dubey, G. A. Kazakov, B. Heizenreder, S. Zhou, S. Bennetts, S. A. Schäffer, A. Sitaram, F. Schreck, and MoSaiQC Collaboration, "Modeling of a continuous superradiant laser on the sub-mhz $^1S_0 \rightarrow {}^3P_0$ transition in neutral strontium-88," *Phys. Rev. Research*, vol. 7, p. 013292, 2025.

[158] W. J. Riley and D. A. Howe, "Handbook of frequency stability analysis," Tech. Rep. Special Publication 1065, National Institute of Standards and Technology, 2008.

[159] A. S. Sheremet, M. I. Petrov, I. V. Iorsh, A. V. Poshakinskiy, and A. N. Poddubny, "Waveguide quantum electrodynamics: Collective radiance and photon-photon correlations," *Rev. Mod. Phys.*, vol. 95, p. 015002, 2023.

[160] K. Lalumière, B. C. Sanders, A. F. van Loo, A. Fedorov, A. Wallraff, and A. Blais, "Input-output theory for waveguide QED with an ensemble of inhomogeneous atoms," *Phys. Rev. A*, vol. 88, p. 043806, 2013.

[161] S. Mahmoodian, M. Čepulkovskis, S. Das, P. Lodahl, K. Hammerer, and A. S. Sørensen, "Strongly correlated photon transport in waveguide quantum electrodynamics with weakly coupled emitters," *Phys. Rev. Lett.*, vol. 121, p. 143601, 2018.

[162] K. J. Kusmierek, S. Mahmoodian, M. Cordier, J. Hinney, A. Rauschenbeutel, M. Schemmer, P. Schneeweiss, J. Volz, and K. Hammerer, "Higher-order mean-field theory of chiral waveguide QED," *SciPost Phys. Core*, vol. 6, p. 041, 2023.

[163] C. J. van Diepen, V. Angelopoulou, O. A. Dall'Alba Sandberg, A. Tiranov, Y. Wang, S. Scholz, A. Ludwig, A. S. Sørensen, and P. Lodahl, "Resonant energy transfer and collectively driven emitters in waveguide QED," *Phys. Rev. Research*, vol. 7, p. 033169, 2025.

[164] A. Bychek, R. Holzinger, and H. Ritsch, "Nanoscale mirrorless superradiant lasing," *Phys. Rev. Lett.*, vol. 135, p. 143601, 2025.

[165] R. Holzinger, D. Plankensteiner, L. Ostermann, and H. Ritsch, "Nanoscale coherent light source," *Phys. Rev. Lett.*, vol. 124, p. 253603, 2020.

[166] R. H. Lehmberg, "Radiation from an N-atom system. I. general formalism," *Phys. Rev. A*, vol. 2, pp. 883–888, 1970.

[167] G. S. Agarwal, "Quantum statistical theories of spontaneous emission and their

relation to other approaches," in *Quantum Optics*, vol. 70 of *Springer Tracts in Modern Physics*, pp. 1–128, Berlin, Heidelberg: Springer, 1974.

[168] L. Novotny and B. Hecht, *Principles of Nano-Optics*. Cambridge University Press, 2 ed., 2012.

[169] C. W. Gardiner and M. J. Collett, "Input and output in damped quantum systems: Quantum stochastic differential equations and the master equation," *Phys. Rev. A*, vol. 31, pp. 3761–3774, 1985.

[170] O. Rubies-Bigorda, S. Ostermann, and S. F. Yelin, "Characterizing superradiant dynamics in atomic arrays via a cumulant expansion approach," *Physical Review Research*, vol. 5, no. 1, p. 013091, 2023.

[171] K. J. Kusmierek, M. Schemmer, S. Mahmoodian, and K. Hammerer, "Emergence of unidirectionality and phase separation in optically dense emitter ensembles," *Phys. Rev. Res.*, vol. 7, p. 043267, Dec 2025.

[172] C. Wang, W. Jin, H. L. Ho, and F. Yang, *Photonic Microcells for Sensing Applications*, pp. 2117–2138. Singapore: Springer Singapore, 2019.

[173] W. Jin, H. Xuan, C. Wang, W. Jin, and Y. Wang, "Robust microfiber photonic microcells for sensor and device applications," *Optics Express*, vol. 22, no. 23, pp. 28132–28141, 2014.

[174] E. Vetsch, D. Reitz, G. Sagué, R. Schmidt, S. T. Dawkins, and A. Rauschenbeutel, "Optical interface created by laser-cooled atoms trapped in the evanescent field surrounding an optical nanofiber," *Physical Review Letters*, vol. 104, p. 203603, 2010.

[175] A. M. Kaufman and K.-K. Ni, "Quantum science with optical tweezer arrays of ultracold atoms and molecules," *Nature Physics*, vol. 17, pp. 1324–1333, Nov. 2021.

[176] K. Kneipp, Y. Wang, H. Kneipp, L. T. Perelman, I. Itzkan, R. R. Dasari, and M. S. Feld, "Single molecule detection using surface-enhanced raman scattering (sers)," *Phys. Rev. Lett.*, vol. 78, pp. 1667–1670, Mar 1997.

[177] P. Törmä and W. L. Barnes, "Strong coupling between surface plasmon polaritons and emitters: a review," *Rep. Prog. Phys.*, vol. 78, p. 013901, dec 2014.

[178] Y. Zhang, J. Aizpurua, and R. Esteban, "Optomechanical collective effects

in surface-enhanced raman scattering from many molecules," *ACS Photonics*, vol. 7, pp. 1676–1688, Jul 2020.

[179] T. Neuman, J. Aizpurua, and R. Esteban, "Quantum theory of surface-enhanced resonant raman scattering (serrs) of molecules in strongly coupled plasmon–exciton systems," *Nanophot.*, vol. 9, no. 2, pp. 295–308, 2020.

[180] R. Chikkaraddy, B. de Nijs, F. Benz, S. J. Barrow, O. A. Scherman, E. Rosta, A. Demetriadou, P. Fox, O. Hess, and J. J. Baumberg, "Single-molecule strong coupling at room temperature in plasmonic nanocavities," *Nature*, vol. 535, pp. 127–130, July 2016.

[181] F. Benz, M. K. Schmidt, A. Dreismann, R. Chikkaraddy, Y. Zhang, A. Demetriadou, C. Carnegie, H. Ohadi, B. de Nijs, R. Esteban, J. Aizpurua, and J. J. Baumberg, "Single-molecule optomechanics in picocavities," *Science*, vol. 354, no. 6313, pp. 726–729, 2016.

[182] J. Schachenmayer, C. Genes, E. Tignone, and G. Pupillo, "Cavity-enhanced transport of excitons," *Phys. Rev. Lett.*, vol. 114, p. 196403, May 2015.

[183] S. M. Menke, W. A. Luhman, and R. J. Holmes, "Tailored exciton diffusion in organic photovoltaic cells for enhanced power conversion efficiency," *Nature Materials*, vol. 12, pp. 152–157, Feb 2013.

[184] J. Galego, F. J. Garcia-Vidal, and J. Feist, "Cavity-induced modifications of molecular structure in the strong-coupling regime," *Phys. Rev. X*, vol. 5, p. 041022, Nov 2015.

[185] J. Feist, J. Galego, and F. J. Garcia-Vidal, "Polaritonic chemistry with organic molecules," *ACS Photonics*, vol. 5, pp. 205–216, Jan 2018.

[186] J. E. Lennard-Jones, "Cohesion," *Proceedings of the Physical Society*, vol. 43, p. 461, sep 1931.

[187] J. N. Israelachvili, "Thermodynamic principles of self-assembly," in *Intermolecular and Surface Forces (Third Edition)* (J. N. Israelachvili, ed.), pp. 503–534, Academic Press, 2011.

[188] S. Ma, S. Du, G. Pan, S. Dai, B. Xu, and W. Tian, "Organic molecular aggregates: From aggregation structure to emission property," *Aggregate*, vol. 2, no. 4, p. e96, 2021.

[189] G. M. Whitesides and M. Boncheva, "Beyond molecules: self-assembly of mesoscopic and macroscopic components," *Proc. Natl. Acad. Sci. U S A*, vol. 99, pp. 4769–4774, Apr. 2002.

[190] R. Zhang, Y. Zhang, Z. Dong, S. Jiang, C. Zhang, L. Chen, L. Zhang, Y. Liao, J. Aizpurua, Y. Luo, J. Yang, and J. Hou, "Chemical mapping of a single molecule by plasmon-enhanced raman scattering," *Nature*, vol. 498, pp. 82–86, 2013.

[191] S. Ribeiro, J. Aizpurua, and R. Esteban, "Influence of direct dipole-dipole interactions on the optical response of two-dimensional materials in strongly inhomogeneous infrared cavity fields," *Phys. Rev. A*, vol. 108, p. 043718, Oct 2023.

[192] R. M. A. Vergauwe, A. Thomas, K. Nagarajan, A. Shalabney, J. George, T. Chervy, M. Seidel, E. Devaux, V. Torbeev, and T. W. Ebbesen, "Modification of enzyme activity by vibrational strong coupling of water," *Angew. Chem., Int. Ed.*, vol. 58, pp. 15324–15328, 2019.

[193] F. Herrera and F. C. Spano, "Cavity-controlled chemistry in molecular ensembles," *Phys. Rev. Lett.*, vol. 116, p. 238301, Jun 2016.

[194] J. Flick, M. Ruggenthaler, H. Appel, and A. Rubio, "Atoms and molecules in cavities, from weak to strong coupling in quantum-electrodynamics (qed) chemistry," *P. Nat. Acad. Sci.*, vol. 114, no. 12, pp. 3026–3034, 2017.

[195] A. Thomas, L. Lethuillier-Karl, K. Nagarajan, R. M. A. Vergauwe, J. George, T. Chervy, A. Shalabney, E. Devaux, C. Genet, J. Moran, and T. W. Ebbesen, "Tilting a ground-state reactivity landscape by vibrational strong coupling," *Science*, vol. 363, no. 6427, pp. 615–619, 2019.

[196] J. Fischer and M. Wendland, "On the history of key empirical intermolecular potentials," *Fluid Phase Equilibria*, vol. 573, p. 113876, 2023.

[197] L. Hand and J. Finch, *Analytical Mechanics*. Cambridge University Press, 1998.

[198] H. Goldstein, C. Poole, and J. Safko, *Classical Mechanics*. Addison Wesley, 3 ed., 2001.

[199] V. Balakrishnan, *Elements of Nonequilibrium Statistical Mechanics*. Springer, 2021.

[200] W. Coffey, Y. Kalmykov, and J. Waldron, *The Langevin Equation: With Applications to Stochastic Problems in Physics, Chemistry, and Electrical Engineering*. World Scientific, Singapore, 2004.

[201] C. Gardiner, *Handbook of stochastic methods for physics, chemistry, and the natural sciences*. Springer, 1985.

[202] Z. Ficek and S. Swain, "A cavity qed test of quantum mechanics," in *Modern Challenges in Quantum Optics* (M. Orszag and J. C. Retamal, eds.), vol. 575 of *Lecture Notes in Physics*, pp. 262–276, Springer, Berlin, Heidelberg, 2001.

[203] M. Barbry, P. Koval, F. Marchesin, R. Esteban, A. G. Borisov, J. Aizpurua, and D. Sánchez-Portal, "Atomistic near-field nanoplasmonics: Reaching atomic-scale resolution in nanooptics," *Nano Lett.*, vol. 15, pp. 3410–3419, May 2015.

[204] B. Doppagne, M. C. Chong, H. Bulou, A. Boeglin, F. Scheurer, and G. Schull, "Electrofluorochromism at the single-molecule level," *Science*, vol. 361, no. 6399, pp. 251–255, 2018.

[205] P. Johansson, "Light emission from a scanning tunneling microscope: Fully retarded calculation," *Phys. Rev. B*, vol. 58, pp. 10823–10834, Oct 1998.

[206] J. J. Baumberg, "Picocavities: a primer," *Nano Letters*, vol. 22, no. 14, pp. 5859–5865, 2022.

[207] D. T. W. Lin and C.-K. Chen, "A molecular dynamics simulation of tip4p and lennard-jones water in nanochannel," *Acta Mechanica*, vol. 173, pp. 181–194, Dec 2004.

[208] M. M. Tirado, C. L. Martínez, and J. G. de la Torre, "Comparison of theories for the translational and rotational diffusion coefficients of rod-like macromolecules. application to short dna fragments," *The Journal of Chemical Physics*, vol. 81, pp. 2047–2052, 08 1984.

[209] J. Gieseler and J. Millen, "Levitated nanoparticles for microscopic thermodynamics—a review," *Entropy*, vol. 20, no. 5, 2018.

[210] S. Chen, Y.-H. Xiao, M. Qin, G. Zhou, R. Dong, R. Devasenathipathy, D.-Y. Wu, and L. Yang, "Quantification of the real plasmonic field transverse distribution in a nanocavity using the vibrational stark effect," *The Journal of Physical Chemistry Letters*, vol. 14, no. 7, pp. 1708–1713, 2023. PMID: 36757268.

[211] T. Giovannini, L. Nicoli, S. Corni, and C. Cappelli, "The electric field morphology of plasmonic picocavities," *Nano Letters*, vol. 25, no. 27, pp. 10802–10808, 2025. PMID: 40560118.

[212] F. Glerean, E. M. Rigoni, G. Jarc, L. D. Negro, and F. Carbone, "Ultrafast pump-probe phase-randomized tomography," *Light: Science & Applications*, vol. 14, no. 115, 2025.

[213] L. Qiao, R. R. Pela, and C. Draxl, "First-principles approach to ultrafast pump-probe spectroscopy in solids," 2025.

[214] X. X. Han, R. S. Rodriguez, C. L. Haynes, Y. Ozaki, and L. Jensen, "Surface-enhanced raman spectroscopy," *Nature Reviews Methods Primers*, vol. 1, no. 87, 2021.

[215] D. Cialla-May, A. Bonifacio, A. Markin, N. Markina, S. Fornasaro, A. Dwivedi, T. Dib, E. Farnesi, C. Liu, A. Ghosh, M. Schmitt, and J. Popp, "Recent advances of surface enhanced raman spectroscopy (sers) in optical biosensing," *TrAC Trends in Analytical Chemistry*, vol. 181, p. 117990, 2024.

[216] L. Anderegg, L. W. Cheuk, Y. Bao, S. Burchesky, W. Ketterle, K.-K. Ni, and J. M. Doyle, "An optical tweezer array of ultracold molecules," *Science*, vol. 365, no. 6458, pp. 1156–1158, 2019.

[217] J. T. Zhang, L. R. B. Picard, W. B. Cairncross, K. Wang, Y. Yu, F. Fang, and K.-K. Ni, "An optical tweezer array of ground-state polar molecules," *Quantum Science and Technology*, vol. 7, p. 035006, may 2022.

[218] D. K. Ruttley, A. Guttridge, S. Spence, R. C. Bird, C. R. Le Sueur, J. M. Hutson, and S. L. Cornish, "Formation of ultracold molecules by merging optical tweezers," *Phys. Rev. Lett.*, vol. 130, p. 223401, May 2023.

[219] D. K. Ruttley, A. Guttridge, T. R. Hepworth, and S. L. Cornish, "Enhanced quantum control of individual ultracold molecules using optical tweezer arrays," *PRX Quantum*, vol. 5, p. 020333, May 2024.

[220] L. R. B. Picard, G. E. Patenotte, A. J. Park, S. F. Gebretsadkan, and K.-K. Ni, "Site-selective preparation and multistate readout of molecules in optical tweezers," *PRX Quantum*, vol. 5, p. 020344, May 2024.

[221] Y. Lu, C. M. Holland, C. L. Welsh, X.-Y. Chen, and L. W. Cheuk, "Probing coherent many-body spin dynamics in a molecular tweezer array quantum

simulator," 2026.

[222] S. Wüster and J.-M. Rost, "Rydberg aggregates," *Journal of Physics B: Atomic, Molecular and Optical Physics*, vol. 51, p. 032001, jan 2018.

[223] D.-W. Wang, M. D. Lukin, and E. Demler, "Quantum fluids of self-assembled chains of polar molecules," *Phys. Rev. Lett.*, vol. 97, p. 180413, Nov 2006.

[224] G. Pupillo, A. Griessner, A. Micheli, M. Ortner, D.-W. Wang, and P. Zoller, "Cold atoms and molecules in self-assembled dipolar lattices," *Phys. Rev. Lett.*, vol. 100, p. 050402, Feb 2008.

[225] J. B. Birks, L. G. Christophorou, and R. H. Huebner, "Excited electronic states of benzene and naphthalene," *Nature*, vol. 217, pp. 809–812, Mar 1968.

[226] D. A. da Silva Filho, R. Friedlein, V. Coropceanu, G. Öhrwall, W. Osikowicz, C. Suess, S. L. Sorensen, S. Svensson, W. R. Salaneck, and J.-L. Brédas, "Vibronic coupling in the ground and excited states of the naphthalene cation," *Chem. Commun.*, pp. 1702–1703, 2004.

[227] W. Zou, R. Kalescky, E. Kraka, and D. Cremer, "Relating normal vibrational modes to local vibrational modes: benzene and naphthalene," *Journal of Molecular Modeling*, vol. 19, pp. 2865–2877, Jul 2013.

[228] M. Fasser and S. Ribeiro, "Supporting data for article "aggregation dynamics of nonpolar molecules in electromagnetically confined picocavities"," *Zenodo*, https://doi.org/10.5281/zenodo.20825383, 2026.

List of Publications

Publications during PhD

- A. Bychek, M. Fasser, I. Vybornyi, K. Hammerer, S. F. Yelin, H. Ritsch, and R. Holzinger, "Continuous Narrow-Linewidth Superradiance in Waveguide QED", *arXiv:2607.06556*, 2026
- M. Fasser, C. Genes, H. Ritsch, and R. Holzinger, "Benchmarking the Cumulant Expansion Method Using Dicke Superradiance", *Photonics, 12(10)*, 2025
- M. Fasser, L. Ostermann, H. Ritsch, and C. Hotter, "Subradiance and superradiant long-range excitation transport among quantum emitter ensembles in a waveguide", *Optica Quantum, 2, 397-403*, 2024
- M. Fasser, C. Hotter, D. Plankensteiner, and H. Ritsch, "Threshold studies for a hot beam superradiant laser including an atomic guiding potential", *Open Research Europe 4:8*, 2024